

Predicting the Thermodynamic Properties of Complex Molecular Systems  
for Environmental Applications

By

Jessica Deloris Haley

Dissertation

Submitted to the Faculty of the  
Graduate School of Vanderbilt University  
in partial fulfillment of the requirements

for the degree of

DOCTOR OF PHILOSOPHY

in

Chemical Engineering

August, 2015

Nashville, Tennessee

Approved:

Clare M<sup>c</sup>Cabe, Ph.D.

Peter Cummings, Ph.D.

Doug LeVan, Ph.D.

Mark Abkowitz, Ph.D.

Copyright © 2015 by Jessica Deloris Haley  
All Rights Reserved

To my family, supportive beyond measure

## ACKNOWLEDGMENTS

Over the past ten years, I have received tremendous support and encouragement from a great number of individuals. Dr. Clare McCabe, my advisor, has been a colleague, coach, and friend. She introduced me to academic research and chemical engineering, allowing me to join her lab group as an undergraduate researcher. After completing my undergraduate studies, she provided me with invaluable information on choosing the next step, and encouraged me to pursue graduate school. Her steadfast support, patient guidance, and thoughtful mentorship made this Ph.D a productive and stimulating journey. Dr. McCabe's intellectual heft, in providing indispensable technical and editorial advice, is matched only by her sincere good nature and humility, and she taught me innumerable lessons and insights into the workings of academic research. In addition—and seemingly effortless—Dr. McCabe was a stellar example of how to succeed in the fields of engineering and research as a woman. I am truly fortunate to have had the opportunity to work with her.

I likewise thank my dissertation committee members, Dr. Peter Cummings, Dr. Doug LeVan, and Dr. Mark Abkowitz: their friendly guidance, thought-provoking input, and support were essential, as I transformed an idea to a completed study. In addition, my laboratory members—Jana Black, Gaurav Das, and Tim Moore—all provided helpful, valuable research advice. Similarly, I recognize Dr. Christopher Iacovella for his meaningful intellectual and practical contributions. His mentorship, guidance, abundance of knowledge, and willingness to assist are greatly appreciated and for which I am forever grateful. In addition, I thank Dean Burgess Mitchell for always being a supportive and listening ear. He is a genuinely kind person, who offered his assistance countless times during my time here at Vanderbilt University.

Through this process, my closest friends, Dr. Kerwin Low and Chante Stubbs spent many countless hours, and some sleepless nights, proofreading and listening to me discuss my research. Dr. Kerwin Low, with his ever-positive attitude, was especially helpful offering uplifting and

encouraging words throughout the past few months. Without his proofreading skills and overall willingness to help in any capacity, my PhD journey would be without a doubt more difficult. Chante Stubbs has been a great friend, since we met our freshman year of undergrad. Her caring, supportive, and protective personality encouraged me to persevere in many moments of doubt. I am eternally grateful for their necessary encouragement and support.

Likely atypical in a Ph.D. dissertation acknowledgments section, I express my deep appreciation and gratitude to the National Football League (“NFL”) Tennessee Titans for allowing me to serve as a cheerleader for the past four years: my time in Nashville was distinctly enjoyable for this reason.

Finally, I would be remiss if I did not acknowledge on whose shoulders I stand: my family. From preschool to this Ph.D, my parents have supported me every step of the way. Although the journey has not been easy, my parents have nevertheless made countless sacrifices in enabling me to reach this mark. They have taught me several valuable life lessons by leading by example: they showed me how to be a hard worker, how to respect myself, how to persist when the odds are against me, and how to be an independent, intelligent, and graceful woman. My father, who is also my hero, ignited my passion for science and engineering. As an electrical engineer, he inspired me to begin in the engineering field. He also made many sacrifices to make my dreams and goals a reality, and I will always look up to him as a source of encouragement and drive. In addition to my father, my mother is the model woman—she exudes resilience, strength, faith, and character, and I will forever strive to embody those attributes. She is my best friend, advisor, and champion. Aside from my parents, I am thankful for my brother, Jeremiah, who provided comedic relief during the most stressful times of this adventure. All in all, I am forever grateful for my family’s love, patience, and encouragement: they have sustained me throughout my pursuits, but especially during the final stages of this Ph.D. Words escape my appreciation and love for them. My simple promise to them is this: I will meet the challenges of life with the good foundation they gave me. Thank you so much.

Finally, I gratefully acknowledge the funding sources that made my Ph.D. work possible. Funding was provided by the National Science Foundation grant numbers CBET-1028374 and CBET-1067642 as well as the U.S. Department of Education for Graduate Assistance in Areas of National Need (GAANN) Fellowship under grant number P200A090323.

## TABLE OF CONTENTS

	Page
DEDICATION.....	iii
ACKNOWLEDGEMENTS.....	iv
LIST OF TABLES.....	ix
LIST OF FIGURES.....	x
Chapter	
I. Introduction.....	1
II. Statistical Associating Fluid Theory Background.....	6
III. Statistical Associating Fluid Theory (SAFT) Equations.....	11
IV. Molecular Simulations.....	23
V. Predicting the Phase Behavior of Fluorinated Organic Molecules using the GC-SAFT-VR Equation of State.....	28
Introduction.....	28
Molecular Model and Theory.....	33
Results and Discussion.....	36
Conclusions.....	54
VI. Modeling Organic Sulfur Molecules with GC-SAFT-VR Theory for Removal of Sulfur Impurities from Crude Oil.....	55
Introduction.....	55
Molecular Model and Theory.....	58
Results and Discussion.....	62
Conclusions.....	74
VII. Predicting the Phase Behavior of Fatty Acid Methyl Esters and their Mixtures Using a Group Contribution Based SAFT Approach.....	76
Introduction.....	76
Molecular Model and Theory.....	83
Results and Discussion.....	86
Conclusions.....	96
VIII. Investigating the Phase Behavior of Carbon Dioxide: A Quadrupolar Fluid Using a SAFT Based Approach.....	98
Introduction.....	98
Molecular Model and Theory.....	101

Results and Discussion.....	106
Conclusions .....	119
IX. Examining the Aggregation Behavior of Polymer Grafted Nanoparticles using Molecular Simulation and Theory .....	120
Introduction .....	120
Simulation Model and Methodology .....	122
Simulation Model.....	122
Simulation Method .....	123
Hetero-SAFT-VR Theory .....	126
Results .....	128
Pure TNP Systems .....	128
TNP+ Solvent Systems.....	135
Conclusions .....	138
X. Future Work and Conclusions .....	140
REFERENCES .....	144



## LIST OF TABLES

Table		Page
5.1.	GC-SAFT-VR parameters for the segment size $\sigma$ and segment number, $m$ , of each functional group studied. ....	37
5.2.	GC-SAFT-VR segment-segment dispersion energy range parameters $\lambda_{ki,lj}$ .....	37
5.3.	GC-SAFT-VR segment-segment dispersion energy well depth parameters $\epsilon_{ki,lj} / k_B$ .....	38
6.1.	GC-SAFT-VR parameters for the segment size $\sigma$ and segment number, $m$ , of each functional group studied .....	65
6.2.	GC-SAFT-VR segment-segment dispersion energy range parameters $\lambda_{ki,lj}$ .....	65
6.3.	GC-SAFT-VR segment-segment dispersion energy well depth parameters $\epsilon_{ki,lj} / k_B$ (K) .....	66
7.1.	Chemical Structure of Fatty Acid Methyl Esters considered.....	76
7.2.	GC-SAFT-VR parameters for the segment size and segment number of each functional group studied.....	87
7.3.	GC-SAFT-VR segment-segment dispersion energy well depth parameters $\epsilon_{ki,lj} / k_B$ (K) .....	87
7.4.	GC-SAFT-VR segment-segment dispersion energy range parameters $\lambda_{ki,lj}$ .....	87
8.1	Intermolecular Parameters for Carbon Dioxide .....	106
8.2	Intermolecular Parameters for Nitrogen.....	114
9.1.	Solvent parameters used in the SAFT predictions.....	128

## LIST OF FIGURES

Figure	Page
2.1. Schematic illustration of the perturbation scheme for a fluid within the GC-SAFT-VR framework. A SAFT fluid is a collection of spherical hard segments that can interact via repulsion and attractive forces (dispersion). The monomers can form chains through covalent bonds and association interactions are accounted for if present. ....	10
3.1. Representation of molecular model for a non-associating homonuclear chain used in the SAFT-VR approach, where $m$ represents the chain length and $\sigma$ is the segment.....	11
3.2. Square well is characterized by three parameters, the interaction diameter $\sigma_{ij}$ , well depth of the square well $\varepsilon_{ij}$ , and the potential range $\lambda_{ij}$ .....	12
4.1. Simulations serve as a bridge between microscopic and macroscopic. Adapted from Introduction to Molecular Dynamic simulation by Michael P. Allen .....	23
4.2. Schematic representation of the quench dynamic method. ....	27
5.1. Electrostatic potential map for perfluorobutylpentane ( $F_4H_5$ ) created using GaussView version 5. The red region represents the lowest electrostatic potential data and the blue region represents the highest. ....	41
5.2. GC-SAFT-VR molecular parameters for the functional groups $CF_3$ , $CF_2$ , and $CF$ as a function of the molecular weight ( $M_w$ ): (a) segment size, (b) potential depth, (c) potential range.....	42
5.3. Predicted composition curves for a.) perfluorohexane + pentane (circles), + heptane (triangles) and + octane (squares), and b.) hexane + perfluoropentane (circles), + perfluorohexane (squares), + perfluoroheptane (triangles) and + perfluorooctane (diamonds). Solid lines represents GC-SAFT-VR predictions and the data points represent experimental data .....	46
5.4. $Pxy$ prediction of a) perfluorohexane + hexane binary mixtures at 298.15K, 308.15K, and 318.15K (bottom to top) and b) perfluorohexane + pentane binary mixture at 293.65 K. The lines correspond to the GC-SAFT-VR predictions and the symbols the experimental data .....	47
5.5. Predictions of the $Txy$ phase diagram for perfluorooctane + perfluoro-2-methylpentane 1.013 bar. The solid lines correspond to the theoretical predictions and the symbols the experimental data .....	48
5.6. $P-x-y$ diagram at 259 K, 253 K, 246 K, and 238 K. (top to bottom) of perfluorobutane and butane binary mixtures. <b>b.)</b> $P-x-y$ diagram at 342 K, 327 K and 312 K (top to bottom) of perfluorobutane and butene binary mixtures. Solid lines represent the GC-SAFT-VR theory while the experimental data points are represented by open circles.....	49

5.7.	a.) LLE diagram with constant pressure of 1.013 bar for binary mixtures of perfluorooctane + alkanes, $n\text{-C}_n\text{H}_{2n+2}$ with $n = 6\text{-}9$ (from $n = 9$ to $n = 6$ from top to bottom). Solid lines represent GC-SAFT-VR theory and open circles represents the experimental data points. b.) LLE diagram with constant pressure of 1.013 bar for binary mixtures of perfluorohexane + hexane. The solid line represents the prediction. The open circles represent the experimental data. ....	50
5.8.	a.) Molar volume as a function of carbon number for PFAA and octane binary mixtures. b.) Partial molar volume as a function of carbon number for PFAA and octane binary mixtures. Solid lines represent theory and the symbols the experimental data. ....	51
5.9.	Constant temperature $P_{xy}$ slices of $\text{CO}_2$ + a) perfluorohexane binary mixture at 303.15 K (squares), 313.15 K (circles), and 323.15 K (triangles), b) perfluorooctane at 293.15 K, 303.15 K, 313.15 K, 323.15 K, 333.15 K, 343.15 K, and 353.15 K (bottom to top) and c) $\text{CO}_2$ + $\text{C}_5\text{H}_3\text{F}_9\text{O}$ at 303.15 K (squares), 313.15 K (circles), and 323.15 K (triangles). Solid lines represent the GC-SAFT-VR predictions and the symbols points the experimental data. ....	53
6.1.	Schematic representation of Thiophene molecular model.....	62
6.2.	a.) Vapor pressure curve as a $p$ vs. $T$ representations for thiophene ( $\text{C}_4\text{H}_4\text{S}$ ) compared with GC-SAFT-VR approach using determined parameters. The blue data points represent experimental data and the continuous curve the GC-SAFT-VR results. b.) Coexisting densities for thiophene compared with the GC-SAFT-VR approach using determined parameters. The blue data points represent experimental data and the continuous curve the GC-SAFT-VR results.....	63
6.3.	Schematic representation of molecular model for thiophene derivatives: 3-methylthiophene, 2-methylthiophene, and Benzothiophene.....	64
6.4.	a.) Thiophene (1) + hexane (2) at 338.15K and 323.15K (top to bottom) b.) Thiophene (1)+ hexene (2) at 333.15K and 323.15K (top to bottom) c.) Thiophene (1) + heptane (2) at 1.0133 bar and d.) Thiophene (1) + methylbutane (2) at 1.0133 bar . The solid lines are the GC-SAFT-VR predictions and the symbols the experimental data.....	67
6.5.	Isothermal VLE for Thiophene (1) + $\text{CO}_2$ (2) at $T=383\text{K}$ , $363\text{K}$ , $334\text{K}$ , and $314\text{K}$ (top to bottom) The solid lines are the GC-SAFT-VR predictions and the symbols the experimental data.....	68
6.6.	Isothermal VLE for Thiophene and Aromatic compounds a.) Thiophene (1) + Toluene (2) at $298\text{K}$ b.) Thiophene (1) + Benzene (2) at $0.9003$ bar. The solid lines are the GC-SAFT-VR predictions and the symbols the experimental data.....	69
6.7.	(a) Thiophene (1) + methanol (2) at 323.15 K, 318.15 K, 313.15 K, 308.15 K (top to bottom), (b) Thiophene (1) + methanol (2) at 0.603 bar, (c) Thiophene (1) + ethanol (2) at 318.15 K, 313.15 K, and 308.15 K (top to bottom) d.) Thiophene (1) + propanol (2) at 318.15 K, 313.15 K, and 308.15K (top to bottom). The solid lines are the GC-SAFT-VR predictions and the symbols the experimental data. ....	70

6.8.	Vapor–liquid equilibria for binary mixtures of (a) 3-methylthiophene + hexane at 333.15 K (b) 3-methylthiophene + hexene at 333.15 K and (c) 3-methylthiophene + heptane at 1 bar. The solid lines represent the theoretical predictions and the symbols represent the experimental results .....	72
6.9.	Vapor–liquid equilibria for binary mixtures of (a) 3-methylthiophene + 2-methylbutane at 1 bar. (b) 3-methylthiophene + 2-methylpentane at 333.15 K. The solid lines represent the theoretical predictions and the symbols represent the experimental results .....	73
6.10.	Vapor–liquid equilibria for binary mixtures of (a) benzothiophene + dodecane at 0.995 bar (b) benzothiophene + octanol at 0.995 bar. The solid lines represent the theoretical predictions and the symbols represent the experimental results .....	74
7.1.	Comparison between theoretical predictions from the GC-SAFT-VR equation and experimental data for the vapor pressure of a) methyl caproate, methyl caprylate, methyl myristate, and methyl oleate (left to right) b) methyl caprate, methyl laurate, methyl palmitate, and methyl stearate (left to right) Symbols correspond to the experimental data and the solid lines to the theoretical results. ....	88
7.2.	Comparison between theoretical predictions from the GC-SAFT-VR equation and experimental data for the saturated liquid density of methyl caprylate (diamonds), methyl caprate (squares), methyl laurate (circles), and methyl myristate (crosses) (top to bottom). Symbols represent the experimental data and solid lines the theoretical results. ....	89
7.3.	Constant pressure $T_{xy}$ slices of the (a) methyl caprylate + methyl caprate phase diagram at 0.0133 MPa, 0.0066 MPa, 0.0053 MPa, and 0.0039 MPa (from top to bottom), (b) methyl caprylate + methyl caproate phase diagram at 0.0066 MPa, 0.0053 MPa, 0.0039 MPa, and 0.0027 MPa (from top to bottom), (c) methyl laurate + methyl caprate phase diagram at 0.0133 MPa, 0.0066 MPa, and 0.0053 MPa (from top to bottom), (d) methyl myristate + methyl laurate phase diagram at 0.0133 MPa, 0.0066 MPa, 0.0053 MPa, and 0.0039 MPa (from top to bottom), and (e) methyl myristate + methyl palmitate phase diagram at 0.0133 MPa, 0.0066 MPa, 0.0053 MPa, and 0.0039 MPa (from top to bottom) (f) methyl palmitate + methyl stearate phase diagram at 0.0040 MPa The solid lines correspond to the theoretical predictions and the symbols represent the experimental data. ....	91
7.4.	$P_{xy}$ (a) and $xy$ (b) diagram for the methyl oleate + methyl stearate binary mixture at 473.15K. The solid lines represent the theoretical predictions and the symbols represent the experimental data. ....	92
7.5.	a.) VLE at atmospheric pressure for the methanol+ methyl myristate and ethanol + methyl myristate b.) VLE at atmospheric pressure for the methanol+ methyl laurate and ethanol + methyl laurate The solid lines represent the predictions from the GC-SAFT-VR equation with fitted cross interaction and the symbols the experimental data. ....	93
7.6.	The solid lines represent the predictions from the GC-SAFT-VR equation with fitted cross interaction and the symbols the experimental data. a.) VLE for methanol + methyl laurate at 493 K, 523 K, 543 K (bottom to top) b.) VLE for methanol + methyl myristate at 493 K, 523 K, 543 K (bottom to top).....	94
7.7.	Constant temperature $P_{xy}$ slice at 343.15 K of the methyl palmitate + CO <sub>2</sub> . The solid lines represent the predictions from the GC-SAFT-VR equation with fitted cross interaction,	

	dotted lines utilized Lorentz Berthelot combining rules and the symbols the experimental data.....	95
7.8.	Constant temperature $P_{xy}$ slices of the (a) methyl myristate, (b) methyl oleate, (c) methyl stearate, and (d) methyl palmitate + CO <sub>2</sub> phase diagrams at 313.15K, 323.15K, 333.15K, 343.15K (bottom to top). The solid lines represent the predictions from the GC-SAFT-VR equation and the symbols the experimental data .....	96
8.1.	Schematic representation of quadrupolar molecule, CO <sub>2</sub> , where quadrupole moment approximated as two dipoles.....	101
8.2.	Schematic representation of the interdipole site coordination system, with polar axis along $r$ .....	102
8.3.	Carbon dioxide a.) vapor pressure b.) vapor liquid coexistence densities. Data points correspond to the experimental data and solid lines correspond to GC-SAFT-VR + D predictions. ....	107
8.4.	$P_x$ slice of the CO <sub>2</sub> + ethane phase diagrams at $T= 210$ K. Solid lines correspond to GC-SAFT-VR+D predictions, Dashed lines correspond to original SAFT-VR predictions using parameters proposed by Galindo <i>et al.</i> , [17], Blue Dashed lines correspond to original SAFT-VR predictions using parameters proposed by Blas <i>et al.</i> [18], symbols correspond the experimental data .....	108
8.5.	$P_x$ slices of the CO <sub>2</sub> + ethane phase diagrams at different temperatures. Solid lines correspond to GC-SAFT-VR+D predictions, Dashed lines correspond to original SAFT-VR predictions using parameters proposed by Galindo <i>et al.</i> , [17], symbols correspond the experimental data .....	109
8.6.	$P_x$ slices of the CO <sub>2</sub> + $n$ -hexane phase diagrams at different temperatures a.) $T = 308.15$ K (black lines), 313.15 K (blue lines), b.) $T = 318.15$ K (black lines), 323.15 K (blue lines), c.) $T = 333.15$ K (black lines), and 353.15 K (blue lines). (bottom to top) Solid lines correspond to GC-SAFT-VR+D predictions, Dashed lines correspond to original SAFT-VR predictions using parameters proposed by Blas <i>et al.</i> and Colina <i>et al.</i> ,.....	110
8.7.	$P_x$ slices of the CO <sub>2</sub> + $n$ -heptane phase diagrams at $T = 310$ K and 353 K. (bottom to top). Solid lines correspond to GC-SAFT-VR+D predictions, Dashed lines correspond to original SAFT-VR predictions using parameters proposed by Blas <i>et al.</i> .....	111
8.8.	$P_x$ slices of the CO <sub>2</sub> + $n$ -octane phase diagrams at $T = 308$ K, 318 K, 333 K, and 343 K. (bottom to top). Solid lines correspond to GC-SAFT-VR+D predictions, Dashed lines correspond to original SAFT-VR predictions using parameters proposed by Blas <i>et al.</i> , symbols correspond the experimental data .....	112
8.9.	a.) $P_x$ slices of the CO <sub>2</sub> + $n$ -decane phase diagrams at $T = 308.15$ K and 313.15 K. b.) $P_x$ slices of the CO <sub>2</sub> + $n$ -dodecane phase diagrams at $T = 312$ K. Solid lines correspond to GC-SAFT-VR+D predictions, Dashed lines correspond to original SAFT-VR predictions using parameters proposed by Blas <i>et al.</i> .....	113
8.10.	a.) Constant temperature $p$ - $x$ slices of the phase diagram for the nitrogen (1) + pentane (2) + binary mixture at 277.43 b.) Constant temperature $p$ - $x$ slices of the phase diagram for	

the methane (1) + nitrogen (2) binary mixture at 95 and 113.7 K (from bottom to top). c.) Constant temperature $p$ - $x$ slices of the phase diagram for the butane (1) + nitrogen (2) binary mixture at 250 K, d.) Constant temperature $p$ - $x$ slices of the phase diagram for the heptane (1) + nitrogen (2) binary mixture at 305.4 K. The continuous curves correspond to predictions from the quadrupolar SAFT-VR approach, red dashed lines correspond to predictions from GC-SAFT-VR +D theory, and the dashed curves, predictions from the original SAFT-VR equation. The circles are experimental results .....	114
8.11. $Px$ slices of the CO <sub>2</sub> + perfluorohexane phase diagrams at $T=$ 298 K, 303 K, 313.15 K, 323.15 K, and 353.15 K. Solid lines correspond to GC-SAFT-VR+D predictions, Dashed lines correspond to original SAFT-VR predictions using parameters proposed by Tochigi <i>et al.</i> [19] Blue Dashed lines correspond to original SAFT-VR predictions using parameters proposed by Colina <i>et al.</i> , symbols correspond the experimental data .....	116
8.12. $Px$ slices of the CO <sub>2</sub> + perfluorooctane phase diagrams at $T=$ 293 K, 303 K, 313.15 K, 323.15 K, 333.15 K, 343.15 K, and 353.15 K. Solid lines correspond to GC-SAFT-VR+D predictions, Blue Dashed lines correspond to original SAFT-VR predictions using parameters proposed by Colina <i>et al.</i> , symbols correspond the experimental data .....	118
9.1. Schematic representation of the quench dynamic method, shown for 1000 TNP building blocks, each with a single 12 bead tether (13000 total particles). A bulk fluid state is first equilibrated. Next, the length of the box is instantaneously expanded and allowed to equilibrate, resulting in a two-phase system at coexistence. A histogram of the number density is constructed along the long dimension of the box; the average density of the dispersed and condensed phases is then computed from the respective regions of the histogram, taking care to exclude the interfacial region. ....	125
9.2. (a) Fluid phase equilibrium of alkane-tethered nanoparticle systems for 12 bead systems with $N_{GRAFT} = 1$ and 12 beads (black), $N_{GRAFT} = 2$ and 6 beads per tether (red), and $N_{GRAFT} = 4$ and 3 beads per tether (blue). Symbols represent the simulation results and in (a) lines correspond to predictions using rectilinear and scaling laws and (b) the SAFT predictions. ....	129
9.3. The potential of mean force (PMF) between different 12 bead per tether grafted nanoparticles at a volume fraction of $\sim 0.003$ and $T^* = 40$ and $N_{GRAFT} = 6$ (blue), $N_{GRAFT} = 4$ (green), $N_{GRAFT} = 2$ (red), and $N_{GRAFT} = 1$ (black). ....	130
9.4. (a) Fluid phase equilibrium of mono-tethered ( $N_{GRAFT} = 1$ ) TNP systems with 8 (black), 12 (red), 18 (blue) beads per tether as predicted from MD simulation. Symbols represent the simulation results and lines the predictions using rectilinear and scaling laws. (b) Fluid phase equilibrium of mono-tethered ( $N_{GRAFT} = 1$ ) TNP systems with 8 (black), 12 (red), 18 (blue), 24 (brown), 36 (green), 48 (light blue), and 100 (magenta) beads per tether as predicted from the SAFT equation of state, (c) Fluid phase equilibrium of di-tethered ( $N_{GRAFT} = 2$ ) TNP systems with total number of beads equal to 12 (black), 18 (red), 24 (blue) as predicted from MD simulation. Symbols represent the simulation results and lines the predictions using rectilinear and scaling laws. (d) Fluid phase equilibrium of di-tethered ( $N_{GRAFT} = 2$ ) TNP systems with total number of beads equal to 12 (black), 18 (red), 24 (blue), 48 (brown), and 96 (light blue) as predicted from the SAFT equation of state. (e) Fluid phase equilibrium of quad-tethered ( $N_{GRAFT} = 4$ ) TNP systems with total	

number of beads equal to 12 (black), 24 (red), and 48 (blue) as predicted from MD simulation. Symbols represent the simulation results and lines the predictions using rectilinear and scaling laws. (f) Fluid phase equilibrium of quad-tethered ( $N_{GRAFT} = 4$ ) TNP systems with total number of beads equal to 12 (black), 24 (red), 48 (blue), 96 (brown), and 192 (green)) as predicted from the SAFT equation of state.....	131
9.5. SAFT equation of state predictions for (a) Critical temperature as a function of the number of grafts for 6 (red), 12 (blue), 24 (green), and 48 (black) beads per tether, (b) Critical temperature as a function of the number of grafts for 12 (blue), 24 (green), and 48 (black) total beads, (c) Critical density as a function of the number of grafts for 6 (red), 12 (blue), 24 (green), and 48 (black) beads per tether, and (d) Critical density as a function of the number of grafts for 12 (blue), 24 (green), and 48 (black) total beads. ....	133
9.6. Fluid distribution ratio of TNP systems as a function of number of grafts in vacuum at $T^* = 21.4$ as predicted from the SAFT equation of state for 6 (red), 12 (green), 24 (blue), and 48 (black) beads per tether. ....	135
9.7. Critical temperature as a function of the number of grafts for 6 (red), 12 (blue), 18 (green), 24 (brown), and 48 (black) beads per tether as predicted from the SAFT equation at $P^* = 0.291$ for (a) nitrogen (b) carbon dioxide (c) ethylene and (d) propane .....	136
9.8. $k$ value as a function of the number of grafts for nanoparticles with 12 beads per tether as predicted from the SAFT equation of state at $T^* = 21.7$ for propane (black), ethylene (blue), nitrogen (red), and carbon dioxide (green).....	137
9.9. $k$ value is shown as a function of number of grafts for 12 (green), 18 (red), 24 (blue), and 48 (black) beads per tether as predicted from the SAFT equation at $T^* = 21.7$ for (a) nitrogen and (b) propane.....	138

## Chapter I

### Introduction

As society advances, energy demand will continue to grow; therefore, creating a more energy conscious environment is essential. The public and private sectors' ever-increasing attention to global climate change has pushed the goal of lowering emissions and waste generation to the forefront for many industries. As a result, there exists a need to fill major gaps in the information required to design more environmentally friendly processes and products. The call for advancement in our ability to design cleaner technologies, as well as to mitigate our ecological footprint, requires further investigation of key systems important to the energy arena.

For example, the unique properties of organic fluorinated molecules (e.g., low surface tension, high fluidity, low dielectric constant, high vapor pressure and compressibility, gas solubility, and excellent spreading properties [20]) are exploited in a wide range of energy applications including: the removal of CO<sub>2</sub> from gaseous effluents [21], environmentally friendly alternatives to cleaning solvents, refrigerants, foaming agents, carrier solvents for coatings, and lubricants [22], and the design of CO<sub>2</sub>-philic surfactants [9]. In addition to energy applications, these fluorinated molecules are also useful for medical applications as excipients for inhalative liquid drug carrier systems [23], eye replacement fluids [24], and oxygen carriers in artificial blood substitutes [9]. However, despite the proven industrial usefulness of these organofluorine molecules, only limited work has been done to experimentally characterize the thermodynamic properties and phase behavior of these molecules.

Another class of relevant environmental systems are those containing organic sulfur molecules (e.g., thiols, sulfides, and thiophene) present in gasoline. These molecules impair the effectiveness of emission control systems and contribute to significant air pollution making their study important in the design of more environmentally friendly processes. Due to these environmental concerns, many countries have employed stricter regulations on sulfur content in diesel fuel and gasoline [25]. Moreover, the call to meet the new sulfur standards of environmental legislation and to avoid air pollution during fuel combustion, poses a significant challenge to the petroleum industry. In order to minimize the cost of producing these fuels, new technology advances and innovations are required; thus, the ability to provide an understanding of the phase behavior of these fluids is important. The use of biodiesel fuels as a biodegradable replacement to petroleum-derived fuels is another area of current interest. Fatty acid methyl esters are molecules, which comprise the biodiesel fuel in different compositions. Investigation of these



molecules and their mixtures can provide key information on how to optimize the mixtures of the molecules to provide the ideal fuel conditions and properties.

Additionally, carbon dioxide is of interest as it is readily available, inexpensive, non-toxic, and non-flammable. Considered an important solvent for supercritical separation processes [26], supercritical CO<sub>2</sub> can serve as an energy efficient replacement for commonly used energy intensive separation processes, such as distillation and liquid–liquid extraction. Its advantages include lower extraction times, decreased degradation of extracts, and reduction of required volume of solvents [27]. Carbon dioxide's green properties are also utilized for such applications as enhanced oil recovery [28], food processing [29], extractions involving natural products and pharmaceuticals [30], environmental and soil remediation [30], semiconductor processing [31], and polymer production and processing [32]. Additionally, the design, optimization and operation of carbon dioxide capture and storage (CCS) systems is an important area of research. As carbon dioxide continues to emerge in the energy arena, phase behavior relationships must be predictable, to allow for both the design of equipment and processes to effectively exploit CO<sub>2</sub>'s green properties.

Finally in this work we consider the aggregation of nanoparticles. Nanoparticles have been explored for use in a wide range of environmental applications and in particular in the purification of water. As freshwater sources become increasingly scarce due to overconsumption and contamination, scientists have begun to consider seawater as a source of drinking water; however, for human consumption, desalination, though expensive, is required. Carbon nanotube membranes have been shown to have the potential to reduce desalination costs [33]. Similarly, nanofilters can be used to remediate or clean up ground water or surface water contaminated with chemicals and hazardous substances [34]. Another environmental related use for nanoparticles is as a fuel additives, [35] which improve fuel consumption and reduce harmful emissions. Furthermore, studies [36] indicate nanoparticles can serve as enhanced oil recovery (EOR) agents in the oil and gas industry. Additional energy applications [37], which utilize nanoparticles, include hydrogen storage, photocatalytic applications, and carbon capture and storage. However, to take advantage of the various applications available, the dispersion and aggregation of nanoparticles must be controlled. This is often a critical requirement and has led to evolution of a variety of strategies for regulating nanoparticle interactions and assembly.

A fundamental understanding of the factors that control the properties and phase behavior of these aforementioned systems is imperative for the continual improvement of processes; phase behavior dictates feasibility of various separation techniques as well as material processing pathways. The knowledge of the phase equilibrium of mixtures under the conditions of a

particular process will allow for [38]: 1) the specification of safe concentration limits for involved impurities, 2) defining the requirements for purification if necessary, and 3) designing efficient and safe processes. As experimental data is often limited or unavailable and experiments, which can provide this phase behavior information, are time consuming and costly, the development of more accurate and predictive modeling approaches is crucial.

### **Statistical Associating Fluid Theory**

Cubic equations of state (EOS) are often used industrially to describe the thermodynamic behavior of fluids. However, these equations are heavily empirical, relying on correlations from experimental data to determine appropriate values of adjustable parameters; thus, extrapolating to thermodynamic conditions outside of the fitting region generally provides limited applicability and delivers poor results. Conversely, statistical mechanics based equations of state are an attractive alternative because they tend to yield a more predictive approach by taking into account the effects of molecular shape, size, and interactions on the thermodynamic properties, i.e., the model parameters relate to physical interactions as opposed to merely adjusting to experimental data. As such, they are a better fit for modeling complex systems, since they can explicitly take into account the effect of molecular level interactions on the macroscopic behavior.

One such equation that embodies the aforementioned benefit is the statistical associating fluid theory (SAFT) [39, 40], which is a molecular-based equation of state founded on Wertheim's first order thermodynamic perturbation theory (TPT1) [41-44]. This approach describes molecules as chains of tangentially bonded homonuclear monomer segments that interact through dispersion and association interactions. Being rooted in statistical mechanics and based on a molecular-level model, SAFT typically lends itself well to the development of an accurate and predictive modeling approach and has been successfully to study the phase behavior of many industrially important systems [45]. In this work, we have focused on the SAFT-VR approach, which describes chain molecules formed from hard-core monomers that interact via attractive potentials of variable range (SAFT-VR) [46]. SAFT-VR has been applied to study the thermodynamics and phase behavior of a diverse group of fluids. A specific form of the SAFT-VR equation of state is the hetero-SAFT-VR, which allows the description of molecules formed from chains of tangentially bonded segments of different size and/or energy parameters rather than a homonuclear chain as in the SAFT-VR approach. This approach is the basis of a more specific heteronuclear group-contribution SAFT based approach (GC-SAFT-VR) [47, 48], which combines the SAFT-VR equation with a group contribution (GC) approach that allows for the description of hetero-segmented chains. The equation has been shown to provide an excellent

description of the phase behavior of pure associating and non-associating fluids and their mixtures, with minimal reliance on fitting the model parameters to experimental data. Parameters for key functional groups are obtained by fitting to experimental vapor pressure and saturated liquid density data for selected low molecular weight fluids and then used to predict the phase behavior of pure non-associating fluids and their mixtures without adjusting the group parameters to binary mixture data. Additional details of the SAFT approach are provided in Chapter 2.

This thesis will investigate the application of variations of the SAFT-VR equation of state including the hetero-SAFT-VR and GC-SAFT-VR approach to systems with significant environmental relevance in order to develop accurate theoretical approaches that can be used to describe phase equilibria in multicomponent systems containing non-polar, polar, and associating compounds. Specifically, the goal is to develop a molecular-based theoretical framework to predict the thermodynamic properties of carbon dioxide, fluorinated molecules, organic sulfur molecules, fatty acid methyl esters, and nanoparticles as well as their mixtures. Chapter 2 and 3 provides background on the SAFT theory and equations used in this work. Chapter 4 describes the molecular simulation background specifically the molecular dynamic technique utilized in this thesis. Chapter 5 describes the molecular models developed for fluorinated molecules, which will offer a predictive approach to describe the phase behavior and thermodynamic properties. Chapter 6 examines organic sulfur fluids, specifically, thiophene (as well as its derivatives), to develop a molecular model to describe the thermodynamic properties and phase equilibrium. This predictive approach will aid in designing and implementing new processes to meet the strict environmental regulations surrounding the petroleum industry. Chapter 7 investigates biodiesel fuel components, fatty acid methyl esters (FAME), which serves as a promising alternative to commonly used petroleum fuels. In this chapter, a theoretical model is developed and tested by comparing the theoretical predictions with experimental data for pure FAME molecules as well as mixtures of CO<sub>2</sub> and other FAME molecules. Chapter 8 explores the role of explicitly describing the long-range interactions (i.e. dipole-dipole, quadrupole-quadrupole) in the structures of quadrupolar molecules, such as carbon dioxide and nitrogen. A model is proposed utilizing the GC-SAFT-VR with dipole contribution (GC-SAFT-VR+D), which mimics the quadrupole with two dipoles oriented in opposite directions, offering a more realistic and predictive approach. In Chapter 9, the factors that control the dispersion and aggregation of tethered nanoparticle (TNP) systems is explored. In this chapter, molecular simulations, as well as the hetero-statistical associating fluid theory for potentials of variable range (hetero-SAFT-VR), have been used to calculate the fluid phase equilibrium of TNPs in both vacuum and in simple solvents under a wide range of conditions to determine how TNP architectures could be used to tune system properties

such as the aggregation/dispersion and dissolution. Finally, Chapter 10 reviews main conclusions of this work and presents discussion of future work.

## Chapter II

### Statistical Associating Fluid Theory Background

Accurately describing the thermodynamic phenomena of complex fluids is of great importance to a large number of industries. Therefore, much effort has been devoted to establish more precise and predictive approaches to determine the thermodynamic properties of fluids. Moreover, the need to develop modeling frameworks that consider association interactions, molecular shape, and electrostatic interactions becomes increasingly important as the complexity of fluids of interest increase. Addressing this issue, in a series of innovative papers [41-44], Wertheim performed a general analysis of the statistical mechanics of fluids that could associate into dimers, as well as higher-order multimers [49]. In the theory, Wertheim expanded the Helmholtz free energy as a series of integrals obtained from cluster expansions. The principal result of this work, Wertheim's thermodynamic perturbation theory (TPT), involves an expression for the Helmholtz free energy that accounts for the effect of intermolecular association and/or solvation forces [41-44]. Wertheim showed that it is possible to determine the properties of an associating or chain fluid based on knowledge of the thermodynamic properties of the monomer fluid [49].

Building on Wertheim's contributions, Chapman and co-workers developed an equation of state for modeling associating fluids, the statistical associating fluid theory (SAFT) [39, 45]. SAFT in its original form described molecules as chains of tangentially bonded homonuclear segments that interact through Lennard – Jones (LJ) dispersion and association interactions. The free energy of the associating fluid is expressed by the summation of different contributions, *viz*

$$A = A^{ideal} + A^{monomer} + A^{chain} + A^{assoc} \quad (2.1)$$

where  $A^{ideal}$  is the ideal free energy,  $A^{monomer}$  is the excess free energy due to the monomer interactions between the LJ segments that form the molecule,  $A^{chain}$  is the contribution due to chain formation, and  $A^{assoc}$  describes the intermolecular association.

After the initial development of the SAFT equation, various modifications to the original expressions were proposed. The widely used SAFT-HR, developed by Huang and Radosz [50], describes monomers as hard spheres that interact using the mean field term proposed by Chen and Kreglewski, which was fitted to the PVT data, second virial coefficient, and internal energy data of argon [51]. The SAFT-HR has been applied to study a number of fluid systems ranging from alkanes[52], cycloalkanes[53], CO<sub>2</sub> [53, 54], nitrogen[54], and polymers[54-57]. .

The simplest SAFT approach, SAFT-HS [40], describes hard-sphere segments interacting

at the van der Waals mean-field level, while the original SAFT equation of state treats the molecules as chains of LJ segments. The SAFT-HS approach has been applied to study a wide range of systems including alkanes [58], water [58], alcohols [59], nonionic surfactants [59, 60], perfluoroalkanes [61], xenon [62], and cyclic molecules [62], but is particularly suited to strongly associating fluids, as the dominant hydrogen-bonding interactions mask the simplified description of the weaker dispersion forces.

In more recent work, Blas and Vega proposed the soft-SAFT [63] approach in which the monomer fluid is modeled as a LJ fluid. The key differences between the original SAFT and the soft-SAFT equations lie in the use of the LJ potential for the reference fluid, hence accounting in a single term for dispersive and repulsive forces, while the original equation is based on a hard-spheres reference fluid [64]. In addition, the original SAFT equation uses the radial distribution function of hard spheres in the chain and association terms, while in soft-SAFT the radial distribution function of the LJ fluid is used. The approach has been used to describe the phase behavior of real fluids such as alkanes [65], perfluoroalkanes [66], water [67], alcohols [68], polymers [69], ionic liquids [70, 71], CO<sub>2</sub> [70], and N<sub>2</sub>O [70].

The perturbed-chain SAFT (PC-SAFT) [72], developed by Gross and Sadowski, considers a hard-chain, rather than a hard sphere, as the reference system for the application of standard high-temperature perturbation theory to obtain the dispersion contribution. The PC-SAFT equation has been shown to accurately describe thermodynamic properties such as vapor pressures, densities, and caloric properties of pure components as well as mixtures of many real systems including: gases, non-spherical solvents, and chainlike polymers.

This work focuses on the SAFT-VR approach, developed by Gil Villegas *et al.* [46], which describes chain molecules formed from hard-core monomers that interact via attractive potentials of variable range (SAFT-VR) [46]. Here, the variable range potential is described by a square well (SW), however, this robust approach allows for the use of other attractive potentials (e.g., Sutherland, Mie or Yukawa potential). In the SAFT-VR equation, the dispersive interactions are treated as a second-order high-temperature perturbation expansion following the work of Barker and Henderson [73-75]. This approach provides a more rigorous description of the thermodynamics than found in simpler versions of the SAFT approach such as the original SAFT equation or SAFT-HS. The SAFT-VR approach has been successfully used to describe the fluid phase equilibria of a wide range of important systems such as, alkanes [76], perfluoroalkanes [77], alcohols [78, 79], water [80, 81], refrigerant systems [82-84], polymers [79], and carbon dioxide [18].

In more recent work, the SAFT-VR equation of state (EOS) has been modified to

describe heteronuclear chain molecules in which chains composed of different kinds of segments are described. This hetero-SAFT-VR approach, allows molecules to be described as chains of tangentially bonded segments that can have different size and/or energy parameters that interact through an attractive potential of variable range [76, 85, 86]. The hetero-SAFT-VR approach was validated using isothermal-isobaric ( $NPT$ ) and Gibbs ensemble Monte Carlo (GEMC) simulation data and shown to successfully capture the effects of interaction energy, segment size, and molecular structure on the PVT and phase behavior of hetero-nuclear diblock fluids [76, 85, 87]. The hetero-SAFT-VR equations has been applied to the study of several hetero-segmented chain fluids both symmetric and asymmetric including: perfluoroalkanes[1, 2], perfluoroalkylalkanes[1, 88-90], and polyhedral oligomeric silsesquioxanes (POSS) systems[85].

A more specific approach is to implement a group contribution theory. In perhaps the first attempt at utilizing a SAFT based group contribution approach, Gros *et al.*[91] proposed the group contribution (GC) with association equation of state (GCA-EoS) where a group contribution associating term is added to the SAFT theory (original SAFT, PC-SAFT, and SAFT-VR). The GCA-EoS model was successfully applied to study the phase equilibria of binary and ternary mixtures containing alcohols, hydrocarbons, gases, and water [91]. In another attempt, Tobaly *et al.* [92-94], proposed a group-contribution SAFT-based equation of state (GC-SAFT), in which the representative groups are defined according to the molecules composition and structure; however, the molecules are modeled as homonuclear chains as the model parameters are obtained by averaging the parameters for the different groups. The GC-SAFT method has been tested using the original SAFT, PC-SAFT, and SAFT-VR equations and applied to study the phase behavior of a range of fluids. Overall, the GC-SAFT equation provides good predictions for the phase behavior of short-chain fluids, though increased deviations from experimental data are observed for the vapor pressures of longer-chain fluids. In addition, fitted binary interaction parameters are necessary for the study of multicomponent systems. In the work of Tihic *et al.* [95], the PC-SAFT equation is combined with the group contribution of Constantinou *et al.* [96], where isomers and proximity effects can be considered [49]. This approach has been used to study a wide range of polymer systems [95, 97, 98]. However, as in previously discussed approaches, the underlying homonuclear model does not enable the differentiation of groups at the molecular level.

Another group contribution SAFT approach is the SAFT- $\gamma$  [99] equation of state was developed to model heteronuclear molecules formed from fused segments. In this approach, each group is described by an integer number of segments and a parameter reflecting the contribution of each group  $k$  to the overall molecular properties. In the SAFT- $\gamma$  equation of state, the chain

term from the SAFT-VR approach is implemented. Using effective parameters, the chain contribution to the Helmholtz free energy is a function of the number of segment-segment contacts in the chain and the contact radial distribution function of an effective fluid [49]. Therefore, the heterogeneity of the chain is not explicitly accounted for in the model. This approach has found success in accurately describing the VLE of many systems including [99]: alkanes, branched alkanes, alkylbenzenes, and alcohols.

### **GC-SAFT-VR**

Based on the hetero-SAFT-VR equation of state, the group-contribution approach (GC-SAFT-VR) EOS, [48] which is explored in this work, combines the SAFT equation for potentials of variable range (VR) [86] with a group contribution [48] approach that allows for the description of hetero-segmented chains. This modification is represented in the schematic in Figure 2.2. In this approach, a collection of heteronuclear segments representing the different functional groups in a given molecule are considered to form the model chain. Thus the different functional groups within the molecule are explicitly represented in the model chain, allowing for a description of the effects of molecular structure on the thermodynamic properties of the fluid. In this approach, the detailed connectivity of the segments can be preserved and hence isomers differentiated. In addition, the location of the functional groups and association sites within a molecule can be specified. Group parameters are obtained by fitting to pure component experimental vapor pressure and saturated liquid density data for the molecules containing the groups of interest. The parameters are then used in a transferrable manner to determine the phase behavior of other fluids not included in the fitting process, thus reducing the reliance on experimental data. Finally, the approach can be extended to multicomponent systems in a transferable manner by utilizing group parameters, which are determined by the pure fluids. Another advantage to utilizing the GC-SAFT-VR approach is that when groups of interest are contained in the same molecule, binary interactions parameters between the groups can be obtained from pure components experimental data alone, without additional fitting to binary experimental data. Thus a predictive approach is developed, where the heterogeneity is considered at both the monomer and chain level. Using this hetero-segmented method, GC-SAFT-VR, [48] parameters have been developed for a wide range of functional groups that allow the phase behavior of compounds such as linear and branched alkenes [48], ketones [48], acetates [48], esters [47], alcohols [47], aldehydes [47], amines [47], carboxylic acids [47] and polymers [100] containing these functional groups to be studied. Details of the GC-SAFT-VR approach, utilized in this work, are provided in Chapter 3.



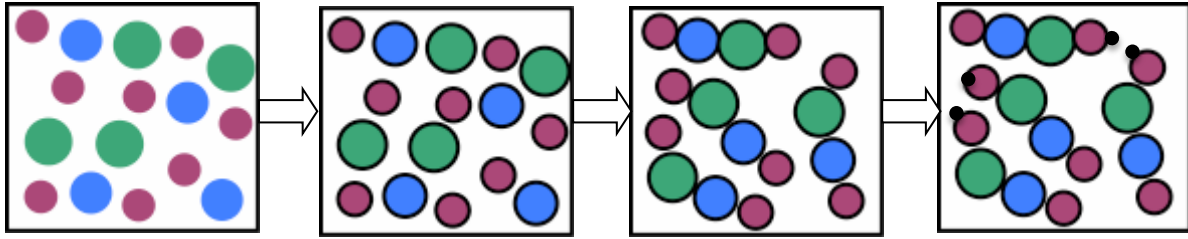


**Figure 2.1:** Schematic illustration of the perturbation scheme for a fluid within the GC-SAFT-VR framework. A SAFT fluid is a collection of spherical hard segments that can interact via repulsion and attractive forces (dispersion). The monomers can form chains through covalent bonds and association interactions are accounted for if present.

## Chapter III

### Statistical Associating Fluid Theory (SAFT) Equations

#### *SAFT-VR Approach for Pure Fluids*

In this approach, the molecular model consists of a chain with  $m$  attractive spherical segments of diameter  $\sigma$  (shown in Figure 3.2) that interact through an intermolecular potential. The potential,  $u^M$ , is expressed as the sum of a repulsive contribution and an attractive term:

$$u^M(r) = u^{HS}(r; \sigma) - \varepsilon \phi(r; \lambda) \quad (3.1)$$

where hard-sphere potential,  $u^{HS}$ , is the repulsive contribution, defined by:

$$u^{HS}(r; \sigma) = \begin{cases} \infty & \text{if } r < \sigma \\ 0 & \text{if } r > \sigma \end{cases} \quad (3.2)$$

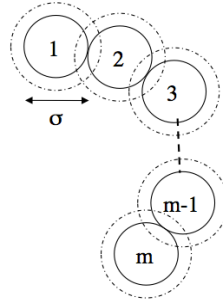


**Figure 3.1:** Representation of molecular model for a non-associating homonuclear chain used in the SAFT-VR approach, where  $m$  represents the chain length and  $\sigma$  is the segment.

The attractive interactions are characterized by the depth  $\varepsilon$  and shape  $\phi(r; \lambda)$ . In this case, we utilize a square well intermolecular potential. The intermolecular potential depends on three parameters to characterize the square well: the interaction diameter  $\sigma$ , well depth of the square well  $\varepsilon$ , and the potential range  $\lambda$ . A representation of the square well potential is provided in Figure 3.2 and can be expressed as:

$$\phi^{sw}(r; \lambda) = \begin{cases} 1 & \text{if } \sigma < r < \lambda\sigma \\ 0 & \text{if } r > \lambda\sigma \end{cases} \quad (3.3)$$

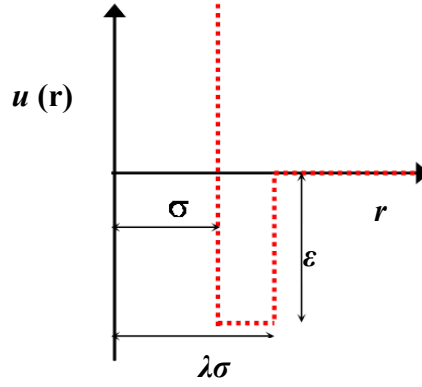


**Figure 3.2:** Square well is characterized by three parameters, the interaction diameter  $\sigma_{ij}$ , well depth of the square well  $\epsilon_{ij}$ , and the potential range  $\lambda_{ij}$ .

The ideal contribution,  $A^{Ideal}$ , [101] represents the free energy of an ideal gas and is given by:

$$\frac{A^{Ideal}}{Nk_B T} = \ln(\rho\Lambda^3) - 1 \quad (3.4)$$

where  $\rho = N/V$  is the number density of chain molecules,  $N$  is the total number of molecules in the system,  $V$  is the volume,  $\Lambda_i$  is the thermal de Broglie wavelength,  $T$  is the temperature, and  $k_B$  is the Boltzmann constant.

The monomer free energy,  $A^{Mono}$ , is given by a second order high temperature expansion using Barker and

$$\frac{A^{Mono}}{Nk_B T} = m \frac{A^M}{N_s k_B T} = m a^M = m(a^{HS} + \beta a_1 + \beta^2 a_2) \quad (3.5)$$

where  $N_s$  is the total number of spherical monomers,  $\beta = 1/k_B T$ , and  $a^M$  is the excess Helmholtz energy per segment. This approach utilizes the hard sphere as the reference system, where  $a^{HS}$  is obtained from the Carnahan and Starling [102] equation of state and can be expressed by:

$$a^{HS} = \frac{4\eta - 3\eta^2}{(1-\eta)^2} \quad (3.6)$$

where  $\eta$  is the packing fraction of the system. The first – order perturbation term,  $a_1$ , is given by [73-75]:

$$a_1 = -2\pi\rho_s \epsilon \int_{\sigma}^{\infty} r^2 \phi(r) g^{HS}(r) dr \quad (3.7)$$

where  $a_1$  corresponds to the average of the monomer-monomer potential energy,  $\rho_s = N_s/V$  is the number density of spherical segments, and  $g^{HS}(r)$  is the pair-radial distribution function of the hard sphere reference system. Gil Villegas and co-workers [46] solved the integral shown in equation 3.9, by using the mean- value theorem, which correlates the first- order perturbation term  $a_1$  with the van der Waals attractive constant.

$$a_1 = a_1^{VDW} g^{HS}(\xi; \eta) \quad (3.8)$$

Using the square well potential, considered here, the attractive van der Waals parameter is given by:

$$a_1^{VDW} = -4\eta\varepsilon(\lambda^3 - 1) \quad (3.9)$$

In addition, Gil Villegas *et al.*, [46] has shown that the  $g^{HS}(\xi; \eta)$  can be expressed by its contact value,  $g^{HS}(1; \eta)$ , but evaluated at an effective packing fraction  $\eta^{eff}$  shown as:

$$g^{HS}(\xi; \eta) = g^{HS}(1; \eta^{eff}) \quad (3.10)$$

Therefore, the first order perturbation term  $a_1$  [103] can be written as:

$$a_1 = a_1^{VDW} g^{HS}(1; \eta^{eff}) \quad (3.11)$$

The radial distribution function of the hard-sphere fluid is obtained from the Carnahan and Starling [102] equation of state, given as:

$$g^{HS}(1; \eta_{eff}) = \frac{1 - \eta_{eff} / 2}{(1 - \eta_{eff})^3} \quad (3.12)$$

where  $\eta_{eff}$  is an effective packing fraction defined by:

$$\eta_{eff} = c_1\eta + c_2\eta^2 + c_3\eta^3 \quad (3.13)$$

The coefficients  $c_i$  are given by the matrix [104]:

$$\begin{pmatrix} c_1 \\ c_2 \\ c_3 \end{pmatrix} = \begin{pmatrix} -3.16492 & 13.35007 & -14.80567 & 5.70286 \\ 43.00422 & -191.66232 & 273.89686 & -128.93337 \\ 65.04194 & -266.46273 & 361.04309 & -162.69963 \end{pmatrix} \times \begin{pmatrix} \frac{1}{\lambda_{ki,lj}} \\ \frac{1}{\lambda_{ki,lj}^2} \\ \frac{1}{\lambda_{ki,lj}^3} \\ \frac{1}{\lambda_{ki,lj}^4} \end{pmatrix} \quad (3.14)$$

The second perturbation term,  $a_2$ , is based on the expression of Barker and Henderson [73, 74]

$$a^2 = \frac{1}{2} K^{HS} \varepsilon \eta \frac{\partial a_1}{\partial \eta} \quad (3.15)$$

where  $K^{HS}$  is the isothermal compressibility of the hard-sphere fluid, which can be obtained from the Perkus-Yevick [74] expression.

$$K^{HS} = \frac{(1 - \eta)^4}{1 + 4\eta + \eta^2} \quad (3.16)$$

The free energy due to chains,  $A^{CHAIN}$ , [39] formed by  $m$  monomers is given by:

$$\frac{A^{CHAIN}}{Nk_B T} = -(m-1) \ln(y^{SW}(\sigma)) \quad (3.17)$$

where  $y^{SW}(\sigma)$  is the background correlation function evaluated at the hard-core contact value for the square-well potential. This can be expressed in terms of the radial distribution function at the contact value  $g^{SW}(\sigma)$ . The background correlation function is given by:

$$y^{SW}(\sigma) = \exp(-\beta\varepsilon)g^{SW}(\sigma) \quad (3.18)$$

where  $g^{SW}(\sigma)$  is the radial distribution function for the square well monomers at the contact distance  $\sigma$  and is approximated by a first-order high-temperature perturbation expansion given by:

$$g^{SW}(\sigma) = g^{HS}(\sigma) + \beta\varepsilon g_1(\sigma) \quad (3.19)$$

$g^{HS}$  is obtained from the Carnahan and Starling [102] equation of state as:

$$g^{HS}(\sigma) = \frac{1-\eta/2}{(1-\eta)^3} \quad (3.20)$$

The Helmholtz energy change due to the association,  $A^{Assoc}$ , [46] is based on the thermodynamics perturbation theory proposed by Wertheim, given by:

$$\frac{A^{ASSOC}}{Nk_B T} = \left[ \left( \sum_{a=1}^s \ln X_a - \frac{X_a}{2} \right) + \frac{s}{2} \right] \quad (3.21)$$

where the sum is over all associating  $s$  sites  $a$  on a molecule.  $X_a$  is the fraction of molecules not bonded at site  $a$ .  $X_a$  [39, 40] is obtained from the solution of the mass balance equations, given by:

$$X_a = \frac{1}{1 + \sum_{b=1}^s \rho X_b \Delta_{a,b}} \quad (3.22)$$

where the  $\Delta_{a,b}$  is the association strength between sites  $a$  and  $b$  on different molecules[40], defined as:

$$\Delta_{a,b} = f_{a,b} K_{a,b} g^{SW}(\sigma) \quad (3.23)$$

The bonding volume [40],  $K_{a,b}$ , can be found directly from the association parameters and is given by:

$$K_{a,b} = 4\pi \frac{\sigma^2}{72r_d^2} \left[ \ln \left( \frac{r_c + 2r_d}{\sigma} \right) (6r_c^3 + 18r_c^2 r_d - 24r_d^3) + \dots \right. \\ \left. (r_c + 2r_d - \sigma)(22r_d^2 - 5r_c r_d - 7r_d \sigma - 8r_c^2 + r_c \sigma + \sigma^2) \right] \quad (3.24)$$

It is important to note that in the usual homonuclear model of SAFT the contribution to the free energy due to bonding at separate sites are independent, and as such, the sites on a molecule are averaged over the whole molecule and not located on a particular segment as is often shown in schematic representations of the SAFT model.

### ***SAFT-VR Approach for Mixtures***

The SAFT-VR approach can be extended to handle mixtures of associating chains. For a mixture with  $n$  chains, each formed by  $m_i$  spherical segments of hard-core diameter  $\sigma_i$ . The interactions between the monomer segments are given by:

$$u_{ij}(r_{ij}) = u_{ij}^{HS}(r_{ij}; \sigma_{ij}) - \varepsilon_{ij} \phi_{ij}(r_{ij}; \lambda_{ij}) \quad (3.25)$$

where hard- sphere potential  $u_{ij}^{HS}$  is the repulsive term, defined by

$$u_{ij}^{HS}(r_{ij}; \sigma_{ij}) = \begin{cases} \infty & \text{if } r_{ij} < \sigma_{ij} \\ 0 & \text{if } r_{ij} > \sigma_{ij} \end{cases} \quad (3.26)$$

and the attractive interactions are characterized by the strength of interaction  $i - j$ ,  $\varepsilon_{ij}$  and the shape  $\phi_{ij}^{SW}(r_{ij}; \lambda_{ij})$ . For the square well, the shape can be described as:

$$\phi_{ij}^{SW}(r_{ij}; \lambda_{ij}) = \begin{cases} 1 & \text{if } \sigma_{ij} < r_{ij} < \lambda_{ij} \sigma_{ij} \\ 0 & \text{if } r_{ij} > \lambda_{ij} \sigma_{ij} \end{cases} \quad (3.27)$$

where  $\lambda_{ij}$  are the parameters associated to the range of the attractive forces.

The ideal contribution,  $A^{Ideal}$  [86, 105] to the free energy is given as the sum over all species  $I$  in the mixture, it is shown as:

$$\frac{A^{Ideal}}{Nk_B T} = \sum_{i=1}^n x_i \ln(\rho_i \Lambda_i^3) - 1 \quad (3.28)$$

where  $N, T, V, x_i, \rho, N_i$  and  $\Lambda_i$  have the same meaning as given above for a pure SAFT- VR fluid.

The contribution to the free energy due to the monomer- monomer [106] interactions can be expressed as:

$$\frac{A^{Mono}}{Nk_B T} = \left( \sum_{i=1}^n x_i m_i \right) \frac{A^M}{N_s k_B T} = \left( \sum_{i=1}^n x_i m_i \right) a^M \quad (3.29)$$

where  $m_i$  is the number of spherical segments of specie  $i$ ,  $A^M$  is the monomer free energy per segment in the mixture, and  $N_s$  is the total number of segments in the system. The monomer free energy per segment in the mixture,  $a^M$ , is obtained from the Barker and Henderson [73-75] high temperature expansion, using similar expressions as for the pure fluids, given as:

$$a^M = a^{HS} + \beta a_1 + \beta^2 a_2 \quad (3.30)$$

where  $a^{HS}$  is the free energy for a mixture of hard spheres and  $a_1$  and  $a_2$  are the first and second perturbation terms, respectively.

The free energy of the reference hard – sphere mixture is obtained from the expression of Boublik [107]

$$a^{HS} = \frac{6}{\pi \rho_s} \left[ \left( \frac{\xi_2^3}{\xi_3^2} - \xi_0 \right) \ln(1 - \xi_3) + \frac{3\xi_1 \xi_2}{1 - \xi_3} + \frac{\xi_2^3}{\xi_3(1 - \xi_3)^2} \right] \quad (3.31)$$

where  $\rho_s$  is the number density of spherical segments in the mixture.  $\rho_s$  can be related to the total number density of molecules  $\rho$  through:

$$\rho_s = \sum_{i=1}^n m_i x_i \rho \quad (3.32)$$

$\xi_l$  are the reduced density and is defined by:

$$\xi_l = \frac{\pi}{6} \rho_s \left[ \sum_{i=1}^n x_{s,i} (\sigma_{ii})^l \right] \quad (3.33)$$

where  $x_{s,i}$  is the mole fraction of the segments type  $i$  in the mixture, given by:

$$x_{s,i} = \frac{m_i x_i}{\sum_{k=1}^n m_k x_k} \quad (3.34)$$

The overall packing fraction of the mixture is given by  $\xi_3$  and is equivalent to  $\eta$ .

The mean attractive energy associated with the first-order perturbation term,  $a_1$ , is given by [46, 106]:

$$a_1 = \sum_{i=1}^n \sum_{j=1}^n x_{s,i} x_{s,j} \alpha_{ij}^{ij} \quad (3.35)$$

Using the mean value theorem[46], we can obtain an expression for  $a_1$  in terms of the contact value of  $g_{ij}^{HS}$ , shown as:

$$a_1 = -\rho_s \sum_{i=1}^n \sum_{j=1}^n x_{s,i} x_{s,j} \alpha_{ij}^{VDW} g_{ij}^{HS} \left[ \sigma_{ij}; \xi_3^{eff} \right] \quad (3.36)$$

where  $\alpha_{ij}^{VDW}$  is the van der Waals attractive constant for the  $i$ - $j$  and is given by:

$$\alpha_{ij}^{VDW} = \frac{2}{3} \pi \epsilon_{ij} \sigma_{ij}^3 (\lambda_{ij}^3 - 1) \quad (3.37)$$

Using the MX1b rules [106] equation 3.38 simplifies to:

$$a_1 = -\rho_s \sum_{i=1}^n \sum_{j=1}^n x_{s,i} x_{s,j} \alpha_{ij}^{VDW} g_0^{HS} [\sigma_x; \zeta_x^{eff}] \quad (3.38)$$

where  $g_0^{HS}[\sigma_x; \zeta_x^{eff}]$  is the contact value of the hard sphere pair distribution function obtained from [102] Carnahan and Starling equation of state:

$$g_0^{HS}[\sigma_x; \zeta_x^{eff}] = \frac{1 - \zeta_x^{eff} / 2}{(1 - \zeta_x^{eff})^3} \quad (3.39)$$

The effective packing fraction  $\zeta_x^{eff}$  is obtained using the vdW-1 fluid approximation from the corresponding packing fraction of the mixture,  $\zeta_x$ :

$$\zeta_x^{eff}(\zeta_x; \lambda_{ij}) = c_1(\lambda_{ij})\zeta_x + c_2(\lambda_{ij})\zeta_x^2 + c_3(\lambda_{ij})\zeta_x^3 \quad (3.40)$$

where

$$\zeta_x = \frac{\pi}{6} \rho_s \sigma_x^3 \quad (3.41)$$

and

$$\sigma_x^3 = \sum_{i=1}^n \sum_{j=1}^n x_{s,i} x_{s,j} \sigma_{ij}^3 \quad (3.42)$$

The coefficients,  $c_i$ , are approximated by those of the pure fluid and are given by [46, 106]:

$$\begin{pmatrix} c_1 \\ c_2 \\ c_3 \end{pmatrix} = \begin{pmatrix} -3.16492 & 13.35007 & -14.80567 & 5.70286 \\ 43.00422 & -191.66232 & 273.89686 & -128.93337 \\ 65.04194 & -266.46273 & 361.04309 & -162.69963 \end{pmatrix} \times \begin{pmatrix} \frac{1}{\lambda_{ki,lj}} \\ \frac{1}{\lambda_{ki,lj}^2} \\ \frac{1}{\lambda_{ki,lj}^3} \\ \frac{1}{\lambda_{ki,lj}^4} \end{pmatrix} \quad (3.43)$$

The second – order term,  $a_2$ , is expressed as [46, 106]:

$$a_2 = \sum_{i=j}^n \sum_{j=1}^n x_{s,i} x_{s,j} a_2^{ij} \quad (3.44)$$

$a_2^{ij}$  is obtained from  $a_1^{ij}$  using the local compressibility approximation [73-75] for mixtures and is given as:



$$a_2^{ij} = \frac{1}{2} K^{HS} \varepsilon_{ij} \rho_s \frac{\partial a_1^{ij}}{\partial \rho_s} \quad (3.45)$$

where  $K^{HS}$  is the hard sphere isothermal compressibility in the Percus-Yevick approximation[108] for mixtures of monomers:

$$K^{HS} = \frac{\xi_0(1-\xi_3)^4}{\xi_0(1-\xi_3)^2 + 6\xi_1\xi_2(1-\xi_3) + 9\xi_2^3} \quad (3.46)$$

The chain contribution to the free energy is expressed in terms of the contact value of the background correlation function of monomers [46, 106]. It is given as:

$$\frac{A^{Chain}}{Nk_B T} = - \sum_{i=1}^n x_i (m_i - 1) \ln y_{ii}^{SW}(\sigma_{ii}) \quad (3.47)$$

where  $y_{ii}^{SW}$  is given as:

$$y_{ii}^{SW}(\sigma_{ii}) = \exp(-\beta \varepsilon_{ii}) g_{ii}^{SW}(\sigma_{ii}) \quad (3.48)$$

The contact pair distribution function for a mixture of square well molecules corresponding to the  $i$ - $j$  interactions can be obtained from a high- temperature expansion up to the first order as:

$$g_{ij}^{SW}(\sigma_{ij}) = g_{ij}^{HS}(\sigma_{ij}) + \beta \varepsilon_{ij} g_1^{ij}(\sigma_{ij}) \quad (3.49)$$

The contact pair distribution function for a hard- sphere mixture is given by the expression of Boublík [107]:

$$g_{ij}^{HS}(\sigma_{ij}; \xi_3) = \frac{1}{1-\xi_3} + 3 \frac{D_{ij} \xi_3}{(1-\xi_3)^2} + 2 \frac{(D_{ij} \xi_3)^2}{(1-\xi_3)^3} \quad (3.50)$$

where the parameters  $D_{ij}$  are defined by:

$$D_{ij} = \frac{\sigma_{ii} \sigma_{jj} \sum_{k=1}^n x_{s,k} \sigma_{kk}^2}{(\sigma_{ii} + \sigma_{jj}) \sum_{k=1}^n x_{s,k} \sigma_{kk}^3} \quad (3.51)$$

The association contribution ( $A^{Assoc}$ ) [46] is the free energy due to the association of  $s_i$  sites on chain molecules of species  $i$ . It is obtained from Wertheim's theory as:

$$\frac{A^{Assoc}}{Nk_B T} = \sum_{i=1}^n x_i \left[ \sum_{a=1}^{s_i} \left( \ln X_{a,i} - \frac{X_{a,i}}{2} \right) + \frac{s_i}{2} \right] \quad (3.52)$$

where the first sum is over the species  $i$ , and the second one is over all  $s_i$  sites of type  $a$  on a molecule of specie  $i$ . The fraction of molecules of type  $i$  not bonded at site  $a$ ,  $X_{a,i}$ , is given by the mass balance equation [39, 40]:

$$X_{a,i} = \frac{1}{1 + \sum_{j=1}^n \sum_{b=1}^{s_j} \rho x_j X_{b,j} \Delta_{a,b,i,j}} \quad (3.53)$$

$\Delta_{a,b,i,j}$  is the parameter that characterizes the association between site  $a$  in molecule  $i$  and site  $b$  in molecule  $j$  in the mixture and is given by:

$$\Delta_{a,b,i,j} = K_{a,b,i,j} F_{a,b,i,j} g_{ij}^{SW}(\sigma_{ij}) \quad (3.54)$$

$K_{a,b,i,j}$  is the volume available for bonding, which is calculated using the following expression:

$$K_{a,b,i,j} = 4\pi \frac{\sigma_{ii}^2}{72r_{d_i}^2} \left[ \ln \left( \frac{r_{c_i} + 2r_{d_i}}{\sigma_{ii}} \right) (6r_{c_i}^3 + 18r_{c_i}^2 r_{d_i} - 24r_{d_i}^3) + \dots \right. \\ \left. (r_{c_i} + 2r_{d_i} - \sigma_{ii})(22r_{d_i}^2 - 5r_{c_i} r_{d_i} - 7r_{d_i} \sigma_{ii} - 8r_{c_i}^2 + r_{c_i}^2 \sigma_{ii} + \sigma_{ii}^2) \right] \quad (3.55)$$

### **GC-SAFT-VR Approach for Pure Fluids**

In the GC-SAFT-VR [100] EOS, the Helmholtz free energy of a molecule is expressed as a combination of four free energy contributions: ideal, monomer, chain and association as in the SAFT approach. The GC-SAFT-VR approach models fluids as chains composed of tangentially bonded segments that represent the functional groups within the molecule [48, 109]. The segments representing each functional group interact via the square well potential, which can be described by,

$$u_{ki,lj}(r) = \begin{cases} +\infty & \text{if } r < \sigma_{ki,lj} \\ -\varepsilon & \text{if } \sigma_{ki,lj} \leq r \leq \lambda_{ki,lj} \sigma_{ki,lj} \\ 0 & \text{if } r \leq \lambda_{ki,lj} \sigma_{ki,lj} \end{cases} \quad (3.56)$$

Here  $u_{ki,lj}$  represents the interaction between a functional group of type  $i$  present in molecule  $k$  with a functional group of type  $j$  in molecule  $l$ ,  $\sigma$  is the segment diameter,  $\varepsilon$  is the depth of the square well,  $\lambda$  is the potential range, and  $r$  is the distance between the two groups.

Within the GC-SAFT-VR approach, the free energy is written as the sum of four separate contributions:

$$\frac{A}{Nk_B T} = \frac{A^{ideal}}{Nk_B T} + \frac{A^{mono}}{Nk_B T} + \frac{A^{chain}}{Nk_B T} + \frac{A^{assoc}}{Nk_B T} \quad (3.57)$$

where  $N$  is the total number of molecules in the system,  $T$  is the temperature,  $k_B$  is the Boltzmann constant,  $A^{ideal}$  is the ideal free energy,  $A^{mono}$  is the contribution to the free energy due to the monomer segments,  $A^{chain}$  is the contribution due to the formation of bonds between monomer segments, and  $A^{assoc}$  is the contribution due to association. The expressions for each of the remaining terms for a mixture system composed of heteronuclear chain molecules are presented below.

The ideal Helmholtz free energy is given by,

$$\frac{A^{ideal}}{Nk_B T} = \sum_{i=1}^{n_{components}} x_i \ln(\rho_i \Lambda_i^3) - 1 \quad (3.58)$$

where  $n_{components}$  represents the number of pure components,  $\rho_i = N_i/V$  (the molecular number density of chains of component  $i$ ),  $x_i$  is the mole fractions of component  $i$  in the mixture, and  $\Lambda_i$  is the thermal de Broglie wavelength.

The monomer free energy is given by a second order high temperature expansion using Barker and Henderson perturbation theory for mixtures [73],

$$\frac{A^{mono}}{Nk_B T} = \sum_{i=1}^{n_{components}} \sum_{k=1}^{n'_k} m_{ki} x_i \left( a^{HS} + \frac{a_1}{k_B T} + \frac{a_2}{(k_B T)^2} \right) \quad (3.59)$$

where  $n'_k$  is the number of types of functional groups  $k$  in a chain of component  $i$  and  $m_{ki}$  the number of segments of type  $k$  in chains of component  $i$ .

In the GC-SAFT-VR framework, the main change in the expression for the free energy is to account for the heterogeneity in the model chain, with the other expressions remaining largely unchanged. The free energy due to chain formation is given by,

$$\frac{A^{chain}}{Nk_B T} = - \sum_{i=1}^n x_i \sum_{kj} \ln y_{ik,ij}^{SW}(\sigma_{ik,ij}) \quad (3.60)$$

where the first sum is over all components in the mixture and the second sum considers the chain formation and connectivity of the segments within a given chain. The background correlation function is given by,

$$y_{ki,kj}^{SW}(\sigma_{ki,kj}) = \exp\left(\frac{-\varepsilon_{ki,kj}}{k_B T}\right) g_{ki,kj}^{SW}(\sigma_{ki,kj}) \quad (3.61)$$

where  $g_{ki,kj}^{SW}(\sigma_{ki,kj})$  is the radial distribution function for the square well monomers at the contact distance  $\sigma_{ki,kj}$  and is approximated by a first-order high-temperature perturbation expansion.

Finally, the contribution due to association, ( $A^{Assoc}$ ), [46] interactions between sites on different functional groups that form the molecules of interest is expressed as:

$$\frac{A^{Assoc}}{Nk_B T} = \sum_{i=1}^n x_i \left[ \sum_{a=1}^{s_i} \left( \ln X_{a,i} - \frac{X_{a,i}}{2} \right) + \frac{s_i}{2} \right] \quad (3.62)$$

where the first sum is over the number of components  $n$ , the second one is over all types of functional groups in the molecule  $k$ , and the third sum is over the total number of site on the function group  $i$ . The fraction of molecules of type  $i$  not bonded at site  $a$ ,  $X_{a,i}$  is obtained from the solution of the mass balance equations and is given in terms of the total number density for the system, shown as [39, 40]:

$$X_{kia} = \frac{1}{1 + \rho \sum_{l=1}^n x_l \sum_{j=1}^{n_l} v_{lj} \sum_{b=1}^{ns_j} n_{jb} x_{ljb} \Delta_{kia,ljb}} \quad (3.63)$$

$\Delta_{a,b,i,j}$  is the parameter that characterizes the association between site  $a$  in molecule  $i$  and site  $b$  in molecule  $j$  in the mixture and is given by:

$$\Delta_{kia,ljb} = K_{kia,ljb}^{HB} f_{kia,ljb} g_{ki,lj}^{SW}(\sigma_{ki,lj}) \quad (3.64)$$

where  $K_{kia,ljb}^{HB}$  is the volume available for bonding,  $f_{kia,ljb}$  the Mayer  $f$ -function, and  $g_{ki,lj}^{SW}$  the radial distribution function for the square well monomers.

At this point, it is important to note that in the usual homonuclear model of SAFT the contribution to the free energy due to bonding at separate sites are independent, and as such, the location of sites on a molecule is arbitrary; the sites are in actuality averaged over the whole molecule. However, in the GC- SAFT-VR equation, because of the hetero-segmented chain model used, the location of the association sites can be specified on a given functional group and hence their position within the model chain defined [86].

### Combining Rules

The study of mixtures requires the determination of unlike interaction parameters. The Lorentz-Berthelot [110] combining rules are used for both the SAFT-VR and GC-SAFT-VR approach. .

The unlike size and energy parameters, are given as:

$$\sigma_{ij} = \frac{(\sigma_{ii} + \sigma_{jj})}{2} \quad (3.65)$$

$$\epsilon_{ij} = (\epsilon_{ii} \epsilon_{jj})^{1/2} \quad (3.66)$$

For the unlike potential range, equation 3.67 is used, viz.,

$$\lambda_{ij} = \frac{\lambda_{ii}\sigma_{ii} + \lambda_{jj}\sigma_{jj}}{\sigma_{ii} + \sigma_{jj}} \quad (3.67)$$

To determine the parameters that characterize the unlike association interactions, the following combining rules are used:

$$\epsilon_{ij}^{ab} = \left( \epsilon_{ii}^{ab} \epsilon_{jj}^{ab} \right)^{1/2} \quad (3.68)$$

$$K_{a,b,i,j} = \left[ \frac{(K_{a,b,i,i})^{1/3} + (K_{a,b,j,j})^{1/3}}{2} \right]^3 \quad (3.69)$$

For systems which deviate from the Lorentz Berthelot [110] combining rules, equations 3.70 and 3.71 are valid and are given by:

$$\epsilon_{ij} = \xi_{ij} \left( \epsilon_{ii} \epsilon_{jj} \right)^{1/2} \quad (3.70)$$

$$\lambda_{ij} = \gamma_{ij} \frac{\lambda_{ii}\sigma_{ii} + \lambda_{jj}\sigma_{jj}}{\sigma_{ii} + \sigma_{jj}} \quad (3.71)$$

where  $\gamma_{ij}$  and  $\xi_{ij}$  are treated as adjustable parameters and are used to obtain a better representation of the experimental data.

## Chapter IV

### Molecular Simulation Background

Monte Carlo (MC) and molecular dynamic (MD), two most widely used molecular simulation (MS) techniques, are routinely used to investigate the dynamics, structure, as well as thermodynamics of atomic or molecular systems. Additionally, molecular simulation (MS) data can be used to assess the statistical mechanics approximations assumed in the development of thermodynamic models, such as the SAFT EOS. This is seen to be a noteworthy advantage over traditional cubic equations of state. MS techniques can serve as a link between the microscopic length and time scales and the macroscopic level (shown in Figure 4.1) [6].

Using MS techniques, a wide variety of thermodynamic properties can be calculated; therefore, these techniques are extremely useful for systems in which there is no experimental data or which experimental data is difficult to obtain at extreme conditions (e.g., high pressure, high temperature). In this thesis, we utilize both the MD simulation technique to assess the validity and accuracy of our proposed SAFT model.

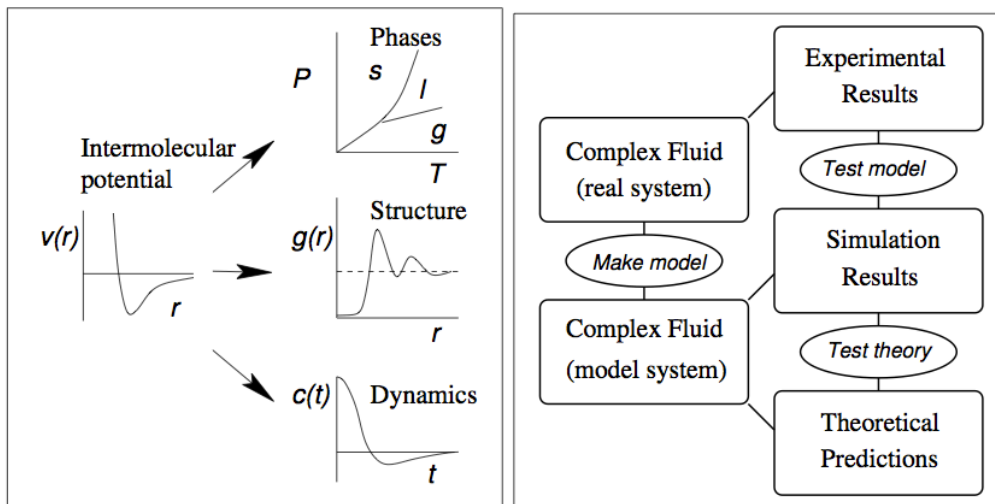


**Figure 4.1:** Simulations serve as a bridge between microscopic and macroscopic. Copied from Introduction to Molecular Dynamic simulation by Michael P. Allen [6]

## Molecular Dynamics Simulation

Molecular dynamics (MD) is a molecular simulation method based on computing the motions of individual atoms or molecules. The trajectories of the atoms or molecules are determined by numerically solving the Newton's equations of motion for a large number of particles, utilizing periodic boundary conditions. The particles interact via intra- and inter molecular potentials and can be solved using various numerical integration methods such as the verlet leapfrog algorithm, a commonly used approach. Even though these simulations cannot be considered to be substitutes for experiments, their results may be particularly useful where experimental measurement is considerably difficult.

MD simulations require the definition of the potential energy to describe the interactions of particles in a system. Force fields use potential functions to describe the interactions between atoms. These interactions include: stretching or compressing of bonds, torsional effects of twisting about bonds, the Van der Waals attractions or repulsions of atoms that come close together, and the electrostatic interactions between partial charges in a molecule[111]. Each interactions can be quantified using a potential function that gives the energy of the interaction as a function of distance, angle, or charge[111].

Two classes of interactions are used: non-bonded interactions and bonded. The bond stretching, bending, stretch-bend, out of plane, and torsion interactions are called bonded interactions. The bond stretch interactions, the bond angle interactions and the dihedral interaction are the most commonly defined. The bond stretch interactions represent the energy associated with stretching or compressing a bond between two atoms. Typically, it is modeled as a harmonic spring, represented by:

$$V = \frac{1}{2} K_b (r_{ij} - r_0)^2 \quad (4.1)$$

where  $r_0$  is the equilibrium length of the spring, and  $K_b$  is the spring constant.

The bond angle interactions is a three particle interaction and is commonly represented as,

$$V = \frac{1}{2} K_\theta (\theta - \theta_0)^2 \quad (4.2)$$

where,  $\theta$  is the angle between two bonds to a common atom,  $\theta_0$  is the equilibrium length, and  $K_\theta$  is the force constant.

The dihedral angle interaction is a four particle interaction. It is usually represented by:

$$V = K_\phi (1 + \cos(n\phi - \phi\delta)) \quad (4.3)$$

The Van der Waals and electrostatic interactions are classified as the non-bonded atoms.

The Van der Waals interactions contribute to the steric interactions in molecules and are often the most important factors in determining the overall molecular conformation[111]. The Van der Waals interactions can be expressed using a 12-6 Lennard Jones potential,

$$V_{LJ} = 4\epsilon \left[ \left( \frac{\sigma}{r_{ij}} \right)^{12} - \left( \frac{\sigma}{r_{ij}} \right)^6 \right] \quad (4.4)$$

where  $\epsilon$  is a constant determining the depth of the potential well, and where  $\sigma$  determines the diameter of the particle.

If bonds in the molecule are polar, partial electrostatic charges will reside on the atoms. The electrostatic interactions are represented with a Coulombic potential function[111] and is given by:

$$V_{Coul} = \frac{q_i q_j}{4\pi\epsilon_0 r_{ij}} \quad (4.5)$$

where  $q_i$  and  $q_j$  are the charges of particle  $i$  and  $j$ ,  $r_{ij}$  is the distance between the particles.

Molecular dynamics is useful in obtaining the fluid phase equilibrium and can be calculated using the volume-quench dynamics (QD) technique [112]. MC methods can also be used to determine the fluid phase equilibrium of a system of interest. However, MC deficiencies make implementation difficult. For instance, using MC methods equilibration is difficult to achieve when simulating dense phases because of the poor statistics associated with the insertion or deletion steps[113]. In addition, MC methods are difficult to apply to systems containing very complex molecules[113]. In contrast, both temperature [114] and volume QD have been used to successfully reproduce the vapor liquid equilibrium (VLE) of LJ particles [115] and investigate the behavior of model nanoparticle systems [112]. This QD method has also been used to investigate the saturated liquid densities of the Gaussian charge polarizable water model and the results were found to be in good agreement with those calculated using Gibbs ensemble Monte Carlo simulations and reported experimentally [116].

The basic algorithm involves initializing the system as a single-phase fluid with periodic boundary conditions and then quenching the system into the coexistence regime by rapidly increasing the box length in one direction (in this case the  $x$  direction). The system is then allowed to reach equilibrium. The rapid density change provides a strong thermodynamic driving force, which allows for the formation of a two-phase system at coexistence. Since the free energy minimization is done by the system through the reduction of the interfacial area, the interfacial region will tend to remain planar, allowing the two regions to be clearly defined and the density



histogram of each of the phases calculated. This general procedure is performed several times over a range of temperatures and the following relationships are then used to fit the fluid phase equilibrium data [117], *viz.*

$$\frac{1}{2}(\rho_L - \rho_V) = \rho_c + C_1(T - T_c) \quad (4.6)$$

$$\rho_L - \rho_V = C_2(T_c - T)^\beta \quad (4.7)$$

Here,  $\rho_L$  and  $\rho_V$  are the high and low densities respectively;  $C_1$ ,  $C_2$ , and  $\beta$  are fitting parameters; and  $\rho_c$  and  $T_c$  are the critical density and critical temperature of the system, respectively.  $\beta$  is assumed to be 0.32 [118] and is not a free parameter in the fitting. Thus, the phase coexistence can be calculated for these complex building blocks in a relatively efficient manner and the information used to develop general trends without the costly sampling of very large regions of phase space. A schematic representation of the QD technique is provided in Figure 4.2.

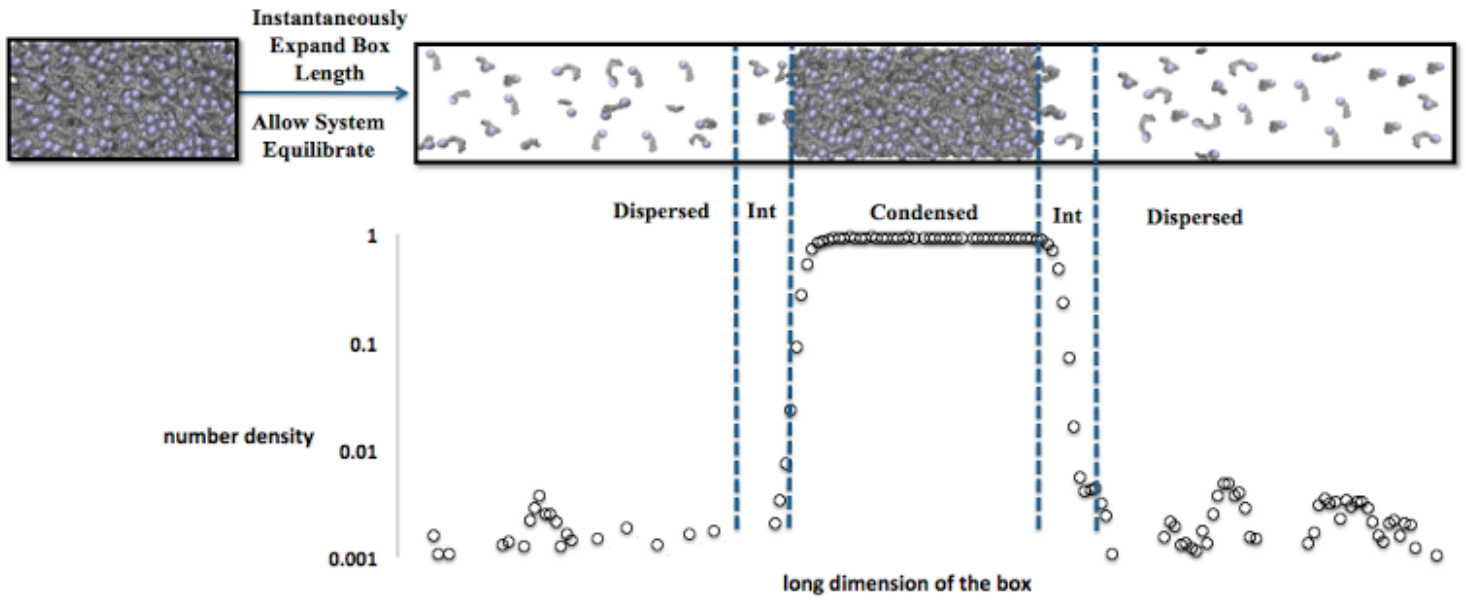


**Figure 4.2:** Schematic representation of the quench dynamic method.

## Chapter 5

### Predicting the Phase Behavior of Fluorinated Organic Molecules Using the GC-SAFT-VR

#### Equation of State

##### Introduction

Fluorinated molecules possess unique characteristics that have proven to be useful in various scientific applications [119]. Many of their advantageous properties, including low surface tension, high fluidity, low dielectric constant, high vapor pressure and compressibility, gas solubility, and excellent spreading properties [20], are due to the overlapping of orbitals in the C-F bonds and the dense electron cloud of the fluorine atoms that protects the chain against reagents. Consequently, fluorinated molecules tend to be chemically and biologically inert [119] and manipulating the structure of organic molecules to include fluorination can introduce dramatically different and often desirable properties.

The simplest of the organofluorine molecules are the perfluoroalkanes (PFA), which are hydrocarbons in which all the C-H bonds are replaced by C-F bonds. Despite the significantly higher molecular weight for PFAs as compared to the corresponding alkane, the boiling points of PFAs are surprisingly similar to those of the corresponding alkanes. This phenomenon suggests that the intermolecular forces between PFA molecules are relatively weak and are also responsible for the high ionization potential and low polarizability of PFA molecules. However, PFA molecules exhibit strong intramolecular bonds that result in excellent spreading properties, high viscosity, immiscibility with hydrocarbons and water, as well as low refractive index [9]. PFAs also exhibit high solubility in CO<sub>2</sub> and oxygen, which has led to their use in several environmental applications, including the removal of CO<sub>2</sub> from gaseous effluents [21], the design of CO<sub>2</sub>-philic surfactants [9], and in medical applications such as oxygen carriers in artificial blood substitutes [9].

A second unique type of fluorinated molecules are the perfluoroalkylalkanes (PFAA) which consist of an alkyl chain bonded to a perfluorinated chain with general structure

$F(CF_2)_n(CH_2)_mH$ . The dual nature of the PFAA structure results in a molecule with amphiphilic character [20], which contributes to many of the distinctive properties that PFAAs exhibit. Additionally, there is a marked difference in the electronegativity of the hydrocarbon side and the fluorinated side of the molecule that leads to a dipole moment along the molecular backbone [120, 121]. These characteristics, along with the fact that PFAAs are thermally, chemically, and biologically inert, have led to a wide range of applications for these molecules, including use as excipients for inhalative liquid drug carrier systems [23], surface-active agents, temporary blood substitutes and eye replacement fluids [24], as well as dewetting and lubricating compounds [119]. In this work, PFAA molecules will be referred to using the  $F_xH_y$  nomenclature, where  $x$  refers to the number of perfluorinated carbon atoms and  $y$  refers to the number of hydrogenated carbon atoms in the PFAA molecule.

Another interesting class of fluorinated molecules that we consider are the dipolar hydrofluoroethers (HFEs) with the structure  $R_X-O-R_Y$  where  $R_X$  and  $R_Y$  represent distinctive chains attached to the oxygen atom. Hydrofluoroethers along with hydrofluorocarbons (HFCs) are used as environmentally friendly alternatives to chlorofluorocarbons (CFCs) and hydrochlorofluorocarbons (HCFCs) [22] and as such many industrial and commercial applications (e.g. cleaning solvents, refrigerants, foaming agents, carrier solvents for coatings, and lubricants [22]) utilize HFEs.

Despite the proven usefulness of these organofluorine molecules, only limited work has been done to experimentally characterize the thermodynamic properties and phase behavior of these molecules. As a result, the accurate calculation of thermodynamic properties from cubic equations of state is difficult since such equations tend to be heavily reliant on experimental data for parameter estimation. Statistical mechanics based equations of state are an appealing alternative since they usually have more predictive ability by taking into account the effects of molecular shape, size, and interactions on the thermodynamic properties. The statistical associating fluid theory (SAFT) [39, 40], based on Wertheim's first order thermodynamic

perturbation theory [41, 43, 44, 122], is one such approach and has been used by several authors to study fluorinated systems. In perhaps the first study, Archer *et al.* [123], utilized the bonded hard-sphere (BHS) theory, which models molecules as chains of tangentially bonded hard-spherical segments that interact through a mean field dispersion term, to examine the critical behavior of the perfluoroalkane homologous series.. The BHS approach was found to predict the trend in critical point for the alkane and perfluoroalkane series. Additionally, the UCSTs of the alkane and perfluoroalkane mixtures were also predicted utilizing the united-atom models. Subsequently, McCabe *et al.* [124] studied the high-pressure phase behavior and critical lines of perfluoromethane + alkanes (C1 – C8) and the symmetric alkanes + perfluoroalkanes mixtures from C<sub>1</sub>-C<sub>4</sub> utilizing pure component parameters proposed by Gil-Villegas [86]. A single binary interaction parameter was fitted to the high-pressure critical line for the perfluoromethane + butane system and found to be transferable to mixtures of similar chain lengths; however, it was observed that as the alkane chain length increased the deviation between the theoretical predictions and experiment increased. Therefore, a different binary interaction parameter was used for mixtures containing longer alkane chains. In related work with the SAFT-VR approach, Morgado *et al.* [3] studied the low-pressure liquid-liquid immiscibility behavior of alkane + PFA binary mixtures with chain lengths of 5 - 8 carbon atoms. A new set of binary interaction parameters was proposed, based on reproducing the UCST and excess volumes of the n-hexane + n-perfluorohexane system, and then used transferably to predict the vapour–liquid equilibria, liquid–liquid equilibria and excess volumes of other binary mixtures without additional fitting to experimental data. Using the soft-SAFT equation for homonuclear LJ chain fluids, Dias *et al.* [9] examined the solubility of xenon and oxygen in perfluoroalkanes as well as the vapor-liquid and liquid-liquid equilibrium of *n*-alkane + *n*-perfluoroalkane mixtures. A single cross interaction parameter was introduced to model the phase behavior of the *n*-perfluoroalkanes + *n*-alkanes of similar chain lengths; however, for the binary mixtures of xenon and oxygen with perfluoroalkanes, binary interaction parameters were adjusted for each mixture. In a later

combined experimental and theoretical study [125], the phase behavior of carbon dioxide and perfluoroalkane mixtures was investigated using a modified soft-SAFT equation that included quadrupolar interactions for carbon dioxide, perfluorobenzene, and perfluorotoluene. In comparison to the original soft-SAFT equation, the approach was found to provide good agreement with experimental data without the use of fitted binary interaction parameters for mixtures involving fluorinated aromatic compounds + carbon dioxide; however, the results obtained for carbon dioxide + other non-aromatic fluorinated molecules were not affected by the addition of the quadrupolar contribution and still required the optimization of binary interaction parameters.

Turning to PFAA molecules, Morgado *et al.* [88] used the so called hetero-statistical associating fluid theory for potentials of variable range (hetero-SAFT-VR) [126, 127], to study, the density and molar volumes of perfluorohexylhexane ( $F_6H_6$ ) and perfluorohexyloctane ( $F_6H_8$ ). The hetero-SAFT-VR approach enables the PFAAs to be described as diblock molecules, i.e., formed from two different chains of tangentially bonded segments representing the perfluoroalkyl and alkyl parts of the molecules with different size and/or energy parameters. The alkyl and perfluoroalkyl segments were described using parameters for the alkanes and perfluoroalkanes developed in earlier work [3, 109] and a binary interaction parameter fitted to the hexane + perfluorohexane binary mixture. Using this approach, experimental densities were predicted within 1% at atmospheric pressure and 3.5% for higher pressures. In a later study [1], the molar volumes and partial molar volumes at infinite dilution of PFA and PFAA molecules in *n*-octane were predicted, again utilizing the hetero-SAFT-VR approach [88]. Using the same parameters and molecular model as the previous study [88], the molar volume and partial molar volumes at infinite dilution of the PFA molecules were found to have deviations from experiment of less than 5% in all cases. The theoretical results for PFAAs in octane were found to be slightly better than those found for the PFAs, with deviations between 0.1% and 2.5%. Following the approach proposed by Morgado [88], dos Ramos *et al.* [128] also utilized the hetero-SAFT-VR approach to

examine the phase equilibria of binary mixtures of *n*-alkanes, PFAs, and PFAAs. The effect of the molecular weight of the *n*-alkanes and perfluoroalkanes on the type of phase behavior observed in these mixtures was studied; however, experimental data was not available and so the accuracy of the theoretical predictions could not be tested.

Hydrofluoroethers (HFEs) have also been studied previously using the SAFT family of equations. In an experimental and theoretical study, Lafitte *et al.* [129] utilized the SAFT-VR Mie equation of state to model and characterize pure hydrofluoroethers. Molecular parameters were determined for the HFEs studied by fitting to heat of vaporization, experimental normal boiling point, compressed liquid density, and speed of sound data for methyl perfluorobutyl ether (HFE – 7000), 2-trifluoromethyl-3-ethoxydodecafluorohexane (HFE-7500), methyl nonafluorobutyl ether (HFE - 7100), and ethyl nonafluorobutyl ether (HFE - 7200). Deviations between theoretical results and experimental data of less than 4% were found in all cases. Saturation pressure, saturated liquid density, isobaric heat capacity, thermal expansivity, and speed of sound data were then predicted at conditions not considered during the fitting procedure. Although, exact deviations were not provided, the theoretical predictions were found to be in good agreement with the available experimental data. Pure HFEs have also been studied using the perturbed-chain SAFT (PC-SAFT) equation of state by Vijande *et al.* [130]. The model parameters were optimized against compressed and saturated liquid densities at several temperatures and pressures and then used to predict the saturation pressure with good results. A group-contribution like approach was also proposed that enables the model parameters to be extrapolated and used to predict the saturation pressure and liquid density of other molecules in the same family.

In present work, to characterize both pure PFA, PFAA, and HFE fluids along with their mixtures, the GC-SAFT-VR equation is used [48]. The GC-SAFT-VR equation combines the SAFT-VR [86] equation with a group contribution (GC) [48] approach that allows for the description of chains built up from segments of different size and/or energy of interaction. This approach allows for the location of the functional groups and association sites within a molecule

to be specified, enabling the heterogeneity in molecular structure to be captured within a SAFT model. An advantage of the GC-SAFT-VR approach, when the groups of interest are present in a single molecule, is the ability to determine group cross-interaction parameters using pure fluid experimental data for molecules containing the groups of interest (i.e., the cross parameters need not be adjusted to mixture experimental data). In earlier work, GC-SAFT-VR parameters were determined for a wide range of functional groups that allow the phase behavior of compounds such as alkanes [48], linear [48] and branched alkenes [48], ketones [48], acetates [48], esters [48], alcohols [47], aldehydes [47], amines [47], carboxylic acids [47], aromatics [131], and polymers [100] to be studied. In this work, GC-SAFT-VR molecular parameters are determined for the CF<sub>3</sub>, CF<sub>2</sub>, CF, CHF, CH<sub>2</sub>F, and CHF<sub>2</sub> functional groups by fitting to experimental data for selected fluoroalkanes, PFAs, and PFAAs. The transferability of the group parameters determined is then examined by predicting the phase behavior of molecules not included in the fitting process and the phase behavior of mixtures. Specifically mixtures of PFAs and PFAAs molecules with each other, and with carbon dioxide, hydrofluoroethers, alkanes, and alkenes have been studied.

### Models and Theory

The GC-SAFT-VR approach models fluids as chains composed of tangentially bonded segments that represent the functional groups within the molecule [48, 109]. The segments representing each functional group interact via the square well potential, which can be described by,

$$u_{ki,lj}(r) = \begin{cases} +\infty & \text{if } r < \sigma_{ki,lj} \\ -\varepsilon & \text{if } \sigma_{ki,lj} \leq r \leq \lambda_{ki,lj}\sigma_{ki,lj} \\ 0 & \text{if } r \leq \lambda_{ki,lj}\sigma_{ki,lj} \end{cases} \quad (5.1)$$

Here  $u_{ki,lj}$  represents the interaction between a functional group of type  $i$  present in molecule  $k$  with a functional group of type  $j$  in molecule  $l$ ,  $\sigma$  is the segment diameter,  $\varepsilon$  is the depth of the square well,  $\lambda$  is the potential range, and  $r$  is the distance between the two groups. The unlike size



and energy interactions can be obtained from the Lorentz-Berthelot combining rules expressed by,

$$\sigma_{ij} = \frac{\sigma_{ii} + \sigma_{jj}}{2} \quad (5.2)$$

$$\varepsilon_{ij} = \sqrt{\varepsilon_{ii}\varepsilon_{jj}} \quad (5.3)$$

and the unlike potential range is given by,

$$\lambda_{ij} = \frac{\lambda_{ii}\sigma_{ii} + \lambda_{jj}\sigma_{jj}}{\sigma_{ii} + \sigma_{jj}} \quad (5.4)$$

As discussed above, for interactions involving polar functional groups which are expected to deviate from the Lorentz-Berthelot combining rules,, the unlike interactions between functional groups can be adjusted by fitting to pure component experimental data for molecules containing the functional groups of interest. As such, a predictive equation for the study of mixture phase behavior is retained.

Within the GC-SAFT-VR approach, the free energy is written as the sum of four separate contributions:

$$\frac{A}{Nk_B T} = \frac{A^{ideal}}{Nk_B T} + \frac{A^{mono}}{Nk_B T} + \frac{A^{chain}}{Nk_B T} + \frac{A^{assoc}}{Nk_B T} \quad (5.5)$$

where  $N$  is the total number of molecules in the system,  $T$  is the temperature,  $k_B$  is the Boltzmann constant,  $A^{ideal}$  is the ideal free energy,  $A^{mono}$  is the contribution to the free energy due to the monomer segments,  $A^{chain}$  is the contribution due to the formation of bonds between monomer segments, and  $A^{assoc}$  is the contribution due to association. The expressions for  $A^{assoc}$  are not included in this work since the systems studied are not associating fluids. The expressions for each of the remaining terms for a mixture system composed of heteronuclear chain molecules are presented below. Since the theory has been well documented [48, 87] only a brief description of the important expressions are provided below.

The ideal Helmholtz free energy is given by,

$$\frac{A^{ideal}}{Nk_B T} = \sum_{i=1}^{n_{components}} x_i \ln(\rho_i \Lambda_i^3) - 1 \quad (5.6)$$

where  $n_{components}$  represents the number of pure components,  $\rho_i = N_i/V$  (the molecular number density of chains of component  $i$ ),  $x_i$  is the mole fractions of component  $i$  in the mixture, and  $\Lambda_i$  is the thermal de Broglie wavelength.

The monomer free energy is given by a second order high temperature expansion using Barker and Henderson perturbation theory for mixtures [73],

$$\frac{A^{mono}}{Nk_B T} = \sum_{i=1}^{n_{components}} \sum_{k=1}^{n'_k} m_{ki} x_i \left( a^{HS} + \frac{a_1}{k_B T} + \frac{a_2}{(k_B T)^2} \right) \quad (5.7)$$

where  $n'_k$  is the number of types of functional groups  $k$  in a chain of component  $i$  and  $m_{ki}$  the number of segments of type  $k$  in chains of component  $i$ .

Finally, the free energy due to chain formation is given by,

$$\frac{A^{chain}}{Nk_B T} = - \sum_{i=1}^n x_i \sum_{kj} \ln y_{ik,ij}^{SW}(\sigma_{ik,ij}) \quad (5.8)$$

where the first sum is over all components in the mixture and the second sum considers the chain formation and connectivity of the segments within a given chain. The background correlation function is given by,

$$y_{ki,kj}^{SW}(\sigma_{ki,kj}) = \exp\left(\frac{-\epsilon_{ki,kj}}{k_B T}\right) g_{ki,kj}^{SW}(\sigma_{ki,kj}) \quad (5.9)$$

where  $g_{ki,kj}^{SW}(\sigma_{ki,kj})$  is the radial distribution function for the square well monomers at the contact distance  $\sigma_{ki,kj}$  and is approximated by a first-order high-temperature perturbation expansion.

Thermodynamic properties, such as the pressure and chemical potential can then be obtained from the summation of the Helmholtz energy using standard thermodynamic relationships.

$$P = - \left( \frac{\partial A}{\partial V} \right)_{T,N} \quad (5.10)$$

$$\mu = \left( \frac{\partial A}{\partial N_i} \right)_{T,V,N_{j \neq i}} \quad (5.11)$$

## Results and Discussion

Molecular parameters for six new functional groups (CF<sub>3</sub>, CF<sub>2</sub>, CF, CH<sub>2</sub>F, CHF<sub>2</sub>, and CHF) within the GC-SAFT-VR approach have been determined by fitting to experimental data for selected members of the different chemical families that contain these functional groups, e.g., PFAs, PFAAs, and HFes. For each chemical family studied, a representative sample of molecules for which experimental vapor pressure and saturated liquid density data is available was chosen for the fitting process while some pure compounds were reserved to test the ability of the approach to accurately predict phase behavior and thus illustrate the transferability of the group parameters. Data close to the triple point of the fluids were excluded from the fitting process since the inclusion of such data has been shown to skew the fitting process [132]. In addition, data near the critical point was also excluded from the fitting process since the GC-SAFT-VR approach, like all analytical equations of state, does not consider the long-range density fluctuations that occur in the critical region and over predicts the critical pressure and temperature of the fluid. Additionally, the lowest members of the homologous series were excluded from the study since their properties typically deviate from the behavior exhibited by the longer chained members [48]. The molecular parameters ( $m_{ki}$ ,  $\sigma_{ki,ki}$ ,  $\epsilon_{ki,lj}$ , and  $\lambda_{ki,lj}$ ) for each new functional group are reported in Tables 5.1-5.3.

**Table 5.1:** GC-SAFT-VR parameters for the segment size  $\sigma$  and segment number,  $m$ , of each functional group studied.

Groups	$\sigma$ (Å)	$m_i$
CF <sub>3</sub>	4.618	0.685
CF <sub>2</sub>	4.345	0.370
CF <sub>2</sub> $\alpha$	4.345	0.370
CF	3.251	0.269
CHF <sub>2</sub>	3.076	1.577
CH <sub>2</sub> F	3.338	1.046
CHF	3.962	0.548

**Table 5.2:** GC-SAFT-VR segment-segment dispersion energy range parameters  $\lambda_{ki,lj}$

	CF <sub>3</sub>	CF <sub>2</sub> $\alpha$	CF <sub>2</sub>	CF	CHF <sub>2</sub>	CH <sub>2</sub> F	CHF
CH <sub>3</sub>	1.398	1.572	1.572	1.644	1.421	1.463	1.421
CH <sub>2</sub>	1.483	1.819	1.654	1.734	1.524	1.560	1.512
CH	1.608	1.786	1.786	1.888	1.678	1.709	1.649
C=O	1.567	1.752	1.752	1.856	1.631	1.666	1.606
CH <sub>2</sub> =CH	1.429	1.303	1.303	1.687	1.461	1.501	1.455
C <sub>6</sub> H <sub>5</sub>	1.605	1.801	1.801	1.918	1.683	1.717	1.650
OCH <sub>2</sub> (esters)	1.435	1.630	1.630	1.721	1.472	1.516	1.465
OCH <sub>3</sub> (esters)	1.455	1.647	1.647	1.739	1.495	1.538	1.486
OCH (esters)	1.323	1.508	1.508	1.575	1.330	1.379	1.341
cis- CH=CH	1.563	1.752	1.752	1.858	1.628	1.663	1.602
trans CH=CH	1.534	1.721	1.721	1.820	1.592	1.628	1.571
OCH <sub>3</sub> (ether)	1.423	1.611	1.611	1.695	1.455	1.498	1.450
OCH <sub>2</sub> (ether)	1.597	1.621	1.621	1.755	1.468	1.555	1.547
OCH (ether)	1.628	1.848	1.848	1.990	1.723	1.760	1.680
C-CH <sub>2</sub>	1.590	1.782	1.782	1.893	1.663	1.697	1.633
OH	1.414	1.561	1.561	1.618	1.436	1.470	1.435

<b>terminal</b>							
<b>OH</b>							
<b>internal</b>	1.700	1.838	1.838	1.919	1.765	1.786	1.736
<b>CH=O</b>	1.410	1.586	1.586	1.659	1.437	1.478	1.435
<b>NH<sub>2</sub></b>	1.413	1.606	1.606	1.692	1.443	1.489	1.440
<b>NH</b>	1.497	1.678	1.678	1.767	1.544	1.581	1.529
<b>COOH</b>	1.431	1.643	1.643	1.747	1.470	1.519	1.463
<b>C<sub>6</sub>H<sub>6</sub></b>	1.489	1.675	1.675	1.768	1.536	1.575	1.521
<b>CO<sub>2</sub></b>	1.398	1.597	1.597	1.684	1.426	1.474	1.425
<b>CF<sub>3</sub></b>	1.321	1.591	1.591	1.526	1.327	1.367	1.336
<b>CF<sub>2</sub><math>\alpha</math></b>	1.476	1.641	1.641	1.717	1.515	1.549	1.504
<b>CF<sub>2</sub></b>	1.476	1.641	1.641	1.717	1.515	1.549	1.504
<b>CF</b>	1.526	1.717	1.717	1.818	1.584	1.621	1.563
<b>CH<sub>2</sub>F</b>	1.367	1.549	1.549	1.621	1.385	1.430	1.389
<b>CHF<sub>2</sub></b>	1.327	1.515	1.515	1.584	1.336	1.385	1.346
<b>CHF</b>	1.336	1.504	1.504	1.563	1.346	1.389	1.354

**Table 5.3:** GC-SAFT-VR segment-segment dispersion energy well depth parameters  $\epsilon_{ki,lj} / k_B$  (K).

	<b>CF<sub>3</sub></b>	<b>CF<sub>2</sub><math>\alpha</math></b>	<b>CF<sub>2</sub></b>	<b>CF</b>	<b>CHF<sub>2</sub></b>	<b>CH<sub>2</sub>F</b>	<b>CHF</b>
<b>CH<sub>3</sub></b>	271.88	226.43	226.43	260.40	258.13	253.82	328.97
<b>CH<sub>2</sub></b>	273.60	227.87	177.96	262.05	259.77	255.43	331.05
<b>CH</b>	177.65	147.95	147.95	170.15	168.67	165.85	214.95
<b>C=O</b>	356.58	296.97	296.97	341.51	338.54	332.89	431.45
<b>CH<sub>2</sub>=CH</b>	263.09	166.52	166.52	251.97	249.78	245.61	318.33
<b>C<sub>6</sub>H<sub>5</sub></b>	192.11	160.00	160.00	184.00	182.40	179.35	232.45
<b>OCH<sub>2</sub> (esters)</b>	183.04	152.44	152.44	175.30	173.78	170.88	221.47
<b>OCH<sub>3</sub> (esters)</b>	221.85	184.76	184.76	212.48	210.63	207.11	268.43
<b>OCH (esters)</b>	160.06	133.31	133.31	153.30	151.97	149.43	193.67
<b>cis-CH=CH</b>	206.28	171.79	171.79	197.56	195.84	192.57	249.59
<b>trans-CH=CH</b>	221.47	184.45	184.45	212.12	210.27	206.76	267.97
<b>OCH<sub>3</sub> (ether)</b>	269.63	224.56	224.56	258.24	255.99	251.72	326.24
<b>OCH<sub>2</sub> (ether)</b>	340.53	191.95	191.95	228.43	224.54	222.66	288.58
<b>OCH (ether)</b>	146.80	122.26	122.26	140.60	139.38	137.05	177.63
<b>C-CH<sub>2</sub></b>	125.61	104.61	104.61	120.30	119.26	117.27	151.98
<b>OH terminal</b>	410.80	342.13	342.13	393.45	390.03	383.52	497.06
<b>OH internal</b>	327.10	272.42	272.42	313.28	310.55	305.37	395.77
<b>CH=O</b>	323.45	269.38	269.38	309.79	307.10	301.97	391.37

<b>NH<sub>2</sub></b>	277.50	231.11	231.11	265.77	263.46	259.07	335.76
<b>NH</b>	441.14	367.40	367.40	422.51	418.83	411.84	533.77
<b>COOH</b>	252.10	209.96	209.96	241.46	239.36	235.36	305.04
<b>C<sub>6</sub>H<sub>6</sub></b>	249.82	208.06	208.06	239.27	237.18	233.23	302.27
<b>CO<sub>2</sub></b>	237.87	198.11	198.11	227.83	225.85	222.08	287.82
<b>CF<sub>3</sub></b>	315.56	262.81	262.81	302.23	299.60	294.60	381.81
<b>CF<sub>2</sub><math>\alpha</math></b>	262.81	218.87	218.87	251.70	249.51	245.35	317.99
<b>CF<sub>2</sub></b>	262.81	218.87	218.87	251.70	249.51	245.35	317.99
<b>CF</b>	302.23	251.70	251.70	289.46	286.94	282.15	365.68
<b>CH<sub>2</sub>F</b>	294.60	245.35	245.35	282.15	279.70	275.03	356.45
<b>CHF<sub>2</sub></b>	299.60	249.51	249.51	286.94	284.45	279.70	362.50
<b>CHF</b>	381.81	317.99	317.99	365.68	362.50	356.45	461.98

### *Pure fluids*

In the GC-SAFT-VR approach, perfluoroalkanes are described by the CF<sub>3</sub> and CF<sub>2</sub> functional groups. In order to reduce the number of fitted parameters for the fluorinated groups, the relationship proposed by Archer [123] for  $m$  was used, which yields  $m_{CF_3} = 0.685$  and  $m_{CF_2} = 0.370$ . The 3 remaining parameters ( $\sigma_{ki,ki}$ ,  $\epsilon_{ki,lj}$ , and  $\lambda_{ki,lj}$ ) were determined by fitting to experimental vapor pressure and saturated liquid density data for perfluorobutane (C<sub>4</sub>F<sub>10</sub>), perfluoropentane (C<sub>5</sub>F<sub>12</sub>), perfluoroheptane (C<sub>7</sub>F<sub>16</sub>), perfluorooctane (C<sub>8</sub>F<sub>18</sub>), and perfluorodecane (C<sub>10</sub>F<sub>22</sub>). These parameters were then used to predict the phase behavior of perfluoropropane (C<sub>3</sub>F<sub>8</sub>), perfluorohexane (C<sub>6</sub>F<sub>14</sub>), and perfluorononane (C<sub>9</sub>F<sub>20</sub>). For the correlated perfluoroalkanes the average deviation in the vapor pressure compared to experiment is 3.86% and for the saturated liquid densities 2.08%, while for the predicted systems the deviations are 6.03% for the vapor pressure and 3.85% for saturated liquid densities. The percentage absolute average deviations (%AAD) obtained from the GC-SAFT-VR approach for the vapor pressure and saturated liquid densities are reported in Table A.1 of the appendix material.

Due to the polarity of the PFAA molecules, the Lorentz Berthelot combining rules do not accurately capture the cross interactions in these systems. Therefore, using the CH<sub>3</sub> and CH<sub>2</sub>

parameters determined in earlier work [39] with the  $\text{CF}_3$  and  $\text{CF}_2$  parameters obtained from fitting to the PFA family, a cross interaction between the  $\text{CH}_2$  and  $\text{CF}_2$  groups in the PFAA molecules has been fitted using vapor pressure and saturated liquid density data for perfluorobutylpentane ( $\text{F}_4\text{H}_5$ ) and perfluorobutylhexane ( $\text{F}_4\text{H}_6$ ). The vapor pressure and saturated liquid densities of perfluorobutyloctane ( $\text{F}_4\text{H}_8$ ), perfluorohexyloctane ( $\text{F}_6\text{H}_8$ ), and perfluorohexylhexane ( $\text{F}_6\text{H}_6$ ) were then predicted. Using only one cross interaction between the  $\text{CH}_2$  and  $\text{CF}_2$  groups accurately captures the behavior of the smaller PFAA molecules giving deviations of 3-4% in vapor pressure and less than 1% for the saturated liquid densities; however, for the larger PFAA molecules, the observed deviations are higher (~10%). Further investigation of the molecular structure of the PFAA molecules was performed and electron density maps, which measure the probability that an electron is present at a specific location in a molecule, calculated. The high electronegativity (4.0 on the Pauling scale) of fluorine results in the fluorine atoms drawing electrons from adjacent atoms, in this case carbon, and results in a partial negative charge on the fluorines and a partial positive charge on the carbons. This is illustrated in Figure 5.1, which provides an electron density map for  $\text{F}_4\text{H}_5$ , and that the electron density is greater for the  $\text{CH}_2$  and  $\text{CF}_2$  groups at the junction of the perfluorinated and hydrogenated section of the molecule compared to the remaining  $\text{CH}_2$  and  $\text{CF}_2$  groups present. Therefore, to better capture the molecular behavior of the PFAA molecules in the model, two  $\text{CF}_2$  groups were defined: one for the  $\text{CF}_2$  group at the junction of the perfluorinated and hydrogenated segments, which we denote as  $\alpha\text{CF}_2$ , and a second general  $\text{CF}_2$  group to describe the remainder of the  $\text{CF}_2$  groups in the molecule. Utilizing this approach, deviations of less than 1% were obtained in liquid density for all correlations and predictions and 5% for the vapor pressures. The percentage absolute average deviations (%AAD) obtained from the GC-SAFT-VR approach for the vapor pressure and saturated liquid densities are reported in the appendix material.

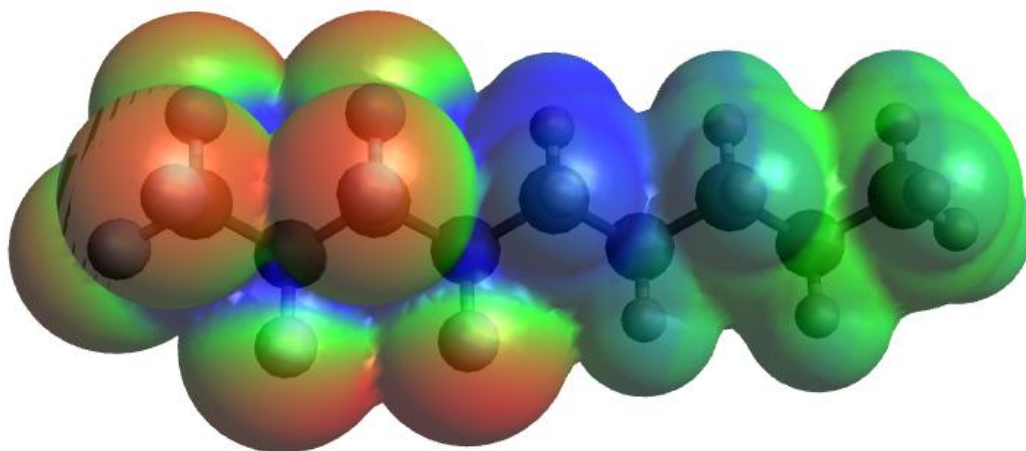


**Figure 5.1:** Electrostatic potential map for perfluorobutylpentane ( $F_4H_5$ ) created using GaussView version 5 [5]. The red region represents the lowest electrostatic potential data and the blue region represents the highest.

To describe branched molecules, a CF group needs to be defined and parameterized. The parameters for the CF segment were determined by fitting to vapor pressure and saturated liquid density data for the 2-fluoro-2-methylbutane molecule, which is comprised of the  $CH_3$ ,  $CH_2$ , and CF groups. The parameters for the CF group were optimized with the  $CH_2$  and  $CH_3$  group parameters being taken from previous work [48]. We note that very limited experimental data is available for molecules containing a CF group and so testing the resulting model parameters by predicting the phase behavior of other pure components was not possible. Having developed parameters for all of the alkyl-fluoro (i.e.,  $CF_3$ ,  $CF_2$ , and CF) groups, in Figure 5.2, we report the molecular parameters obtained for the  $CF_3$ ,  $CF_2$ , and CF groups as a function of molecular weight. As can be seen from the figure the values for,  $m\lambda$ ,  $m\sigma^3$ , and  $m\epsilon/k_b$  essentially increase linearly with molecular mass. The same trend was observed in previous work for the  $CH_3$ ,  $CH_2$ , and CH functional groups [48].



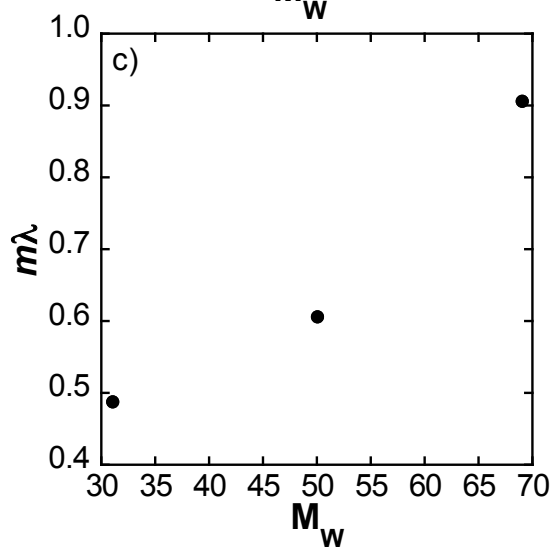
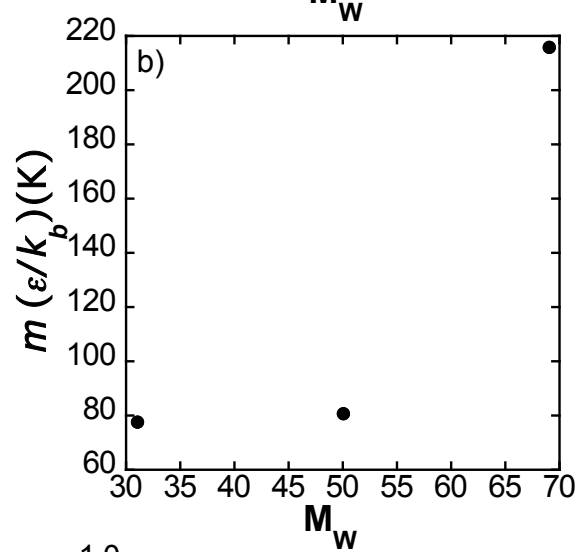
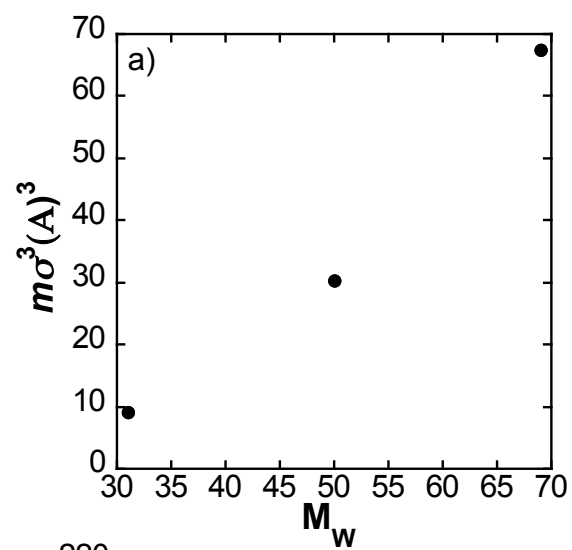


**Figure 5.2:** GC-SAFT-VR molecular parameters for the functional groups  $\text{CF}_3$ ,  $\text{CF}_2$ , and  $\text{CF}$  as a function of the molecular weight ( $M_w$ ): (a) segment size, (b) potential depth, (c) potential range

In addition to the  $\text{CF}$  group, the  $\text{CHF}_2$  group is also necessary to describe branched fluorinated molecules and fluorinated ethers. To obtain parameters for this group, the 1,1-difluoroalkane family, comprised of the groups  $\text{CHF}_2$ ,  $\text{CH}_2$ , and  $\text{CH}_3$ , was studied. Using parameters for the  $\text{CH}_2$  and  $\text{CH}_3$  groups from previous work [48], parameters were determined for the  $\text{CHF}_2$  group by fitting to the experimental vapor pressure and saturated liquid density for 1,1-difluoropentane and 1,1-difluorohexane. The phase behavior of 1,1-difluoroheptane and 1,1-difluorooctane were then predicted in order to test the model parameters. The larger members of this group were chosen since their behavior exhibited group additivity unlike the smaller members, 1,1-difluoropropane and 1,1-difluorobutane, which tend to deviate significantly. Including the smaller molecules in the study leads to increased deviations from experimental results. The molecules fitted had an average deviation of 6.53% in vapor pressure and 0.098% in liquid density from experiment, while the predicted molecules exhibited deviations of 9.75% in vapor pressure and 0.127% in saturated liquid density. The %AAD obtained from the GC-SAFT-VR correlations and predictions are reported in Appendix.

To enable the GC-SAFT-VR approach to describe a greater number of fluorinated molecules, including the hydrofluoroethers, parameters for the  $\text{CH}_2\text{F}$  group have also been defined. The  $\text{CH}_2\text{F}$  group can be found in the 1-fluoroalkane family, which also contains the  $\text{CH}_3$  and  $\text{CH}_2$  groups. Parameters for the  $\text{CH}_2\text{F}$  group were determined by fitting to vapor pressure and saturated liquid density data for 1-fluoroheptane and 1-fluorooctane and the phase behavior of 1-fluoropentane, 1-fluorohexane, and 1-fluorononane was then predicted. As reported in Appendix, the average %AAD between experiment and the GC-SAFT-VR predictions for the vapor pressure and saturated liquid density for was found to be 5.22% and 0.33% respectively.

As a final step to complete the groups needed to study the organofluorine molecules of interest, the  $\text{CHF}$  group present in the 2-fluoroalkanes and 3-fluoroalkanes molecules was

characterized. 3-fluorohexane was used to determine the group parameters by fitting to the vapor pressure and saturated liquid density, while the phase behavior of the 3-fluoropropane and 2-fluorobutane was predicted. An absolute average deviation between the experimental data and GC-SAFT-VR predictions of 4.95% in vapor pressure and 1.53% in saturated liquid density was obtained as reported in Appendix.

Using the molecular parameters determined from the fluorinated group fittings discussed above, the phase behavior of pure HFEs were then studied. HFE molecules are formed using the functional groups  $\text{CF}_3$ ,  $\text{CF}_2$ ,  $\text{CH}_2$ ,  $\text{CHF}$ , and  $\text{CHF}_2$  as defined in this work and  $\text{OCH}_2$ , the parameters for which were taken from previous work [48]. For example, HFE-347pc-f ( $\text{CHF}_2\text{-CF}_2\text{-OCH}_2\text{-CF}_3$ ) is formed using the four groups  $\text{CF}_3$ ,  $\text{OCH}_2$ ,  $\text{CF}_2$  and  $\text{CHF}_2$ , while HFE-449mec-f ( $\text{CF}_3\text{-CHF-CF}_2\text{-OCH}_2\text{-CF}_3$ ) contains the groups  $\text{CF}_3$ ,  $\text{CHF}$ ,  $\text{CF}_2$ , and  $\text{OCH}_2$ . The presence of the ether oxygens in alkanes usually leads to chain polarity due to the C-O bond [133] and so deviation from Lorentz-berthelot combining rules are to be expected. To address this, cross interaction are introduced between the following groups:  $\text{OCH}_2$  and  $\text{CF}_3$ ,  $\text{OCH}_2$  and  $\text{CF}_2$ ,  $\text{OCH}_2$  and  $\text{CHF}$ , and  $\text{OCH}_2$  and  $\text{CHF}_2$ . The  $\text{OCH}_2$  and  $\text{CF}_3$  cross interaction was determined by fitting to the vapor pressure of HFE-356mf-f ( $\text{CF}_3\text{-OCH}_2\text{-CH}_2\text{-CF}_3$ ) and a deviation in vapor pressure from the experimental data of 0.21% was found. The  $\text{OCH}_2$  and  $\text{CF}_2$ , cross interaction was determined by fitting to the vapor pressure of HFE-467mccf ( $\text{CF}_3\text{-CF}_2\text{-CF}_2\text{-OCH}_2\text{-CH}_3$ ) and a deviation in vapor pressure of 0.74% was found. The  $\text{OCH}_2$  and  $\text{CHF}$  cross interaction was determined by fitting to the vapor pressure of HFE-449mec-f ( $\text{CF}_3\text{-CHF-CF}_2\text{-OCH}_2\text{-CF}_3$ ) and a deviation in vapor pressure of 7.6% was found. Finally, the cross interaction between the  $\text{OCH}_2$  and  $\text{CHF}_2$  groups was determined by fitting to the vapor pressure of HFE-347mcf ( $\text{CF}_3\text{-CF}_2\text{-OCH}_2\text{-CHF}_2$ ); deviations in vapor pressure were found to be 4.0%. Using the determined fitted cross interactions, the vapor pressure of the remaining HFE molecules, HFE-347pc-f ( $\text{CHF}_2\text{-CF}_2\text{-OCH}_2\text{-CF}_3$ ), HFE-374pcf ( $\text{CHF}_2\text{-CF}_2\text{-OCH}_2\text{-CH}_3$ ), HFE-449mcf-c ( $\text{CF}_3\text{-CF}_2\text{-OCH}_2\text{-CF}_2\text{-CHF}_2$ ), HFE-458pcf-c ( $\text{CHF}_2\text{-CF}_2\text{-OCH}_2\text{-CF}_2\text{-CHF}_2$ ), and HFE-569mccc ( $\text{CF}_3\text{-CF}_2\text{-CF}_2\text{-CF}_2\text{-OCH}_2\text{-CH}_3$ ),

were then predicted and the calculated average deviations from the experimental data was found to be 5.7% in vapor pressure. The percentage absolute average deviations (%AAD) obtained from the GC-SAFT-VR approach for the vapor pressures are reported in Table A.1 of the appendix material. In the work of Vijande [130], the phase behavior of the HFE molecules was studied using a more complicated model than proposed here, where two sets of parameters for each of the CH<sub>3</sub>, CH<sub>2</sub>, CF<sub>3</sub>, and CF<sub>2</sub> groups were used to describe the interactions due to the chain polarity.

### *Binary Mixtures*

With the new molecular parameters for organic fluorine groups determined and validated the phase behavior of binary mixtures containing these functional groups can be examined. The phase behavior of perfluoroalkane and alkane binary mixtures were first considered. Although both alkanes and perfluoroalkanes are nonpolar species, and thus it would be expected that their mixtures behave almost ideally, in reality these mixtures display large positive deviations from ideality [134, 135], which typically necessitates the fitting of cross interaction parameters to binary mixture data in equation of state studies. However, with the GC-SAFT-VR approach no additional fitting beyond the group parameters already determined is required to predict the phase behavior. In Figure 5.3 results are presented for binary mixtures of perfluorohexane + *n*-alkanes pentane, heptane and octane and hexane + perfluoroalkanes, perfluorooctane, perfluoroheptane, perfluorohexane, and perfluoropentane. From the figures, we can see that the theory is able to accurately predict the phase behavior of each binary mixture studied. We note that similar results were observed in the work of Morgado *et al.* [3] where binary interaction parameters were fitted to UCST and excess volume data for the *n*-hexane + *n*-perfluorohexane system.

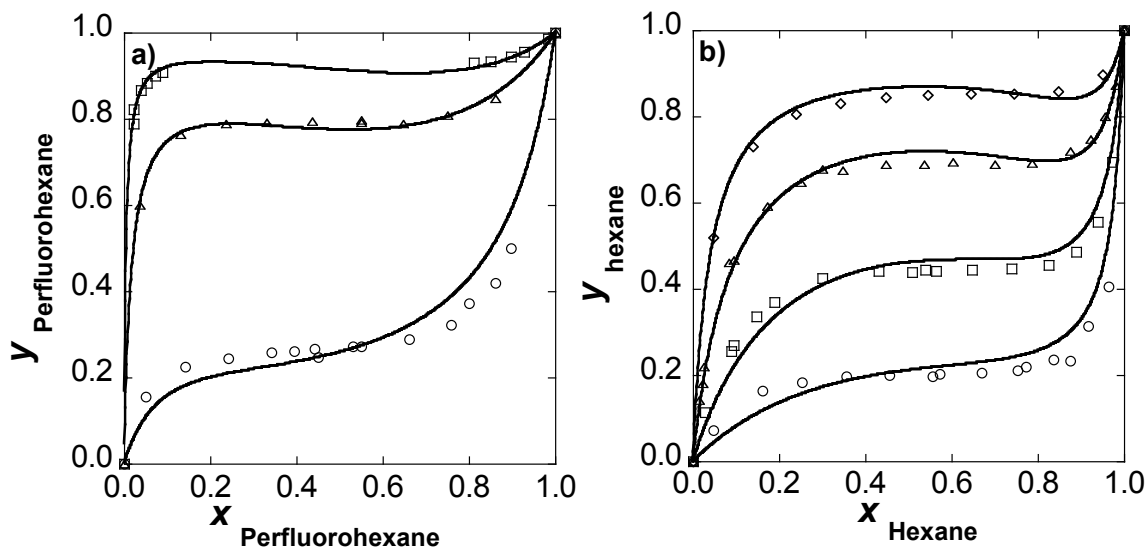


**Figure 5.3:** Predicted composition curves for a.) perfluorohexane + pentane (circles), + heptane (triangles) and + octane (squares), and b.) hexane + perfluoropentane (circles), + perfluorohexane (squares), + perfluoroheptane (triangles) and + perfluorooctane (diamonds). Solid lines represents GC-SAFT-VR predictions and the data points represent experimental data [9].

Next we predict, again with no additional fitting, the phase diagrams of the perfluorohexane + hexane and perfluorohexane and pentane binary mixtures. The  $P_{xy}$  phase diagrams at three different constant temperatures slices (318.15 K, 308.15 K, and 298.15 K) are shown in Figure 5.4a for perfluorohexane + hexane. We note that this mixture was also studied in the work of Morgado *et al.* [3], who observed a slight under-prediction in the pressure with the hetero-SAFT-VR approach, and in the work of Colina *et al.* [136], where SAFT-VR predictions over-predicted the pressure as well as the pure vapor pressure. In our work, using a purely predictive group contribution approach, the theory also correctly captures the shape of the curves but results in lower deviations for the vapor pressure than in earlier studies. In addition, the GC-SAFT-VR approach accurately captures the experimentally observed azeotropic behavior; however, as temperature increases the deviations between the predicted azeotrope vapor pressure and experimental data increases as the azeotrope is slightly under-predicted. In Figure 5.4b, the

phase behavior of binary mixture perfluorohexane + pentane is predicted at 293.15 K. Although a slight over prediction in vapor pressure is observed near the azeotrope, improved agreement with experimental data for the vapor pressure as compared to the work of Dias *et al.* [9] is observed.

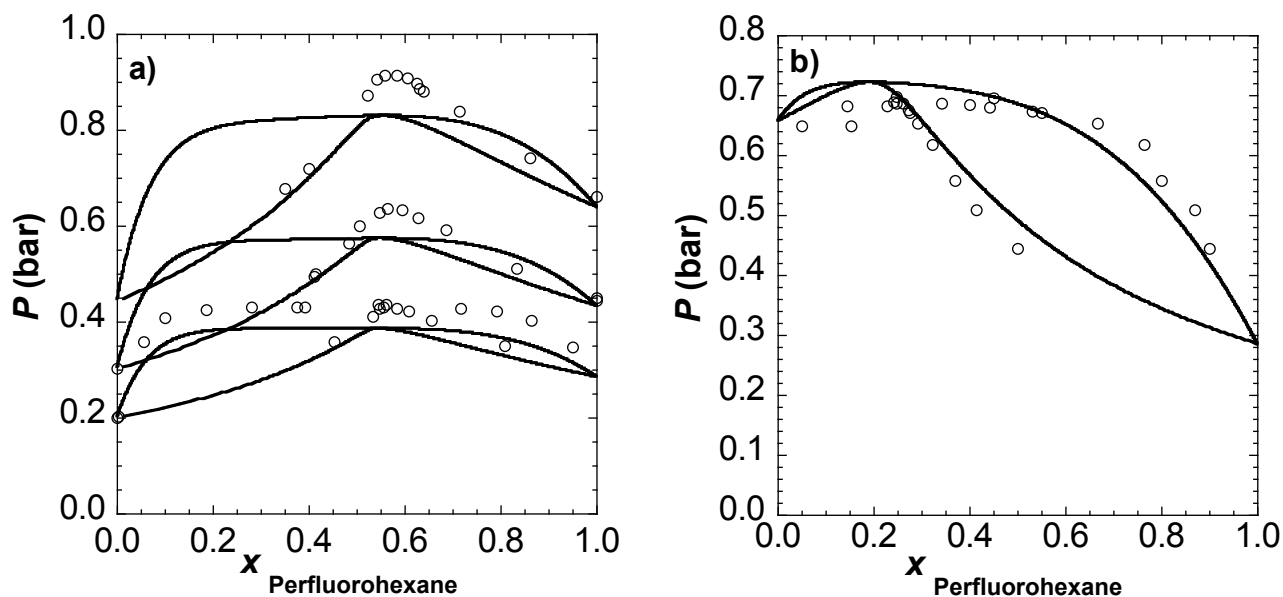


**Figure 5.4:**  $P_{xy}$  prediction of a) perfluorohexane + hexane binary mixtures at 298.15K, 308.15K, and 318.15K (bottom to top) and b) perfluorohexane + pentane binary mixture at 293.65 K. The lines correspond to the GC-SAFT-VR predictions and the symbols the experimental data [3, 4]

Additionally, we find that the theory is able to capture the change in phase behavior as the length of the perfluoroalkane is increased to perfluorooctane. This is shown in Figure 5.5, where we examine the  $T_{xy}$  representation of the perfluorooctane and a branched fluorinated alkane, perfluoro-2-methylpentane phase diagram. We observe good agreement in the vapor predictions; however, we see slight deviations in the liquid predictions for lower temperatures. Nonetheless, considering this mixture has been predicted with no fitting to binary mixture data, we consider the results to be very good.

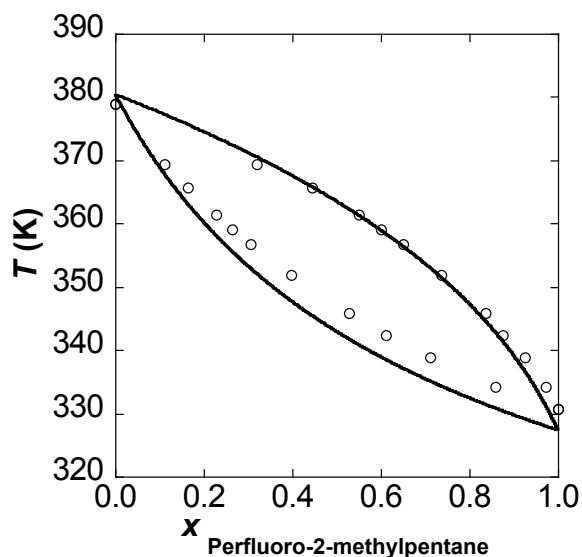


**Figure 5.5:** Predictions of the  $T_{xy}$  phase diagram for perfluorooctane + perfluoro-2-methylpentane 1.013 bar. The solid lines correspond to the theoretical predictions and the symbols the experimental data [8].

We now consider in Figure 5.6 the phase behavior of the binary mixture of perfluorobutane with butane and butene. Constant temperature  $P_{xy}$  slices of the phase diagram for the perfluorobutane + butane binary mixture are presented in Figure 5.6a. Both McCabe *et al.* [124] and Aparicia [137] have previously studied this mixture, with the results also in good agreement with experimental data. In the case of butene, pure fluid data is not available to determine the correct cross interaction between the  $\text{CH}_2 = \text{CH}$  and  $\text{CF}_2$  groups. Therefore, the cross interaction between  $\text{CH}_2 = \text{CH}$  and  $\text{CF}_2$  was fitted to the experimental mixture data at 312 K and used in a transferable manner to predict the phase behavior at 327 K and 342 K. We note that although agreement between experimental results and predictions are good, at higher temperatures, the pressure near the azeotrope is slightly over-predicted. Figure 5.6b shows the  $P_{xy}$  representation for the perfluorobutane and butene binary mixture at three constant temperature slices of 342 K, 327 K and 312 K.

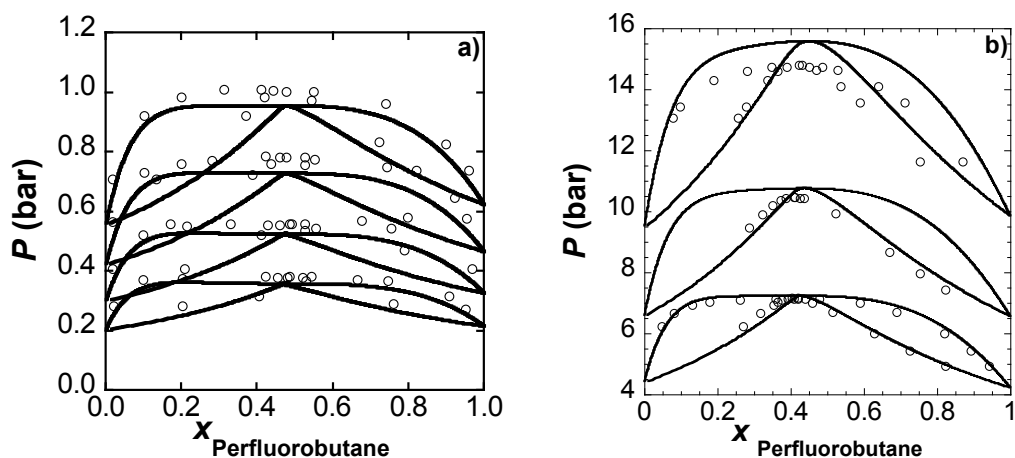


**Figure 5.6:** a.)  $P$ - $x$ - $y$  diagram at 259 K, 253 K, 246 K, and 238 K. (top to bottom) of perfluorobutane and butane binary mixtures. b.)  $P$ - $x$ - $y$  diagram at 342 K, 327 K and 312 K (top to bottom) of perfluorobutane and butene binary mixtures. Solid lines represent the GC-SAFT-VR theory while the experimental data points [14] are represented by open circles.

In addition to presenting information on the VLE, the liquid-liquid equilibrium (LLE) of binary mixtures of PFAs and alkanes has also been studied. Specifically, the symmetric mixture of perfluorohexane + hexane as well as binary mixtures of perfluorooctane + alkanes from hexane to nonane have been studied. The theory is able to capture the increase in upper critical solution temperature (UCST) with increasing molecular weight of the alkanes as shown in Figure 5.7a. Agreement between the experimental data and theoretical predictions is good considering that the binary interaction parameters are not fitted to binary mixture data and thus are used in a transferable fashion. As can be seen from the figure, the GC-SAFT-VR over predicts the UCST in most cases, especially for the longer alkane chains, which is consistent with the work of Dias *et al.*[9] where over-prediction of the UCST was observed for all systems. Colina *et al.*, [136] avoided the discrepancy found in the critical region by rescaling to the critical point. Figure 5.7b, shows the predictions of the symmetric mixture perfluorohexane + hexane. Results found are similar to the work of Morgado *et al.* [3].



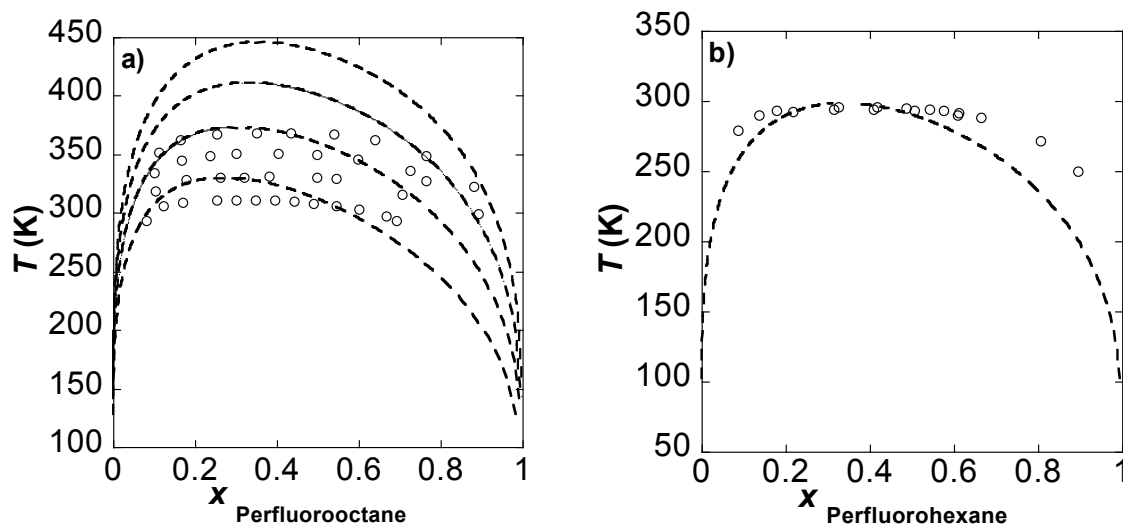


**Figure 5.7:** a.) LLE diagram with constant pressure of 1.013 bar for binary mixtures of perfluorooctane + alkanes,  $n\text{-C}_n\text{H}_{2n+2}$  with  $n = 6-9$  (from  $n = 9$  to  $n = 6$  from top to bottom). Solid lines represent GC-SAFT-VR theory and open circles represents the experimental data points [13]. b.) LLE diagram with constant pressure of 1.013 bar for binary mixtures of perfluorohexane + hexane [13]. The solid line represents the prediction. The open circles represent the experimental data [13].

As an additional test of the transferability of the fluorinated group parameters, the apparent molal volumes,  $V_{\phi}$ , of several PFAA and alkane binary mixtures have been investigated. The apparent molal volumes,  $V_{\phi}$ , of the solutes in all solutions was calculated from the equation:

$$V_{\phi} = \frac{MPd^0 - MPd}{pdd^0} + \frac{M}{d} \quad (5.12)$$

where  $M$  is the molecular weight of the solute,  $P$  and  $p$  are the masses of the solvent and solute, and  $d^0$  and  $d$  are the densities of the pure solvent and solution, respectively.

In Figure 5.8a, the theoretical results (molar volume) are compared with the experimental results [1, 2] as a function of carbon number. Figure 5.8b shows the partial molar volume as a function of carbon number. We observe that as the number of carbons present in the fluorinated chain is increased the molar volume is also increased. Good agreement was found between the experimental and theoretical predictions for all mixtures, with the exception of slight deviations

found for a carbon chain of ten, where we over-predict the molar volume. These results were predicted without the use of fitting to binary experimental data. Investigating the molar volumes, Morgado *et al.* [1] found similar results as shown here.

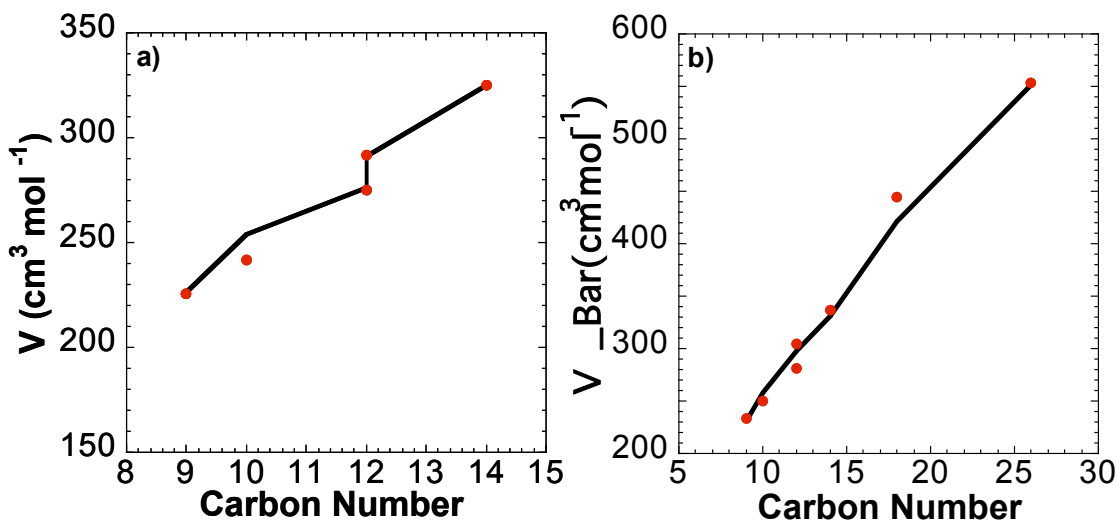


**Figure 5.8:** a.) Molar volume as a function of carbon number for PFAA and octane binary mixtures. b.) Partial molar volume as a function of carbon number for PFAA and octane binary mixtures. Solid lines represent theory and the symbols the experimental data [1, 2].

Finally, due to the importance and application of systems involving  $\text{CO}_2$  and fluorinated molecules, systems involving  $\text{CO}_2$  were also studied. The SAFT-VR  $\text{CO}_2$  parameters were taken from the literature [17, 138] and are provided in Tables 5.1-5.3. Using the  $\text{CO}_2$ ,  $\text{CF}_3$ , and  $\text{CF}_2$  parameters, the GC-SAFT-VR approach was then used to determine the phase behavior of the  $\text{CO}_2$  + perfluorohexane and  $\text{CO}_2$  + perfluorooctane mixtures. Excellent predictions can be achieved with the use of a single fitted cross interaction between the  $\text{CO}_2$  molecule and  $\text{CF}_2$  group. The perfluorooctane +  $\text{CO}_2$  binary mixture at 333.15K was used to determine the fitted cross interaction. As can be seen from Figure 5.9, good agreement is seen between the theoretical predictions (solid line) and experimental data points. Dias *et al.*[9], found similar results with the

soft-SAFT equation of state implementing two fitted binary interactions, Thus, we are able to reduce the number of fitted while increasing the accuracy of the results. Figure 5.9a and 5.9b shows a  $P_{xy}$  slice of the  $\text{CO}_2$  + perfluorohexane and  $\text{CO}_2$  + perfluorooctane phase diagrams. In addition,  $T_{xy}$  slices of the  $\text{CO}_2$  + 1,1,2,3,3,3-hexafluoropropyl (2,2,2-trifluoroethyl) (i.e., HFPE) ether binary mixture was predicted, and as shown in Figure 5.9b, found to be in good agreement with experimental data, requiring no additional fitting to experimental data.

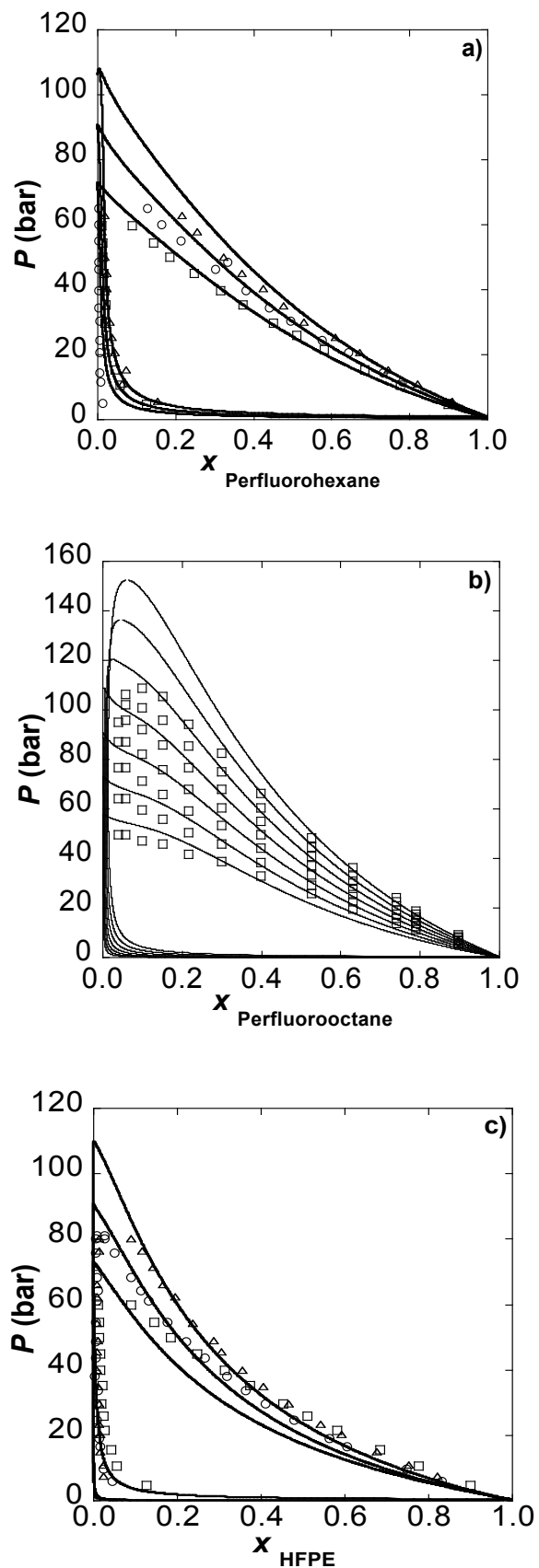


**Figure 5.9:** Constant temperature  $P_{xy}$  slices of  $\text{CO}_2$  + a) perfluorohexane binary mixture at 303.15 K (squares), 313.15 K (circles), and 323.15 K (triangles), b) perfluorooctane at 293.15 K, 303.15 K, 313.15 K, 323.15 K, 333.15 K, 343.15 K, and 353.15 K (bottom to top) and c)  $\text{C}_5\text{H}_3\text{F}_9\text{O}$  at 303.15 K (squares), 313.15 K (circles), and 323.15 K (triangles). Solid lines represent the GC-SAFT-VR predictions and the symbols the experimental data [9].

## Conclusions

In this work, the GC-SAFT-VR approach has been expanded to include the groups required to model organofluorine molecules. Several new functional groups ( $\text{CF}_3$ ,  $\text{CF}_2$ ,  $\text{CF}$ ,  $\text{CH}_2\text{F}$ ,  $\text{CHF}_2$ , and  $\text{CHF}$ ) have been defined in order to describe the fluorinated molecules of interest by fitting to experimental vapor pressure and saturated liquid density data for selected fluorinated molecules within each class of molecule studied. The parameters are then used in a transferable fashion to predict the phase behavior of other molecules not included in the fitting process. In addition, by studying the electron density maps of the complex PFAA molecules, the electron density is found to be greater for the  $\text{CH}_2 - \text{CF}_2$  groups at the junction of the molecule compared to the remaining  $\text{CH}_2\text{-CF}_2$  groups in the molecule. Through examining the electron density maps, an accurate model for the polar PFAA molecules is developed. This allows us to better capture the inter-molecular and intra-molecular interactions between unlike groups without introducing fitted cross interaction to the mixtures.

Both VLE and LLE mixtures are studied and show good representation of experimental observations. Utilizing the cross interaction determined from the PFAA mixtures provides qualitative agreement between theory and experiment, however, we see an overprediction of the critical region, which is expected.

The transferability of the parameters was demonstrated by extending the GC-SAFT-VR approach to molecules outside of the families of interest and to binary mixtures, which is an example of one of the advantages of utilizing a group contribution approach. As a result of the heteronuclear group contribution approach, an improvement is seen in the predictive ability for mixtures of PFA and PFAA as compared to other SAFT approaches.

It is expected that this model will give precise predictions for systems in which no experimental data exists, therefore, this model and group contribution can be used in the future research of organofluorine molecules and their mixtures with molecules such as  $\text{CO}_2$ .

## Chapter VI

### Modeling Organic Sulfur Molecules with a Group Contribution Based Statistical Associating Fluid Theory Approach (GC-SAFT-VR)

#### Introduction

Sulfur is one of most abundant chemical elements in petroleum, occurring at concentrations over 10 weight percent [139]. The organic sulfur containing molecules (e.g., thiols, sulfides, and thiophene) impair the effectiveness of emission control systems and contribute to significant air pollution. These molecules also present significant processing problems within the oil and gas industry, for example, thiophene, which is a major impurity present in crude oil, is problematic as conventional removal technologies such as hydrodesulphurization are not very effective on thiophene containing systems [140]. Due to recent environmental concerns, many countries have employed stricter regulations on the sulfur content in diesel fuel and gasoline [25]. With stricter fuel regulations, minimizing the cost of producing petroleum-based fuels will require new technological advances and innovations. One proposed new method to extract thiophene and its derivatives from petroleum is to utilize supercritical CO<sub>2</sub> as a solvent [141]. Knowledge of the phase behavior and volumetric properties of mixtures containing CO<sub>2</sub>, thiophene, and other solvents at high pressures are therefore needed for the continued development of these new sulfur processing processes. Specifically, the determination of the vapor liquid equilibrium (VLE) and the thermodynamic properties of sulfur compounds are essential to investigating the feasibility of the separation of sulfur impurities from petroleum. However, experimental investigations of organic sulfur systems are limited.

With limited experimental data available for parameterization, the use of simple cubic equations of state to study these systems is difficult, since such equations contain adjustable parameters, whose values are determined from the correlation of experimental data. Molecular-based equations of state such as the statistical associating fluid theory (SAFT) [39, 40], typically provide a more predictive approach, as the theory based on Wertheim's first order

thermodynamic perturbation theory [41, 43], takes into account the effect of molecular shape, size, and interactions on the thermodynamic properties. As a result the molecular parameters have a physical basis and are less dependent on the thermodynamic conditions at which they were fit, thus offering a more predictive approach than typical cubic equations of state.

The advantages of the SAFT family of equations [47], have been exploited by several authors to study organic sulfur systems. In the work of Zuniga-Moreno *et al.* [142], the phase behavior of carbon dioxide + thiophene was studied using the perturbed chain statistical associating fluid theory [72] (PC-SAFT) equation of state (EoS). The molecular parameters for carbon dioxide were taken from the literature [143] while the parameters of thiophene were obtained by fitting to vapor pressure and saturated liquid density data from the triple point to the critical point. Absolute deviation in pressure and saturated liquid density was found to be 0.76 and 0.58%, respectively. The liquid densities of thiophene at six different temperatures were then calculated using the molecular parameters determined, finding deviations of less than 1%. In order to model the volumetric properties of the mixture, a binary interaction parameter was determined from a fit to vapor liquid equilibria data at 4 different temperatures. The deviations in pressure and vapor composition were found to be less than 5% and 1%, respectively. Densities and excess molar volumes were then calculated utilizing the determined adjusted binary interaction parameter and found to be within 1% of experimental results for thiophene rich mixtures; however, deviations increased with increasing concentrations of carbon dioxide. For the excess molar volumes, large deviations (35 - 130%) were obtained and the authors suggested an improved approach be explored that offers a better representation of CO<sub>2</sub> rich mixtures in the presence of sulfur compounds.

Also utilizing the PC-SAFT equation, Khelassi-Sefaour *et al.* [144] studied thiophene, pyridine, and the ionic liquid, 1-ethyl-3-methylimidazolium thiocyanate (EMIM)[SCN] at pressures close to atmospheric pressure and temperatures between 273 K and 363 K. These mixtures are of interest due to the use of ionic liquids in extractive desulfurization of gasoline and

diesel [145]. The parameters for thiophene were taken from the work of Zuniga-Moreno *et al.* [142] and a fitted temperature dependent binary interaction parameter determined to describe the VLE of the mixture of Thiophene + [EMIM][SCN]. This binary interaction parameter varied for each temperature studied. The PC-SAFT model was found to have difficulty representing the VLLE behavior, predicting VLE when LLE is experimentally observed.

In the work of Chen *et al.* [145], thiophene + ionic liquid mixtures were also studied using the PC-SAFT approach. Thiophene parameters were taken from the work of Zuniga-Moreno *et al.* [142] while the parameters for the ionic liquids were characterized in this work by fitting to density data for the ionic liquids of interest. In this work, the phase behavior of the binary mixtures of thiophene + 1,3-dimethylimidazolium methylphosphonate ([DMIM][Ph]) and [EMIM][SCN], were compared to experimental results and found to be in good agreement for VLE data. However, as seen in the work of Khelassi-Sefaour, for the mixture of thiophene + {EMIM} {SCN} VLE was again observed instead of the experimentally determined LLE.

As discussed above, equations of state based on homonuclear versions of the SAFT theory have been used with limited success to describe the phase behavior of some thiophene mixtures. In this work, we, employ a group contribution approach; allowing for a model which can capture the  $\pi$ - $\pi$  electronic interactions present in the molecule by separating the thiophene ring into several smaller segments. As compared to a homonuclear SAFT approach, where new molecules require additional fitting to experimental data, in a group contribution approach the phase behavior of new molecules, such as thiophene derivatives, can be investigated by combining the groups of interest without additional fitting to experimental data. Another advantage to utilizing a group contribution approach is that when groups of interest are contained in the same molecule, binary interactions parameters between the groups can be obtained from pure components experimental data alone, without additional fitting to binary experimental data, as required in an homonuclear approach. Here we use the group contribution statistical associating fluid theory for potentials of variable range (GC-SAFT-VR), which combines the



hetero-SAFT-VR equation, which forms chain molecules from hetero-nuclear segments interacting through attractive potentials of variable attractive range, with a group contribution approach (GC) [48]. The GC-SAFT-VR approach thus describes molecules as chains of tangentially bonded segments of different size and/or energy parameters, which represent various functional groups within the molecule. The location of the functional groups and association sites can be specified within a molecule, enabling the heterogeneity in molecular architecture to be captured within a SAFT model. In recent studies [47, 48, 131], the GC-SAFT-VR approach has been successfully applied to study a wide range of associating and non-associating molecules including hydrocarbons [48], ketones [48], alcohols [47], polymers [47], and aromatics [131]. In this work the applicability of this predictive equation of state is expanded by characterizing the CH=(Thiophene) and –S- functional groups and determining their cross interactions with other groups of interest. The theoretical predictions are compared with experimental results for pure thiophene, 3-methylthiophene, and benzothiophene, as well as binary mixtures containing the above-mentioned fluids with alkanes, alkenes, aromatics, carbon dioxide, and alcohols.

The remainder of the paper is organized as follows: the GC-SAFT-VR equation is presented in Section 2, the functional group parameter estimation and results for pure fluids and binary mixtures are discussed in Section 3, and conclusions drawn in Section 4.

### **Molecular Model and Theory**

As a modification to the hetero-SAFT-VR equation [127], which allows the description of molecules formed from chains of tangentially bonded segments of different size and/or energy parameters, the GC-SAFT-VR approach was proposed by Peng *et al.* [48, 127] to model molecules as chains tangentially bonded segments that represent various functional groups within the molecule. In this approach, molecular heterogeneity and connectivity is explicitly accounted for within the SAFT-VR framework. The segments representing each functional group interact via a square well potential, which can be described by,

$$u_{ki,lj}(r) = \begin{cases} +\infty & \text{if } r < \sigma_{ki,lj} \\ -\varepsilon & \text{if } \sigma_{ki,lj} \leq r \leq \lambda_{ki,lj}\sigma_{ki,lj} \\ 0 & \text{if } r \leq \lambda_{ki,lj}\sigma_{ki,lj} \end{cases} \quad (6.1)$$

where  $u_{kl,lj}$  represents the interaction between a functional group of type  $i$  present in molecule  $k$  with a functional group of type  $j$  in molecule  $l$ ,  $\sigma$  is the segment diameter,  $\varepsilon$  is the depth of the square well,  $\lambda$  is the potential range, and  $r$  is the distance between the two groups. The unlike size and energy interactions can be obtained from the Lorentz-Berthelot combining rules expressed by,

$$\sigma_{ij} = \frac{\sigma_{ii} + \sigma_{jj}}{2} \quad (6.2)$$

$$\varepsilon_{ij} = \sqrt{\varepsilon_{ii}\varepsilon_{jj}} \quad (6.3)$$

and the unlike potential range is given by,

$$\lambda_{ij} = \frac{\lambda_{ii}\sigma_{ii} + \lambda_{jj}\sigma_{jj}}{\sigma_{ii} + \sigma_{jj}} \quad (6.4)$$

For interactions involving polar functional groups, which are expected to deviate from the Lorentz-Berthelot combining rules, an advantage of the group-contribution approach is that these unlike interactions can be fitted to pure component experimental data for molecules containing the functional groups of interest. As such, a predictive equation for the study of mixture phase behavior is retained.

The GC-SAFT-VR approach written in terms of the Helmholtz free energy is described as the sum of four separate contributions, *viz*

$$\frac{A}{Nk_B T} = \frac{A^{ideal}}{Nk_B T} + \frac{A^{mono}}{Nk_B T} + \frac{A^{chain}}{Nk_B T} + \frac{A^{assoc}}{Nk_B T} \quad (6.5)$$

where  $N$  is the total number of molecules in the system,  $T$  is the temperature, and  $k_B$  is the Boltzmann constant and  $A^{ideal}$ ,  $A^{mono}$ ,  $A^{chain}$ , and  $A^{assoc}$  are the contributions to the free energy due

to the ideal, monomer, chain, and association interactions, respectively. The expressions for each of the remaining terms for a mixture system composed of heteronuclear chain molecules are presented below. Since the theory has been well documented [48] [87] a short overview of the GC-SAFT-VR theoretical framework is given and the reader is referred to the original work for additional details.

The ideal Helmholtz free energy,  $A^{ideal}$ , is given by,

$$\frac{A^{ideal}}{Nk_B T} = \sum_{i=1}^{n_{components}} x_i \ln(\rho_i \Lambda_i^3) - 1 \quad (6.6)$$

where  $n_{components}$  represents the number of pure components,  $\rho_i = N_i/V$  is the molecular number density of chains of component  $i$ ,  $x_i$  is the mole fractions of component  $i$  in the mixture, and  $\Lambda_i$  is the thermal de Broglie wavelength.

The monomer free energy,  $A^{mono}$ , is given by a second order high temperature expansion using Barker and Henderson perturbation theory for mixtures [73]

$$\frac{A^{mono}}{NkT} = \sum_{i=1}^{n_{components}} \sum_{k=1}^{n'_k} m_{ki} x_i \left( a^{HS} + \frac{a_1}{k_B T} + \frac{a_2}{(k_B T)^2} \right) \quad (6.7)$$

where  $n'_k$  is the number of types of functional groups  $k$  in a chain of component  $i$  and  $m_{ki}$  the number of segments of type  $k$  in chains of component  $i$ .

The contribution to the free energy due to chain formation,  $A^{chain}$ , from a mixture of hetero-segmented square-well monomer segments is given by,

$$\frac{A^{chain}}{NkT} = - \sum_{i=1}^n x_i \sum_{kj} \ln y_{ik,ij}^{SW}(\sigma_{ik,ij}) \quad (6.8)$$

where the first sum is over all components in the mixture and the second sum considers the chain formation and connectivity of the segments within a given chain. The background correlation function is given by,

$$y_{ki,kj}^{SW}(\sigma_{ki,kj}) = \exp\left(\frac{-\varepsilon_{ki,kj}}{k_B T}\right) g_{ki,kj}^{SW}(\sigma_{ki,kj}) \quad (6.9)$$

where  $g_{ki,kj}^{SW}(\sigma_{ki,kj})$  is the radial distribution function for the square well monomers at the contact distance  $\sigma_{ki,kj}$  and is approximated by a first-order high-temperature perturbation expansion.

Finally, the contribution due to association, ( $A^{Assoc}$ ), [86] interactions between sites on different functional groups that form the molecules of interest is expressed as:

$$\frac{A^{Assoc}}{Nk_B T} = \sum_{i=1}^n x_i \left[ \sum_{a=1}^{s_i} \left( \ln X_{a,i} - \frac{X_{a,i}}{2} \right) + \frac{s_i}{2} \right] \quad (6.10)$$

where the first sum is over the number of components  $n$  and the second over all types of functional groups in the molecule  $k$ . The fraction of molecules of type  $i$  not bonded at site  $a$ ,  $X_{a,i}$ , is obtained from the solution of the mass balance equations and is given in terms of the total number density for the system, shown as [39, 40]:

$$X_{kia} = \frac{1}{1 + \rho \sum_{l=1}^n x_l \sum_{j=1}^{n_l} v_{lj} \sum_{b=1}^{n_s} n_{jb} x_{ljb} \Delta_{kia,ljb}} \quad (6.11)$$

$\Delta_{a,b,i,j}$  is the parameter that characterizes the association between site  $a$  in molecule  $i$  and site  $b$  in molecule  $j$  in the mixture and is given by:

$$\Delta_{kia,ljb} = K_{kia,ljb}^{HB} f_{kia,ljb} g_{ki,lj}^{SW}(\sigma_{ki,lj}) \quad (6.12)$$

where  $K_{kia,ljb}^{HB}$  is the volume available for bonding,  $f_{kia,ljb}$  the Mayer  $f$ -function, and  $g_{ki,lj}^{SW}$  the radial distribution function for the square well monomers.

At this point, it is important to note that in the usual homonuclear model of SAFT the contribution to the free energy due to bonding at separate sites are independent, and as such, the sites on a molecule are distributed over the whole molecule and not located on a particular segment as is often shown in schematic representations of the SAFT model. However, in the GC-SAFT-VR equation, because of the hetero-segmented chain model used, the location of the

association sites can be specified on a given functional group and hence their position within the model chain defined [86].

With the Helmholtz free energy defined other thermodynamic properties, such as the pressure and chemical potential can then be obtained from the summation of the Helmholtz energy using standard thermodynamic relationships.

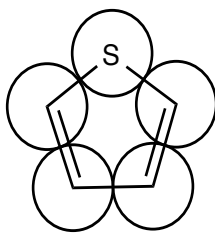
$$P = -\left(\frac{\partial A}{\partial V}\right)_{T,N} \quad (6.13)$$

$$\mu = \left(\frac{\partial A}{\partial N_i}\right)_{T,V,N_{j \neq i}} \quad (6.14)$$

## Results and Discussion

### *Pure compounds*

Thiophene (C<sub>4</sub>H<sub>4</sub>S) belongs to a class of heterocyclic compounds containing a five membered ring with one sulfur atom, as shown in Figure 6.1. In the proposed molecular model of thiophene, the ring is implicitly described and fragmented into 4 CH= groups and 1 -S- group similar to work of Das et al. [131], in which the molecular models for benzene and alkylbenzene molecules



Thiophene

**Figure 6.1:** Schematic representation of Thiophene molecular model

were developed. This allows for a model that is capable of capturing the  $\pi$ - $\pi$  electronic interactions present in the thiophene molecule. The CH=(thiophene) and -S- groups, which comprise the thiophene molecule, are determined following the same procedure as described in previous work [47, 48, 131]. That is the molecular parameters ( $\sigma$ ,  $\varepsilon$ ,  $\lambda$ ,  $m$ ) were determined by

adjusting the model parameters to experimental vapor pressure and saturated liquid density for the thiophene molecule. For the CH=(thiophene) group, only three parameters ( $\sigma$ ,  $\varepsilon$ , and  $\lambda$ ) were included in the fitting process. Due to the similarities between the thiophene and the alkylbenzene molecule, the segment number,  $m$ , was fixed at 0.35, which is the  $m$  value determined for the CH= group used in the alkylbenzene molecules (CH=(aBz)) group [131]. The -S- group, parameters were also determined from fitting to the vapor pressure and saturated liquid density experimental data of thiophene. For the fitting process, experimental data points near the critical region and vapor pressures near the triple point were excluded from the fitting process as this data is known to skew the results [132]. Using the model described above, the parameters for which are reported in Tables 6.1-6.3, the absolute deviations in vapor pressure (AADP) and saturated liquid density (AADL) were found to be 2.4% and 0.037 %, respectively. As compared to the homonuclear approach used in the work of Zuniga-Moreno *et al.*[142], we find a lower value for AADL and a slightly higher deviations in pressure. In Figure 6.2, the GC-SAFT-VR correlations are shown for vapor pressure and saturated liquid density. The results are compared with experimental data [146].

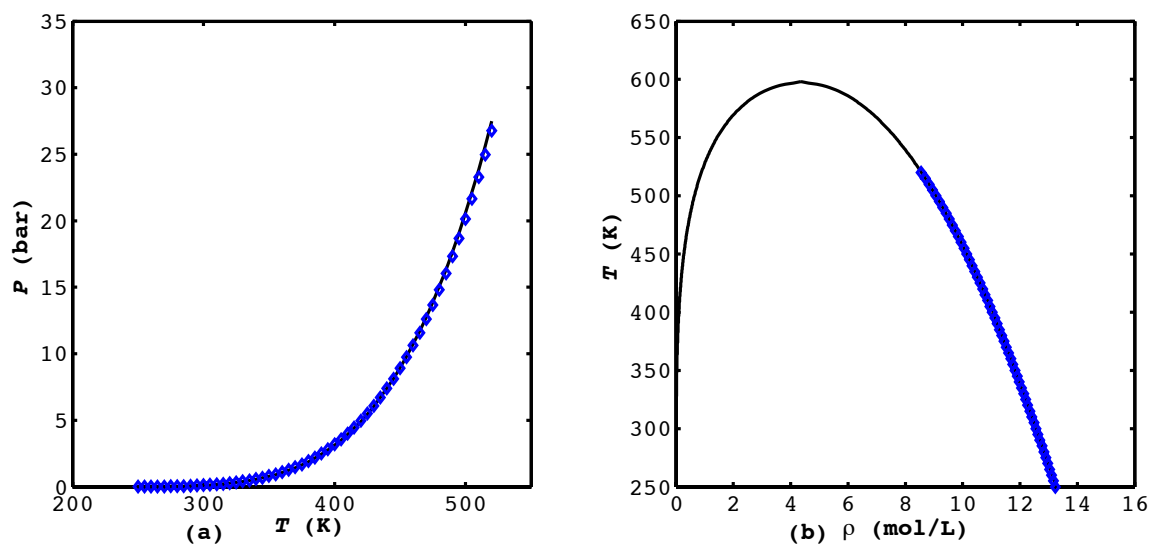


**Figure 6.2:** a.) Vapor pressure curve as a  $p$  vs.  $T$  representations for thiophene ( $C_4H_4S$ ) compared with GC-SAFT-VR approach using determined parameters. The blue data points represent experimental data [147] and the continuous curve the GC-SAFT-VR results. b.) Coexisting

densities for thiophene compared with the GC-SAFT-VR approach using determined parameters. The blue data points represent experimental data [147] and the continuous curve the GC-SAFT-VR results

After determining the optimal parameters for the newly defined functional groups, the phase behavior of the derivatives of thiophene, namely 3-methylthiophene, 2-methylthiophene, and benzothiophene, were then predicted as a means of testing and validating the new parameters. The molecular models for the derivatives of thiophene are shown in Figure 6.3, where the red spheres represent the CH=(thiophene) group, the yellow spheres represent the C= segments, and the light blue spheres represent the CH=(benzene) groups. The C= and CH=(benzene) groups were taken from previous work [131]. The vapor pressure and saturated liquid density of each molecule were predicted, with no additional fitting to experimental data, using the described model. Comparing theoretical predictions with experimental results, for the 3-methylthiophene molecule, which consists of 3 CH=(thiophene) groups, 1 C= group, and 1 methyl group, the AADP and AADL was found to be 2.3% and 5.7% respectively. While the 2-methylthiophene molecule, which contains the same functional groups as the 3-methylthiophene molecule, but in a different arrangement, the AADP and AADL were calculated and determined to be 7.1% and 6.7%, respectively. Finally the prediction of the vapor pressure and saturated liquid density of the benzothiophene molecule, which consists of the functional groups CH=(benzene) and CH=(thiophene), as well as 2 C= segments, the AADP and AADL was determined to be 4.9% and 6.5 %, respectively.

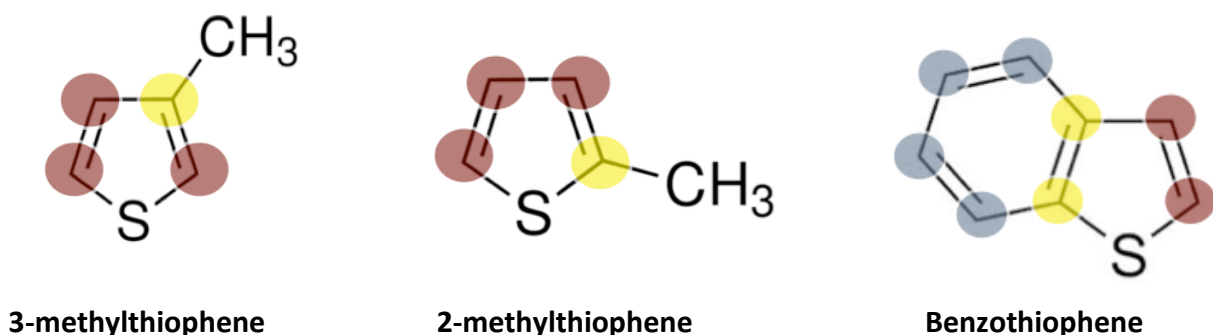


**Figure 6.3:** Schematic representation of molecular model for thiophene derivatives: 3-methylthiophene, 2-methylthiophene, and Benzothiophene

**Table 6.1:** GC-SAFT-VR parameters for the segment size  $\sigma$  and segment number,  $m$ , of each functional group studied.

Groups	$\sigma$ (Å)	$m_i$
-S-	3.919	0.85
CH=(Thiophene)	3.511	0.35
CH= (Benzene)	3.028	0.619
CH=(ABz)	3.928	0.35
C=	2.112	0.382

**Table 6.2:** GC-SAFT-VR segment-segment dispersion energy range parameters  $\lambda_{ki,lj}$

Type	-S-	CH (Thiophene)	CH= (Benzene)	CH= (ABz)	C=
CH <sub>3</sub>	1.51701	1.37585	1.60988	1.49148	1.38398
CH <sub>2</sub>	1.60490	1.47417	1.70485	1.58024	1.50425
CH	1.74358	1.61842	1.86298	1.71841	1.68251
CH <sub>2</sub> =CH	1.5538	1.4115	1.6539	1.5277	1.4286
OH terminal	1.51444	1.39819	1.58961	1.49323	1.40881
CO <sub>2</sub>	1.53501	1.37340	1.64607	1.50580	1.38242
-S-	1.54086	1.40447	1.63435	1.51589	1.41898
CH(Thiophene)	1.40447	1.25224	1.48521	1.37830	1.22993
CH=(Benzene)	1.63435	1.48521	1.75536	1.60607	1.52422
CH=(ABz)	1.51589	1.37830	1.60607	1.49099	1.38674
C=	1.41898	1.22993	1.52422	1.38674	1.19284



**Table 6.3:** GC-SAFT-VR segment-segment dispersion energy well depth parameters  $\epsilon_{ki,lj} / k_B$  (K).

Type	-S-	CH (Thiophene)	CH= (Benzene)	CH= (ABz)	C=
<b>CH<sub>3</sub></b>	404.97297	209.60988	185.23752	293.44157	153.86132
<b>CH<sub>2</sub></b>	407.54076	210.93894	186.41204	295.30218	154.83689
<b>CH</b>	264.61765	136.96340	121.03800	191.74075	100.53614
<b>CH<sub>2</sub>=CH</b>	385.6702	202.8312	179.2470	283.9518	148.8855
<b>OH terminal</b>	611.90479	316.71568	279.88961	443.38342	232.48089
<b>CO<sub>2</sub></b>	354.32107	183.39297	232.48089	256.73943	134.61715
<b>-S-</b>	678.12000	362.37497	320.23988	507.30377	265.99648
<b>CH(Thiophene)</b>	362.37497	187.56159	165.75289	262.57526	137.67707
<b>CH=(Benzene)</b>	320.23988	165.75289	146.48000	232.04436	121.66868
<b>CH=(ABz)</b>	507.30377	262.57526	232.04436	367.59000	192.73984
<b>C=</b>	265.99648	137.67707	121.66868	192.73984	101.06000

### Binary Mixtures

We now consider constant temperature and pressure slices of the phase diagrams of binary mixtures of organic sulfur molecules with several fluids including: alkanes, alkenes, alcohols, carbon dioxide, and aromatics molecules. First, we consider binary mixtures of thiophene with linear alkanes, namely, hexane, hexene, heptane, and methylbutane, have been studied. To our knowledge this is the first time the SAFT approach has been applied to the study of these mixtures. The molecular group parameters for the alkanes, branched alkanes, and alkenes, (i.e., CH<sub>3</sub>, CH<sub>2</sub>, CH, and CH<sub>2</sub>=CH) are taken from previous work [48]. A fitted binary interaction was introduced between the CH<sub>2</sub> and -S- groups that was fitted to the VLE of heptane + thiophene at 1.0133 bar. In Figure 6.4, the predicted phase behavior of thiophene + hexane at a constant 338.15K and 323.15K is presented and excellent agreement is obtained with experimental results. The system thiophene ( $T_b=357.31$  K) + *n*-hexane ( $T_b=341.88$  K) show positive deviations from Raoult's law and maximum pressure azeotropy [148]. The azeotrope forms when the boiling points of the pure components are very close; the closer the boiling points of the pure components and the less ideal the mixture, the greater the likelihood of an azeotrope. Considering a mixture

with an unsaturated compound, the thiophene + hexene binary mixture at 333.15K and 323.15K is predicted and found to be in good agreement with experimental results. The thiophene + 1-hexene system presents positive deviation and strong nonideality. Although, no azeotropes are formed in this system at the temperatures studied. This is a result of the large difference in the boiling points of the pure components[148]. Additionally, a  $Txy$  slice of the thiophene + methylbutane phase diagram at 1.0133 bar has also been studied and again good agreement with experimental data is obtained for this branched molecule.

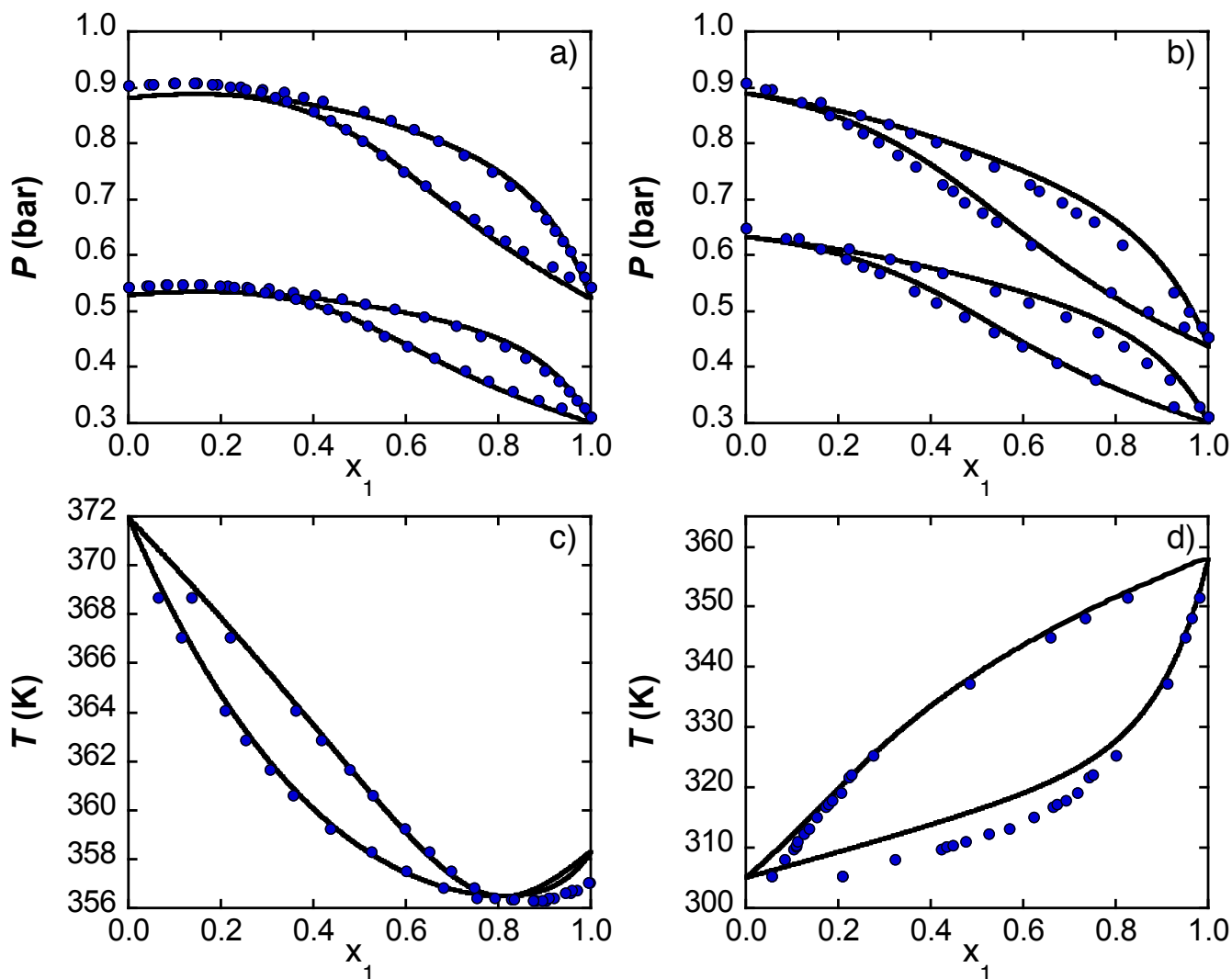


**Figure 6.4:** a.) Thiophene (1) + hexane (2) at 338.15K and 323.15K (top to bottom) b.) Thiophene (1)+ hexene (2) at 333.15K and 323.15K (top to bottom) c.) Thiophene (1) + heptane

(2) at 1.0133 bar and d.) Thiophene (1) + methylbutane (2) at 1.0133 bar . The solid lines are the GC-SAFT-VR predictions and the symbols the experimental data[149].

Here, we present the CO<sub>2</sub> and thiophene isothermal binary mixtures over a range of temperatures from 314K - 383K [150]. A single fitted binary cross interaction parameters between the CO<sub>2</sub> molecule and the -S- groups was determined by fitting to the VLE data of the mixture at 363.15K. The determined parameters are then used to predict the remaining temperature with no additional fitting to experimental data. Aside from the overprediction of the critical region, which is expected from an analytical equation of state [151, 152], the theoretical predictions describe the experimental results well. As can be seen from the figures, the proposed model is able to capture the changes in phase behavior as a function of temperature and at a similar level of agreement to the work of Zuniga-Moreno *et al.*[142]; however, we note that in this work only one isotherm was used to determine the fitted binary interaction parameter.

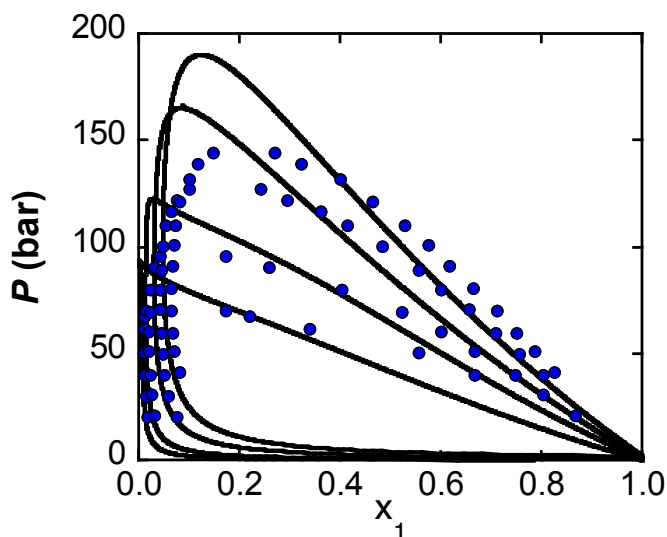


**Figure 6.5:** Isothermal VLE for Thiophene (1) + CO<sub>2</sub> (2) at 383K, 363K, 334K, and 314K (top to bottom) [153]. The solid lines are the GC-SAFT-VR predictions and the symbols the experimental data.

Next we study the phase behavior of the aromatic compounds + thiophene binary mixtures. This study is the first SAFT approach applied to the study of aromatic mixtures and thiophene. The CH=(Benzene), CH=(Alkylbenzene), C= and CH<sub>3</sub> group parameters needed to

describe toluene and benzene are taken from previous work [131]. In Figure 6.5a, a constant pressure  $P_{xy}$  slice of the benzene + thiophene phase diagram is predicted at 298 K for which excellent agreement with the experimental data is obtained. In Figure 6.5b, the isobaric VLE curve is predicted for the toluene + thiophene binary mixture. We note that the thiophene + toluene binary mixture shows nearly ideal behavior. In both cases, good agreement is seen between the theoretical predictions and experimental results, although we observe some deviation for the toluene + thiophene mixture due to the over prediction of the pure toluene vapor pressure.

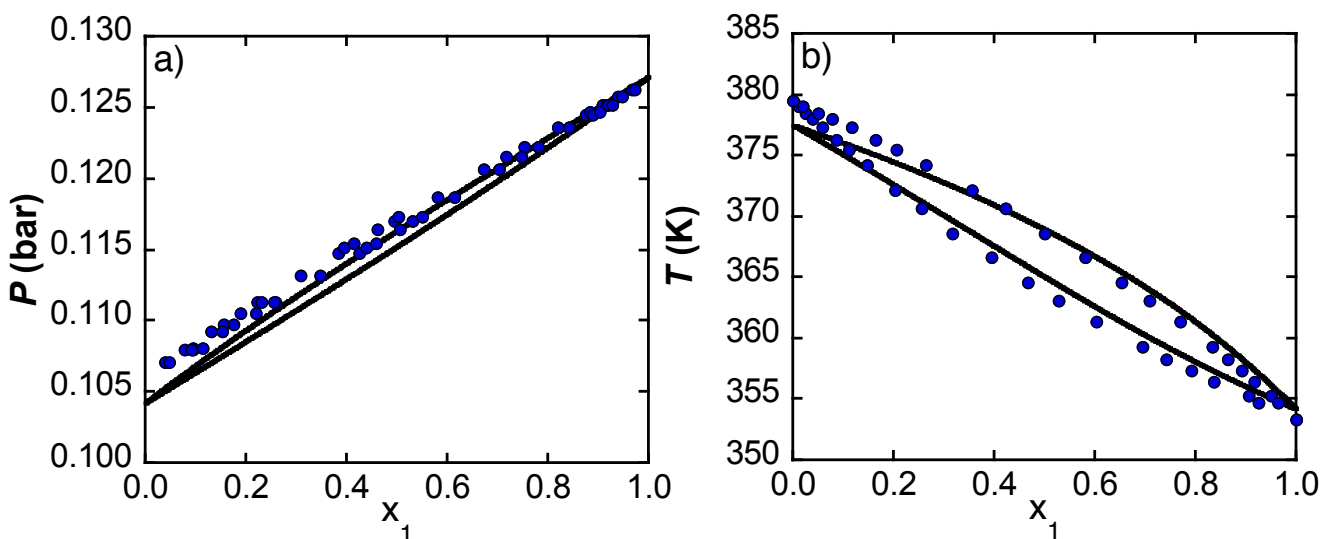


**Figure 6.6:** Isothermal VLE for Thiophene and aromatic compounds a.) Thiophene (1) + toluene (2) at 298K b.) Thiophene (1) + benzene (2) at 0.9003 bar. The solid lines are the GC-SAFT-VR predictions and the symbols the experimental data[154, 155].

Next we study mixtures of strongly associating fluids such as alcohols with compounds containing thiophene. The theory's ability to capture the complex interactions between the lone pair of electrons present on the alcohol oxygen atom and the thiophene ring is tested. In Figure 6.7, the phase behavior of thiophene and alcohol molecules are studied. The parameters for the OH, CH<sub>2</sub>, and CH<sub>3</sub> groups needed to describe alcohols are taken from the previous work [47]. In Figure 6.7a, we present four isotherms for the thiophene + methanol binary mixture at 323.15 K, 318.15 K, 313.15 K, 308.15 K and in Figure 7b one isobaric binary mixture at 0.603 bar.

Although the proposed model is able to capture the changes in phase behavior as a function of temperature, we observe some deviation for the thiophene + methanol mixture, due to the over prediction of the vapor pressure of pure methanol. As the chain length of the alcohol is increased, better agreement is observed as the GC-SAFT-VR approach provides a better description of the pure limits for higher chain lengths of alcohols as can be seen figures 6.7c and 6.7d where we present the phase behavior of ethanol + thiophene and propanol + thiophene respectively. The azeotrope is also predicted accurately agreeing well in pressure and composition with experimental results for longer alcohol chains.

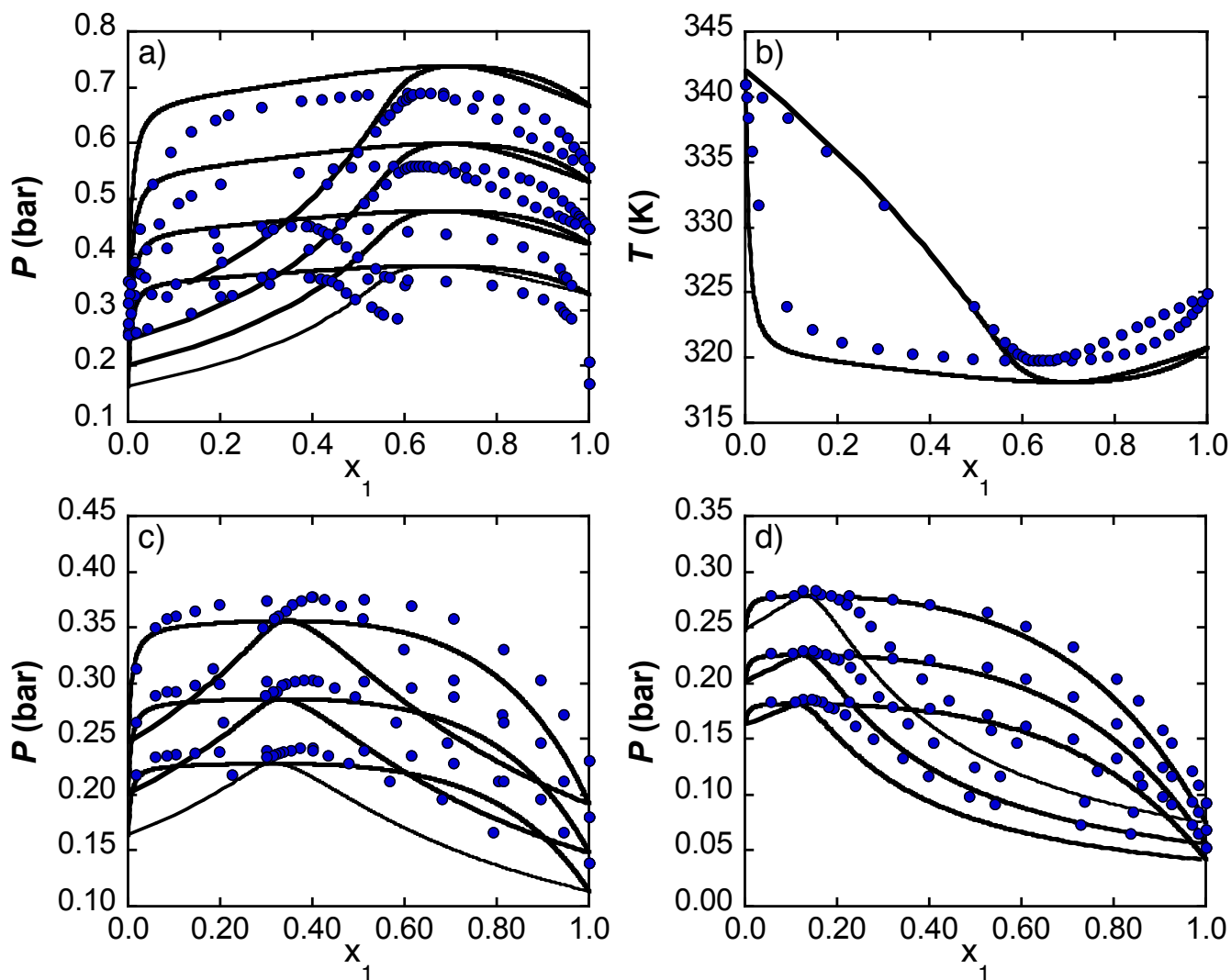


**Figure 6.7:** (a) Thiophene (1) + methanol (2) at 323.15 K, 318.15 K, 313.15 K, 308.15 K (top to bottom), (b) Thiophene (1) + methanol (2) at 0.603 bar, (c) Thiophene (1) + ethanol (2) at 318.15 K, 313.15 K, and 308.15 K (top to bottom) d.) Thiophene (1) + propanol (2) at 318.15 K, 313.15 K, and 308.15K (top to bottom). The solid lines are the GC-SAFT-VR predictions and the symbols the experimental data[154, 156].

To test the accuracy of our model with molecules other than the thiophene, the phase behavior of 3-methylthiophene molecules with binary mixtures of alkanes, branched alkanes, and the aromatic molecule, toluene, is studied. As these mixtures are not studied by any other SAFT approach the ability to predict these mixtures using a group contribution SAFT approach is ideal.

In Figure 6.8a and 6.8b, the vapor–liquid equilibria for binary mixtures of 3-methylthiophene + hexane and 3-methylthiophene + hexene at 333.15 K are presented, respectively. Also the isobaric VLE mixture of 3-methylthiophene + heptane at 1 bar is also predicted. Good agreement between experimental results and theoretical predictions are observed in all cases. We note that the theory accurately captures the changes in phase behavior with the increase in the number of CH<sub>2</sub> groups in the linear alkane. The phase behavior is also predicted for saturated as well as unsaturated alkanes. These results are encouraging as no fitting to experimental data is done to determine the phase behavior.

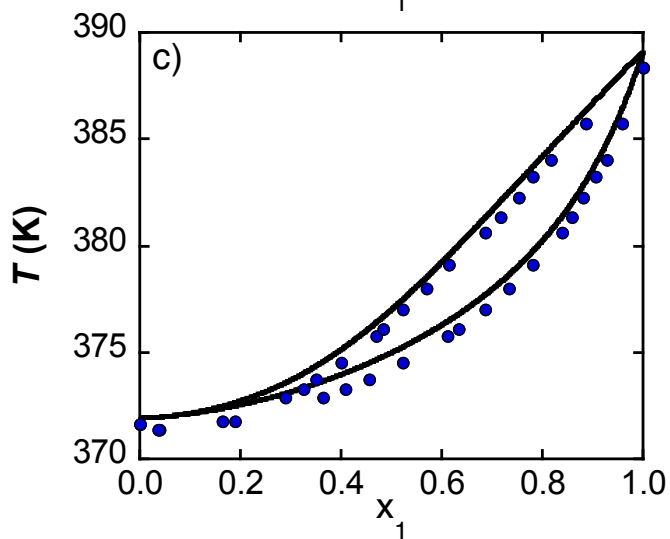
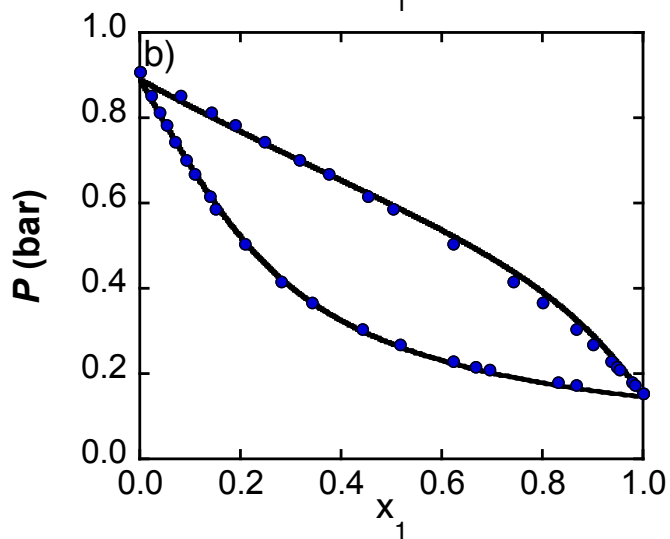
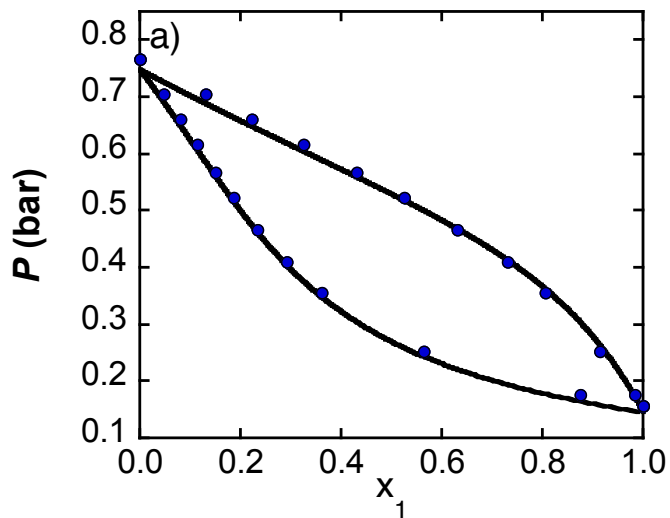


**Figure 6.8:** Vapor–liquid equilibria for binary mixtures of (a) 3-methylthiophene + hexane at 333.15 K (b) 3-methylthiophene + hexene at 333.15 K and (c) 3-methylthiophene + heptane at 1 bar. The solid lines represent the theoretical predictions and the symbols represent the experimental results[157].

We now turn to VLE mixtures containing branched alkanes and the 3-methylthiophene molecule. Results for constant temperature (333.15 K)  $Px$  slices of 3-methylthiophene + 2-methylbutane phase diagrams are compared with experimental data in Figure 6.9a. Excellent agreement between the theoretical predictions and the experimental results is observed. However, for the 3-methylthiophene + 2-methylpentane mixture, we see slight deviation at 1 bar at the pure limit of 2 methylpentane due to the overprediction of the pure vapor pressure of 2 methylpentane.

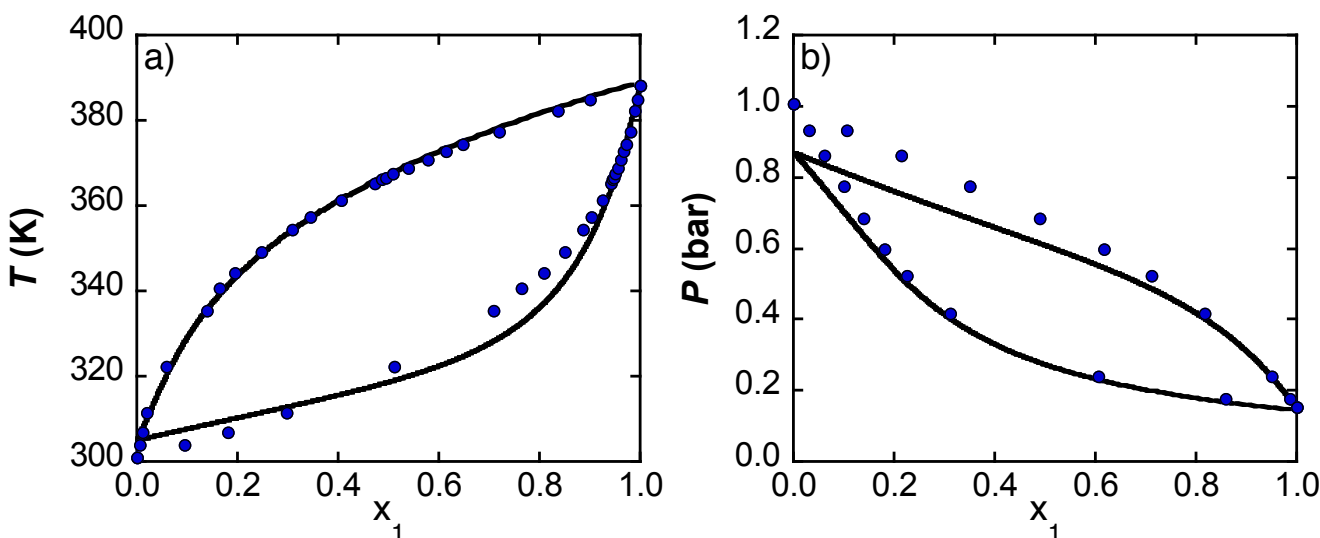


**Figure 6.9:** Vapor–liquid equilibria for binary mixtures of (a) 3-methylthiophene + 2-methylbutane at 1 bar. (b) 3-methylthiophene + 2-methylpentane at 333.15 K. The solid lines represent the theoretical predictions and the symbols represent the experimental results[157].

The phase behavior of the aromatic organic compound, benzothiophene, is also predicted. The benzothiophene molecule is considerably more complex than thiophene and thus should present more difficulties in predicting the mixtures of the two molecules. However, using the proposed model with no additional fitting, we are able to accurately predict phase behavior of the binary mixtures of benzothiophene + dodecane and benzothiophene + octanol. Figure 6.10a and



6.10b present the constant pressure slices at  $P = 0.995$  bar. To our knowledge no other SAFT theory has been used to study the mixtures of benzothiophene + thiophene.

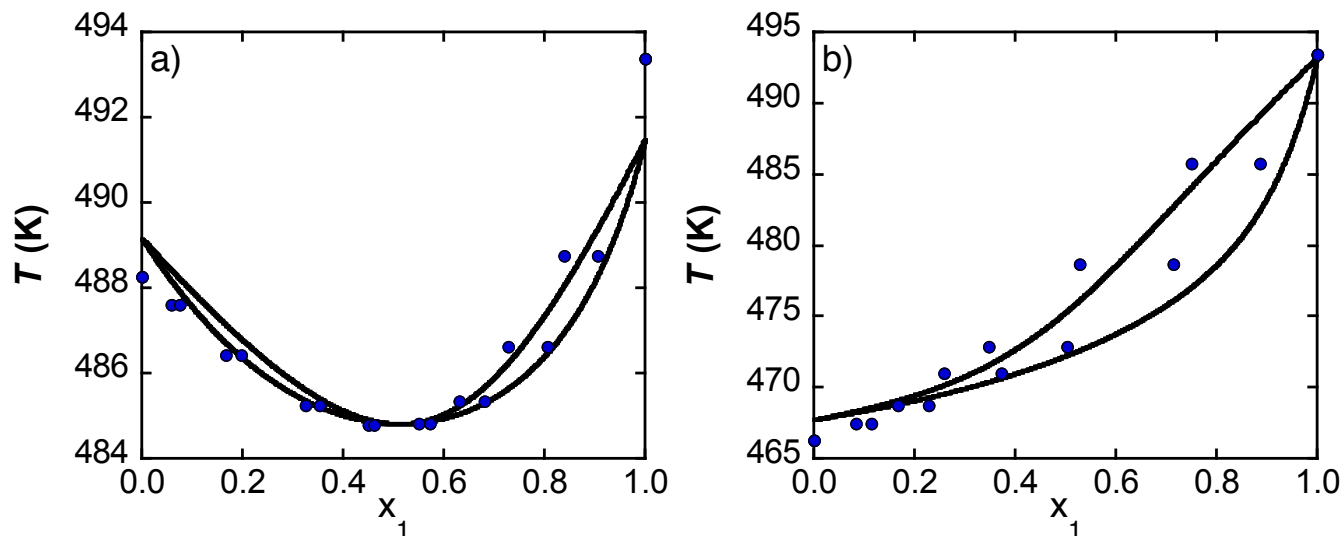


**Figure 6.10:** Vapor–liquid equilibria for binary mixtures of (a) benzothiophene + dodecane at 0.995 bar (b) benzothiophene + octanol at 0.995 bar. The solid lines represent the theoretical predictions and the symbols represent the experimental results [148]

## Conclusion

In this paper, we have extended the application of the GC-SAFT-VR approach to study the phase equilibrium of organic sulfur molecules, namely, thiophene, 3-methylthiophene, and benzothiophene. These sulfur compounds found in crude oil cause many handling, transportation, storage, and manufacturing difficulties. This is due to the extreme toxicity and corrosiveness of the compounds. A model has been proposed which will allow the phase behavior of these molecules to be studied using a predictive approach. Molecular parameters are determined for thiophene by fitting to the experimental vapor pressure and saturated liquid density while the other derivatives of thiophene were predicted without additional fitting to experimental results. The proposed model takes advantage of previous work, of Das *et al.* [131] where groups are fragmented into smaller groups to capture the interaction associated with the ring. Theoretical

predictions of vapor pressure and saturated liquid density provide low deviations as compared to the experimental data. Binary mixtures of these molecules with other relevant fluids are studied and found to be in excellent agreement with experimental data. Two binary cross interactions are introduced to correct for deviations from ideal behavior, which is assumed by the use of the Lorentz Berthelot combining rules. The cross interaction between the group -S- and the two groups CH<sub>2</sub> and CO<sub>2</sub> and are each fitted to one isothermal VLE mixture while the other temperatures not included in the fitting process and used to predict the phase behavior. Good agreement is seen with experimental data. Accordingly, we can conclude that our parameters can be used successfully in a predictive and transferable fashion to predict the phase equilibrium of pure fluids and mixtures of thiophene and its derivatives without the reliance of experimental data.

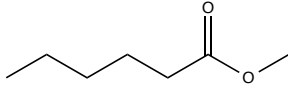
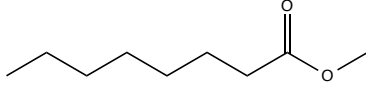
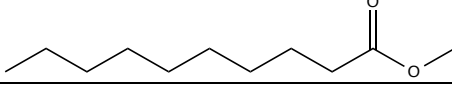
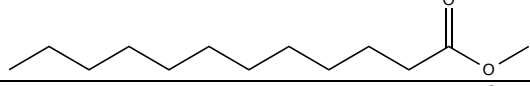
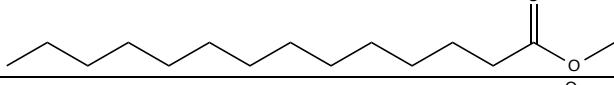
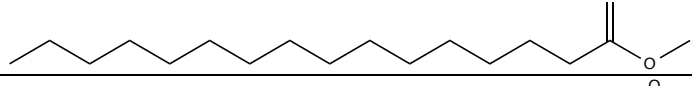
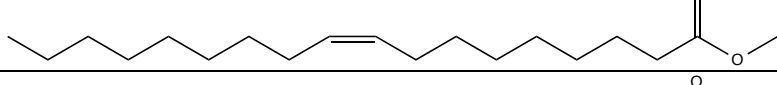
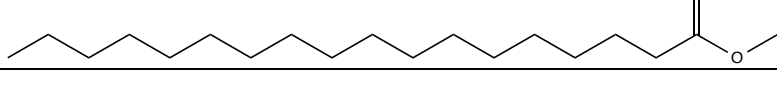
## Chapter VII

### Predicting the Phase Behavior of Fatty Acid Methyl Esters and their Mixtures Using the GC-SAFT-VR Approach

#### Introduction

Due to the depletion of non-renewable resources, the search for alternatives to petroleum-derived fuels is an active area of research. One proposed alternative, biodiesel, is a renewable and biodegradable energy source made up of a mixture of esters of long chain fatty acids [158, 159]. The most common compounds utilized in biodiesel are fatty acid methyl esters (FAME) with molecular formula  $\text{CH}_3(\text{CH}_2)_n\text{COOCH}_3$  (Table 7.1).

**Table 7.1:** Chemical Structure of Fatty Acid Methyl Esters considered in this work.

Compound	Formula	Chemical Structure
Methyl Caproate	$\text{C}_7\text{H}_{14}\text{O}_2$	
Methyl Caprylate	$\text{C}_9\text{H}_{18}\text{O}_2$	
Methyl Caprate	$\text{C}_{11}\text{H}_{22}\text{O}_2$	
Methyl Laurate	$\text{C}_{13}\text{H}_{26}\text{O}_2$	
Methyl Myristate	$\text{C}_{15}\text{H}_{30}\text{O}_2$	
Methyl Palmitate	$\text{C}_{17}\text{H}_{34}\text{O}_2$	
Methyl Oleate	$\text{C}_{19}\text{H}_{36}\text{O}_2$	
Methyl Stearate	$\text{C}_{19}\text{H}_{38}\text{O}_2$	

Although the molecular size of the components of biodiesel and petroleum diesel are similar, they differ in chemical composition and structure [160], which results in several notable variations in the physical properties of the two fuels [160]. Specifically, biodiesel has superior characteristics in terms of flash point, aromatic content, lubricity, sulfur and oxygen content, and toxicity [159, 160]. In addition, the use of biofuels for transportation could result in an average greenhouse gas emission reduction of about 57% as compared to the emissions that would have occurred from the production and use of equivalent quantities of petroleum fuels [161].

Presently, the cost of biodiesel is twice that of petroleum derived diesel fuel [162], presenting significant economic challenges to its implementation on a larger scale. Understanding the thermodynamics and phase behavior of these fluids and their mixtures can provide insight into how to optimize the molecular composition in order to provide more ideal fuel conditions and properties, as well as to reduce costs. For example, the vapor pressure, which is an important thermodynamic property of biodiesel fuel as it controls the volatility, safety, and stability of the fuel [163], can be adjusted by changing the fuel composition. A higher value of vapor pressure can favor evaporative emissions while a lower value can lead to delayed ignition, poor atomization, and problematic combustion [163]. It is impractical to experimentally determine the vapor pressure at every necessary condition, because the decomposition of feed oils usually takes place at high temperatures. Therefore, the limited experimental data for the vapor pressure of FAME molecules hinders process development and necessitates the development of accurate and predictive models for the determination of such data.

While modeling tools, which utilize correlations derived from a limited number of data points, are readily implemented, the development of accurate models, that are not heavily reliant on experimental data, to predict the properties of biodiesel fuels and their blends is more difficult [164]. However, more recently, statistical mechanics based equations of state, such as the statistical associating fluid theory (SAFT) [39-44] have been applied. Based on Wertheim's theory of association [41-44], the SAFT equation of state describes molecules as chains of

tangentially bonded homonuclear segments that interact through dispersion and association interactions. Being rooted in statistical mechanics and based on a molecular-level model, SAFT typically lends itself well to the development of a predictive modeling approach. For a detailed discussion of the various versions of SAFT and its applications, the reader is directed to the recent review of McCabe and Galindo [49].

To date several versions of SAFT have been used to examine the thermodynamic properties and phase behavior of FAME molecules [11, 48, 94, 165-171], with some investigating the phase behavior of light FAME molecules [48, 170] only. In this work, we focus on heavy FAME systems, which constitute the major components of biodiesel fuels and for which limited studies of the VLE have been performed. In the first study, Perdomo *et al.* [165] examined three common biodiesel compounds (methyl palmitate, methyl linoleate, and methyl oleate) with the SAFT-VR [46] equation of state, which describes chain molecules formed from hard-core segments that interact via square well (SW) potentials of variable range (VR). The molecules of interest were modeled as associating chains and model parameters were determined by fitting to saturated liquid density and vapor pressure data with deviations found to be less than 1%. Improvements to the vapor liquid equilibrium (VLE) predictions were observed when a discretized version of a modified Lennard–Jones potential, instead of the usual SW interaction, was used to describe the segment–segment interactions. Extending the study to mixtures, Perdomo *et al.*, [166] used the SW SAFT-VR approach, to describe model biodiesel blends containing FAME molecules methyl palmitate, methyl linoleate, and methyl oleate. Parameters for the pure fluids were taken from earlier work [165] and cross binary-interaction parameters were obtained by fitting to liquid densities and speed of sound data for each mixture studied. Isochoric heat capacities, speed of sound, and phase diagrams for binary and ternary mixtures were then predicted at conditions not considered in the fitting procedure. Although, exact deviations were not reported, in general good agreement was found between the experimental results and predicted isochoric heat capacities; however, the speed of sound predictions showed

fairly significant deviations at low temperatures. In a subsequent study, Perdomo *et al.* [167] utilized the group contribution based SAFT- $\gamma$  approach to study several FAME molecules and esters that contain hydroxyl groups. In the SAFT- $\gamma$  [99] approach molecules are represented by segments of different types that represent the chemical functional groups within the molecule and are combined to describe a homonuclear model chain. To describe the phase coexistence properties of the molecules of interest, ester (COOCH<sub>3</sub>) and hydroxyl ester (CHOH) functional groups were defined and characterized by fitting to experimental vapor pressure and saturated liquid density data for secondary alcohols and methyl alkanoates, respectively whilst the remaining model parameters were taken from earlier work [99]. The absolute average deviation in vapor pressure (AADP%) was found to be 3.62% for the ester series (methyl ethanoate to methyl heptanoate) and 2.42% for the secondary alkanols series (2-propanol to 4-decanol). Deviations were not provided for the saturated liquid density predictions, however, from graphical representations comparing saturated liquid densities with experimental results they appear to be greater than for the vapor pressure. Using these parameters, the thermophysical properties of long chain pure biodiesel components and the specific gravity and flash point of commercial biodiesel blends were then predicted; however, significant deviations from experimental data for the specific gravity was observed, especially for blends containing high fractions of unsaturated FAME molecules.

In another study, Oliveira *et al.* [168] used the density gradient theory approach coupled with the soft-SAFT equation to describe the interfacial properties of several fatty acid esters. The esters were modeled as non-associating homonuclear chain fluids with the model parameters fitted to vapor pressure and liquid density data. Deviations from experimental data were found to be 0.047% for the liquid density and of 5.8% for the vapor pressure. Density, surface tension, viscosity, and speed of sound data were then predicted for fatty acid methyl and ethyl esters with deviations of less than 5%. In a subsequent study, Oliveira *et al.* [11], extended their work to study binary mixtures of FAMEs with alcohols. Parameters for the FAME molecules were

combined with those for alcohols from the literature [172] and an adjustable cross interaction parameter fitted to experimental data for mixtures of ethyl butanoate + methanol and hexyl acetate + methanol. The fitted energy parameter was then transferred to the study of other FAME + methanol mixtures; however, it was not transferable to other alcohols and so mixtures with ethanol required a new fitted interaction, thus reducing the predictability of the theory. Additionally, when pressures above atmospheric were studied (2 – 16 MPa) significant deviations were observed and a new fitted cross interaction proposed for the FAME + methanol systems by fitting to methanol + methyl laurate at 523 K. More recently, also utilizing the soft-SAFT equation, Llovel *et al.* [169] investigated the solubility of supercritical CO<sub>2</sub> in fatty acid methyl esters. The parameters for the ester family was taken from the work of Oliveira *et al.* [168] and used to predict the VLE of mixtures of methyl myristate, methyl palmitate, methyl stearate, and methyl oleate and CO<sub>2</sub>. Two fitted binary interaction parameters, to account for the differences in molecular size ( $\eta$ ) and dispersive energy ( $\xi$ ) between the CO<sub>2</sub> and the ester mixtures, were required. The dispersive energy parameters,  $\xi$ , were adjusted for each mixture studied, as slight chain length dependence was observed, while the molecular size interaction parameter, which adjusts the molecular diameter,  $\sigma$ , was held constant for all mixtures studied. Although, exact deviations were not reported, good agreement was generally found between the theoretical results and experimental data using this approach.

The polar group contribution statistical associating fluid (GC-SAFT) [92] has also been used to investigate the phase equilibrium and thermodynamic properties of the FAME molecules in three separate SAFT studies using three different versions of SAFT (SAFT [39], SAFT-VR [86], and PC-SAFT [72, 173]) modified to include a polar term. In the GC-SAFT approach, parameters for the chemical groups are obtained by fitting to vapor pressure and saturated liquid density experimental data for molecules containing the chemical group of interest and then averaged using established relations to predict pure and mixture properties, as a result the theory reduces to the original SAFT equation (i.e., it describes a homonuclear chain at both the segment

(monomer) and chain levels). In the first study, Nguyen Thi *et al.* [94] determined parameters for the groups not previously studied with the polar GC-SAFT approach (i.e., the COO and HCOO groups) by simultaneous regression of all the available vapor pressure and saturated liquid density data. The dipole moment was also determined during the fitting process for the COO group. The thermodynamic properties of esters, formates, and acetates were then investigated with similar results obtained from the three different versions of SAFT. The vapor pressure of pure long chain esters not included in the fitting process were also studied and deviations from experimental data of 15.82%, 15.25%, and 36.24% for methyl palmitate, methyl stearate, and methyl tetracosanoate respectively were obtained. Subsequently Nguyen Huynh *et al.* [170] extended the work of Nguyen Thi *et al.* to mixtures; however, the pure ester parameters were reinvestigated using a multipolar segment approach, where multipole moments are assumed to be localized on certain segments in the chain. Though we believe the value of this approach is unclear given that the group parameters are averaged in the GC-SAFT approach and so the model reverts to that of a homonuclear fluid; it is perhaps there not surprising that comparable results are found using both the multipolar segment and molecule approach. Again the results from three different versions of SAFT were compared and deviations were observed to increase with chain length, resulting in average deviations in vapor pressure of greater than 10 % for all three approaches. As for mixtures, only light ester molecules such as methyl acetate and methyl octanoate were considered.

Although several SAFT approaches [11, 165, 166, 168] have been shown to provide an accurate description of the thermodynamic properties of FAME molecules [165, 166], these theories require parameters for every molecule studied to be fit to experimental data and additional fitted binary interaction parameters need to be introduced when considering mixtures. To overcome these issues, group contribution approaches provide an attractive alternative as new molecules can in principal be studied by combining the groups of interest without fitting to experimental data. However, although GC approaches have been applied to the study of FAME



systems [94, 167, 170], additional functional groups (and in the case of polar GC-SAFT additional parameters) fitted to experimental data for FAME molecules needed to be defined. In contrast the group-contribution SAFT-VR (GC-SAFT-VR) approach used in this work does not require the definition of any new groups to study FAME molecules and therefore represents a truly predictive approach. We also note that GC-SAFT-VR considers the chemical makeup of the molecules being studied more explicitly through the definition of a hetero-nuclear model chain i.e., molecules are described as chains of tangentially bonded segments of different size and/or energy parameters. The GC-SAFT-VR approach thus combines the SAFT-VR equation, where chain molecules are formed from hard-core segments interacting through attractive potentials of variable range [86] with a group contribution [48] approach. The different functional groups within the molecule are therefore explicitly represented in the model chain, allowing for a description of the effects of molecular structure on the thermodynamic properties of the fluid. As in other GC approaches, group parameters are obtained by fitting to pure component experimental vapor pressure and saturated liquid density data for the molecules containing the groups of interest. The parameters are then used in a transferrable manner to determine the phase behavior of other fluids not included in the fitting process and mixtures. Another advantage to utilizing a GC approach is that when groups of interest are contained in the same molecule, binary interactions parameters between the groups can be obtained from pure component experimental data alone, without fitting to binary experimental data. Thus a truly predictive approach is developed. The GC-SAFT-VR approach has been successfully applied to study the thermodynamics and phase behavior of a wide range of fluids including hydrocarbons [48], ketones [48], alcohols [47], polymers [100], and aromatics [131]. In this work, the predictive character of the GC-SAFT-VR equation of state is further evaluated through the description of the thermophysical properties and phase behavior of several long chain FAME molecules as well as mixtures of CO<sub>2</sub>, alcohols, and other FAME molecules. By utilizing groups already developed, a

predictive approach is realized that allows the phase behavior of FAME systems to be accurately predicted.

The remainder of the paper is organized as follows: the molecular model and theory are presented, the functional group parameter estimation and results for both pure components and mixtures studied are discussed, and finally conclusions drawn.

### **Molecular Model and Theory**

The GC-SAFT-VR approach allows for the predictive study of the thermodynamic properties of fluids and their mixtures. Molecules are described by tangentially bonded segments in which each type of segment represents a functional group present in the molecule [48, 109]. The segments representing each functional group interact via a square well potential, which can be described by,

$$u_{ki,lj}(r) = \begin{cases} +\infty & \text{if } r < \sigma_{ki,lj} \\ -\varepsilon & \text{if } \sigma_{ki,lj} \leq r \leq \lambda_{ki,lj} \sigma_{ki,lj} \\ 0 & \text{if } r \leq \lambda_{ki,lj} \sigma_{ki,lj} \end{cases} \quad (7.1)$$

where  $u_{ki,lj}$  represents the interaction between a functional group of type  $i$  present in molecule  $k$  with a functional group of type  $j$  in molecule  $l$ ,  $\sigma$  is the segment diameter,  $\varepsilon$  is the depth of the square well,  $\lambda$  is the potential range, and  $r$  is the distance between the two groups. The unlike size and energy interactions can be obtained from the Lorentz-Berthelot combining rules expressed by,

$$\sigma_{ij} = \frac{\sigma_{ii} + \sigma_{jj}}{2} \quad (7.2)$$

$$\varepsilon_{ij} = \sqrt{\varepsilon_{ii} \varepsilon_{jj}} \quad (7.3)$$

and the unlike potential range is given by,

$$\lambda_{ij} = \frac{\lambda_{ii} \sigma_{ii} + \lambda_{jj} \sigma_{jj}}{\sigma_{ii} + \sigma_{jj}} \quad (7.4)$$

For non-ideal interactions, deviations from the Lorentz-Berthelot combining rules are expected. To account for these non-idealities, the unlike interactions between functional groups can be fitted to pure component experimental data for molecules containing both functional groups.

The GC-SAFT-VR equation of state is written in terms of the total Helmholtz free energy, expressed as a sum of four separate contributions:

$$\frac{A}{Nk_B T} = \frac{A^{ideal}}{Nk_B T} + \frac{A^{mono}}{Nk_B T} + \frac{A^{chain}}{Nk_B T} + \frac{A^{assoc}}{Nk_B T} \quad (7.5)$$

where  $N$  is the total number of molecules in the system,  $T$  is the temperature, and  $k_B$  is the Boltzmann constant. In equation 5,  $A^{ideal}$  is the ideal free energy,  $A^{mono}$  is the contribution to the free energy due to the monomer segments,  $A^{chain}$  is the contribution due to the formation of bonds between monomer segments, and  $A^{assoc}$  is the contribution due to association.. Since the theory has been presented previously [48] [87] only a brief overview of the main expressions are provided below.

The ideal Helmholtz free energy,  $A^{ideal}$ , is given by,

$$\frac{A^{ideal}}{Nk_B T} = \sum_{i=1}^{n_{components}} x_i \ln(\rho_i \Lambda_i^3) - 1 \quad (7.6)$$

where  $n_{components}$  represents the number of pure components,  $\rho_i = N_i/V$  (the molecular number density of chains of component  $i$ ),  $x_i$  is the mole fractions of component  $i$  in the mixture, and  $\Lambda_i$  is the thermal de Broglie wavelength,  $N$  is the total number of molecules in the system,  $T$  is the temperature, and  $k_B$  is the Boltzmann constant.

The monomer free energy,  $A^{mono}$ , is given by a second order high temperature expansion using Barker and Henderson perturbation theory for mixtures [73]

$$\frac{A^{mono}}{NkT} = \sum_{i=1}^{n_{components}} \sum_{k=1}^{n_k} m_{ki} x_i \left( a^{HS} + \frac{a_1}{k_B T} + \frac{a_2}{(k_B T)^2} \right) \quad (7.7)$$

where the first sum is over the components in the system, the second sum is over all  $n'_k$  types of functional groups within each component and  $m_{ki}$  is the number of segments of type  $k$  in chains of component  $i$ .

The chain term,  $A^{chain}$ , for a mixture of heterosegmented chain molecules is given by,

$$\frac{A^{chain}}{NkT} = -\sum_{i=1}^n x_i \sum_{kj} \ln y_{ik,ij}^{SW}(\sigma_{ik,ij}) \quad (7.8)$$

where the first sum is over all components in the mixture and the second sum considers the chain formation and connectivity of the segments within a given chain. The background correlation function is given by,

$$y_{ki,kj}^{SW}(\sigma_{ki,kj}) = \exp\left(\frac{-\epsilon_{ki,kj}}{k_B T}\right) g_{ki,kj}^{SW}(\sigma_{ki,kj}) \quad (7.9)$$

where  $g_{ki,kj}^{SW}(\sigma_{ki,kj})$  is the radial distribution function for the square well monomers at the contact distance  $\sigma_{ki,kj}$  and is approximated by a first-order high-temperature perturbation expansion.

Finally, the contribution due to association, ( $A^{Assoc}$ ), [46] interactions between sites on different functional groups that form the molecules of interest is expressed as:

$$\frac{A^{Assoc}}{Nk_B T} = \sum_{i=1}^n x_i \left[ \sum_{a=1}^{s_i} \left( \ln X_{a,i} - \frac{X_{a,i}}{2} \right) + \frac{s_i}{2} \right] \quad (7.10)$$

where the first sum is over the number of components  $n$ , the second one is over all types of functional groups in the molecule  $k$ , and the third sum is over the total number of site on the function group  $i$ . The fraction of molecules of type  $i$  not bonded at site  $a$ ,  $X_{a,i}$  is obtained from the solution of the mass balance equations and is given in terms of the total number density for the system, shown as [39, 40]:

$$X_{kia} = \frac{1}{1 + \rho \sum_{l=1}^n x_l \sum_{j=1}^{n'_l} v_{lj} \sum_{b=1}^{n'_s} n_{jb} x_{ljb} \Delta_{kia,lib}} \quad (7.11)$$

$\Delta_{a,b,i,j}$  is the parameter that characterizes the association between site  $a$  in molecule  $i$  and site  $b$  in molecule  $j$  in the mixture and is given by:

$$\Delta_{kia,ljb} = K_{kia,ljb}^{HB} f_{kia,ljb} g_{ki,lj}^{SW}(\sigma_{ki,lj}) \quad (7.12)$$

where  $K_{kia,ljb}^{HB}$  is the volume available for bonding,  $f_{kia,ljb}$  the Mayer  $f$ - function, and  $g_{ki,lj}^{SW}$  the radial distribution function for the square well monomers.

At this point, it is important to note that in the usual homonuclear model of SAFT the contribution to the free energy due to bonding at separate sites are independent, and as such, the location of sites on a molecule is arbitrary; the sites are in actuality averaged over the whole molecule. However, in the GC- SAFT-VR equation, because of the hetero-segmented chain model used, the location of the association sites can be specified on a given functional group and hence their position within the model chain defined [86].

With the Helmholtz free energy defined, thermodynamic properties such as pressure, temperature, and chemical potential, can then be obtained using standard thermodynamic relationships.

$$P = -\left(\frac{\partial A}{\partial V}\right)_{T,N} \quad (7.13)$$

$$\mu = \left(\frac{\partial A}{\partial N_i}\right)_{T,V,N_{j \neq i}} \quad (7.14)$$

## Results and Discussion

### *Pure Fluids*

Taking advantage of the transferability of the GC-SAFT-VR approach, as stated above previously reported parameters [48] were utilized for the functional groups (i.e., the CH<sub>3</sub>, CH<sub>2</sub>, CH=CH<sub>2</sub>, C=O, OCH<sub>3</sub>, and OCH<sub>2</sub>) that comprise the FAME molecules of interest. These group parameters were determined in the work of Peng *et al.* [48] by fitting to experimental vapor pressure and saturated liquid density data for molecules containing the group of interest (i.e., alkanes, alkenes,

ketones, alkyl acetates, and esters). The molecular parameters ( $m$ ,  $\sigma$ ,  $\lambda$ , and  $\varepsilon$ ) used to describe the FAME molecules studied (i.e., methyl laurate, methyl myristate, methyl caprate, methyl caprylate, methyl palmitate, methyl oleate, and methyl stearate) are reported in Tables 7.2-7.4. Also reported in Table 7.2 are the parameters for carbon dioxide that were taken from the work of Blas and Galindo [138, 174] and the cross interaction between the CH<sub>2</sub> group and the CO<sub>2</sub> molecule that was fitted to the hexane and CO<sub>2</sub> binary mixture at 313.15K.

**Table 7.2:** GC-SAFT-VR parameters for the segment size and segment number of each functional group studied.

Groups	$\sigma$ (Å)	$m_i$
CH <sub>3</sub>	3.737	0.667
CH <sub>2</sub>	4.041	0.333
CH=CH <sub>2</sub>	3.574	1.052
C=O	3.496	0.58
OCH <sub>2</sub> (esters)	2.9499	1.0
OCH <sub>3</sub> (esters)	3.0783	1.33
CO <sub>2</sub>	2.7864	2.0

**Table 7.3:** GC-SAFT-VR segment-segment dispersion energy well depth parameters  $\varepsilon_{ki,lj}/k_B$ (K).

Type	CH <sub>3</sub>	CH <sub>2</sub>	CH=CH <sub>2</sub>	C=O	OCH <sub>2</sub>	OCH <sub>3</sub>	CO <sub>2</sub>
CH <sub>3</sub>	234.250	235.735	226.675	307.22	157.702	191.144	204.951
CH <sub>2</sub>	235.735	237.230	228.112	309.17	158.702	192.355	206.251
CH=CH <sub>2</sub>	226.675	228.112	219.344	297.28	152.602	184.962	198.323
C=O	307.223	309.171	297.288	402.92	206.829	250.689	268.797
OCH <sub>2</sub>	157.702	158.702	152.602	206.82	106.168	128.682	137.977
OCH <sub>3</sub>	191.144	192.356	184.962	250.68	128.682	155.970	167.237
CO <sub>2</sub>	204.951	206.251	198.323	268.79	137.977	167.237	179.317

**Table 7.4:** GC-SAFT-VR segment-segment dispersion energy range parameters  $\lambda_{ki,lj}$

Type	CH <sub>3</sub>	CH <sub>2</sub>	CH=CH <sub>2</sub>	C=O	OCH <sub>2</sub>	OCH <sub>3</sub>	CO <sub>2</sub>
CH <sub>3</sub>	1.492	1.583	1.529	1.685	1.546	1.566	1.506
CH <sub>2</sub>	1.583	1.667	1.621	1.586	1.645	1.662	1.609
CH=CH <sub>2</sub>	1.529	1.621	1.568	1.728	1.764	1.608	1.550
C=O	1.685	1.586	1.728	1.891	1.764	1.558	1.729

<b>OCH<sub>2</sub> (ester)</b>	1.546	1.645	1.764	1.764	1.614	1.635	1.571
<b>OCH<sub>3</sub> (ester)</b>	1.566	1.662	1.558	1.558	1.635	1.655	1.594
<b>CO<sub>2</sub></b>	1.506	1.609	1.550	1.729	1.571	1.594	1.526

Utilizing the model described above, the vapor pressure and saturated liquid density for other pure FAME fluids were then predicted. Figure 7.1 and 7.2 shows the comparison between theoretical results and the experimental data for vapor pressure and saturated liquid density, respectively for the molecules: methyl laurate, methyl myristate, methyl caprate, methyl caprylate, methyl palmitate, methyl oleate, and methyl stearate. Table 7.1 in the Appendix summarizes the absolute average deviation in pressure (AADP) and saturated liquid density (AADL), respectively. We note that good agreement between the theoretical predictions and experimental data (AADP=5.37% and AADL=2.48%) are observed over a wide temperature range. As discussed previously, these long chain FAME molecules were also studied by Nguyen Thi *et al.* [94] using the polar GC-SAFT equation [92] and four different chemical groups (CH<sub>3</sub>, CH<sub>2</sub>, COO and HCOO) with deviations in vapor pressure for methyl palmitate, methyl stearate, and methyl tetracosanoate of 10.31%, 15.30%, and 51.77%, respectively. Using a simpler approach (i.e., no dipole term and associated additional fitted parameter), we find significantly lower deviations using the GC-SAFT-VR equation. We also note that although Oliveira *et al.* [168] for the same molecules obtained comparable average deviations from experimental data, the model parameters were fitted to experimental FAME data, while the GC-SAFT-VR approach provides similar results using a truly predictive approach.

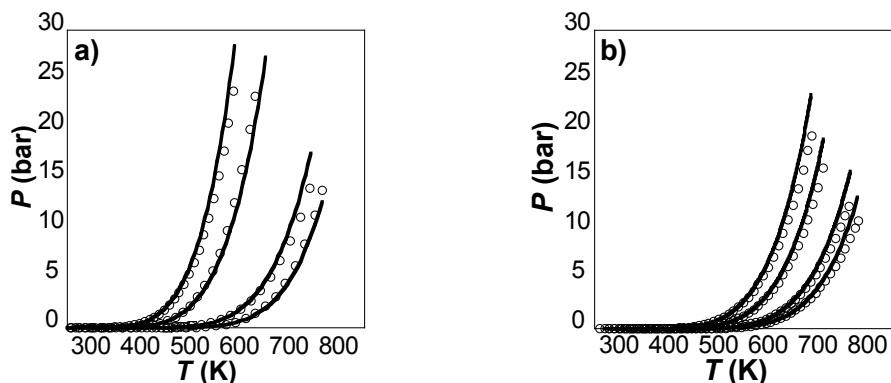


**Figure 7.1:** Comparison between theoretical predictions from the GC-SAFT-VR equation and experimental data for the vapor pressure of a) methyl caproate, methyl caprylate, methyl myristate, and methyl oleate (left to right) b) methyl caprate, methyl laurate, methyl palmitate, and methyl stearate (left to right) Symbols correspond to the experimental data [10] and the solid lines to the theoretical results.

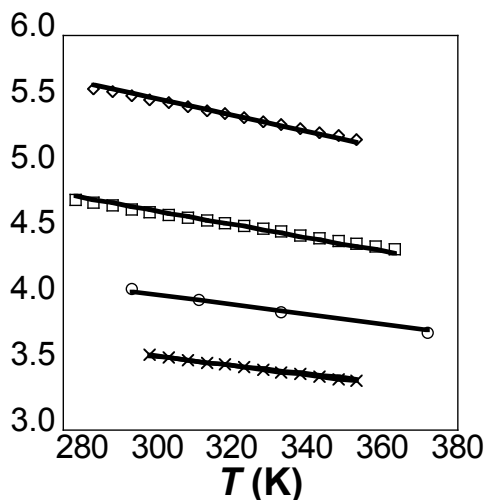


**Figure 7.2:** Comparison between theoretical predictions from the GC-SAFT-VR equation and experimental data for the saturated liquid density of methyl caprylate (diamonds), methyl caprate (squares), methyl laurate (circles), and methyl myristate (crosses) (top to bottom). Symbols represent the experimental data [10] and solid lines the theoretical results.

### *Binary Mixtures*

To model the binary mixtures of interest, model parameters taken from previous work in a transferable manner are again used to determine the properties of the mixtures of interest. The results shown are therefore pure predictions as no model parameters have been adjusted to experimental binary mixture data.

First we consider the VLE of binary mixtures of FAME molecules. We focus on mixtures of long chain FAME molecules, for which to our knowledge, no other SAFT studies have been performed. In Figure 7.3a and 7.3b the isobaric VLE of the binary mixture of methyl caprylate ( $C_9H_{18}O_2$ ) + methyl caprate ( $C_{11}H_{22}O_2$ ) and methyl caprylate + methyl caproate ( $C_7H_{14}O_2$ ),



respectively are presented. From the figures we can see that good agreement between the theoretical predictions and experimental data is obtained and that the theory is able to capture the change in phase behavior as the number of CH<sub>2</sub> groups present is increased. Next, increasing the length of the molecule, we investigate in Figure 7.3c the methyl laurate (C<sub>13</sub>H<sub>26</sub>O<sub>2</sub>) + methyl caprate (C<sub>11</sub>H<sub>22</sub>O<sub>2</sub>), binary mixture at 0.0053 MPa, 0.0066 MPa, and 0.0133 MPa. Good agreement is again found as compared to experimental results. Further increasing the length of the carbon backbone of the FAME fluid, we show in Figure 7.3d that the theory accurately predicts the phase behavior of mixtures of methyl myristate (C<sub>15</sub>H<sub>30</sub>O<sub>2</sub>) + methyl laurate (C<sub>13</sub>H<sub>26</sub>O<sub>2</sub>), again without fitting to experimental results. Finally, the isobaric VLE curves of the binary mixture of methyl myristate (C<sub>15</sub>H<sub>30</sub>O<sub>2</sub>) + methyl palmitate (C<sub>17</sub>H<sub>34</sub>O<sub>2</sub>) are predicted in Figure 7.3e. In all cases as the chemical structures of the ester molecules changes the theory is able to predict and capture the changes in phase behavior without fitting to any experimental data. Finally, we consider a binary mixture of the longest saturated FAME molecules studied. The *T<sub>xy</sub>* phase behavior of methyl palmitate (C<sub>17</sub>H<sub>34</sub>O<sub>2</sub>) + methyl stearate (C<sub>19</sub>H<sub>38</sub>O<sub>2</sub>) is investigated in Figure 7.3f at a constant pressure of 0.0040 MPa. From the figure we can see that good agreement is obtained between the theoretical predictions and experimental data even for the long chain molecules. Following the classifications scheme for binary mixtures given by Scott and van Konynenburg [175, 176], the theory suggests Type 1 phase diagrams for binary mixtures of the saturated FAME molecules that have a difference in carbon chain length of up to 12, which is the difference between the shortest and longest FAME molecule of interest in this study.

Turning to unsaturated FAME molecules, in Figure 7.4 we present experimental results and GC-SAFT-VR predictions for the methyl oleate (C<sub>19</sub>H<sub>36</sub>O<sub>2</sub>) + methyl stearate (C<sub>19</sub>H<sub>38</sub>O<sub>2</sub>) binary mixture at 473.15 K. The theoretical predictions for the *xy* distribution are seen to be in good agreement with the experimental data however, experimental results are not available for comparison with the corresponding *Pxy* behavior (Figure 7.4a), for which the theory predicts azeotropic behavior implying separation would present difficulties.

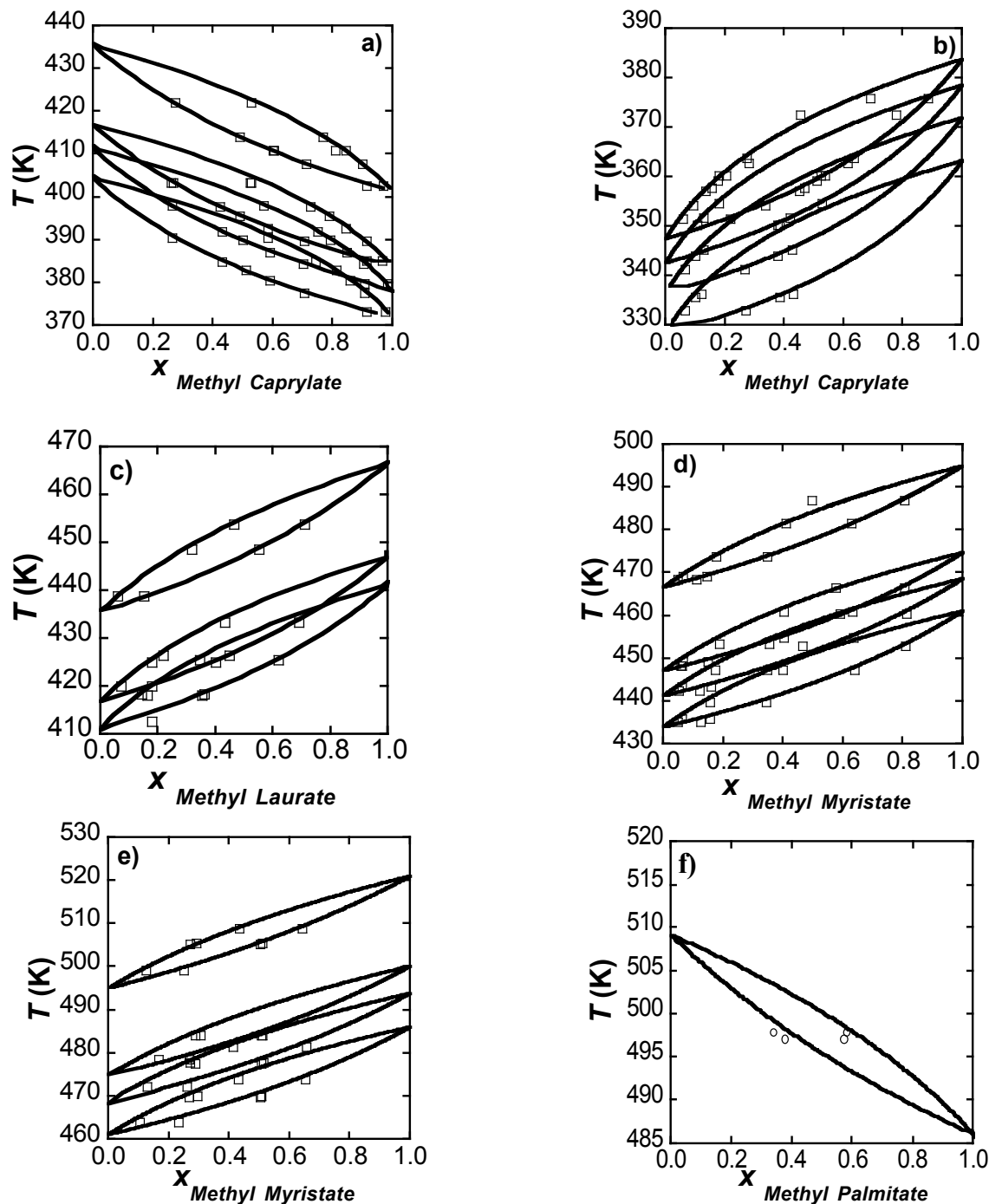


**Figure 7.3:** Constant pressure  $T_{xy}$  slices of the (a) methyl caprylate + methyl caprylate phase diagram at 0.0133 MPa, 0.0066 MPa, 0.0053 MPa, and 0.0039 MPa (from top to bottom), (b) methyl caprylate + methyl caproate phase diagram at 0.0066 MPa, 0.0053 MPa, 0.0039 MPa, and 0.0027 MPa (from top to bottom), (c) methyl laurate + methyl caprylate phase diagram at 0.0133 MPa, 0.0066 MPa, and 0.0053 MPa (from top to bottom), (d) methyl myristate + methyl laurate phase diagram at 0.0133 MPa, 0.0066 MPa, 0.0053 MPa, and 0.0039 MPa (from top to bottom), and (e) methyl myristate + methyl palmitate phase diagram at 0.0133 MPa, 0.0066 MPa, 0.0053 MPa, and 0.0039 MPa (from top to bottom) (f) methyl palmitate + methyl stearate phase diagram at 0.0040 MPa. The solid lines correspond to the theoretical predictions and the symbols represent the experimental data [12].

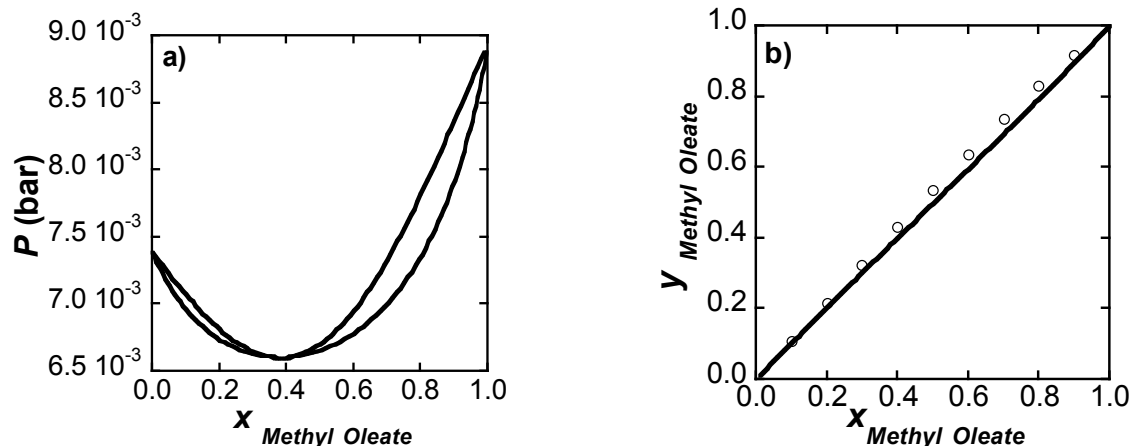


**Figure 7.4:**  $P_{xy}$  (a) and  $xy$  (b) diagram for the methyl oleate + methyl stearate binary mixture at 473.15K. The solid lines represent the theoretical predictions and the symbols represent the experimental [12, 15], [16] data.

We next consider binary mixtures of FAMES with the light alcohols methanol and ethanol. Experimentally it has been shown that in mixtures of alcohols and esters hydrogen bonding occurs between the hydrogen atom in the OH group of the alcohol and the oxygen atom in the ester [177-180]. In previous work [47], this was accounted for through the addition of an association site on the carbonyl group (C=O) that enabled cross association between the alcohol and ester. We note that the energy and range parameters ( $\epsilon^{\text{HB}}$  and  $K^{\text{HB}}$ ) for the cross association were of the same *strength* as the self-association between alcohol groups ( $\epsilon^{\text{HB}} = 2797$  K and  $K^{\text{HB}} = 0.16014 \text{ \AA}^3$  [47]) and so were not fitted parameters. Using this same approach, in Figure 7.7(a) we consider the VLE at atmospheric pressure for methyl laurate + methanol and ethanol and for methyl myristate + methanol and ethanol in Figure 7.7(b). As can be seen from the figure, good agreement with the experimental data is found in all cases, without fitting to experimental mixture data. As previously discussed, in the work of Oliveira *et al.* [11], adjustable cross interaction parameters fitted to experimental data for the ester + alcohol mixtures studied was required to obtain good agreement with the experimental data, thus limiting the predictability

of the approach. In our work, no cross interactions fitted to ester + alcohol binary mixtures are needed, thus the theory is fully predictive.

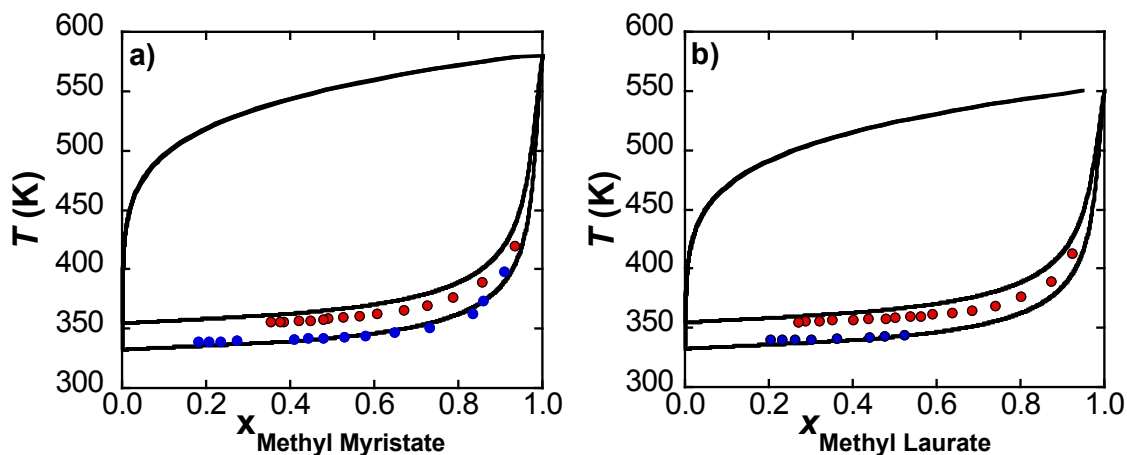


**Figure 7.5:** a.) VLE at atmospheric pressure for the methanol+ methyl myristate and ethanol + methyl myristate b.) VLE at atmospheric pressure for the methanol+ methyl laurate and ethanol + methyl laurate The solid lines represent the predictions from the GC-SAFT-VR equation with fitted cross interaction and the symbols the experimental data[11].

Next we consider high pressure VLE data for binary mixtures of methanol with methyl laurate and methyl myristate at 493 K, 523 K, and 543 K [11, 181]. As can be seen from Figures 7.6 (a) and 7.6 (b), good agreement with experimental data is obtained, although deviations due to the over-prediction of the vapor pressure of pure methanol and ethanol fluids are observed. We note, however, that these results are pure predictions, while Oliveira *et al.* [11] observed smaller deviations from the experimental data fitted cross interaction parameters were used that were pressure dependent.

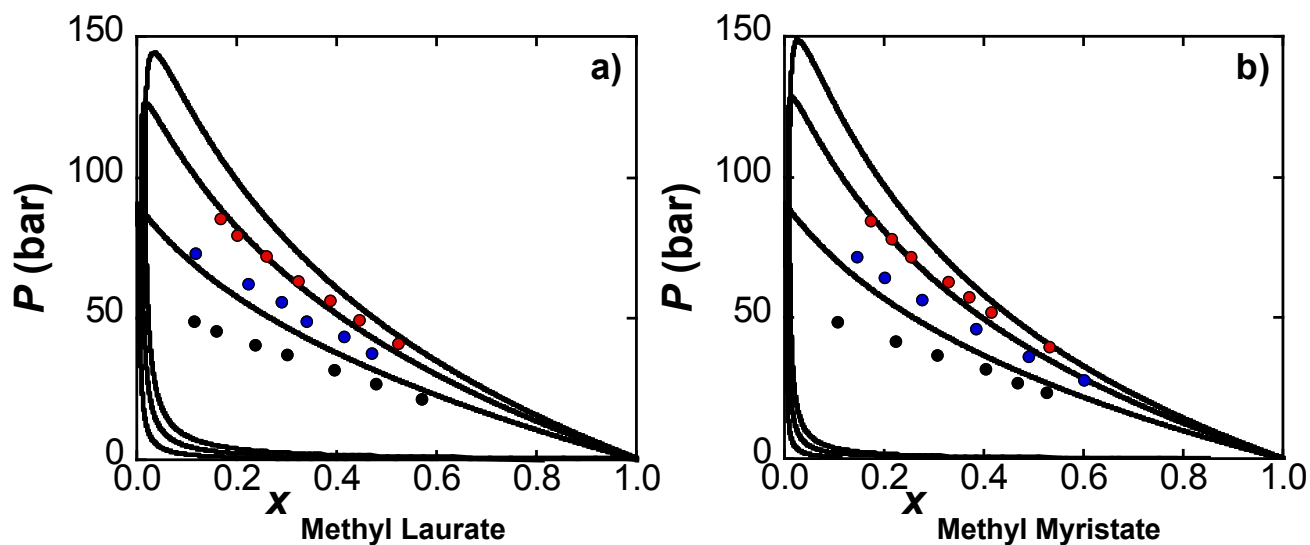


**Figure 7.6:** The solid lines represent the predictions from the GC-SAFT-VR equation with fitted cross interaction and the symbols the experimental data [11]. a.) VLE for methanol + methyl laurate at 493 K, 523 K, 543 K (bottom to top) b.) VLE for methanol + methyl myristate at 493 K, 523 K, 543 K (bottom to top)

Finally, results are presented using the GC-SAFT-VR approach to predict the phase behavior of FAME + CO<sub>2</sub> mixtures. FAME+ CO<sub>2</sub> mixtures display large deviations from ideal behavior due to electron donor-acceptor complexes formed between CO<sub>2</sub> and the carbonyl group being more energetically favorable when compared to the CO<sub>2</sub>-CO<sub>2</sub> interactions and the carbonyl-carbonyl interactions established between the ester molecules [182]. Due to the non-ideal nature of the FAME+ CO<sub>2</sub> mixtures, Lorentz Berthelot combining rules (shown in Figure 7.7 for the methyl palmitate + CO<sub>2</sub> at 343.15 K) fail to accurately predict the phase behavior of the system. However, if the cross interaction between CO<sub>2</sub> and the CH<sub>2</sub> group determined in previous work [174], by fitting to the phase behavior of CO<sub>2</sub> + alkane mixtures is used, excellent agreement is obtained. Using this approach, in Figure 7.8 the phase behavior of the binary mixtures of methyl myristate, methyl oleate, methyl stearate, and methyl palmitate with CO<sub>2</sub> are predicted over a range of temperatures and good agreement with the experimental data points obtained. We note that in order to obtain a similar level of agreement in the work of Llovell *et al.* [169], two fitted binary interaction parameters were introduced, with the dispersive energy parameters adjusted for

each mixture studied.

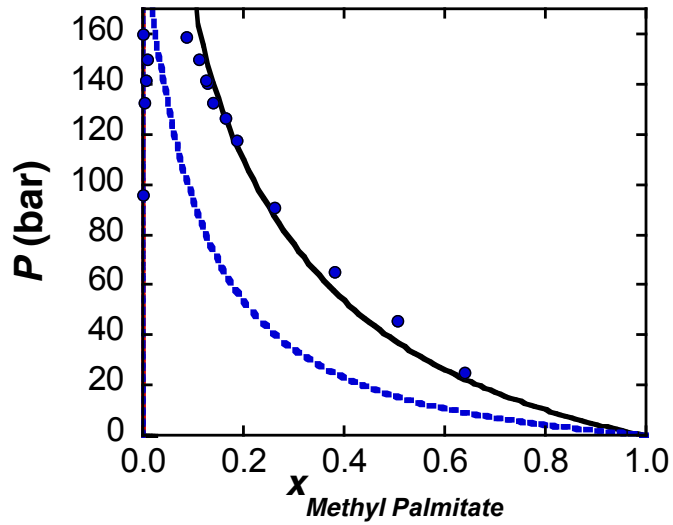


**Figure 7.7:** Constant temperature  $Pxy$  slice at 343.15 K of the methyl palmitate +  $\text{CO}_2$ . The solid lines represent the predictions from the GC-SAFT-VR equation with fitted cross interaction, dotted lines utilized Lorentz Berthelot combining rules and the symbols the experimental data [7].

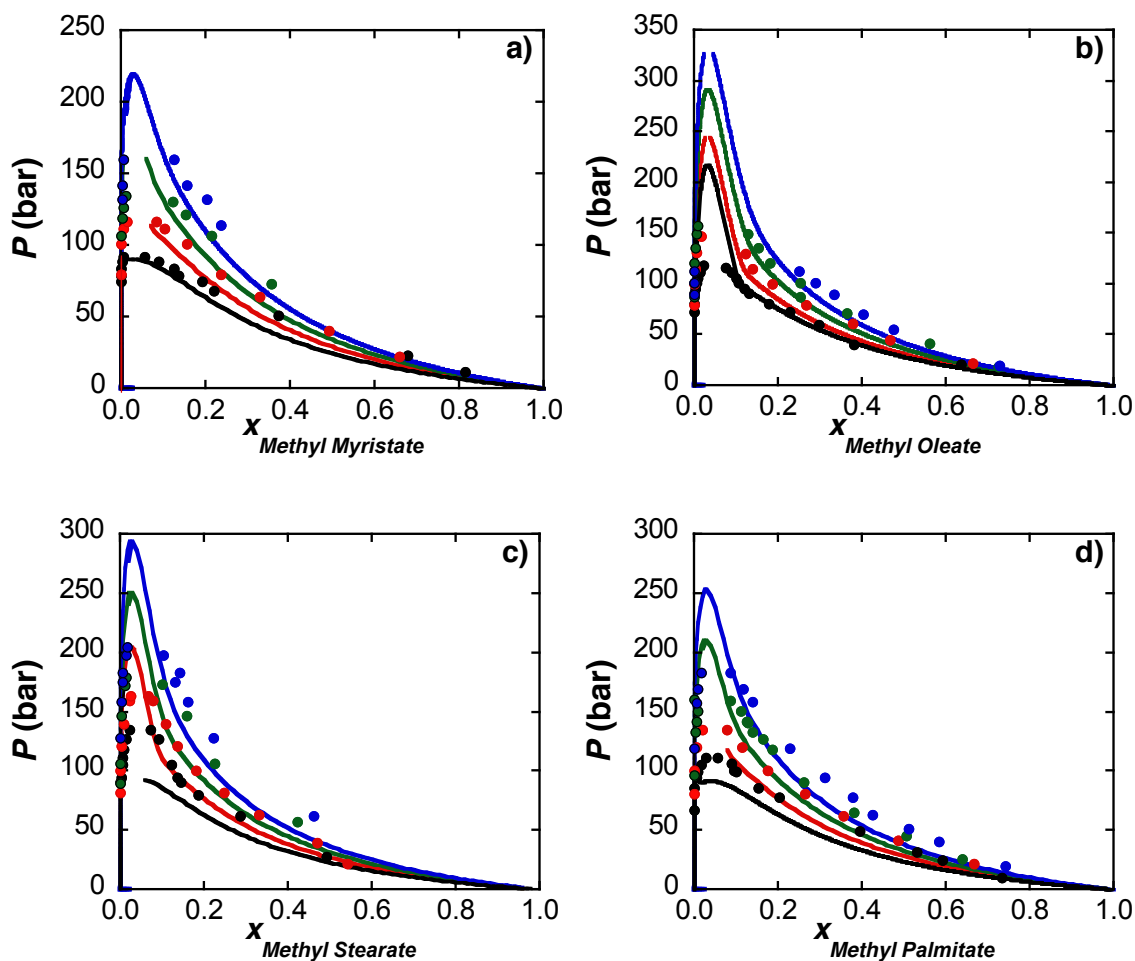


**Figure 7.8:** Constant temperature  $P_{xy}$  slices of the (a) methyl myristate, (b) methyl oleate, (c) methyl stearate, and (d) methyl palmitate +  $\text{CO}_2$  phase diagrams at 313.15K, 323.15K, 333.15K, 343.15K (bottom to top). The solid lines represent the predictions from the GC-SAFT-VR equation and the symbols the experimental data [7].

## Conclusions

In this work, the GC-SAFT-VR approach has been used to predict the phase behavior of fatty acid methyl ester (FAME) molecules and their binary mixtures. The parameters for the groups that comprise the FAME molecules were determined in previous work and used in a transferable fashion to describe the FAME molecules of interest. The phase behavior of binary mixtures of FAME molecules with alcohols,  $\text{CO}_2$  and other FAME molecules were then predicted without fitting any cross interactions to experimental data for the binary mixtures being studied.

Accordingly, we can conclude that the GC-SAFT-VR approach can be used successfully in a predictive fashion to predict the phase behavior of FAME pure fluids and mixtures without reliance on experimental data. The theory has also been used to predict the global phase behavior for binary mixtures of FAME molecules in the classification scheme of Scott and van Konynenburg.



## Chapter VIII

### Investigating the Phase Behavior of Carbon Dioxide: A Quadrupolar Fluid Using a Group Contribution SAFT Based Approach

#### Introduction

Carbon dioxide (CO<sub>2</sub>) is among one of the most abundant naturally occurring compounds. Although it was one of the first compounds to be studied, over three centuries ago, the science community still lacks a clear understanding of CO<sub>2</sub>'s phase behavior and thermodynamic properties [183]. The call for advancements in the design, optimization and operation of carbon dioxide capture and storage (CCS) systems suggest that finding more accurate ways of modeling the properties of CO<sub>2</sub> is paramount. This is underpinned by the fact that one of the biggest challenges facing more accurate CO<sub>2</sub> characterization is the lack of experimental data within certain operational regimes of the CCS process. For instance, the vapor-liquid equilibrium (VLE) of CO<sub>2</sub> mixtures is one of the basic parameters required to design the capture of CO<sub>2</sub> and non-condensable gas separation processes [184, 185]. The volume property is also important in the design and operation of compression, transportation and storage [184]. Thus, a deeper understanding of the thermodynamic properties of CO<sub>2</sub> mixtures can provide key information for developing new CCS and other CO<sub>2</sub> dependent processes.

Recently, novel thermodynamic models have been developed which provide an accurate description of the phase behavior and thermodynamic properties required to utilize industrially relevant systems such as carbon dioxide [97]. Using equations such as molecular based equations of state is ideal, given the shift towards developing accurate modeling methods that anchor more on physics than empirics. Molecular based equations of state boast a superior predictive capability to that of the cubic equations of state, yielding more accurate phase behavior and thermodynamic prediction. This not only allows for a deeper understanding of the inherent properties, but also provides better characterization of how the interactions between the molecules affect the thermodynamics. The statistical mechanics based equation of state, statistical associating fluid theory (SAFT) [39, 40], is one such theory belonging to the molecular based equation of state family. SAFT based approaches, describe molecules as chains of tangentially bonded homonuclear segments that interact through dispersion and association interactions. Rooted in statistical mechanics and based on a molecular-level model, SAFT typically lends itself well to the development of a predictive modeling approach. Numerous modifications and improvements of different versions of SAFT have been proposed and applied to various mixtures over recent years including: SAFT- Hard Sphere (SAFT-HS) [40], SAFT Lennard-Jones (SAFT-

LJ) [186, 187], perturbed-chain SAFT (PC-SAFT) [72], and SAFT variable range (SAFT-VR) [86, 106]. For a detailed discussion concerning the various versions of SAFT and its applications, the reader is directed to the recent review of McCabe and Galindo [49].

The interesting and complex behavior of carbon dioxide and its mixtures has drawn the attention of many researchers. Thus, there have been a number of important theoretical studies, specifically SAFT approaches, dedicated to determining the thermodynamic properties, including the phase behavior, of carbon dioxide systems. In the first SAFT study focusing on carbon dioxide, Huang and Radosz [50] used the original SAFT [39] approach to correlate the molecular parameters for the pure carbon dioxide fluid. In a subsequent study, Huang and Radosz [188], extended the approach to mixtures where the phase behavior of carbon dioxide was studied with light alcohols, decane, and 1-methylnaphthalene. Also using the original SAFT equation, the mutual solubility of alkanes in carbon dioxide was studied by Passarello *et al.* [189]. The study considered alkanes from C<sub>3</sub>H<sub>8</sub> to C<sub>44</sub>H<sub>90</sub> as well as branched alkanes. Reasonable agreement (within 8% of experimental results) is found for the VLE calculations with the introduction of two fitted binary interaction parameters.

Using the statistical associating fluid theory for potentials of variable range (SAFT-VR) approach, where chain molecules are formed from hard-core segments interacting through attractive potentials of variable range (VR) [86], the phase behavior of the CO<sub>2</sub> + alkane homologous series was examined by Blas *et al.* [18]. The intermolecular parameters for the non-associating, non-spherical CO<sub>2</sub> molecule were determined by fitting to experimental vapor pressure and saturated densities. Parameters were then rescaled to experimental critical points to provide a better description of the critical region. The quadrupole moment present in CO<sub>2</sub> is treated in an effective way through the square-well potentials. In the study, the transitions, following classifications for binary mixtures given by Scott and van Konynenburg [175, 176], occurring between the mixtures of CO<sub>2</sub> + dodecane (Type II), CO<sub>2</sub> + tridecane (Type IV), and CO<sub>2</sub> + tetradecane (Type III) were investigated. The theory is able to describe these changes by introducing two adjustable transferable parameters, which were determined from fitting to the phase equilibrium of the binary mixture of CO<sub>2</sub> + tridecane. In addition, a global phase diagram for mixtures of CO<sub>2</sub> + alkanes in terms of the critical end points of the mixtures is determined. In a follow up paper, Galindo *et al.*, [17] examined in greater detail the phase behavior of the alkanes from ethane to hexadecane. This group found the parameters determined in the work of Blas *et al.*, [18] provide accurate predictions of the global fluid phase behavior.

Utilizing the abovementioned SAFT-VR approach and parameters, Colina *et al.* [136] investigated the phase behavior of CO<sub>2</sub> with alkanes and perfluoroalkanes. Model parameters for

perfluoroalkanes (perfluorohexane and perfluoroheptane) were determined by fitting to vapor pressure and saturated liquid densities and then rescaled to the critical region. The predictive approach is shown to provide a good description of the phase behavior of the CO<sub>2</sub> mixtures studied in this work.

In a combined experimental and theoretical study, Tochigi *et al.* [19] utilized the SAFT-VR approach to model the VLE of CO<sub>2</sub> + *n*-octane, methanol, ethanol, and perfluorohexane. The optimized parameters for octane[76], perfluorohexane [136], and CO<sub>2</sub> [18] were taken from previous work. SAFT-VR parameters for methanol and ethanol were determined by fitting to vapor pressure and saturated liquid density data for each pure component. The phase behavior at 313.14 K of CO<sub>2</sub> + *n*-octane mixtures are compared using the Lorentz Berthelot combining rule and the cross interactions optimized by Blas and Galindo. Deviations were observed in each of the schemes; therefore, a new cross interaction was optimized, reducing deviations between the experimental compositions and total pressures to 0.12 mol% and 1.4%, respectively. For the CO<sub>2</sub> + methanol and CO<sub>2</sub> + ethanol mixtures, Lorentz Berthelot combining rules are used to predict the phase diagrams, resulting in a deviations in composition and pressure of 0.6% and 12%, respectively for the methanol systems and 0.34% and 25% for the ethanol system. In addition, a new cross interaction is proposed by fitting to binary experimental data for the alcohol + CO<sub>2</sub> mixtures. By implementing fitted cross interactions, deviations are reduced to 0.51% and 0.46% in composition and pressure respectively for methanol and for ethanol the deviations are shown to be 0.18% and 4.03%. Finally for the CO<sub>2</sub> + perfluorohexane system, a cross interaction is proposed by fitting to the experimental data for 303.15K. The proposed cross interaction is then used to predict the phase behavior at other temperatures studied. Average deviations between experimental compositions and total pressures are 0.78% and 2.79%, respectively.

In an attempt to account for the effect of the explicit inclusion of the quadrupole moment on CO<sub>2</sub>, Dias *et al.* [125], added a polar term to the original soft-SAFT equation of state. An expansion of the Helmholtz free energy in terms of the perturbed quadrupole- quadrupole potential with the Padé approximation is implemented in the theory. The phase behavior of mixtures of CO<sub>2</sub> with perfluorobenzene, perfluorotoluene, and perfluorooctane were studied at three temperatures with and without the inclusion of the quadrupole. Experimental values of the quadrupole moment are used for CO<sub>2</sub> and perfluorobenzene molecules. The quadrupole moment for perfluorotoluene was approximated as that of perfluorobenzene. The fraction of segments in the chain, which contain the quadrupole,  $x_p$ , was fixed at 1/3 for CO<sub>2</sub> and 1/6 for perfluorotoluene and perfluorobenzene. The remaining model parameters were determined by fitting to experimental vapor pressure and saturated liquid density data in the usual way. Deviations from

experimental results for pressure and density were found to be 0.5% and 0.9%, respectively. The quadrupole had a significant influence on the description of the phase behavior of the mixtures involving aromatic compounds, providing better agreement with experimental results and capturing the changes in the curvature with a function of temperature without fitting binary parameters. However, for the perfluorodecalin, perfluoromethylcyclohexane, and perfluorooctane mixtures the quadrupole effect on the phase equilibria is not as noticeable, requiring the use of fitted binary interaction parameters. Two interaction parameters were introduced and determined by fitting to experimental data at 323.15 K for each mixture considered in the study.

In this work, we extend the scope of the recently developed statistical associating fluid theory for potential of variable range for the description of dipolar fluids [190] (SAFT-VR+D) to the study of CO<sub>2</sub> by including a group contribution approach. The GC-SAFT-VR+D equation explicitly accounts for dipolar interactions and their effect on the thermodynamics and structure of a fluid by using the generalized mean spherical approximation (GMSA) to describe a reference fluid of dipolar square-well segments. With the goal of developing a molecular model to accurately describe the phase behavior of the carbon dioxide molecule and its mixtures, interactions due to the quadrupole moment are explicitly included at the molecular and structural level. This is done by embedding a dipolar site in each of two segments oriented in opposite directions thus representing the large quadrupole moment of CO<sub>2</sub>. The phase behavior of CO<sub>2</sub> with alkanes and perfluoroalkanes are then examined comparing the results with the original SAFT-VR and the GC-SAFT-VR +D approach. Additionally, results are compared with the work of Zhao *et al.* [191], where the phase behavior of binary mixtures of nitrogen and alkanes are investigated using the Quadrupolar SAFT-VR theory. In mentioned work, nitrogen is described as a chain molecule with a net point axial quadrupole moment located at the center of the molecule.

### **Molecular Model and Theory**

In this approach, CO<sub>2</sub> is described as a quadrupolar, non- associating, chain molecule. In the model chain, a dipolar site is embedded in each of the two segments oriented in opposite directions, representing the large quadrupole moment associated with CO<sub>2</sub>.

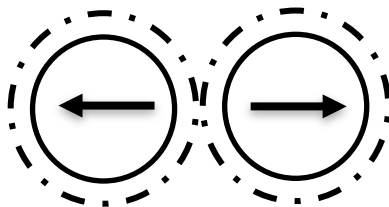


**Figure 8.1:** Schematic representation of quadrupolar molecule, CO<sub>2</sub>, where quadrupole moment approximated as two dipoles

The molecular parameters, which are taken from previous work [150], are given as:  $\sigma_{11}$ : segment size,  $\lambda_{11}$ : range of square well interactions,  $\epsilon_{11}$ : depth of square well interactions, and  $m_{11}$ : number of segments forming the model chain. These parameters were determined from adjusting parameters to vapor pressure and saturated liquid density. The inclusion of the dipole-dipole interactions introduce three additional parameters, the dipole moment,  $\mu$ , and the orientation of the dipole, which is determined by the azimuthal,  $\theta$ , and the polar  $\phi$  angles of the intersegment axis along  $r$ , as shown in Figure 8.2.

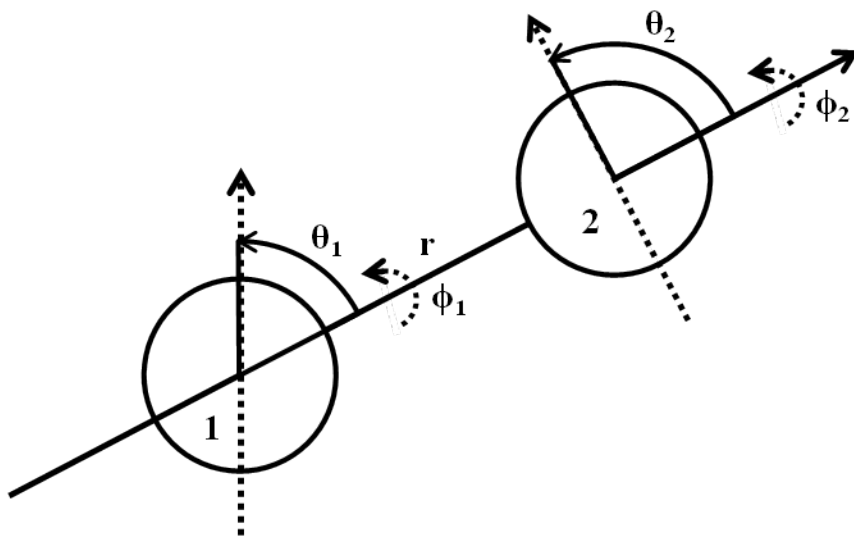


**Figure 8.2:** Schematic representation of the interdipole site coordination system, with polar axis along  $r$  [192].

The SAFT-VR [76] model for alkanes is used in this work; this model has been shown to provide a good description of the vapor pressure and coexisting densities of alkanes, in previous work. The  $n$ -alkane family, non- associating, and nonpolar chain molecules are described by four molecular parameters described above and given as:  $\sigma_{22}$ ,  $\lambda_{22}$ ,  $\epsilon_{22}$ , and  $m_{22}$ . The number of segments,  $m_{22}$ , in the model chain is determined from the number of carbon atoms  $C$  in the molecule using the expression:  $m = (C-1) / 3 + 1.0$ .

In the GC-SAFT-VR with dipole approach, the inclusion of the dipole-dipole interactions are accounted for through the dipole moment  $\mu$  and the orientation of the dipoles which is

determined by the azimuthal  $\theta$  and polar  $\phi$  angles of the inter-segment axis along  $r$ , as shown in Figure 8.2 [193]. Therefore, the pair potential for the dipolar fluids studied is defined as,

$$u_{ij}(\mathbf{r}_{ij}; \mathbf{w}_1, \mathbf{w}_2) = u_{ij}^{HS}(r_{ij}; \sigma_{ij}) - \varepsilon_{ij} \phi_{ij}^{SW}(r_{ij}; \lambda_{ij}) + u_{ij}^{dipole}(\mathbf{r}_{ij}; \mathbf{w}_1, \mathbf{w}_2) \quad (8.1)$$

where  $\mathbf{r}_{ij}$  is the vector between the center of monomers  $i$  and  $j$ ,  $r_{ij} = |\mathbf{r}_{ij}|$  the distance between segments of species  $i$  and  $j$ ;  $\mathbf{w}_i = (\theta_i, \phi_i)$  the set of angles that define the orientation of the dipole moment in the monomer of species  $i$ . The monomer-monomer isotropic potential consist of a hard sphere repulsive interaction  $u_{ij}^{HS}(r_{ij}; \sigma_{ij})$  defined by,

$$u_{ij}^{HS}(r_{ij}; \sigma_{ij}) = \begin{cases} \infty & \text{if } r_{ij} < \sigma_{ij} \\ 0 & \text{if } r_{ij} > \sigma_{ij} \end{cases} \quad (8.2)$$

and an attractive term  $-\varepsilon_{ij} \phi_{ij}^{SW}(r_{ij}; \lambda_{ij})$  modelled by a square-well potential of depth  $\varepsilon_{ij}$  and shape  $\phi_{ij}^{SW}(r_{ij}; \lambda_{ij})$  defined by,

$$\phi_{ij}^{SW}(r_{ij}; \lambda_{ij}) = \begin{cases} 1 & \text{if } \sigma_{ij} < r_{ij} < \lambda_{ij} \sigma_{ij} \\ 0 & \text{if } r_{ij} > \lambda_{ij} \sigma_{ij} \end{cases} \quad (8.3)$$

where  $\lambda_{ij}$  is the parameter associated with the range of the square-well potential. The dipole-dipole potential  $u_{ij}^{dipole}(\mathbf{r}_{ij}; \mathbf{w}_1, \mathbf{w}_2)$  is a long-range anisotropic interaction, which can be expressed as,

$$u_{ij}^{dipole}(\mathbf{r}_{ij}; \mathbf{w}_1, \mathbf{w}_2) = -\frac{\mu_i \mu_j}{r_{ij}^3} D_{ij}(\mathbf{n}_1 \mathbf{n}_2 \hat{\mathbf{r}}_{ij}) \quad (8.4)$$

Within the SAFT framework, the Helmholtz free energy,  $A$ , can be written in the form

$$\frac{A}{Nk_B T} = \frac{A^{IDEAL}}{Nk_B T} + \frac{A^{MONO}}{Nk_B T} + \frac{A^{CHAIN}}{Nk_B T} + \frac{A^{ASSOC}}{Nk_B T} \quad (8.5)$$

where  $A^{IDEAL}$  is the ideal free energy,  $A^{MONO}$  is the contribution to the free energy due to the monomer segments,  $A^{CHAIN}$  is the contribution due to the formation of bonds between monomer segments, and  $A^{ASSOC}$  is the contribution due to association. The expressions for  $A^{ASSOC}$  are not included in this work since the systems studied are not associating fluids.  $N$  is given as the total

number of molecules,  $T$  is the temperature,  $k_B$  is the Boltzmann constant. A brief discussion of each term is provided below.

### Ideal Contribution

The ideal Helmholtz free energy is given by,

$$\frac{A^{IDEAL}}{Nk_B T} = \sum_{i=1}^n x_i \ln(\rho_i \Lambda_i^3) - 1 \quad (8.8)$$

where  $\rho_i = N_i/V$  is the number density,  $N$  the number of molecules,  $x_i$  the molar fraction and  $\Lambda_i$  the thermal de Broglie wavelength of species  $i$ .

### Monomer Contribution

The contribution to the Helmholtz free energy due to the monomer segments is given by,

$$\frac{A^{MONO}}{Nk_B T} = \left( \sum_{i=1}^n x_i m_i \right) \frac{A^M}{N_s k_B T} = \left( \sum_{i=1}^n x_i m_i \right) a^M \quad (8.7)$$

where  $N_s$  is the total number of spherical monomers. Within the GMSA the excess Helmholtz free energy per monomer  $a^M$  is given by the free energy per monomer of the dipolar square well reference fluid  $a^{DSW}$  which in turn can be written as,

$$a^M = a^{DSW} = a^{dipole} + a^{isotropic} \quad (8.8)$$

where  $a^{dipole}$  describes the contribution to the free energy due to the anisotropic dipolar interactions and  $a^{isotropic}$  is written in terms of the inverse of the temperature  $\beta = 1/k_B T$  within the second-order high temperature perturbation expansion of Barker and Henderson[194-196] as

$$a^{isotropic} = a^{HS} + \beta a_1 + \beta^2 a_2 \quad (8.9)$$

where  $a^{HS}$  is the free energy due to repulsive interactions between the hard cores, and  $a_1$  and  $a_2$  are the first and second order perturbation terms associated with the isotropic attractive interactions, respectively. The residual free energy of the hard-sphere mixture is obtained from the expression of Boublik [197] and Mansoori *et al.* [198]. The mean-attractive energy associated with the first-order perturbation term is treated in the context of the MIXb mixing rules [199] and the second-order perturbation term is obtained using the local compressibility approximation.

The excess free energy due to the dipolar interactions is given by

$$a^{DIPOLE} = -\frac{8}{\eta} \xi^2 \left[ \frac{(1+\xi)^2}{(1-2\xi)^4} + \frac{(2-\xi)^2}{8(1+\xi)^4} \right] \quad (8.10)$$

where  $\xi = \kappa\eta$  and  $\kappa$  is the scaling parameter.  $\kappa$  is determined by  $y$ , the so-called strength of the dipolar effect[200]

$$3y = q_{PY}(2\kappa\eta) - q_{PY}(-\kappa\eta) \quad (8.11)$$

and is a dimensionless function of the temperature  $\beta$ , the effective density  $\hat{\rho}$  and dipole moment  $\hat{\mu}$

$$y = \frac{4\pi}{9} \beta \hat{\rho} \hat{\mu}^2 \quad (8.12)$$

$q_{PY}$  is the dimensionless inverse compressibility of Percus-Yevick (PY), given by[200]

$$q_{PY}(\eta) = \frac{(1+2\eta)^2}{(1-\eta)^4} \quad (8.13)$$

where  $\eta$  is the packing fraction of the mixture giving by,

$$\eta = \frac{\pi}{6} \hat{\rho} \left[ \sum_{i=1}^n m_i x_i \sigma_{ii}^3 \right] \quad (8.14)$$

### Chain Contribution

The contribution to the free energy due to chain formation from dipolar square-well monomers is given by,

$$\frac{A^{CHAIN}}{Nk_B T} = - \sum_{i=1}^n (m_i - 1) \ln y_{ii}^{DSW} \quad (8.15)$$

where  $m_i$  is the number of segments of component  $i$ ,  $y_{ii}^{DSW}$  is the dipolar square-well monomer background correlation function evaluated at hard-core contact for species  $i$ ,

$$y_{ii}^{DSW}(\mathbf{r}_{ii}, \mathbf{w}_1^i, \mathbf{w}_2^i) = \exp \left[ \beta u_{ii}^{DSW}(\mathbf{r}_{ii}, \mathbf{w}_1^i, \mathbf{w}_2^i) \right] g_{ii}^{DSW}(\mathbf{r}_{ii}, \mathbf{w}_1^i, \mathbf{w}_2^i; \rho, T) \quad (8.18)$$

and  $g_{ii}^{DSW}(\mathbf{r}_{ii}, \mathbf{w}_1^i, \mathbf{w}_2^i; \rho, T)$  is the pair distribution function for the dipolar square-well molecules and is obtained from the GMSA.

The study of phase equilibrium in mixtures also requires the determination of a number of cross interaction parameters, which account for the interactions between unlike components in the mixture. The Lorentz-Berthelot arithmetic mean is used for the unlike hard-core diameter,



$$\sigma_{12} = \frac{\sigma_{11} + \sigma_{22}}{2} \quad (8.17)$$

the unlike square-well dispersive energy is given by the Lorentz-Berthelot rule as follows,

$$\varepsilon_{ij} = \sqrt{\varepsilon_{ii}\varepsilon_{jj}} \quad (8.18)$$

and the unlike square-well potential range is given by

$$\lambda_{ij} = \frac{\lambda_{ii}\sigma_{ii} + \lambda_{jj}\sigma_{jj}}{\sigma_{ii} + \sigma_{jj}} \quad (8.19)$$

For interactions involving polar groups, we expect deviations from the Lorentz-Berthelot combining rules and so the unlike interactions between functional groups can also be fitted to pure component experimental data for molecules containing both functional groups.

## Results and Discussion

### *Pure Fluid*

The carbon dioxide is treated as a non-spherical, non-associating quadrupolar molecule with  $m = 2.0$  and two embedded dipole moments. Model parameters ( $\sigma$ ,  $\lambda$ ,  $\varepsilon$ ,  $m$ ) are taken from the work of Blas *et al.* [18], where the SAFT-VR approach is shown to successfully predict the phase behavior of CO<sub>2</sub> and its mixtures. The value of the dipole moment is determined by fitting to experimental vapor pressure and saturated liquid density data. The dipoles are oriented in opposite directions to approximate the quadrupole moment. The parameters and dipole moments are presented in Table 8.1. In the proposed approach, the inclusion of the quadrupolar term reduces the need to use effective parameters by explicitly including interactions due to the quadrupole moment at the molecular and structural level. The GC-SAFT-VR +D results obtained provide a good description of the vapor pressure and saturated liquid density of CO<sub>2</sub> as shown in Figure 8.3a and Figure 8.3b, respectively. The percentage of absolute average deviation for vapor pressure and saturated liquid density was found to be 0.187 % and 1.95%, respectively.

**Table 8.1:** Intermolecular Parameters for Carbon Dioxide

$m$	$\lambda$	$\varepsilon/k_B$ (K)	$\sigma$ (Å)	$\mu$
<b>2.0</b>	<b>1.5157</b>	<b>179.27</b>	<b>2.7884</b>	<b>0.84</b>

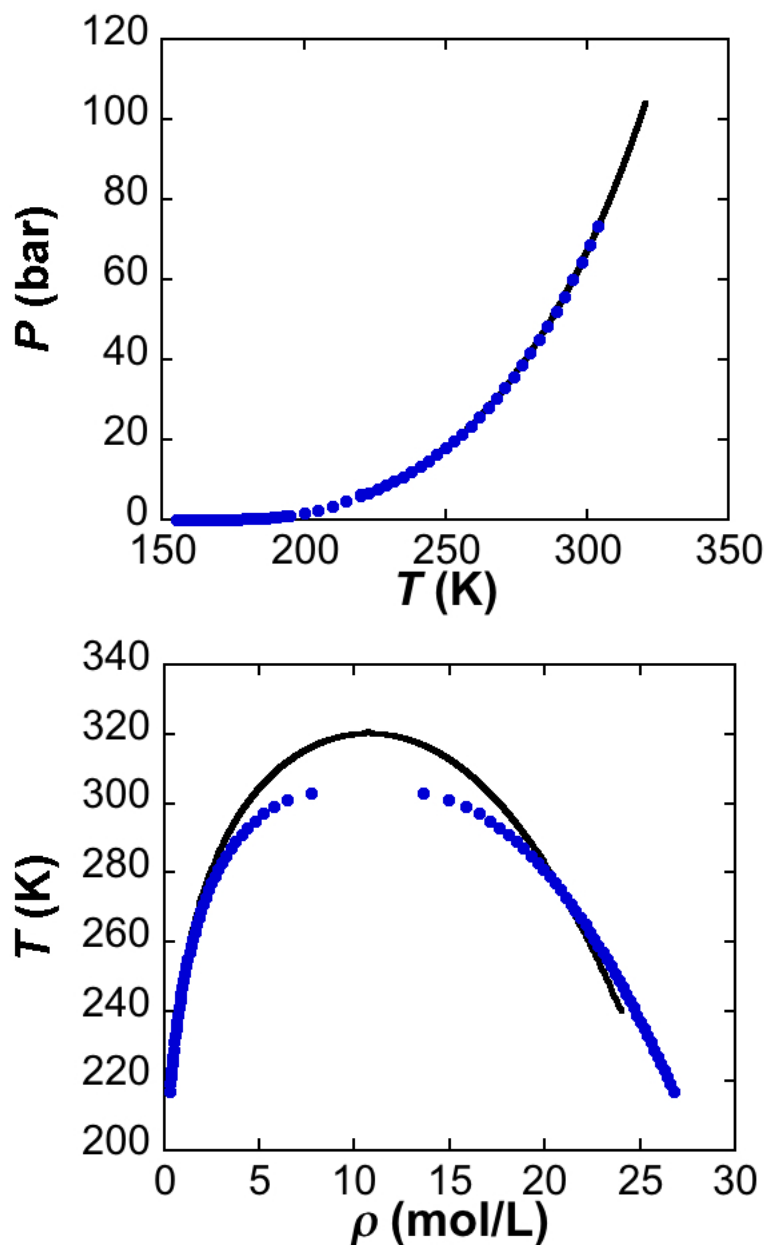


**Figure 8.3:** Carbon dioxide a.) vapor pressure b.) vapor liquid coexistence densities. Data points correspond to the experimental data and solid lines correspond to GC-SAFT-VR + D predictions.

### Binary Mixtures

Here, applying the proposed approach to the study of mixtures, we have examined the phase behavior of carbon dioxide + alkane and carbon dioxide + perfluoroalkane. In addition, we have applied our proposed theory to study the phase behavior of nitrogen + alkanes. Results are compared to Zhao *et al.*, [191], where the SAFT-VR theory is extended to include a quadrupolar

contribution to the free energy using a Pade-approximation term derived from the perturbation theory.

### Carbon Dioxide + Alkanes

Similar to earlier SAFT work [17, 19] which focused on studying the phase behavior of CO<sub>2</sub> and alkane systems, we introduce adjustable mixture parameters, as using Lorentz Berthelot combining rules significantly over predicts the liquid phase composition of alkane and CO<sub>2</sub> mixtures [19]. In this work, an adjustable parameter,  $\gamma$ , is determined by fitting to the experimental phase behavior of the CO<sub>2</sub> + hexane mixture at  $T = 313\text{K}$ . The adjustable parameters are found to be  $\xi=1.0$  and  $\gamma = 0.985$ . It is noted that only one set of parameters is required for the description of the phase behavior of the all mixtures considered in this study. Using these intermolecular parameters, the phase behavior of the CO<sub>2</sub> + alkane systems are accurately predicted.

In Figure 8.4, we have examined the phase equilibrium of CO<sub>2</sub> + ethane at 210 K. Here, we compare the predictions utilizing both the new CO<sub>2</sub> model with GC-SAFT-VR +D as well as the original SAFT-VR equation of state. In previous SAFT-VR work two sets of fitted binary interaction parameters are proposed, one set proposed in the work of Blas *et al.* [18] (blue dashed line),  $\xi = 0.88$  and  $\gamma = 0.989$ . The other set of binary interaction parameters,  $\xi = 0.94$  and  $\gamma = 0.989$ , which was proposed by Galindo *et al.*, [17], for short chain alkanes (black dashed line). As can be seen in Figure 8.5, we show improved agreement (solid black line) with experimental results for the ethane mixture. In addition, we obtain improved results by utilizing less fitted parameters, as only 1 adjustable parameters is introduced to accurately describe the phase behavior of the mixture.

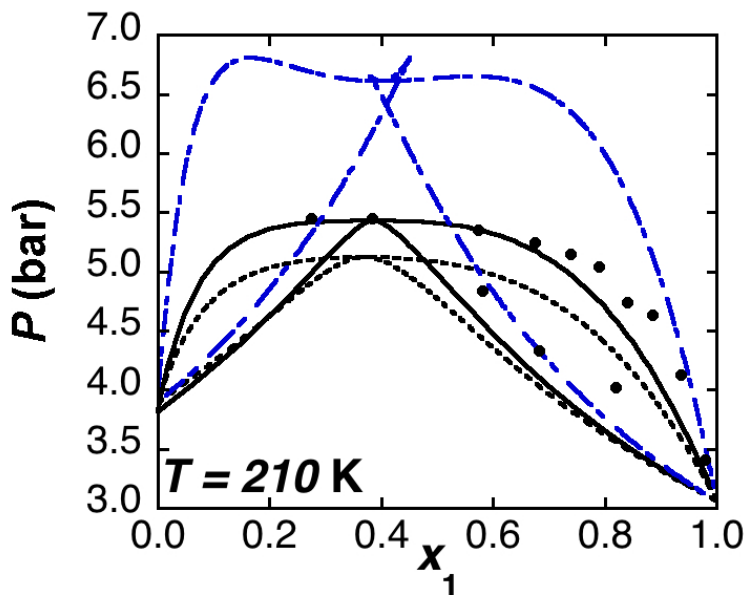


**Figure 8.4:**  $Px$  slice of the  $\text{CO}_2 + \text{ethane}$  phase diagrams at  $T= 210 \text{ K}$ . Solid lines correspond to GC-SAFT-VR+D predictions, Dashed lines correspond to original SAFT-VR predictions using parameters proposed by Galindo *et al.*, [17], Blue Dashed lines correspond to original SAFT-VR predictions using parameters proposed by Blas *et al.* [18], symbols correspond the experimental data[19]

Further testing the predictability and transferability of the  $\text{CO}_2$  model proposed, we present the phase behavior of the  $\text{CO}_2 + \text{ethane}$  isothermal mixture at  $T = 210 \text{ K} - 293 \text{ K}$ . As can be seen in the figure, we show good agreement with experimental results. The theory is able to capture the shift in pressure as the temperature is increased. In addition, the azeotrope predictions agree well with experimental results.

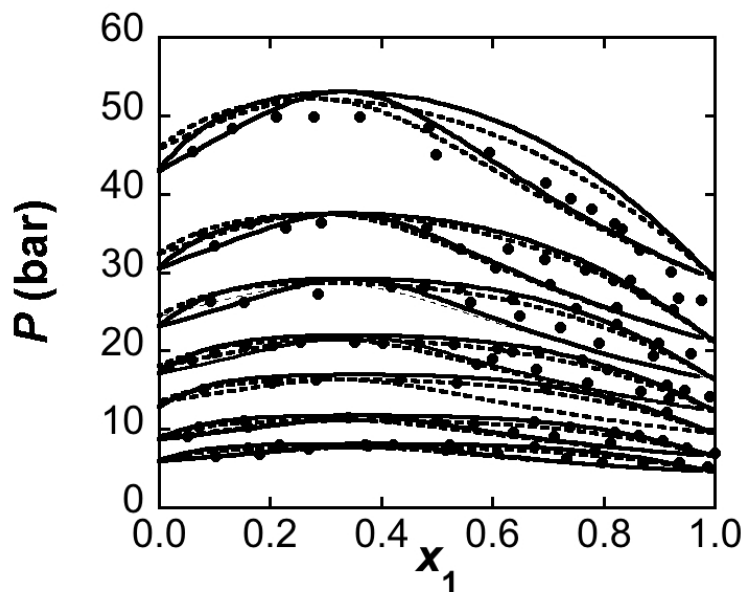


**Figure 8.5:**  $Px$  slices of the  $\text{CO}_2 + \text{ethane}$  phase diagrams at different temperatures. Solid lines correspond to GC-SAFT-VR+D predictions, Dashed lines correspond to original SAFT-VR predictions using parameters proposed by Galindo *et al.*, [17], symbols correspond the experimental data [19]

To test the transferability of our parameters and model, we examine the phase behavior of longer alkane chains, such as *n*-hexane, *n*-heptane, *n*-octane, *n*-decane, and *n*-dodecane with carbon dioxide. In Figure 8.6, we present the phase behavior of the  $\text{CO}_2 + n\text{-hexane}$  mixture (used to determine the cross interactions between the alkane and  $\text{CO}_2$  molecule at 313 K). The phase behavior of the *n*-hexane +  $\text{CO}_2$  mixtures were then predicted at other thermodynamic conditions,  $T = 308.15 \text{ K}$ ,  $313.15 \text{ K}$ ,  $318.15 \text{ K}$ ,  $323.15 \text{ K}$ ,  $333.15 \text{ K}$ , and  $353.15 \text{ K}$ . Good agreement is observed with experimental results. This mixture is also studied at  $T=313 \text{ K}$  and  $353.15 \text{ K}$  in the

work of Colina *et al.*, where parameters are taken from by Blas *et al.* Comparing the phase behavior predictions from Colina *et al.* we see that by implementing the new model for CO<sub>2</sub>, we are able to observe improved results of both temperatures as compared to experimental results. The GC-SAFT-VR+D approach, like all analytical equations of state, does not consider the long-range density fluctuations that occur in the critical region. Therefore, we observe deviations near the critical region.

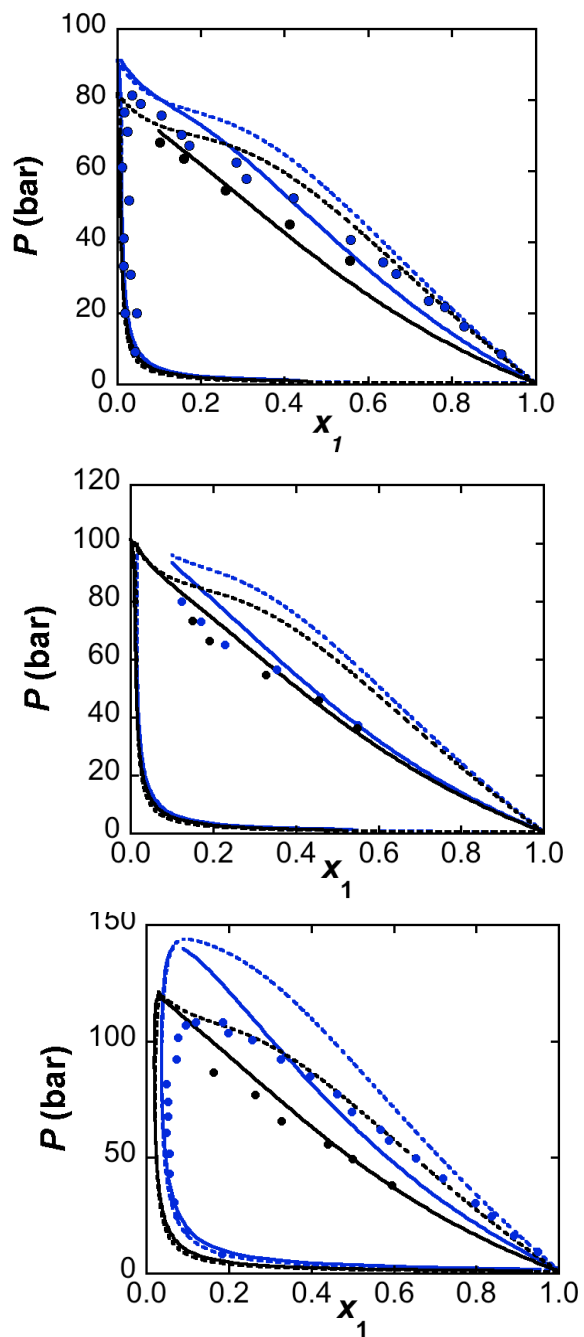


**Figure 8.6:**  $Px$  slices of the  $\text{CO}_2 + n\text{-hexane}$  phase diagrams at different temperatures a.)  $T = 308.15$  K (black lines),  $313.15$  K (blue lines), b.)  $T = 318.15$  K (black lines),  $323.15$  K (blue lines), c.)  $T = 333.15$  K (black lines), and  $353.15$  K (blue lines). (bottom to top) Solid lines correspond to GC-SAFT-VR+D predictions, Dashed lines correspond to original SAFT-VR predictions using parameters proposed by Blas *et al.* and Colina *et al.*, [19].

In Figure 8.7, the phase behavior of the carbon dioxide +  $n\text{-heptane}$  mixture is predicted at  $T = 310$  K and  $353$  K. As can be seen from the figure, utilizing the new model for  $\text{CO}_2$ , we show an improvement in the liquid phase results as compared to the original SAFT-VR predictions. Again we note these results were obtained by using only one fitted cross interaction.

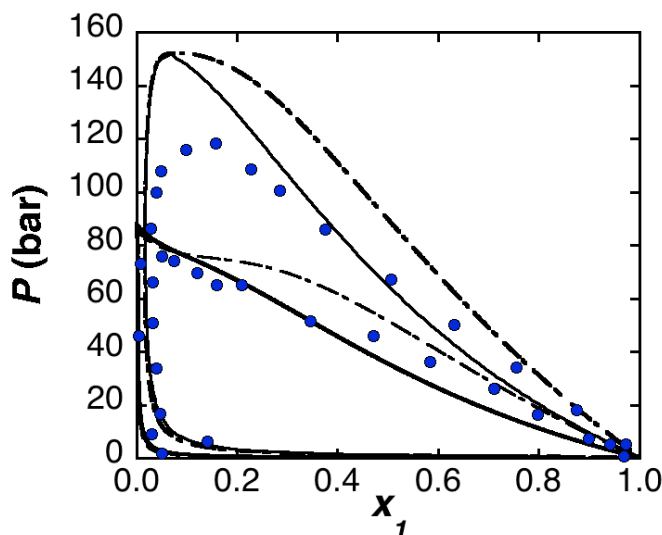


**Figure 8.7:**  $Px$  slices of the  $\text{CO}_2 + n\text{-heptane}$  phase diagrams at  $T = 310$  K and  $353$  K. (bottom to top) . Solid lines correspond to GC-SAFT-VR+D predictions, Dashed lines correspond to original SAFT-VR predictions using parameters proposed by Blas *et al.*

In Figure 8.8, we present GC-SAFT-VR +D predictions for the  $\text{CO}_2 + n\text{-octane}$  systems at  $T = 308$  K,  $318$  K,  $333$  K, and  $343$  K. Exhibiting type II phase behavior, this mixture is expected to exhibit non-ideal characteristics. The transferable parameters proposed by Blas *et al.* [18], shown as dashed lines in Figure 8.8, provide good agreement with experimental data obtained at low carbon dioxide compositions, however, as mole fractions of carbon dioxide increase, deviations increase. These deviations are likely due to cross interactions being optimized to molecular parameters, which were rescaled to experimental results from the critical region. However, by using the parameters proposed in this work (shown as the solid lines in Figure 8.8) better agreement with experimental results are observed. We note only a single, transferable,

cross-range parameter is required when the new CO<sub>2</sub> model is utilized term is considered, whereas a cross-energy parameter is also needed with the original SAFT-VR approach.

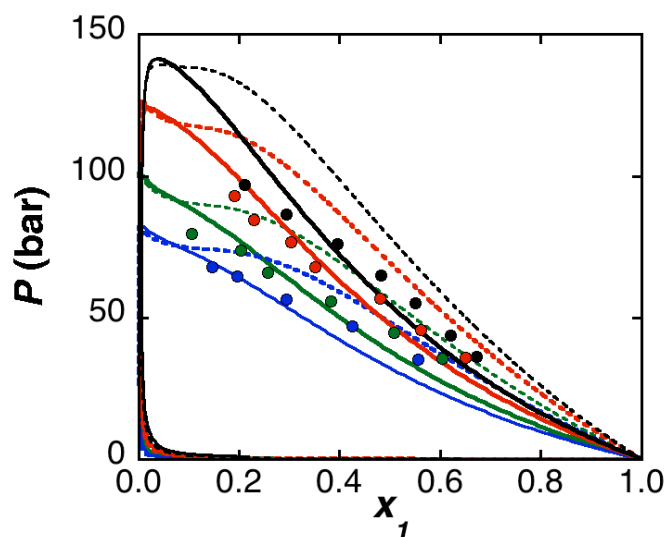


**Figure 8.8:**  $Px$  slices of the CO<sub>2</sub> +  $n$ -octane phase diagrams at  $T = 308$  K, 318 K, 333 K, and 343 K. (bottom to top). Solid lines correspond to GC-SAFT-VR+D predictions, Dashed lines correspond to original SAFT-VR predictions using parameters proposed by Blas *et al.*, symbols correspond the experimental data[19].

Finally, the phase behavior of CO<sub>2</sub> +  $n$ -decane and CO<sub>2</sub> +  $n$ -dodecane are predicted and compared to results from the original SAFT-VR approach. In Figure 8.9a and 8.9b, we present isothermal vapor liquid equilibrium results using both the GC-SAFT-VR +D approach and the original SAFT-VR approach. The phase behavior of CO<sub>2</sub> +  $n$ -decane mixtures is studied at  $T = 308.15$  K and 313.15 K. Both theories are able to capture the curvature and pure limits of this mixture. However, as can be seen in Figure 8.9b, considering the CO<sub>2</sub> +  $n$ -dodecane mixture ( $T = 312$  K), the results from the GC-SAFT-VR +D approach show slightly better agreement with experimental results.

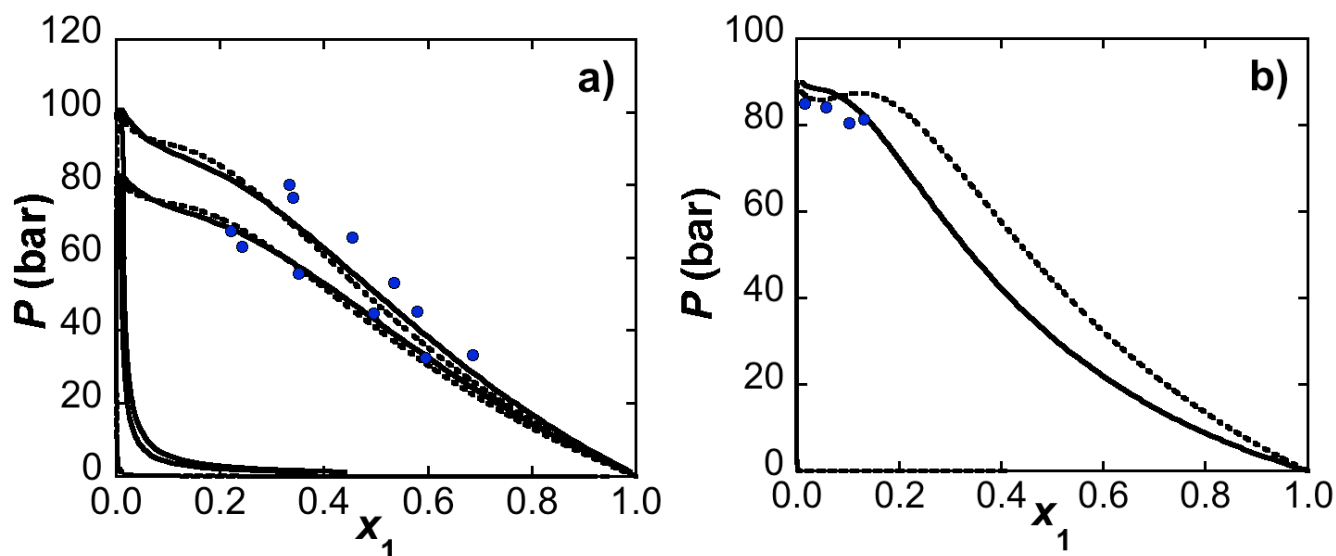


**Figure 8.9:** a.)  $P$ - $x$  slices of the  $\text{CO}_2 + n$ -decane phase diagrams at  $T = 308.15$  K and  $313.15$  K. b.)  $P$ - $x$  slices of the  $\text{CO}_2 + n$ -dodecane phase diagrams at  $T = 312$  K. Solid lines correspond to GC-SAFT-VR+D predictions, Dashed lines correspond to original SAFT-VR predictions using parameters proposed by Blas *et al.*

### Nitrogen + Alkanes

In the work of Zhao *et al.* [191], the SAFT-VR theory is extended to include a quadrupolar contribution to the free energy using a Pade-approximation term derived from perturbation theory. In mentioned work, nitrogen is described as a chain molecule with a net point axial quadrupole moment located at the center of the molecule. To test our proposed model and to determine if including the quadrupolar interactions in the structure of the molecule improves the SAFT predictions, the phase behavior of nitrogen + alkane mixtures are investigated using the original SAFT-VR, SAFT-VR + Quadrupole, and GC-SAFT-VR +D (this work) approach. To determine the nitrogen parameters, the dipole moment is fit to experimental vapor pressure and saturated liquid density data. The model parameters ( $\sigma$ ,  $\epsilon$ ,  $\lambda$ , and  $m$ ) are taken from the original SAFT approach for the nitrogen molecule. Using this model, deviations in pressure and saturated liquid density are found to be 0.073 % and 0.39%, respectively. We have examined the constant temperature  $p$ - $x$  slices of the phase diagrams for nitrogen + pentane ( $T = 277.43$  K), methane+ nitrogen ( $T = 95$  and  $113.7$  K), butane + nitrogen ( $T = 250$  K), and heptane + nitrogen ( $T = 305.4$  K) binary mixtures. As can be observed in Figure 8.10 below, results utilizing the GC-SAFT-VR +D theory are found to improve results of predictions and utilizing less fitted parameters.



**Table 8.2:** Intermolecular Parameters for Nitrogen

$m$	$\lambda$	$\varepsilon/k_B$ (K)	$\sigma$ (Å)	$\mu$
1.33	1.55	81.4851	3.1588	0.31

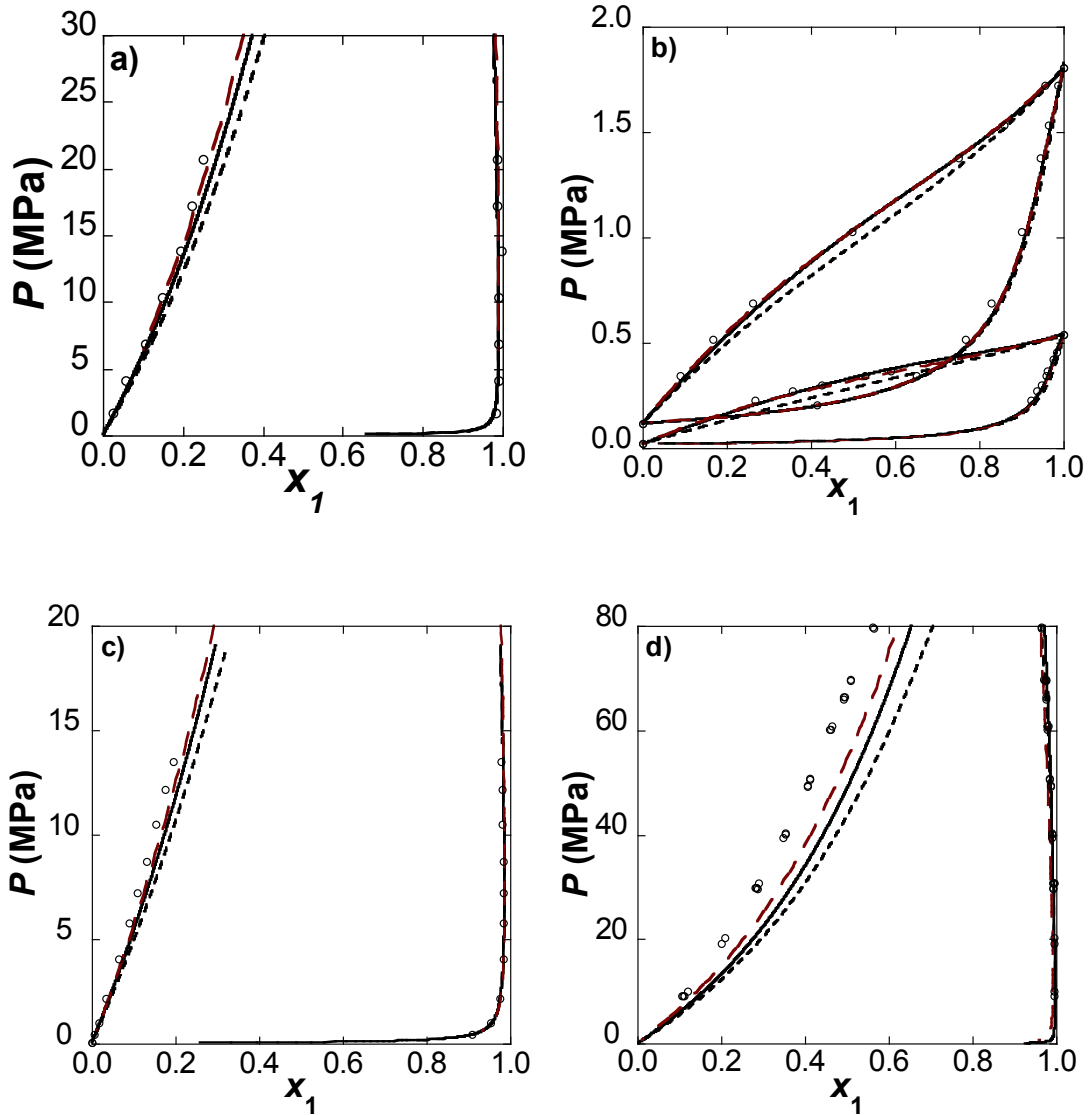


**Figure 8.10:** a.) Constant temperature  $p$ - $x$  slices of the phase diagram for the nitrogen (1) + pentane (2) + binary mixture at 277.43 b.) Constant temperature  $p$ - $x$  slices of the phase diagram for the methane (1) + nitrogen (2) binary mixture at 95 and 113.7 K (from bottom to top). c.) Constant temperature  $p$ - $x$  slices of the phase diagram for the butane (1) + nitrogen (2) binary mixture at 250 K, d.) Constant temperature  $p$ - $x$  slices of the phase diagram for the heptane (1) + nitrogen (2) binary mixture at 305.4 K. The continuous curves correspond to predictions from the quadrupolar SAFT-VR approach, red dashed lines correspond to predictions from GC-SAFT-VR + D theory, and the dashed curves, predictions from the original SAFT-VR equation. The circles are experimental results.

### **Carbon Dioxide + Perfluoroalkanes**

The isothermal phase behavior of carbon dioxide and perfluorohexane mixtures are studied at five temperature slices, shown in Figure 8.11. As can be seen from the results, better representation is observed with the addition of the quadrupolar interactions in the structure of the molecule as opposed to explicitly defining such interaction in an effective way through the square well. This mixture was also studied in the work of Tochigi *et al.* [19], in mentioned work the cross interactions proposed by Colina *et al.* were found to inadequately predict the phase diagram of carbon dioxide and perfluorohexane, thus a new cross interaction was fitted to experimental data at 303.15 K. Similar results are obtained in our study, however, results obtained in this work represent predictions.

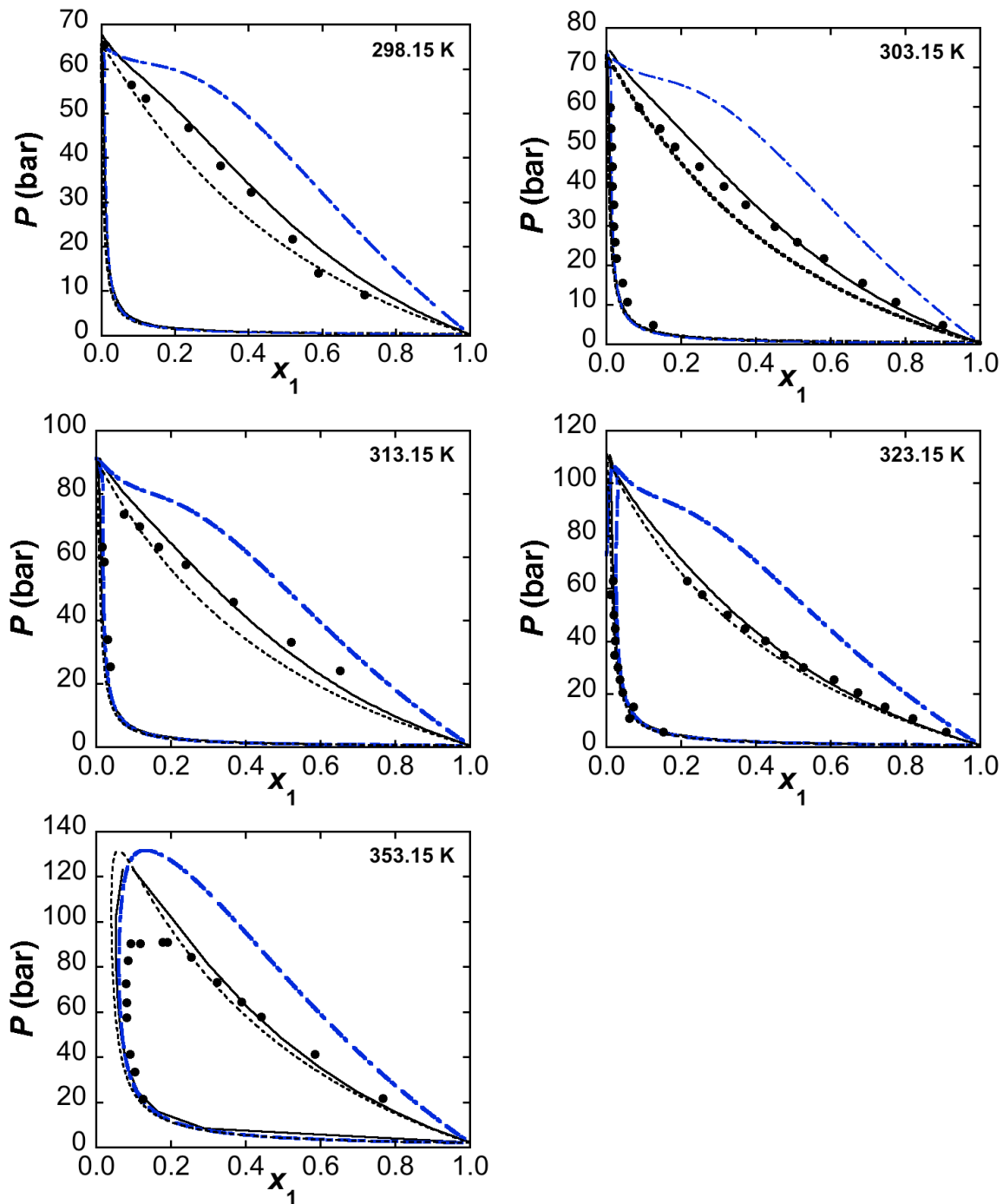


**Figure 8.11:**  $Px$  slices of the CO<sub>2</sub> + perfluorohexane phase diagrams at  $T= 298$  K, 303 K, 313.15 K, 323.15 K, and 353.15 K. Solid lines correspond to GC-SAFT-VR+D predictions, Dashed lines correspond to original SAFT-VR predictions using parameters proposed by Tochigi *et al.* [19] Blue Dashed lines correspond to original SAFT-VR predictions using parameters proposed by Colina *et al.*, symbols correspond the experimental data[19].

The isothermal phase behavior of carbon dioxide and perfluorooctane mixtures are studied at five temperature slices, shown in Figure 8.12. In the work of Dias *et al.*, this mixture was studied using the soft-SAFT + Quadrupole approach. In this work, Dias *et al.* introduced a polar term to the original soft-SAFT equation of state. An expansion of the Helmholtz free energy in terms of the perturbed quadrupole- quadrupole potential with the Padé approximation is implemented in the theory. Dias *et al.* found the explicit definition of the quadrupole did not significantly influence the description of the phase behavior of mixtures for non-aromatic molecules such as perfluorooctane, requiring the use of fitted binary interaction parameters. However, in our proposed model, we find that by inclusion of the quadrupolar interactions in the structure of the CO<sub>2</sub> molecule as well as to the Helmholtz free energy provides a better representation of the experimental. In comparison to both the work of Dias *et al.* and the original SAFT-VR approach we see better agreement with experimental data, especially at higher temperatures.

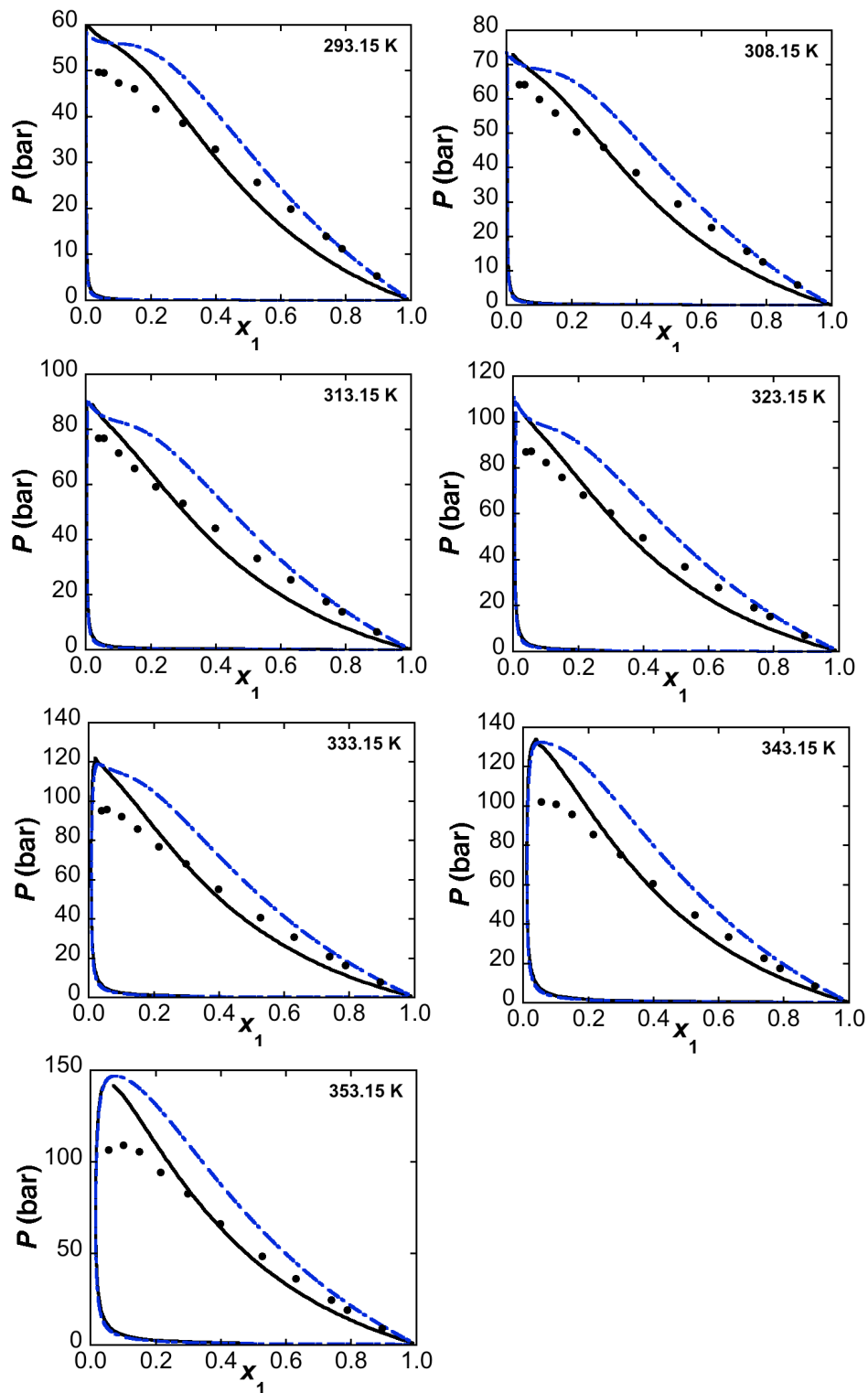


**Figure 8.12:**  $Px$  slices of the  $\text{CO}_2$  + perfluorooctane phase diagrams at  $T= 293$  K, 303 K, 313.15 K, 323.15 K, 333.15 K, 343.15 K, and 353.15 K. Solid lines correspond to GC-SAFT-VR+D predictions, Blue Dashed lines correspond to original SAFT-VR predictions using parameters proposed by Colina *et al.*, symbols correspond the experimental data[19].

## Conclusion

The GC-SAFT-VR equation of state was extended to account for quadrupolar interactions using the generalized mean spherical approximation (GMSA) to describe a reference fluid of dipolar square-well segments to describe the carbon dioxide molecule. By implementing one dipole moment in each segment of carbon dioxide, the quadrupole moment is approximated. The GC-SAFT-VR+D approach was then applied to predict the phase diagrams of binary mixtures of alkanes and perfluoroalkanes with carbon dioxide and compared directly with the original SAFT-VR equation and with experimental results. The GC-SAFT-VR+D equation is found to be in better agreement with experimental data. Moreover, only a single, transferable, cross-range parameter is required when the quadrupolar term is considered, whereas a cross-energy parameter is also needed with the original SAFT-VR approach. This cross-range parameter can be fitted to a single system and successfully used to predict the phase behavior of other binary mixtures without additional fitting. Further, we have compared our approach to the results found in the work of Zhao *et al.*, where the SAFT-VR theory is extended to include a quadrupolar contribution to the free energy using a Pade-approximation term derived from perturbation theory. By implementing the model developed for carbon dioxide for the study of Nitrogen + alkane mixtures, we see improvement of results as compared to the work of Zhao *et al.* Finally, we study the carbon dioxide and perfluoroalkane mixtures, where again only a single, transferable, cross-range parameter is required, as opposed to the original SAFT-VR approach where a cross-energy parameter is also needed. We can therefore conclude that inclusion of the quadrupolar interaction into the GC-SAFT-VR equation, specifically in the chain term, improves the predictive ability of the SAFT-VR EOS when studying the phase behavior of alkane + carbon dioxide systems and reduces the need to use effective parameters by explicitly including at the molecular and structural level interactions due to the quadrupole moment.

## Chapter IX

### Examining the Aggregation Behavior of Polymer Grafted Nanoparticles Using Molecular Simulation and Theory

#### Introduction

The aggregation and dispersion of nanoparticles can have a significant impact on system behavior, such as enhancing physical, electrical, or optical properties [201]. Understanding what controls the aggregation and dispersion of nanoparticles is also important to the development of self-assembled functional nanomaterials and must be fundamentally understood to effectively control and tune the targeted properties [202]. Grafting polymers directly to a nanoparticle is one known approach used to control self-assembly [203-215] and alter the physical and mechanical properties of the materials (e.g., critical point, melting point, solubility, strength, and ductility) [216-218]. For example, grafted buckyball systems have been observed to provide up to a 3 order of magnitude increase in fracture toughness as compared to the polymers alone [219] and ionic-liquid grafted zirconia nanoparticles have been shown to provide excellent mechanical, electrochemical, and thermal stability for use in Li-ion batteries [220]. The tunable nature of grafted nanoparticles has been leveraged to enhance carbon dioxide capture [221], and similarly, supercritical carbon dioxide has been used to improve the dispersion of nanoparticles in a polymer matrix [222]. Thus, changing the interactions of both the nanoparticle and polymer constituents, as well as the solvent matrix, can result in significant changes to the structure and properties of the system [216] [223-226], which can be used to tune the resulting behavior.

Molecular simulation has played an important role in understanding, and thus predicting, the behavior of TNPs. Simulations have been used to propose design rules for the formation of a variety of complex phases in dense nanoparticle systems [215-218] [227-238], although less emphasis has been placed on developing design rules to control the fundamental aspects of aggregation versus dispersion [225, 239, 240]. While TNPs allow for many ways in which behavior can be tuned and controlled, it also creates a vast parameter landscape that is computationally expensive to explore via brute-force computation. Instead, a convenient and informative approach to explore this parameter landscape is to study changes to the fluid phase equilibria that result from changes to the TNP architecture, interactions, solvent properties, etc. For example, changes to the critical temperature,  $T_c$ , that result from parameter changes provides information on the characteristic interaction energy between TNPs, e.g., a decrease in  $T_c$  indicates a reduction in effective interaction strength between TNPs. Additionally, the coexistence envelope specifically identifies the TNP phase (i.e., aggregated versus dispersed fluid versus dense fluid)

and also identifies which system parameters can be used to tune this behavior via examination of the changes in critical density. The coexistence envelope also provides information regarding the TNP solubility that results from solvent-TNP interactions.

Previous molecular dynamics (MD) simulation studies of pure nanoparticle systems have demonstrated a strong dependency of the fluid phase equilibrium behavior of the system on the interaction potential between the nanoparticles [112], e.g., the critical temperature and density were found to increase with increasing nanoparticle diameter where interactions become increasing shorter ranged (relative to particle diameter) as nanoparticle diameter is increased. An alternative technique to using molecular simulation is to apply a theoretical approach such as the statistical associating fluid theory (SAFT) [39, 40, 45]. An advantage of utilizing SAFT for thermodynamic calculations is the significant increase in speed as compared to molecular simulations, allowing a greater number of systems as well as larger molecules to be studied efficiently. Since the development of the original SAFT approach, numerous versions of SAFT have been proposed and applied to study a wide range of systems [241]. Of particular relevance is the SAFT-VR equation of state, which describes chain molecules formed from hard-core segments that interact via attractive potentials of variable range (VR) [46]. SAFT-VR has been applied to study the thermodynamics and phase behavior of a diverse group of fluids (from hydrocarbons [76, 242, 243] to polymers[244] and electrolytes [245, 246]), including polymer tethered silica nanocubes [85] using the hetero-SAFT-VR approach [127]. Hetero-SAFT-VR allows the description of molecules formed from chains of tangentially bonded segments of different size and/or energy parameters rather than a homonuclear chain as in the SAFT-VR approach and is the basis of a more general heteronuclear group-contribution approach (GC-SAFT-VR)[48]. For example, using the hetero-SAFT-VR approach to study silica nanocubes [247], a reduction in critical temperature and critical density was observed as graft length was increased for systems with a single graft alkyl chain, while a reduction in critical density was observed as the number of grafts was increased.

These prior works, using simulation and theory, lay the foundation for understanding the ways in which the aggregation behavior of TNPs can be controlled through nanoparticle interactions, polymer grafting, and solvent interactions. Here we explore this further through a combination of Brownian dynamics simulations using the volume-quench dynamics (QD) technique [112] and the hetero-SAFT-VR calculations to explore a coarse-grained model of a TNP. Specifically, the aggregation and dispersion behavior of a model polymer tethered silica nanoparticle system is explored with Brownian dynamics simulations for pure TNP systems, while the hetero-SAFT-VR approach is used to study pure TNPs and TNP systems in solvent.



The coexistence behavior for each system studied is calculated and used to provide an efficient means to quantify the behavior of TNPs as a function of graft length, graft density, and solvent interactions.

## Simulation Model and Methodology

### *Simulation Model*

In this work, a coarse-grained (CG) representation of TNPs is considered, generic enough to be widely applicable, but with interaction strengths directly relatable to experiments; the simulation model was also chosen such that it lends itself well to SAFT calculations. Here, parameters for silica are used to model the nanoparticle and parameters for alkanes are used to model the polymer tethers. Since the goal is to examine the behavior of a generic TNP system with realistic interactions, we present all results in reduced units, scaled relative to the characteristic values of a CH<sub>3</sub> pseudo atom. As such the silica nanoparticles are represented by a single spherically symmetric site with diameter  $\sim 1$  nm; following reference [248]. The nanoparticles are assumed to be composed of a spherical Si<sub>6</sub>O<sub>12</sub> particle that interacts via a 12-6 Lennard-Jones (LJ) potential with  $\sigma = 6.2$  Å and  $\varepsilon/k_B = 1560$  K. This interaction strength is similar in magnitude to the well depth of  $\varepsilon/k_B \sim 1000$  K computed for  $\sim 1$  nm silica cubes in Chan et al. [249] using density functional theory. To provide a good approximation of the polymer interactions relative to the nanoparticles, tethers are modeled using a united-atom model, with interactions taken from the TraPPE force fields for alkyl chains developed by Martin and Siepmann [250], as this forcefield was developed to provide accurate predictions of the phase coexistence. CH<sub>2</sub> pseudo atoms in the alkyl chain are modeled as a Lennard-Jones sphere with  $\sigma = 3.95$  Å and  $\varepsilon/k_B = 46.0$  K. CH<sub>3</sub> pseudo atoms that terminate the polymer graft are also modeled as Lennard-Jones spheres with  $\sigma = 3.75$  Å and  $\varepsilon/k_B = 97.94$  K. We note that the epsilon parameters for nanoparticle-nanoparticle interactions are  $\sim 34$  times stronger than between two CH<sub>3</sub> pseudo atoms. For comparability with SAFT, the polymer grafts are free to move around the surface of the nanoparticle; the separation between the first bead (attached to the nanoparticle) and the center-of-mass of the nanoparticle is set to 1.54 Å via a stiff harmonic spring. Cross interactions are calculated using standard Lorentz-Berthelot [105] combining rules, *viz*

$$\sigma_{ij} = \frac{\sigma_{ii} + \sigma_{jj}}{2} \quad (9.1)$$

$$\varepsilon_{ij} = \xi_{ij} \sqrt{\varepsilon_{ii} \varepsilon_{jj}} \quad (9.2)$$

where  $\xi_{ij} = 1.0$ . Interactions between polymer beads were cut off at  $10\text{\AA}$  and nanoparticle-nanoparticle interactions at  $15\text{\AA}$ ; XPLOR style shifting starting at  $0.5\text{\AA}$  prior to the cut off was used to ensure that the well depth was not altered (i.e., a cubic spline is used to smooth the value to zero). Angles and dihedrals follow Martin and Siepmann [250] and bonds are treated as harmonic springs with spring constant taken from OPLS-AA [251] parameters for C-C bond interactions in alkanes, rather than using a fixed separation as in the original force field.

### *Simulation Method*

In all cases, simulations were performed at constant number of particles  $N$ , volume  $V$ , and temperature  $T$  (NVT), using the Langevin thermostat in the GPU-enabled HOOMD-Blue simulation package [247] for systems with 1000 tethered nanoparticle building blocks, where the number of grafts and length of the grafts is systematically varied to probe the trends, ranging from a single graft to six grafts and from as short as 2 to 18 beads per graft. Systems were initially equilibrated as fluid states (i.e., single phase), in boxes with aspect ratio 2:1:1. This ratio was used to provide sufficient contrast between the liquid and vapor phases in the quench dynamics approach, as discussed below.

The fluid phase equilibrium was calculated using the volume-quench dynamics (QD) technique [112]. Both temperature and volume QD have been used to reproduce the VLE of LJ particles [115] and investigate the behavior of model nanoparticle systems [112]. This QD method has also been used to investigate the saturated liquid densities of the Gaussian charge polarizable water model and the results were found to be in good agreement with those calculated using Gibbs ensemble Monte Carlo simulations and reported experimentally [116].

The basic algorithm involves initializing the system as a single fluid phase with periodic boundary conditions and then quenching the system into the coexistence regime by rapidly increasing the box length in one direction (in this case the  $x$  direction). The length in the  $x$  direction was chosen to be at three times the size of the dense phase to minimize effects of the interface and ensure high- and low-density phases can equilibrate. The rapid density change provides a strong thermodynamic driving force, which allows for the formation of a two-phase system at coexistence. The system is then allowed to reach equilibrium, as indicated by convergence of the potential energy and density histogram, as a function of time. Since the free energy minimization is done by the system through the reduction of the interfacial area, the interfacial region will tend to remain planar, allowing the two regions to be clearly defined and the density histogram of each of the phases to be calculated. This general procedure is performed several times over a range of temperatures and the following relationships are then used to fit the fluid phase equilibrium data [117], *viz*

$$\frac{1}{2}(\rho_L - \rho_V) = \rho_c + C_1(T - T_c) \quad (9.3)$$

$$\rho_L - \rho_V = C_2(T_c - T)^\beta \quad (9.4)$$

Here,  $\rho_l$  and  $\rho_v$  are the high and low densities respectively,  $C_1$ ,  $C_2$ , and  $\beta$  are fitting parameters, and  $\rho_c$  and  $T_c$  are the critical density and critical temperature of the system respectively.  $\beta$  is assumed to be 0.32 and is not a free parameter in the fitting [118]; 0.32 is used rather than 0.5 as the simulations do provide the correct non-analytical scaling behavior near the critical point. Thus, the phase coexistence can be calculated for these complex building blocks in a relatively efficient manner and the information used to develop general trends without the costly sampling of very large regions of phase space. A schematic representation of the QD technique is provided in Figure 9.1.

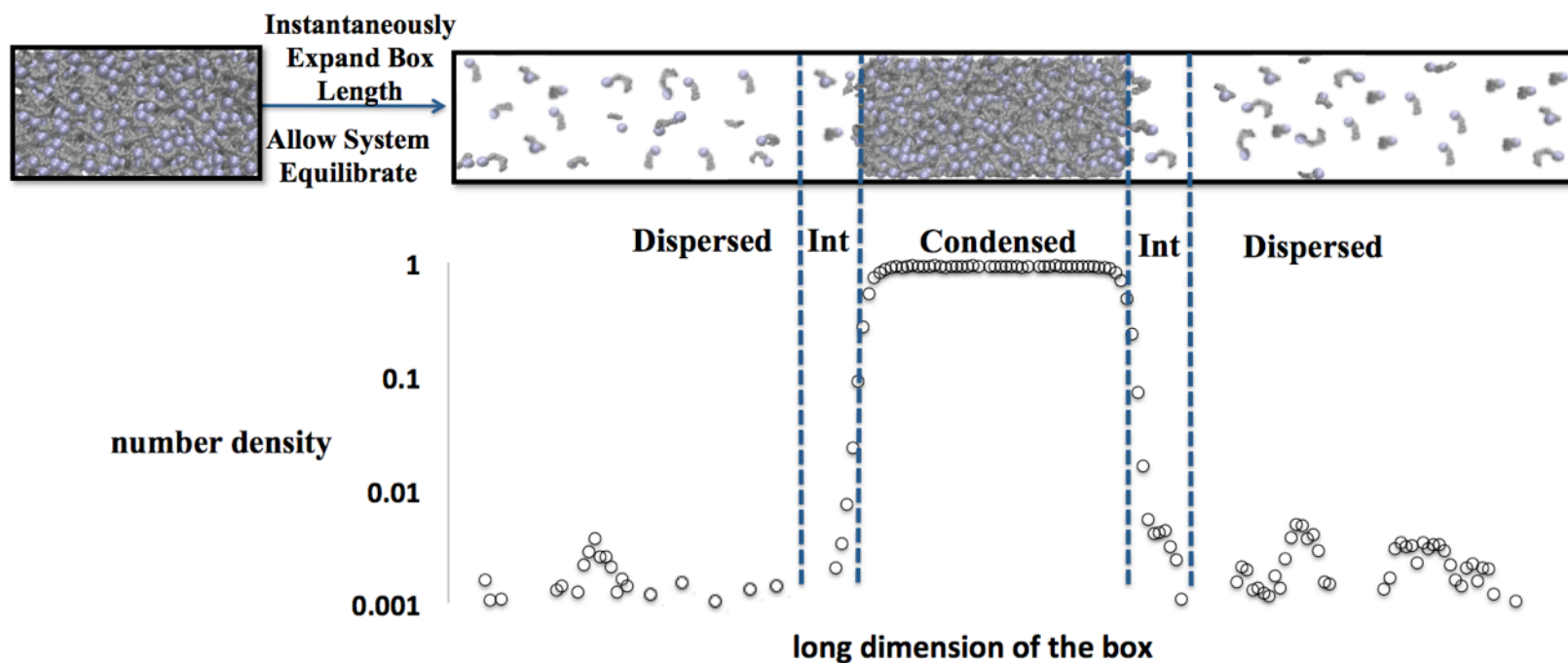


**Figure 9.1.** Schematic representation of the quench dynamic method, shown for 1000 TNP building blocks, each with a single 12 bead tether (13000 total particles). A bulk fluid state is first equilibrated. Next, the length of the box is instantaneously expanded and allowed to equilibrate, resulting in a two-phase system at coexistence. A histogram of the number density is constructed along the long dimension of the box; the average density of the dispersed and condensed phases is then computed from the respective regions of the histogram, taking care to exclude the interfacial region.

## Hetero-SAFT-VR

The hetero-SAFT-VR approach allows molecules to be described as chains of tangentially bonded segments that can have different size and/or energy parameters that interact through an attractive potential of variable range [76, 85, 86]. In earlier work, the hetero-SAFT-VR approach was validated using isothermal-isobaric ( $NPT$ ) and Gibbs ensemble Monte Carlo (GEMC) simulation data and shown to successfully capture the effects of interaction energy, segment size, and molecular structure on the PVT and phase behavior of hetero-nuclear diblock fluids [76, 85, 87]. In this work, the hetero-SAFT-VR approach allows us to model alkyl tethered nanospheres as a single nanosphere connected to several smaller segments that describe the alkyl tethers. Each segment in the model interacts through a square well potential,

$$u_{ki,lj}(r) = \begin{cases} +\infty & \text{if } r < \sigma_{ki,lj} \\ -\varepsilon & \text{if } \sigma_{ki,lj} \leq r \leq \lambda_{ki,lj}\sigma_{ki,lj} \\ 0 & \text{if } r > \lambda_{ki,lj}\sigma_{ki,lj} \end{cases} \quad (9.5)$$

where  $\sigma_{ij}$  is the segment diameter,  $\varepsilon_{ij}$  the well depth of the square well potential,  $\lambda_{ij}$  the potential range, and  $r$  is the distance between the two segments. The inter- and intra- molecular cross interactions between segments can be obtained from the Lorentz-Berthelot [105] combining rules expressed in equations 9.1 and 9.2 for interaction diameter and well depth. The cross range parameter is obtained using the arithmetic mean given by, equation 9.6:

$$\lambda_{ij} = \gamma_{ij} \frac{\lambda_{ii}\sigma_{ii} + \lambda_{jj}\sigma_{jj}}{\sigma_{ii} + \sigma_{jj}} \quad (9.6)$$

In the hetero-SAFT-VR approach the Helmholtz free energy is expressed as the sum of the contributions from the ideal  $A^{\text{ideal}}$ , the segment-segment (monomer)  $A^{\text{mono}}$ , chain  $A^{\text{chain}}$ , and association  $A^{\text{assoc}}$  interactions. The expressions for  $A^{\text{assoc}}$  are not included in this work since the systems studied are not associating fluids.

$$\frac{A}{Nk_B T} = \frac{A^{\text{ideal}}}{Nk_B T} + \frac{A^{\text{mono}}}{Nk_B T} + \frac{A^{\text{chain}}}{Nk_B T} + \frac{A^{\text{assoc}}}{Nk_B T} \quad (9.7)$$

Since the theory has been well documented [87, 127] only a brief description of the main expressions are provided below.

The ideal Helmholtz free energy is given by,

$$\frac{A^{\text{ideal}}}{NkT} = \ln(\rho\Lambda^3) - 1 \quad (9.8)$$

where  $\rho$  is the number density of chain molecules,  $N$  is the total number of molecules,  $k$  Boltzmann's constant, and  $\Lambda_k$  the thermal de Broglie wavelength.

The monomer free energy is expressed as

$$\frac{A^{mono}}{NkT} = ma^M = m \left( a^{HS} + \frac{a_1}{k_B T} + \frac{a_2}{(k_B T)^2} \right) \quad (9.9)$$

where  $m$  is the number of segments per molecule,  $a^M$  is the free energy per monomer segment, which in turn is given in terms of the free energy of the hard-sphere reference fluid ( $a^{HS}$ ), and the first ( $a_1$ ) and second ( $a_2$ ) perturbation terms associated with the attractive interactions,  $u_{ij}(r)$ . Finally, the free energy due to chain formation from monomer segments is given in terms of the background correlation function  $y_{ij}^{SW}$  as,

$$\frac{A^{chain}}{NkT} = - \sum_{ij\_bonds} \ln y_{ij}^{SW}(\sigma_{ij}) \quad (9.10)$$

where the sum is over all bonds in the chain molecule and for a diblock system as in this work becomes,

$$\frac{A^{chain}}{NkT} = -N_t [\ln y_{12}^{SW}(\sigma_{12}) + (m_2 - 1) \ln y_{22}^{SW}(\sigma_{22})] \quad (9.11)$$

where  $N_t$  is the number of tethers per molecule and  $m_2$  is the number of alkyl segments per tether.

Given that the silica nanoparticle is represented as a LJ sphere in the simulation model, the hetero-SAFT-VR parameters for nanoparticles are determined by fitting to pure LJ VLE data obtained from the grand canonical transition - matrix Monte Carlo simulation method with histogram re-weighting over a reduced temperature range of 0.70 to 1.20 at increments of 0.05, reported in Ref. [252]. The percentage absolute average deviation of the liquid density and vapor density (shown in equation 9.12 and 9.13), AADL and AADV respectively, were minimized. The resulting parameters for the bare  $\text{Si}_6\text{O}_{12}$  nanoparticle were determined to be  $\sigma = 6.977$ ,  $\varepsilon/k_B = 1507$  K,  $\lambda = 1.554$  and  $m = 1.0$  with AADL = 0.467% and AADV = 6.45%. Comparing to the work of Peng [85] for a similar silica nanoparticle model, the potential used here is slightly shorter ranged ( $\lambda = 1.554$  compared to 1.8) and slightly stronger ( $\varepsilon/k_B = 1507$  compared to 815.5K).

$$AADP(\%) = \frac{1}{N_{pt}} \sum_{i=1}^{N_{pt}} \left| \frac{P_i^{theo} - P_i^{exp}}{P_i^{exp}} \right| \times 100\% \quad (9.12)$$

$$AAD L\%) = \frac{1}{N_{pt}} \sum_{i=1}^{N_{pt}} \left| \frac{\rho_i^{theo} - \rho_i^{exp}}{\rho_i^{exp}} \right| \times 100\% \quad (9.13)$$

The parameters for the alkyl tethers were taken from the linear expressions for the alkane homologous series provided by McCabe and Jackson [76]. For interactions between the alkyl segment and Si<sub>6</sub>O<sub>12</sub> nanoparticles, the well depth of the square-well potential was scaled by  $\zeta = 1.1$  and the range scaled by  $\gamma = 0.95$  as these parameters were found to provide better agreement between the coexistence behavior predicted by theory and simulation for a mono-tethered 12 bead system, although we note that combining rules (i.e.,  $\zeta = 1$  and  $\gamma = 1$ ) predict the same trends. The hetero-SAFT-VR approach will henceforth be referred to as SAFT for convenience.

To model systems with solvent, SAFT parameters have been taken from previous work [18, 76, 244] for several solvents of interest. Here solvents are chosen that range from weakly interacting, such as nitrogen and carbon dioxide, to more strongly interacting ethylene and propane, where it is noted that carbon dioxide is widely used as a solvent for nanoparticles as part of the rapid expansion supercritical solutions (RESS) approach [253-255]. The solvent parameters are given in Table 9.1 below.

**Table 9.1.** Solvent parameters used in the SAFT predictions.

	$\sigma$ (Å)	$\lambda$	$\varepsilon/k_B$ (K)	$m$	<i>Ref.</i>
Nitrogen	3.159	1.55	81.5	1.33	[191]
Carbon Dioxide	2.786	1.52	179.3	2.00	[18]
Ethylene	3.743	1.45	236.1	1.20	[244]
Propane	3.873	1.45	261.9	1.67	[76]

## Results

### *Pure TNP systems*

The fluid phase equilibrium of the pure TNP systems was calculated using both the simulation-based QD approach and the SAFT-based approach. The fluid phase equilibrium is calculated as a function of the number of tethers in Figures 9.2a and 9.2b for QD and SAFT, respectively, for a fixed “composition” where in all cases 1000 total TNP building blocks were used (13000 total particles). That is the systems are fixed such that there are a total of 12 polymer beads; the only

significant difference is the topological distribution of the polymer beads. For example, a di-tethered ( $N_{GRAFT} = 2$ ) system with 12 total beads corresponds to a system where the lengths of the two tethers are fixed at 6 beads each whereas, a quad-tethered ( $N_{GRAFT} = 4$ ) system with 12 total beads corresponds to a system where the lengths of the four tethers are fixed at 3 beads each. Both approaches provide close agreement, e.g., a mono-tethered nanoparticle system with 12-carbon chains results in  $T^* = 32.19$  for QD, as compared to  $T^* = 33.97$  from SAFT; exact agreement is not expected given that SAFT exhibits classical behavior in the critical region rather than the non-analytical [151, 152], singular behavior seen experimentally and in QD. A simulation snapshot of the TNP system with a single 12-bead chain in coexistence is shown in Fig. 9.1. Matching trends are also observed, where a clear reduction in critical temperature is observed as the number of grafts is increased. Calculations of the potential of mean force (PMF) (i.e., inversion of the radial distribution function (RDF)) of the nanoparticles at low density (i.e., in the dispersed phase), shown in Figure 9.3, illustrate a transition from an effectively attractive to repulsive potential as the number of grafts are increased, consistent with prior work [230]; as the number of grafts are increased, the strong nanoparticle-nanoparticle interactions are shielded causing a decrease in the critical temperature, and, as such, changing the number of grafts effectively changes the interaction strength between the nanoparticle building blocks. Only minimal changes to the critical density are observed as the number of grafts are changed, which appears to be related to the overall conservation of building block composition.

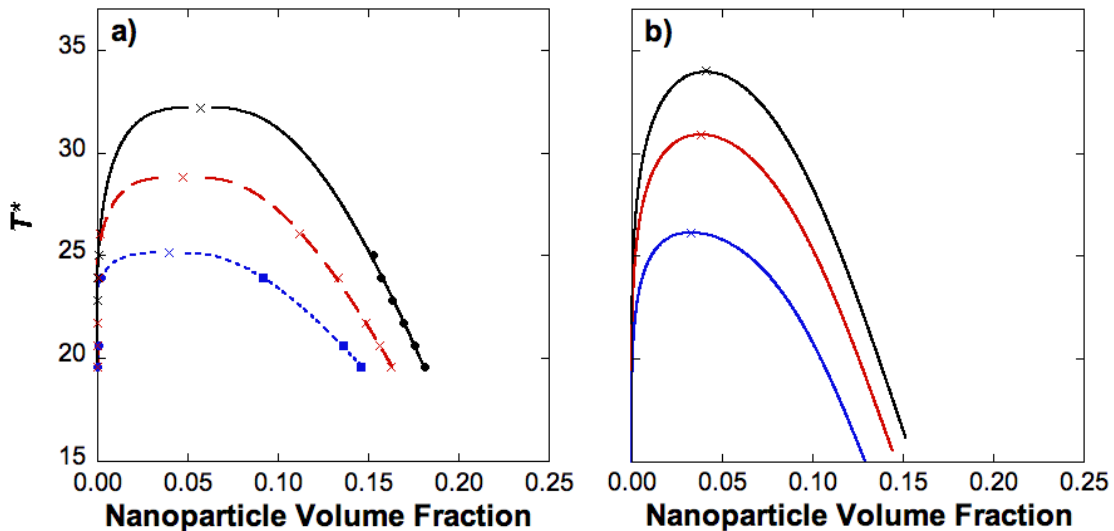


**Figure 9.2.** (a) Fluid phase equilibrium of alkane-tethered nanoparticle systems for 12 bead systems with  $N_{GRAFT} = 1$  and 12 beads (black),  $N_{GRAFT} = 2$  and 6 beads per tether (red), and  $N_{GRAFT} = 4$  and 3 beads per tether (blue). Symbols represent the simulation results and in (a) lines correspond to predictions using rectilinear and scaling laws and (b) the SAFT predictions.



In Figures 9.4a and 9.4b, the fluid phase equilibrium of a mono-tethered ( $N_{GRAFT} = 1$ ) system is presented for various graft lengths (8 – 48 beads), as predicted by QD and SAFT, respectively. Due to the efficiency of SAFT calculations as compared to QD, chains of 100 beads are also considered with SAFT. As can be seen from the figure, for both methods, as the length of the graft increases, both the critical temperature and density decrease, consistent with the work of Peng for grafted silica nanocubes [85]. This trend in critical temperature for the TNPs is the inverse of what is seen for pure alkanes, where critical temperature increases with increasing chain length [76]. The decrease in critical temperature with increasing chain length is consistent as the number of grafts attached to the nanoparticle is increased to two, as shown in Figures 9.4c and 9.4d; however, the shift is less significant than was seen for the single graft system. In both cases, an increase in the graft length reduces the region where coexistence is observed with respect to density, providing a wider range where pure component systems are observed and thus a reduction in the regime where aggregates form. However, for systems with a higher grafting density, such as the quad tethered ( $N_{GRAFT} = 4$ ) systems shown in Figures 9.4e and 9.4f, the critical temperature does not show a clear trend with increasing graft length, although the critical density is still reduced with increasing chain length. These behaviors are consistent between both the QD and SAFT results.

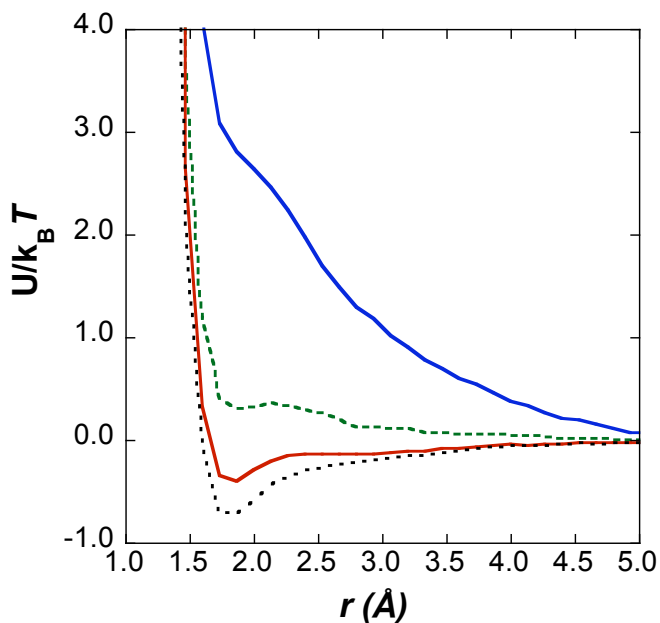


**Figure 9.3.** The potential of mean force (PMF) between different 12 bead per tether grafted nanoparticles at a volume fraction of  $\sim 0.003$  and  $T^* = 40$  and  $N_{GRAFT} = 6$  (blue),  $N_{GRAFT} = 4$  (green),  $N_{GRAFT} = 2$  (red), and  $N_{GRAFT} = 1$  (black).

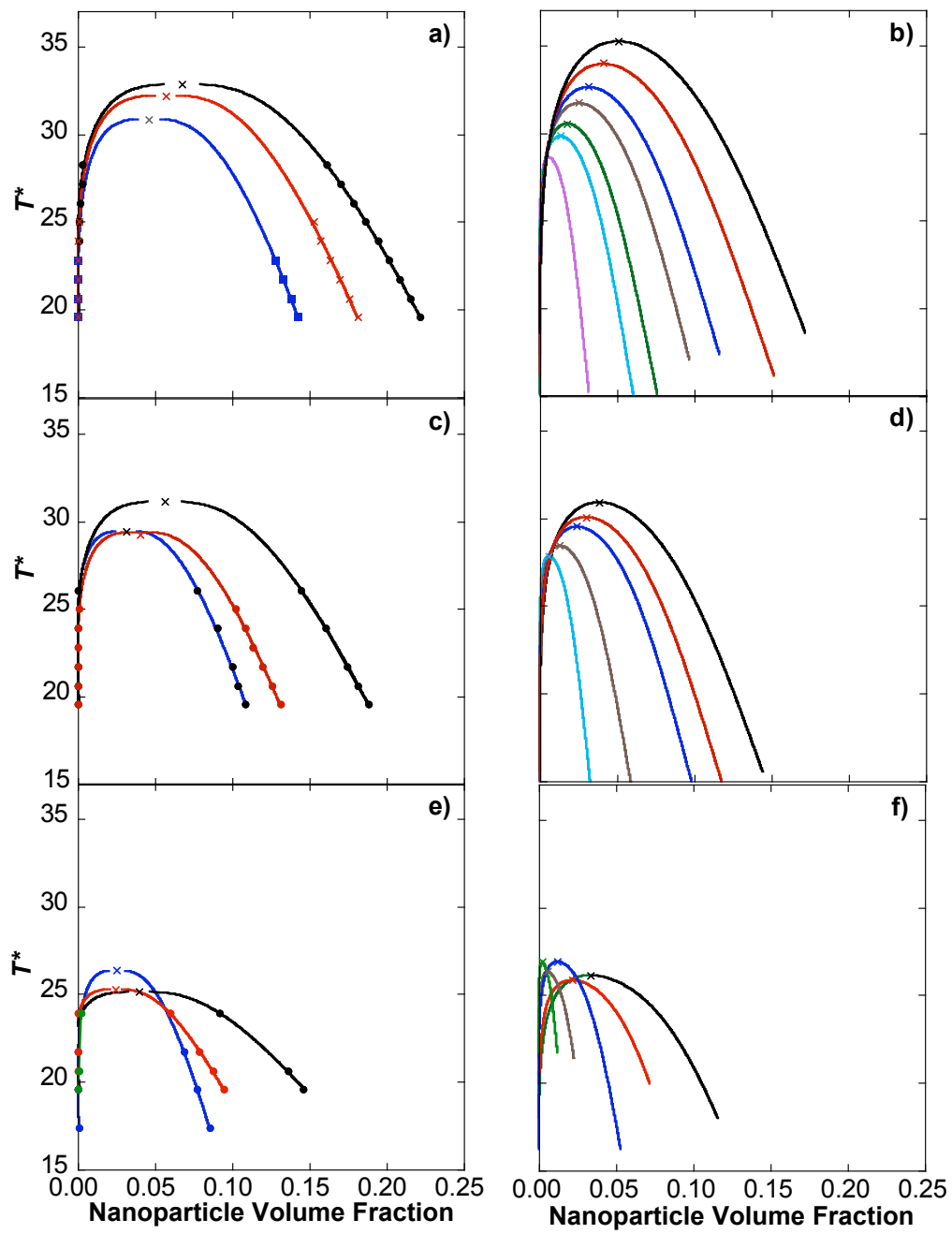


**Figure 9.4.** (a) Fluid phase equilibrium of mono-tethered ( $N_{GRAFT} = 1$ ) TNP systems with 8 (black), 12 (red), 18 (blue) beads per tether as predicted from MD simulation. Symbols represent the simulation results and lines the predictions using rectilinear and scaling laws. (b) Fluid phase equilibrium of mono-tethered ( $N_{GRAFT} = 1$ ) TNP systems with 8 (black), 12 (red), 18 (blue), 24 (brown), 36 (green), 48 (light blue), and 100 (magenta) beads per tether as predicted from the SAFT equation of state, (c) Fluid phase equilibrium of di-tethered ( $N_{GRAFT} = 2$ ) TNP systems with total number of beads equal to 12 (black), 18 (red), 24 (blue) as predicted from MD simulation. Symbols represent the simulation results and lines the predictions using rectilinear and scaling laws. (d) Fluid phase equilibrium of di-tethered ( $N_{GRAFT} = 2$ ) TNP systems with total number of beads equal to 12 (black), 18 (red), 24 (blue), 48 (brown), and 96 (light blue) as predicted from the SAFT equation of state. (e) Fluid phase equilibrium of quad-tethered ( $N_{GRAFT} = 4$ ) TNP systems with total number of beads equal to 12 (black), 24 (red), and 48 (blue) as predicted from MD simulation. Symbols represent the simulation results and lines the predictions using rectilinear and scaling laws. (f) Fluid phase equilibrium of quad-tethered ( $N_{GRAFT} = 4$ ) TNP systems with total number of beads equal to 12 (black), 24 (red), 48 (blue), 96 (brown), and 192 (green)) as predicted from the SAFT equation of state.

For a more complete view of the trends, in particular as a function of graft density, Figure 9.5 summarizes the critical temperature and densities for systems under various conditions calculated from SAFT. Figures 9.5a and 9.5b plot the critical points as a function of the number of grafts, for various graft lengths, as predicted from the SAFT calculations. In Figure 9.5a, we show that the critical temperature decreases with increasing chain length in systems with fewer than 4 grafts, however the trend reverses for systems with greater than 4 grafts. This trend seen for the higher grafted density regime is consistent with behavior seen for pure alkane systems (i.e., increasing critical temperature with increasing polymer length); the transition at 4 grafts appears to be the cause of the unclear trends shown in figures 4e and 4f. In Figure 9.5b, the critical density is plotted as a function of the number of grafts for various graft lengths and it can be seen that the critical density changes most significantly for systems with shorter grafts as compared to longer grafts. Critical temperature and critical density for long chain systems, e.g. 48 beads per tether, do not appear to depend strongly on the number of grafts, when  $N_{GRAFT}$  exceeds 4; more generally as the number of grafts increases, the critical densities appears to approach limiting behavior for all systems considered. This behavior is consistent with structural phase diagrams seen in the work Akcora, *et al.* [215] for dilute polymer grafted silica nanoparticles, where the structure of systems with higher grafting densities show little dependence on the number of grafts, and structural transitions are only seen as a function of graft length. As such, two different regimes of aggregation behavior are observed; those systems with low grafting density will see increased characteristic TNP-TNP interaction strength as graft length is reduced

(i.e., increased tendency to aggregate), whereas those systems with higher grafting density will see characteristic TNP-TNP interaction strength decreased as graft length is decreased (i.e., reduced tendency to aggregate).

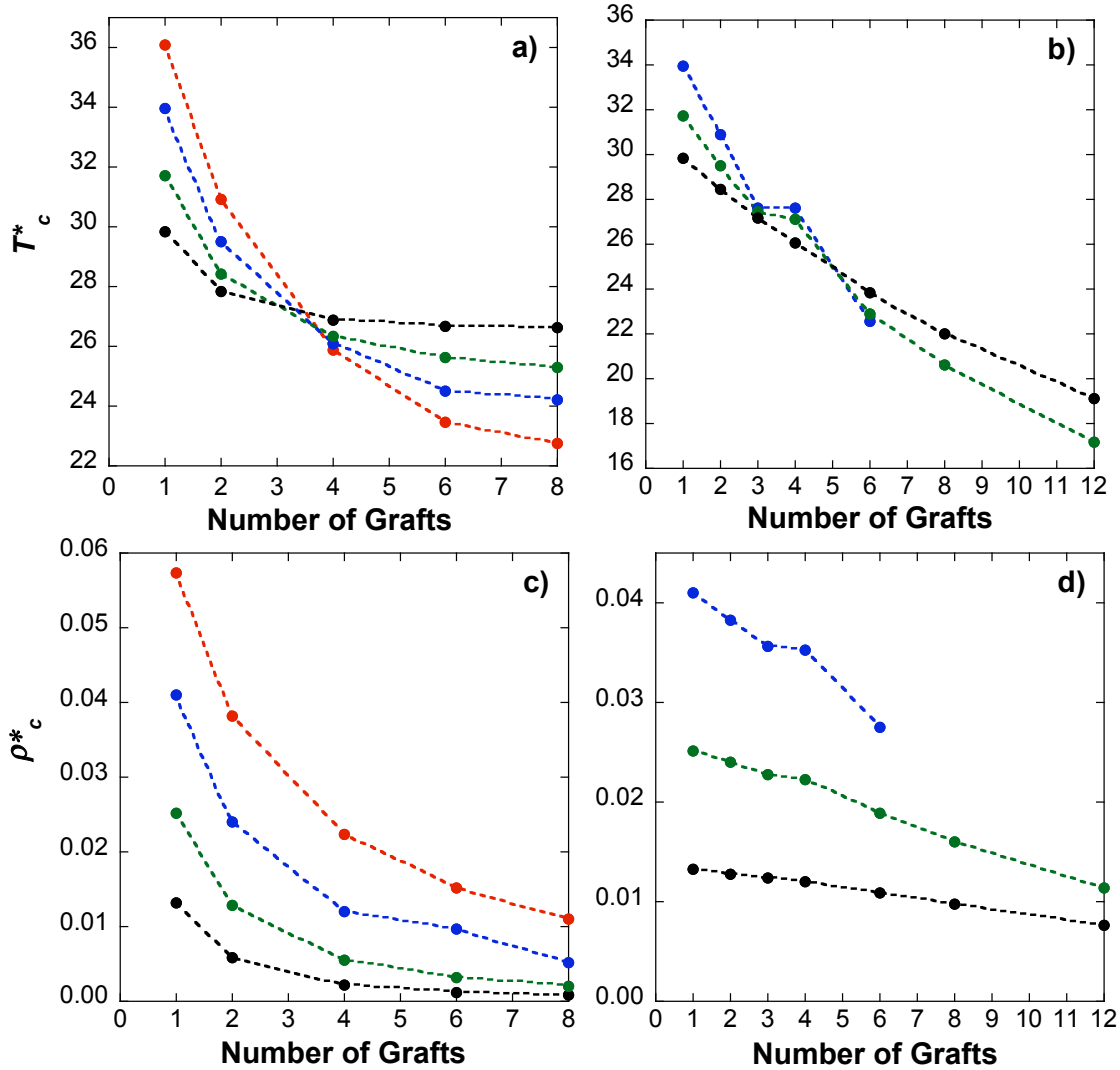


**Figure 9.5.** SAFT equation of state predictions for (a) Critical temperature as a function of the number of grafts for 6 (red), 12 (blue), 24 (green), and 48 (black) beads per tether, (b) Critical temperature as a function of the number of grafts for 12 (blue), 24 (green), and 48 (black) total beads, (c) Critical density as a function of the number of grafts for 6 (red), 12 (blue), 24 (green), and 48 (black) beads per tether, and (d) Critical density as a function of the number of grafts for 12 (blue), 24 (green), and 48 (black) total beads.

Figures 9.5c and 9.5d, plot the behavior of systems as a function of the number of grafts, but where each line corresponds to a conservation of the number of graft beads (similar to the results

in Figure 9.2). In Figures 9.5c, we find a consistent reduction in critical temperature as the number of grafts is increased. Longer grafts have a lower critical temperature than shorter grafts until a transition point is reached at 6 grafts per TNP, where this trend is reversed and shorter grafts exhibit a lower critical temperature than longer grafts. However, the differences between the systems appears less significant than those where the total number of beads is not fixed (Figure 9.5a). All of the systems with fixed composition demonstrate roughly the same change in characteristic “energy scale” resulting from the increase in number of grafts (i.e., same changes in critical temperature). Further, in Figure 9.5d, it is again observed that there is a minimal reduction in critical density as the number of grafts is increased, but this behavior is most prominent for TNPs with longer chains. This suggests that the region where aggregates are found is not strongly influenced by the number of grafts when composition is preserved, and graft length is what must be changed in order to alter the phase envelope significantly.

To further quantify the aggregation/dispersion behavior, the fluid distribution ratio or  $k$ -value ( $k$ -value =  $y_i$  (mole fraction of TNP in low density dispersed fluid)/ $x_i$  (mole fraction of TNP in high density fluid)) is reported in Figure 6 for a TNP system at  $T^* = 21.4$ . SAFT calculations are used to determine the  $k$ -value as a function of number of beads and grafts. As the length of the tether is increased, the amount of TNP in the low-density dispersed phase is decreased. As the number of grafts is increased, the amount of TNP in the dispersed phase is increased for the short tethers (6 and 12), and decreased for longer tethers (24 and 48), although the magnitude of the changes for 12, 24, and 48 bead systems are much less significant than for the shortest 6-bead case considered.

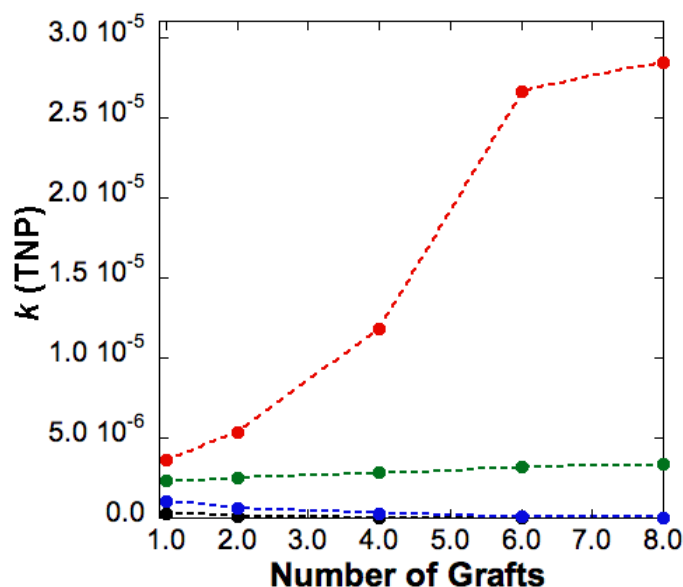


**Figure 9.6.** Fluid distribution ratio of TNP systems as a function of number of grafts in vacuum at  $T^* = 21.4$  as predicted from the SAFT equation of state for 6 (red), 12 (green), 24 (blue), and 48 (black) beads per tether.

### *TNP + Solvent Systems*

Given the close agreement between SAFT and simulation for systems in pure TNP systems (i.e., vacuum), SAFT is used to explore the addition of simple solvents to TNP systems, specifically: carbon dioxide, nitrogen, ethylene, and propane. For the solvent + TNP systems, the effect of the architecture of the TNPs on the phase behavior and the solubility of the mixture is investigated. Figure 9.7 shows the  $T_c^*$  for TNP systems as a function of the number of beads and grafts for all four solvents studied at a reduced pressure,  $P^* = 0.291$ , where  $T_c^*$  is reduced from the pure case with the addition of the solvent.  $T_c^*$  is also reduced as the interaction strength of the solvent is increased as shown in Figure 9.7. More generally, as the value of  $m\varepsilon$  increases (i.e., interaction energy scaled by the number of segments) the  $T_c^*$  is reduced. For the nitrogen, carbon dioxide, and ethylene TNP systems, as the number of TNP graft beads is increased, the critical temperature decreases, consistent with the systems in vacuum. Furthermore, as the graft length is increased,  $T_c^*$  is decreased until a transition point is reached, at which point the trend reverses, as seen in vacuum. Note that in vacuum, this transition point was seen at  $N_{GRAFT} = 4$ , similar to the case of the weakest interaction solvent considered, nitrogen (Figure 9.7a). In the case of propane, shown in Figure 9.7d, the results deviate from the other solvents and vacuum, where a crossover point is not observed. However, as the number of TNP graft beads is increased, the critical temperature decreases for all graft lengths considered, which is still consistent with the other

systems. These differences are likely related to the strong attraction between the propane and the alkane tethers on the TNPs.

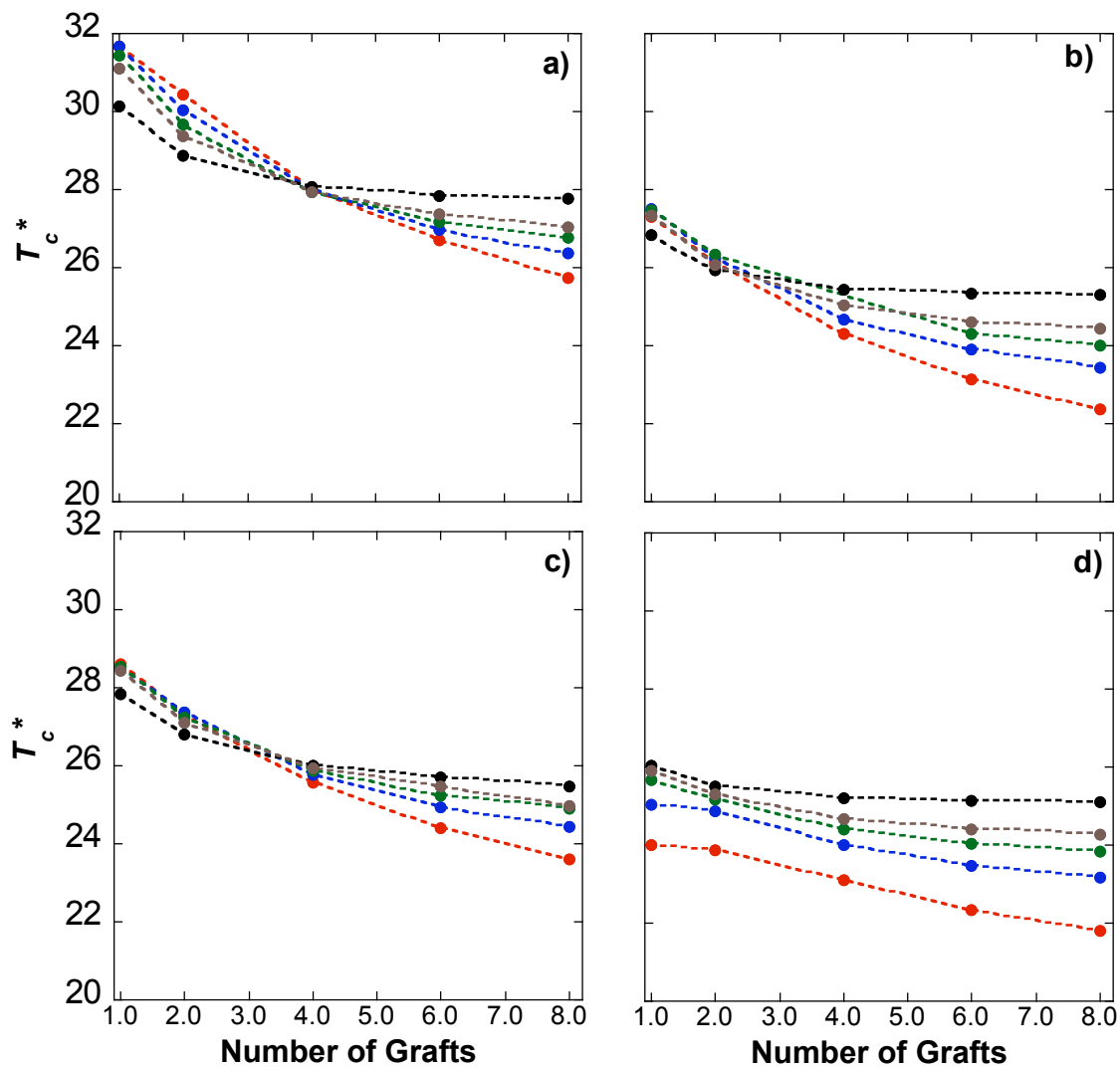


**Figure 9.7.** Critical temperature as a function of the number of grafts for 6 (red), 12 (blue), 18 (green), 24 (brown), and 48 (black) beads per tether as predicted from the SAFT equation at  $P^* = 0.291$  for (a) nitrogen (b) carbon dioxide (c) ethylene and (d) propane

By analyzing the fluid distribution ratio, i.e., the  $k$ -value, the solvent that allows more of the TNPs to be present in the dilute fluid can be identified by the largest  $k$ -value. Figure 9.8 represents a system with 12 beads per tether at  $T^* = 21.7$  for all four solvents considered. In Figure 9.8, the  $k$ -value is shown as a function of the number of grafts, from which it can be seen that as the number of grafts increases the solubility is reduced, although the changes are most

significant for the strongly interacting propane solvent. It is also interesting to note that the  $k$ -value decreases as the value of  $m\epsilon$  is decreased, demonstrating significant sensitivity to relatively small changes in solvent interaction strength.

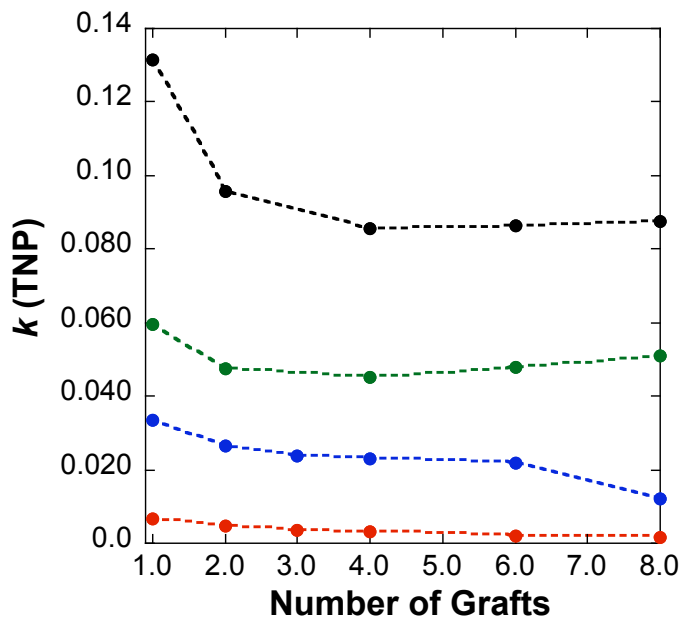


**Figure 9.8.**  $k$  value as a function of the number of grafts for nanoparticles with 12 beads per tether as predicted from the SAFT equation of state at  $T^* = 21.7$  for propane (black), ethylene (blue), nitrogen (red), and carbon dioxide (green).

Figures 9.9a and b report the  $k$ -value for TNPs with 6, 12, 24, and 48 beads per tether in nitrogen and propane as a function of the number of grafts. From the figures, it is clear that increasing the beads per tether also decreases the  $k$ -value, i.e., the TNPs exhibit decreased solubility. As the number of grafts increases for the weakly interacting nitrogen system (Figure 9.9a), the  $k$ -value decreases for all chain lengths considered. Interestingly, the strongly interacting propane system (Figure 9.9b), demonstrates an increase in  $k$ -value as the number of grafts increases, for the shorter graft system, and a reduction in  $k$ -value as the number of grafts increase for the longer systems. For both the nitrogen and propane systems, the  $k$ -value does not appear to be strongly sensitive to the number of grafts for longer chains. As such, solvent interactions can be used to alter the aggregation/dispersion behavior of the TNPs, however, the way in which solvent influences the behavior depends on building block architecture (i.e., length and number of grafts) and the relative interaction strength of the solvent, and changing the solvent has the largest impact on the solubility.



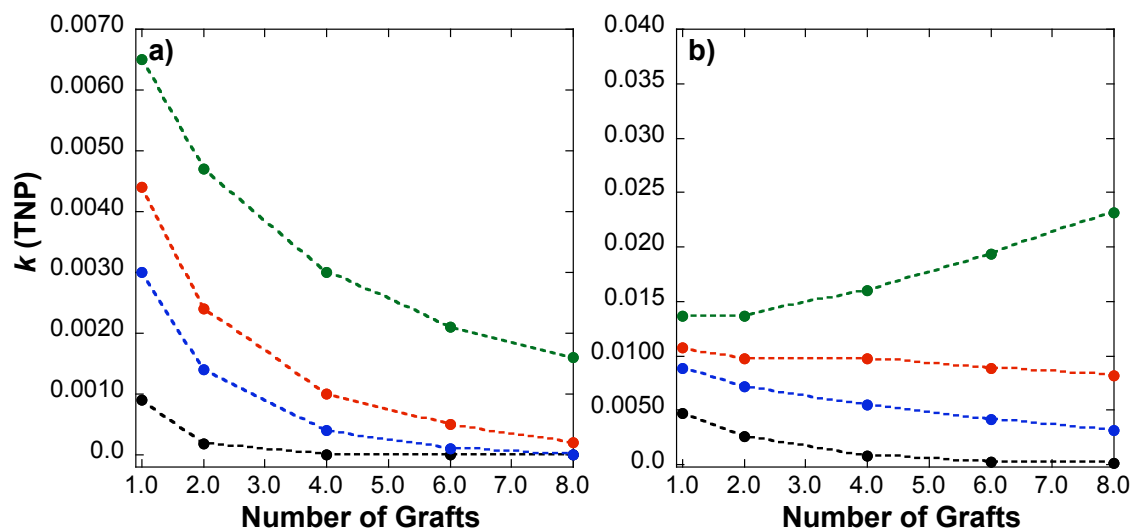


**Figure 9.9.**  $k$  value is shown as a function of number of grafts for 12 (green), 18 (red), 24 (blue), and 48 (black) beads per tether as predicted from the SAFT equation at  $T^*=21.7$  for (a) nitrogen and (b) propane.

### Conclusions

Volume-quench molecular dynamics and the hetero-SAFT-VR equation of state have been applied to investigate the fluid phase coexistence behavior of alkane-tethered silica nanoparticle (TNP) systems. Utilizing a coarse-grained model for the TNP system, it is found that the critical temperature of the TNP systems decrease with an increase in the number of grafted chains on the nanoparticle surface, in agreement with the prior studies of Ref. [247]. This observation can be explained by the steric effect exhibited by the tethers as the grafting density is increased, that is, as the graft density increases, strong interactions between nanoparticles are shielded. However, these changes are less significant as the number of grafts is increased. For  $N_{GRAFT} = 4$  the temperature dependence is lost and at  $N_{GRAFT} > 4$  the trends reverse, with shorter chains showing a lower critical temperature as compared to longer chains which is more consistent with behavior seen for pure alkane systems. As graft length increases, the coexistence region shrinks both the critical density and temperature, the latter of which is the opposite of that seen for pure alkanes. This is due to the tethers sterically hindering the structural aggregation of nanoparticles, resulting in the effective screening of strong nanoparticle interactions. It is also shown that the critical density changes most significantly for systems with shorter grafts as compared to longer chain systems. From these results, we can conclude that graft length needs to be considered as a

variable to make significant changes to the phase envelope and thus the aggregation behavior of nanoparticle based systems, in agreement with combined simulation/experimental work of Ref. [34]. In addition, the solvating ability of common solvents is evaluated and the solubility of the TNP shown to decrease as the number of beads and tethers is increased for several different solvents, however strongly interacting solvents may exhibit altered trends. In addition, guidelines are provided to determine the most effective solvent to use based on the desired system characteristics. Overall, excellent qualitative agreement between simulations and the hetero-SAFT-VR calculations were found for the grafted nanoparticles systems studied. Furthermore, from the trends implied by the results of this study, design rules to control the fundamental aspects of aggregation versus dispersion can be developed. The changes to the phase envelope that result from architectural changes in the TNPs are connected to the aggregation and dispersion behavior of the system. In addition, the coexistence region identifies where aggregates are formed and thus the correct operating conditions required to achieve specific system characteristics, whether aggregated or dispersed.

## Chapter X

### Conclusions and Future Work

Fluids including carbon dioxide, organic sulfur and fluorine molecules, fatty acid methyl esters, and nanoparticle systems possess physical and chemical properties that can aid in the continued development of environmentally conscious industrial processes. In this thesis, versions of the SAFT-VR equation of state have been successfully used to develop a molecular-based theoretical framework to predict the thermodynamic properties and phase behavior of these environmentally significant molecular systems.

Specifically, new organic fluorine and sulfur molecules were characterized, and implemented in the GC-SAFT-VR approach. From limited pure fluid experimental data, the phase behavior of multicomponent systems was successfully predicted, demonstrating the proposed approach can be used as a means for predicting the phase behavior of molecules for which limited or no experimental data is available. The GC-SAFT-VR approach, used in this thesis, offers an improvement in the prediction of the binary mixtures by providing more accurate results, as compared to homonuclear based SAFT approaches. In addition, the number of fitted parameters required to determine the phase behavior of binary mixtures containing the sulfur and fluorine molecules using the GC-SAFT-VR equation is less than for homonuclear based approaches. Therefore, utilizing the GC-SAFT-VR equation of state offers a more predictive approach with transferable parameters that can then be extended to predict the phase behavior of systems well beyond the conditions covered by available experimental data.

Further examining the predictive ability of the GC-SAFT-VR approach, the phase behavior of the biodiesel components, fatty acid methyl esters (FAME), was explored in a fully predictive study. All model parameters were taken from previous work. The FAME model, which was developed in previous GC-SAFT-VR work to study the phase behavior of light FAME molecules, was used in a transferable and predictive fashion to examine the phase behavior of heavy FAME molecules. The approach was then applied to study the phase behavior of FAME molecules with alcohols, CO<sub>2</sub>, and other FAME molecules. As compared to other homonuclear SAFT approaches, the GC-SAFT-VR approach provides more accurate predictions of thermophysical properties for FAME pure fluids. Additionally, homonuclear SAFT approaches require additional fitting to experimental data to determine parameters for new molecules, while the group contribution approach proposed is more attractive, since new molecules can be studied by combining the groups of interest without any fitting. By utilizing this approach, we are able to

reduce the number of fitted parameters required to study the phase behavior of binary mixtures of FAME molecules and carbon dioxide. As promising results were found using the proposed GC-SAFT-VR model, this study can be extended by comparing SAFT predictions to real biodiesel systems (i.e., multicomponent mixtures greater than 3 FAME molecules), as well as mixtures of diesel fuel and biodiesel fuels. The study of such systems is directly relevant and important to industrial applications. Additionally, using the GC-SAFT-VR FAME model tested in this work, derivative properties such as surface tension, viscosity, and speed of sound can be predicted (although selection of an alternative potential model should be investigated), and compared to experimental systems, with the goal of providing information for systems where experimental data is unavailable. Additionally, the GC-SAFT-VR approach can provide a convenient means as compared to experimental investigation to scan the rather large parameter space associated with the many combinations of FAME molecules, which comprise the biodiesel fuels.

Additionally, in this thesis, a molecular model, which explicitly includes interactions due to the quadrupole moment at the molecular and structural level, was successfully developed to accurately describe the phase behavior of carbon dioxide. The large quadrupole moment in CO<sub>2</sub> was represented by embedding opposing dipolar site in each of two segments. The GC-SAFT-VR with dipole equation of state was applied to predict the phase behavior of binary mixtures of alkanes and perfluoroalkanes with carbon dioxide and compared directly with the original SAFT-VR equation. By employing a molecular framework, which accounts for the quadrupolar interactions at both the molecular and structural level, the number of fitted parameters required to predict the phase behavior of both alkanes and perfluoroalkanes molecules with carbon dioxide was reduced. Furthermore, we observe improved results as compared to the work of Zhao *et al.*, where the SAFT-VR theory is extended to include a quadrupolar contribution to the free energy using a Pade-approximation term derived from perturbation theory. The new model for carbon dioxide offers a more predictive approach for the study of binary mixtures including carbon dioxide. The CO<sub>2</sub> model developed is ideally suited in future work to study the phase behavior of carbon dioxide and ionic liquid (IL) mixtures. ILs are organic salts composed of cations and anions that are liquid at conditions around room temperature. Due to the high solubility of carbon dioxide in ILs, their implementation for carbon capture and separation processes is of interest. Recent focus of research on ILs has predominantly been on their applicability as solvents. However, investigation and development of separation methods is equally essential and relatively unexplored [1-3], specifically the knowledge of the phase behavior of the carbon dioxide + IL should be investigated with the goal of determining a predictive framework. Since the improved

CO<sub>2</sub> model proposed here explicitly accounts for the large quadrupole moment present in the CO<sub>2</sub> molecule, we expect improved predictions when applied to mixtures of ILs and CO<sub>2</sub>.

Finally, the strong connection between the fluid phase coexistence behavior and the grafting architecture of the TNP is used as an informative approach to explore aggregation vs. dispersion of nanoparticles. Molecular simulations and the hetero-SAFT-VR equation are used to examine the phase coexistence of polymer-tethered nanoparticles, coupling the detailed structural understanding gleaned from simulation with the efficiency of SAFT for thermodynamic properties. Using SAFT, and verifying our results using molecular simulations, design rules have been successfully developed in an effort to understand the factors that control the aggregation/dispersion. The steric effect exhibited by the tethers is found to be an important factor associated with the aggregation behavior of the TNP system. It is shown that as the grafting density is increased; strong interactions between nanoparticles are shielded. The importance of these changes becomes less profound as the number of grafts is increased. From SAFT calculations it is shown that the temperature dependence is lost and the trends reversed, with shorter chains showing a lower critical temperature as compared to longer chains which is more consistent with behavior seen for pure alkane systems. Further, graft length needs to be considered as a variable to make significant changes to the phase envelope and, thus, the aggregation behavior of nanoparticle based systems. In addition, the solvating ability of common solvents is evaluated and the solubility of the TNP is shown to decrease as the number of beads and tethers is increased for several different solvents. However, strongly interacting solvents may exhibit altered trends. In addition, guidelines are provided to determine the most effective solvent to use based on the desired system characteristics. Further research in this area can be done to characterize the aggregation behavior of the TNPs. Investigation of the shape and number of nanoparticles comprising the aggregates as a function of TNP architecture and solvent can provide additional information on the most effective method to control the aggregation and size of the nanoparticles. Additionally, the stability of the aggregates as a function of the architecture of the tethered nanoparticle can be investigated. Systems dominated by nanoparticle- nanoparticle interactions and systems that allow close nanoparticle contact are likely to be very stable because of the strong interaction strength. However, those dominated by weaker polymer-polymer (i.e., dense graft) will likely be less stable. The stability can be quantitatively investigated by calculating the interaction energy of the system. For example if the interaction energy of the system is much greater than  $k_B T$ , the system will be stable. This information is required for the implementation of TNPs for industrial and commercial use. Further examination of the effect of

the solvent matrix could also be examined efficiently using the hetero-SAFT-VR model developed in this work.

## REFERENCES

1. Morgado, P., et al., *Perfluoroalkanes and perfluoroalkylalkane surfactants in solution: Partial molar volumes in n-octane and hetero-SAFT-VR modelling*. Fluid Phase Equilibria, 2011. **306**(1): p. 76-81.
2. Morgado, P., et al., *Solution behavior of perfluoroalkanes and perfluoroalkylalkane surfactants in n-octane*. Journal of Physical Chemistry C, 2007. **111**(43): p. 15962-8.
3. Morgado, P., C. McCabe, and E.J.M. Filipe, *Modelling the phase behaviour and excess properties of alkane + perfluoroalkane binary mixtures with the SAFT-VR approach*. Fluid Phase Equilibria, 2005. **228-229**: p. 389-393.
4. Tochigi, K., et al., *Measurement and prediction of high-pressure vapor-liquid equilibria for binary mixtures of carbon dioxide ;n-octane, methanol, ethanol, and perfluorohexane*. The Journal of Supercritical Fluids, 2010. **55**(2): p. 682-689.
5. Dennington, R., T. Keith, and J. Millam, *GaussView*. 2009, Semichem Inc.: Shawnee Mission KS.
6. Allen, M.P., *Computational Soft Matter: From Synthetic Polymers to Proteins*, 2004. **23**: p. 1-28.
7. Lockemann, C.A., *High-pressure phase equilibria and densities of the binary mixtures carbon dioxide-oleic acid, carbon dioxide-methyl myristate, and carbon dioxide-methyl palmitate and of the ternary mixture carbon dioxide-methyl myristate-methyl palmitate*. Chemical Engineering and Processing, 1994. **33**: p. 171-187.
8. Tochigi, K., et al., *Vapor-Liquid Equilibrium Data for the Four Binary Systems Containing Fluorocarbon, Hydrofluorocarbon, and Fluorinated Ethers at 101.3 kPa*. Journal of Chemical & Engineering Data, 2001. **46**(4): p. 913-917.
9. Dias, A.M.A., et al., *SAFT Modeling of the Solubility of Gases in Perfluoroalkanes*. The Journal of Physical Chemistry B, 2003. **108**(4): p. 1450-1457.
10. Design Institute for Physical Property Data (U.S.) and Knovel (Firm), *DIPPR Project 801, full version evaluated standard thermophysical property values*. 2005, BYU DIPPR, Thermophysical Properties Laboratory: Provo, Utah.
11. Oliveira, M.B., et al., *Phase equilibria description of biodiesels with water and alcohols for the optimal design of the production and purification process*. Fuel, 2014. **129**(0): p. 116-128.
12. Rose, A. and W.R. Supina, *Vapor Pressure and Vapor-Liquid Equilibrium Data for Methyl Esters of the Common Saturated Normal Fatty Acids*. Journal of Chemical and Engineering Data, 1961. **6**(2): p. 173-179.
13. Pratas de Melo, M.J., et al., *Liquid-liquid equilibrium of (perfluoroalkane and alkane) binary mixtures*. Fluid Phase Equilibria, 2006. **242**(2): p. 210-219.
14. Subramoney, S.C., et al., *Experimental (vapour+liquid) equilibrium data and modelling for binary mixtures of decafluorobutane with propane and 1-butene*. The Journal of Chemical Thermodynamics, 2013. **67**(0): p. 134-142.
15. Hou, J., et al., *Isobaric Vapor-Liquid Equilibrium of the Mixture of Methyl Palmitate and Methyl Stearate at 0.1 kPa, 1 kPa, 5 kPa, and 10 kPa*. Journal of Chemical & Engineering Data, 2012. **57**(10): p. 2632-2639.
16. Rose, A. and V.N. Schrodtt, *Vapor-liquid Equilibria for the Methyl Oleate and Methyl Stearate Binary System*. Journal of Chemical and Engineering Data, 1964. **9**(1): p. 12-16.
17. Galindo, A. and F.J. Blas, *Theoretical Examination of the Global Fluid Phase Behavior and Critical Phenomena in Carbon Dioxide + n-Alkane Binary Mixtures*. The Journal of Physical Chemistry B, 2002. **106**(17): p. 4503-4515.
18. Blas, F.J. and A. Galindo, *Study of the high pressure phase behaviour of CO<sub>2</sub>+n-alkane mixtures using the SAFT-VR approach with transferable parameters*. Fluid Phase Equilibria, 2002. **194-197**: p. 501-509.

19. Tochigi, K., et al., *Measurement and prediction of high-pressure vapor–liquid equilibria for binary mixtures of carbon dioxide+ n-octane, methanol, ethanol, and perfluorohexane*. The Journal of Supercritical Fluids, 2010. **55**(2): p. 682-689.
20. Krafft, M.P., *Fluorocarbons and fluorinated amphiphiles in drug delivery and biomedical research*. Advanced Drug Delivery Reviews, 2001. **47**(2–3): p. 209-228.
21. Cui, S.T., H.D. Cochran, and P.T. Cummings, *Vapor-liquid phase coexistence of alkane-carbon dioxide and perfluoroalkane-carbon dioxide mixtures*. Journal of Physical Chemistry B, 1999. **103**(21): p. 4485-4491.
22. Tsai, W.-T., *Environmental risk assessment of hydrofluoroethers (HFEs)*. Journal of Hazardous Materials, 2004: p. 69-78.
23. Tsagogiorgas, C., et al., *Semifluorinated alkanes--a new class of excipients suitable for pulmonary drug delivery*. Eur J Pharm Biopharm, 2010. **76**(1): p. 75-82.
24. Meinert, H. and T. Roy, *Semifluorinated alkanes – A new class of compounds with outstanding properties for use in ophthalmology*. European Journal of Ophthalmology, 2000. **10**(3): p. 189-197.
25. Sapei, E., et al., *Phase Equilibria of Organic Sulfur Compounds for Cleaner Fuels*. Distillation Absorption, 2010: p. 365-370.
26. Nieuwoudt, I. and M. du Rand, *Measurement of phase equilibria of supercritical carbon dioxide and paraffins*. Journal of Supercritical Fluids 2002. **22**: p. 185–199.
27. Camel, V., A. Tambute, and M. Caude, *Supercritical fluid extraction in analysis*. Analisis 1992. **20**: p. 503–528.
28. Parrish, D.R., *Method for enhanced oil recovery*. 1982, Google Patents.
29. Raventós, M., S. Duarte, and R. Alarcón, *Application and possibilities of supercritical CO<sub>2</sub> extraction in food processing industry: an overview*. Food Science and Technology International, 2002. **8**(5): p. 269-284.
30. Lim, M., et al., *Environmental Remediation and Conversion of Carbon Dioxide (CO<sub>2</sub>) into Useful Green Products by Accelerated Carbonation Technology*. International Journal Environmental Research Public Health, 2010. **7**(1): p. 203-228.
31. DeSimone, J.M., *Practical approaches to green solvents*. Science, 2002. **297**(5582): p. 799-803.
32. Nalawade, S.P., F. Picchioni, and L.P.B.M. Janssen, *Supercritical carbon dioxide as a green solvent for processing polymer melts: Processing aspects and applications*. Progress in Polymer Science, 2006. **31**(1): p. 19-43.
33. Shannon, M.A., et al., *Science and technology for water purification in the coming decades*. Nature, 2008. **452**(7185): p. 301-310.
34. Ahn, Y.C., et al., *Development of high efficiency nanofilters made of nanofibers*. Current Applied Physics, 2006. **6**(6): p. 1030-1035.
35. Sajith, V., C.B. Sobhan, and G.P. Peterson, *Experimental investigations on the effects of cerium oxide nanoparticle fuel additives on biodiesel*. Advances in Mechanical Engineering, 2010. **2010**.
36. Ogolo, N.A., O.A. Olafuyi, and M.O. Onyekonwu, *Enhanced Oil Recovery Using Nanoparticles*. Society of Petroleum Engineers.
37. Fermeglia, M. and S. Pricl, *Multiscale molecular modeling in nanostructured material design and process system engineering*. Computers & Chemical Engineering, 2009. **33**(10): p. 1701-1710.
38. Hailong, L., et al., *Review of available experimental data and models for the transport properties of CO<sub>2</sub>-mixtures relevant for CO<sub>2</sub> capture, transport and storage*. 2009.
39. Chapman, W.G., et al., *New reference equation of state for associating liquids*. Industrial and Engineering Chemistry Research, 1990. **29**(8): p. 1709-1721.
40. Chapman, W.G., G. Jackson, and K.E. Gubbins, *Phase equilibria of associating fluids: chain molecules with multiple bonding sites*. Molecular Physics, 1988. **65**(5): p. 1057-79.



41. Wertheim, M.S., *Fluids with highly directional attractive forces. I. Statistical thermodynamics*. Journal of Statistical Physics, 1984. **35**(1-2): p. 19-34.
42. Wertheim, M.S., *Fluids with highly directional attractive forces. II. Thermodynamic perturbation theory and integral equations*. Journal of Statistical Physics, 1984. **35**(1-2): p. 35-47.
43. Wertheim, M.S., *Fluids with highly directional attractive forces. III. Multiple attraction sites*. Journal of Statistical Physics, 1986. **42**(3-4): p. 459-76.
44. Wertheim, M.S., *Fluids with highly directional attractive forces. IV. Equilibrium polymerization*. Journal of Statistical Physics, 1986. **42**(3-4): p. 477-92.
45. Chapman, W.G., et al., *SAFT: Equation-of-state solution model for associating fluids*. Fluid Phase Equilibria, 1989. **52**(0): p. 31-38.
46. Gil-Villegas, A., et al., *Statistical associating fluid theory for chain molecules with attractive potentials of variable range*. The Journal of Chemical Physics, 1997. **106**(10): p. 4168-4186.
47. dos Ramos, M.C., et al., *Extending the GC-SAFT-VR approach to associating functional groups: Alcohols, aldehydes, amines and carboxylic acids*. Fluid Phase Equilibria, 2011. **306**(1): p. 97-111.
48. Peng, Y., et al., *Developing a predictive group-contribution-based SAFT-VR equation of state*. Fluid Phase Equilibria, 2009. **277**(2): p. 131-144.
49. McCabe, C.G., A., *SAFT Associating Fluids and Fluid Mixtures*. In *Applied Thermodynamics of Fluids*, in Royal Society of Chemistry. 2010: Cambridge. p. 215-279.
50. Huang, S.H. and M. Radosz, *Equation of state for small, large, polydisperse, and associating molecules*. Industrial & Engineering Chemistry Research, 1990. **29**(11): p. 2284-2294.
51. Chen, S.S. and A. Kreglewski. *Applications of the augmented van der Waals theory of fluids. I. Pure fluids*. in *76th General Assembly of the German Bunsen Society for Physical Chemistry, 19-21 May 1977*. 1977. West Germany.
52. Lee, S.-H., M.A. LoStracco, and M.A. McHugh, *Cosolvent Effect on the Phase Behavior of Poly(ethylene-co-acrylic acid)–Butane Mixtures*. Macromolecules, 1996. **29**(4): p. 1349-1358.
53. Behme, S., G. Sadowski, and W. Arlt, *Modeling of the separation of polydisperse polymer systems by compressed gases*. Fluid Phase Equilibria, 1999. **158–160**(0): p. 869-877.
54. Wiesmet, V., et al., *Measurement and modelling of high-pressure phase equilibria in the systems polyethyleneglycol (PEG)–propane, PEG–nitrogen and PEG–carbon dioxide*. The Journal of Supercritical Fluids, 2000. **17**(1): p. 1-12.
55. Chen, S.J., I.G. Economou, and M. Radosz, *Density-tuned polyolefin phase equilibria. 2. Multicomponent solutions of alternating poly(ethylene-propylene) in subcritical and supercritical olefins. Experiment and SAFT model*. Macromolecules, 1992. **25**(19): p. 4987-4995.
56. Han, S.J., C.J. Gregg, and M. Radosz, *How the Solute Polydispersity Affects the Cloud-Point and Coexistence Pressures in Propylene and Ethylene Solutions of Alternating Poly(ethylene-co-propylene)*. Industrial & Engineering Chemistry Research, 1997. **36**(12): p. 5520-5525.
57. Orbey, H., C.P. Bokis, and C.-C. Chen, *Polymer–Solvent Vapor–Liquid Equilibrium: Equations of State versus Activity Coefficient Models*. Industrial & Engineering Chemistry Research, 1998. **37**(4): p. 1567-1573.
58. Galindo, A., P.J. Whitehead, and G. Jackson, *Predicting the High-Pressure Phase Equilibria of Water + n-Alkanes Using a Simplified SAFT Theory with Transferable Intermolecular Interaction Parameters*. The Journal of Physical Chemistry, 1996. **100**(16): p. 6781-6792.

59. M. Nieves Garcia-Lisbona Amparo Galindo George Jackson Andrew N, B., *Predicting the high-pressure phase equilibria of binary aqueous solutions of 1-butanol, n-butoxyethanol and n-decylpentaoxyethylene ether (C10E5) using the SAFT-HS approach*. Molecular Physics, 1998. **93**(1): p. 57-72.
60. Garcia-Lisbona, M.N., et al., *An Examination of the Cloud Curves of Liquid–Liquid Immiscibility in Aqueous Solutions of Alkyl Polyoxyethylene Surfactants Using the SAFT-HS Approach with Transferable Parameters*. Journal of the American Chemical Society, 1998. **120**(17): p. 4191-4199.
61. Clements, P.J., et al., *Thermodynamics of ternary mixtures exhibiting tunnel phase behaviour Part 3.-Hexane-hexamethylsiloxane-perfluorohexane*. Journal of the Chemical Society, Faraday Transactions, 1997. **93**(7): p. 1331-1339.
62. Filipe, E.J.M., et al., *Shape Effects in Molecular Liquids: Phase Equilibria of Binary Mixtures Involving Cyclic Molecules*. The Journal of Physical Chemistry B, 1997. **101**(51): p. 11243-11248.
63. Blas, F.J. and L.F. Vega, *Prediction of binary and ternary diagrams using the statistical associating fluid theory (SAFT) equation of state*. Industrial and Engineering Chemistry Research, 1998. **37**(2): p. 660-674.
64. Pàmies, J.C. and L.F. Vega, *Vapor–Liquid Equilibria and Critical Behavior of Heavy n-Alkanes Using Transferable Parameters from the Soft-SAFT Equation of State*. Industrial & Engineering Chemistry Research, 2001. **40**(11): p. 2532-2543.
65. Llovel, F., R.M. Marcos, and L.F. Vega, *Transport Properties of Mixtures by the Soft-SAFT + Free-Volume Theory: Application to Mixtures of n-Alkanes and Hydrofluorocarbons*. The Journal of Physical Chemistry B, 2013. **117**(17): p. 5195-5205.
66. Dias, A.M.A., et al., *Thermodynamic characterization of pure perfluoroalkanes, including interfacial and second order derivative properties, using the crossover soft-SAFT EoS*. Fluid Phase Equilibria, 2009. **286**(2): p. 134-143.
67. Vega, L.F., F. Llovel, and F.J. Blas, *Capturing the Solubility Minima of n-Alkanes in Water by Soft-SAFT*. The Journal of Physical Chemistry B, 2009. **113**(21): p. 7621-7630.
68. Llovel, F. and L.F. Vega, *Phase equilibria, critical behavior and derivative properties of selected n-alkane/n-alkane and n-alkane/1-alkanol mixtures by the crossover soft-SAFT equation of state*. The Journal of Supercritical Fluids, 2007. **41**(2): p. 204-216.
69. Pedrosa, N., et al., *Modeling the Phase Equilibria of Poly(ethylene glycol) Binary Mixtures with soft-SAFT EoS*. Industrial & Engineering Chemistry Research, 2007. **46**(13): p. 4678-4685.
70. Pereira, L.M.C., et al., *Assessing the N<sub>2</sub>O/CO<sub>2</sub> high pressure separation using ionic liquids with the soft-SAFT EoS*. The Journal of Supercritical Fluids, 2014. **92**(0): p. 231-241.
71. Oliveira, M.B., et al., *Surface Tension of Binary Mixtures of 1-Alkyl-3-methylimidazolium Bis(trifluoromethylsulfonyl)imide Ionic Liquids: Experimental Measurements and Soft-SAFT Modeling*. The Journal of Physical Chemistry B, 2012. **116**(40): p. 12133-12141.
72. Gross, J. and G. Sadowski, *Perturbed-Chain SAFT: An Equation of State Based on a Perturbation Theory for Chain Molecules*. Industrial & Engineering Chemistry Research, 2001. **40**(4): p. 1244-1260.
73. Leonard, P.J., D. Henderson, and J.A. Barker *Perturbation theory and liquid mixtures*. Transactions of the Faraday Society, 1970. **66**(574): p. 2439-2452.
74. Barker, J.A. and D.J. Henderson, *Reviews of Modern Physics*, 1976. **48**(4): p. 587-671.
75. Barker, J.A. and D. Henderson, *Perturbation Theory and Equation of State for Fluids. II. A Successful Theory of Liquids*. The Journal of Chemical Physics, 1967. **47**(11): p. 4714-4721.
76. McCabe, C. and G. Jackson, *SAFT-VR modelling of the phase equilibrium of long-chain n-alkanes*. Physical Chemistry Chemical Physics, 1999. **1**(9): p. 2057-2064.

77. McCabe, C., et al., *Predicting the High-Pressure Phase Equilibria of Binary Mixtures of Perfluoro-*n*-alkanes + *n*-Alkanes Using the SAFT-VR Approach*. The Journal of Physical Chemistry B, 1998. **102**(41): p. 8060-8069.
78. Cristino, A.F., et al., *High-temperature vapour–liquid equilibrium for the (water+alcohol) systems and modelling with SAFT-VR: 2. Water-1-propanol*. The Journal of Chemical Thermodynamics, 2013. **60**(0): p. 15-18.
79. Clark, G.N.I., et al., *Modeling and Understanding Closed-Loop Liquid–Liquid Immiscibility in Aqueous Solutions of Poly(ethylene glycol) Using the SAFT-VR Approach with Transferable Parameters*. Macromolecules, 2008. **41**(17): p. 6582-6595.
80. Cristino, A.F., et al., *High-temperature vapour-liquid equilibrium for the water-alcohol systems and modeling with SAFT-VR: 1. Water-ethanol*. Fluid Phase Equilibria, 2013. **341**: p. 48-53.
81. Cristino, A.F., et al., *High-temperature vapour-liquid equilibrium for the (water + alcohol) systems and modelling with SAFT-VR: 2. Water-1-propanol*. Journal of Chemical Thermodynamics, 2013. **60**: p. 15-18.
82. Galindo, A., et al., *Prediction of Phase Equilibria for Refrigerant Mixtures of Difluoromethane (HFC-32), 1,1,1,2-Tetrafluoroethane (HFC-134a), and Pentafluoroethane (HFC-125a) Using SAFT-VR*. The Journal of Physical Chemistry B, 1998. **102**(39): p. 7632-7639.
83. Swaminathan, S. and D.P. Visco, *Thermodynamic Modeling of Refrigerants Using the Statistical Associating Fluid Theory with Variable Range. 1. Pure Components*. Industrial & Engineering Chemistry Research, 2005. **44**(13): p. 4798-4805.
84. Swaminathan, S. and D.P. Visco, *Thermodynamic Modeling of Refrigerants Using the Statistical Associating Fluid Theory with Variable Range. 2. Applications to Binary Mixtures*. Industrial & Engineering Chemistry Research, 2005. **44**(13): p. 4806-4814.
85. Y. Peng and C. McCabe, *Molecular simulation and theoretical modeling of polyhedral oligomeric silsesquioxanes*. Molecular Physics, 2007. **105**(2): p. 261-272.
86. Gil-Villegas, A., et al., *Statistical associating fluid theory for chain molecules with attractive potentials of variable range*. Journal of Chemical Physics, 1997. **106**(10): p. 4168-86.
87. Peng, Y., H. Zhao, and C. McCabe, *On the thermodynamics of diblock chain fluids from simulation and heteronuclear statistical associating fluid theory for potentials of variable range*. Molecular Physics, 2006. **104**(4): p. 571-586.
88. Morgado, P., et al., *Liquid phase behavior of perfluoroalkylalkane surfactants*. Journal of Physical Chemistry B, 2007. **111**(11): p. 2856-63.
89. Morgado, P., et al., *Viscosity of liquid perfluoroalkanes and perfluoroalkylalkane surfactants*. Journal of Physical Chemistry B, 2011. **115**(29): p. 9130-9139.
90. Morgado, P., et al., *Systems involving hydrogenated and fluorinated chains: Volumetric properties of perfluoroalkanes and perfluoroalkylalkane surfactants*. Journal of Physical Chemistry B, 2011. **115**(50): p. 15013-15023.
91. Gros, H.P., S. Bottini, and E.A. Brignole, *A group contribution equation of state for associating mixtures*. Fluid Phase Equilibria, 1996. **116**(1–2): p. 537-544.
92. Tamouza, S., et al., *Group contribution method with SAFT EOS applied to vapor liquid equilibria of various hydrocarbon series*. Fluid Phase Equilibria, 2004. **222–223**(0): p. 67-76.
93. Tamouza, S., et al., *Application to binary mixtures of a group contribution SAFT EOS (GC-SAFT)*. Fluid Phase Equilibria, 2005. **228–229**(0): p. 409-419.
94. Nguyen Thi, T.X., et al., *Application of group contribution SAFT equation of state (GC-SAFT) to model phase behaviour of light and heavy esters*. Fluid Phase Equilibria, 2005. **238**(2): p. 254-261.

95. Tihic, A., et al., *A Predictive Group-Contribution Simplified PC-SAFT Equation of State: Application to Polymer Systems*. Industrial & Engineering Chemistry Research, 2008. **47**(15): p. 5092-5101.
96. Constantinou, L. and R. Gani, *New group contribution method for estimating properties of pure compounds*. AIChE Journal, 1994. **40**(10): p. 1697-1710.
97. Tihic, A., et al., *Applications of the simplified perturbed-chain SAFT equation of state using an extended parameter table*. Fluid Phase Equilibria, 2006. **248**(1): p. 29-43.
98. Tihic, A., et al., *Application of sPC-SAFT and group contribution sPC-SAFT to polymer systems—Capabilities and limitations*. Fluid Phase Equilibria, 2009. **281**(1): p. 70-77.
99. Lymperiadis, A., et al., *A group contribution method for associating chain molecules based on the statistical associating fluid theory (SAFT- $\gamma$ )*. The Journal of Chemical Physics, 2007. **127**(23): p. 234903.
100. Peng, Y., et al., *Predicting the phase behavior of polymer systems with the GC-SAFT-VR approach*. Industrial and Engineering Chemistry Research, 2010. **49**: p. 1378-1394.
101. Hansen, J.P. and I.R. McDonald, *Theory of simple liquids*. Vol. 2. 1990, London: Academic Press.
102. Carnahan, N.F. and K.E. Starling, *Journal of Chemical Physics*, 1969. **51**(2): p. 635.
103. Barker, J.A. and D. Henderson, *Perturbation Theory and Equation of State for Fluids: The Square-Well Potential*. The Journal of Chemical Physics, 1967. **47**(8): p. 2856-2861.
104. Patel, B.H., et al., *Generalized equation of state for square-well potentials of variable range*. Molecular Physics, 2005. **103**(1): p. 129-139.
105. Rowlinson, J.S. and F.L. Swinton, *Liquids and Liquid Mixtures*. 3rd Edition ed. 1982, London: Butterworth Scientific.
106. Amparo Galindo Lowri A. Davies Alejandro Gil-Villegas George, J., *The thermodynamics of mixtures and the corresponding mixing rules in the SAFT-VR approach for potentials of variable range*. Molecular Physics, 1998. **93**(2): p. 241-252.
107. T, J.B., *Journal of Chemical Physics*, 1970. **53**: p. 471.
108. Reed, T.M. and K.E. Gubbins, *Applied statistical mechanics*, ed. McGraw-Hill. 1973, New York American Institute of Chemical Engineers.
109. McCabe, C., et al., *The thermodynamics of heteronuclear molecules formed from bonded square-well (BSW) segments using the SAFT-VR approach*. Molecular Physics, 1999. **97**(4): p. 551-558.
110. Rowlinson, J.S.S., F.L., *Liquids and liquid mixtures*. 1982, Boston: Butterworth Scientific: London.
111. Shattuck, T., *Molecular Mechanics Tutorial*, C. College, Editor. 2008: Waterville, Maine.
112. Veld, P.J.i.t., et al., *Liquid-vapor coexistence for nanoparticles of various size*. Journal of Chemical Physics, 2008. **129**: p. 164504.
113. Li, C., *Toward Molecular Dynamics Simulation of Complex Molecular Systems*. . 2006, University of Tennessee.
114. Martínez-Veracoechea \*, F. and E.A. Müller, *Temperature-quench Molecular Dynamics Simulations for Fluid Phase Equilibria*. Molecular Simulation, 2005. **31**(1): p. 33-43.
115. Gelb, L.D. and E.A. Müller, *Location of phase equilibria by temperature-quench molecular dynamics simulations*. Fluid Phase Equilibria, 2002. **203**(1-2): p. 1-14.
116. Paricaud, P., et al., *From dimer to condensed phases at extreme conditions: Accurate predictions of the properties of water by a Gaussian charge polarizable model*. The Journal of Chemical Physics, 2005. **122**(24): p. 244511.
117. Smit, B., in *PhD Thesis*. 1990, University of Utrecht: Netherlands.
118. Wu, D., D. Chandler, and B. Smit, *Electrostatic analogy for surfactant assemblies*. The Journal of Physical Chemistry, 1992. **96**(10): p. 4077-4083.

119. Betzemeier, B. and P. Knochel, *Perfluorinated Solvents — a Novel Reaction Medium in Organic Chemistry Modern Solvents in Organic Synthesis*, P. Knochel, Editor. 1999, Springer Berlin / Heidelberg. p. 60-78.
120. Klein, C.O., et al., *Viscoelasticity of semifluorinated alkanes at the air/water interface*. *Soft Matter*, 2011. **7**(17): p. 7737-7746.
121. Gaurav Das, Eduardo Filipe, and C. McCabe, *Vapour Pressure of Perfluoroalkylalkanes: The Role of the Dipole*. *The Journal of Physical Chemistry B*, 2014.
122. Wertheim, M.S., *Fluids with Highly Directional Attractive Forces. II. Thermodynamic Perturbation Theory and Integral Equations*. *Journal of Statistical Physics*, 1984. **35**(1-2): p. 35-47.
123. Archer, A.L., et al., *The theoretical prediction of the critical points of alkanes, perfluoroalkanes, and their mixtures using bonded hard-sphere (BHS) theory*. *International Journal of Thermophysics*, 1996. **17**(1): p. 201-211.
124. McCabe, C., et al., *Predicting the high-pressure phase equilibria of binary mixtures of perfluoro-n-alkanes + n-alkanes using the SAFT-VR approach*. *Journal of Physical Chemistry B*, 1998. **102**(41): p. 8060-8069.
125. Dias, A.M.A., et al., *Vapor–Liquid Equilibrium of Carbon Dioxide–Perfluoroalkane Mixtures: Experimental Data and SAFT Modeling*. *Industrial & Engineering Chemistry Research*, 2006. **45**(7): p. 2341-2350.
126. Y. Peng and C. McCabe, *Molecular Physics*, 2007: p. 261-272.
127. McCabe, C., et al., *The thermodynamics of heteronuclear molecules formed from bonded square-well (BSW) segments using SAFT-VR approach*. *Molecular Physics* 1999. **97**(4): p. 551-558.
128. dos Ramos, M.C. and F.J. Blas, *Theory of phase equilibria for model mixtures of n-alkanes, perfluoroalkanes and perfluoroalkylalkane diblock surfactants*. *Molecular Physics*, 2007. **105**(10): p. 1319-1334.
129. Lafitte, T., et al., *Accurate Global Thermophysical Characterization of Hydrofluoroethers through a Statistical Associating Fluid Theory Variable Range Approach, Based on New Experimental High-Pressure Volumetric and Acoustic Data*. *Industrial & Engineering Chemistry Research*, 2007. **46**(21): p. 6998-7007.
130. Vijande, J., et al., *Description of PVT behaviour of hydrofluoroethers using the PC-SAFT EOS*. *Physical Chemistry Chemical Physics*, 2004. **6**(4): p. 766-770.
131. Das, G., M.C.d. Ramos, and C. McCabe, *Accurately modeling benzene and alkylbenzenes using a group contribution based SAFT approach*. *Fluid Phase Equilibria*, 2014. **362**(0): p. 242-251.
132. Lafitte, T., et al., *Simultaneous estimation of phase behavior and second-derivative properties using the statistical associating fluid theory with variable range approach*. *Journal of Chemical Physics*, 2006. **124**.
133. Tschierske, C., *Liquid Crystals: Material Design and Self Assembly*. 2012. 410.
134. Lepori, L., et al., *Volume changes on mixing perfluoroalkanes with alkanes or ethers at 298.15 K*. *Fluid Phase Equilibria*, 2002. **201**(1): p. 119-134.
135. Maciejewski, A., *The application of perfluoroalkanes as solvents in spectral, photophysical and photochemical studies*. *Journal of Photochemistry and Photobiology A: Chemistry*, 1990. **51**(2): p. 87-131.
136. Colina, C.M., et al., *Phase behavior of carbon dioxide mixtures with n-alkanes and n-perfluoroalkanes*. *Fluid Phase Equilibria*, 2004. **222–223**(0): p. 77-85.
137. Aparicio, S., *Phase equilibria in perfluoroalkane + alkane binary systems from PC-SAFT equation of state*. *The Journal of Supercritical Fluids*, 2008. **46**(1): p. 10-20.
138. Blas, F.J. and A. Galindo, *Study of the high pressure phase behaviour of CO<sub>2</sub>+n-alkane mixtures using the SAFT-VR approach with transferable parameters*. *Fluid Phase Equilibria*, 2002. **194–197**(0): p. 501-509.

139. Waldo, G.S., et al., *Sulfur speciation in heavy petroleums: Information from X-ray absorption near-edge structure*. *Geochimica et Cosmochimica Acta*, 1991. **55**(3): p. 801-814.
140. Gabric, B., et al., *Extraction of S- and N-Compounds from the Mixture of Hydrocarbons by Ionic Liquids as Selective Solvents*. *The Scientific World Journal*, 2013. **2013**: p. 11.
141. Elizalde-Solis, O. and L. Galicia-Luna, *Solubility of thiophene in carbon dioxide and carbon dioxide+ 1-propanol mixtures at temperatures from 313 to 363K*. *Fluid phase equilibria*, 2005. **230**(1): p. 51-57.
142. Zúñiga-Moreno, A., L.A. Galicia-Luna, and F.F. Betancourt-Cárdenas, *Compressed liquid densities and excess volumes of CO<sub>2</sub> thiophene binary mixtures from 313 to 363K and pressures up to 25MPa*. *Fluid Phase Equilibria*, 2005. **236**(1–2): p. 193-204.
143. Müller, E.A. and K.E. Gubbins, *Molecular-Based Equations of State for Associating Fluids: A Review of SAFT and Related Approaches*. *Industrial & Engineering Chemistry Research*, 2001. **40**(10): p. 2193-2211.
144. Khelassi-Sefaoui, A., et al., *Measurement and correlation of vapour pressures of pyridine and thiophene with [EMIM][SCN] ionic liquid*. *The Journal of Chemical Thermodynamics*, 2014. **72**(0): p. 134-138.
145. Chen, Y., F. Mutelet, and J.-N. Jaubert, *Experimental Measurement and Modeling of Phase Diagrams of Binary Systems Encountered in the Gasoline Desulfurization Process Using Ionic Liquids*. *Journal of Chemical & Engineering Data*, 2014. **59**(3): p. 603-612.
146. AIChE, *Design Institute for Physical Properties DIPPR Project 801 - Full Version*. *Design Institute for Physical Property Research/AIChE*.
147. Design Institute for Physical Property, D., *DIPPR Project 801, full version evaluated standard thermophysical property values*. 2005.
148. Sapei, E., et al., *Isobaric vapor–liquid equilibrium for binary systems containing benzothiophene*. *Fluid Phase Equilibria*, 2011. **307**(2): p. 180-184.
149. Bai, J., et al., *Isobaric vapor–liquid equilibrium for four binary systems of thiophene*. *Fluid Phase Equilibria*, 2012. **315**(0): p. 84-90.
150. Blas, F.J. and A. Galindo, *Study of the high pressure phase behaviour of CO<sub>2</sub> + n-alkane mixtures using the SAFT-VR approach with transferable parameters*. *Fluid phase equilibria*, 2002. **194**: p. 501-509.
151. McCabe, C. and S.B. Kiselev, *Application of Crossover Theory to the SAFT-VR Equation of State: SAFT-VRX for Pure Fluids*. *Industrial & Engineering Chemistry Research*, 2004. **43**(11): p. 2839-2851.
152. Wyczalkowska, A.K., J.V. Sengers, and M.A. Anisimov, *Critical fluctuations and the equation of state of Van der Waals*. *Physica A: Statistical Mechanics and its Applications*, 2004. **334**(3–4): p. 482-512.
153. Zúñiga-Moreno, A. and L.A. Galicia-Luna, *Compressed Liquid Densities and Excess Volumes for the Binary System CO<sub>2</sub> + N,N-Dimethylformamide (DMF) from (313 to 363) K and Pressures up to 25 MPa*. *Journal of Chemical & Engineering Data*, 2005. **50**(4): p. 1224-1233.
154. Toghiani, H., R.K. Toghiani, and D.S. Viswanath, *Vapor-liquid equilibria for the methanol-benzene and methanol-thiophene systems*. *Journal of Chemical & Engineering Data*, 1994. **39**(1): p. 63-67.
155. Erlin, S., et al., *Vapor–Liquid Equilibrium for Binary System of 1-Propanethiol, Thiophene, and Diethyl Sulfide with Toluene at 90.03 kPa*. *Journal of Chemical & Engineering Data*, 2006. **51**(4): p. 1372-1376.
156. Triday, J.O., *Vapor-liquid equilibria in binary systems formed by thiophene and light alcohols*. *Journal of Chemical & Engineering Data*, 1983. **28**(3): p. 307-310.
157. Guo, B., et al., *Isobaric vapor–liquid equilibrium for four binary systems of 3-methylthiophene*. *Fluid Phase Equilibria*, 2012. **320**(0): p. 26-31.

158. Freitas, S.V.D., et al., *Measurement and prediction of speeds of sound of fatty acid ethyl esters and ethylic biodiesels*. 2013.
159. Demirbas, A., *Biodegradability of biodiesel and petrodiesel fuels*. Energy Sources, Part A: Recovery, Utilization and Environmental Effects, 2009. **31**(2): p. 169-174.
160. Ciolkosz, D. *Renewable and Alternative Energy Fact Sheet*. 2009.
161. *Global Renewable Fuels Alliance*. 2009.
162. Okechukwu, A.C., *Calculation of Physical and Phase Equilibrium Properties for Biofuels Processes*, in *Department of Chemical Engineering and Chemical Technology*. 2010, Imperial College London.
163. Saxena, P., J.C. Patel, and M.H. Joshipura, *Prediction of Vapor Pressure of Fatty Acid Methyl Esters*. Procedia Engineering, 2013. **51**(0): p. 403-408.
164. Saxena, P., S. Jawale, and M.H. Joshipura, *A Review on Prediction of Properties of Biodiesel and Blends of Biodiesel*. Procedia Engineering, 2013. **51**(0): p. 395-402.
165. Perdomo, F.A. and A. Gil-Villegas, *Molecular thermodynamics of biodiesel fuel compounds*. Fluid Phase Equilibria, 2010. **293**(2): p. 182-189.
166. Perdomo, F.A. and A. Gil-Villegas, *Predicting thermophysical properties of biodiesel fuel blends using the SAFT-VR approach*. Fluid Phase Equilibria, 2011. **306**(1): p. 124-128.
167. Perdomo, F.A., B.M. Millán, and J.L. Aragón, *Predicting the physical–chemical properties of biodiesel fuels assessing the molecular structure with the SAFT– $\gamma$  group contribution approach*. Energy, 2014. **72**(0): p. 274-290.
168. Oliveira, M.B., et al., *Development of simple and transferable molecular models for biodiesel production with the soft-SAFT equation of state*. Chemical Engineering Research and Design, 2014. **92**(12): p. 2898-2911.
169. Llovell, F. and L.F. Vega, *Accurate modeling of supercritical CO<sub>2</sub> for sustainable processes: Water + CO<sub>2</sub> and CO<sub>2</sub> + fatty acid esters mixtures*. The Journal of Supercritical Fluids, 2015. **96**(0): p. 86-95.
170. NguyenHuynh, D., et al., *Predicting VLE of heavy esters and their mixtures using GC-SAFT*. Fluid Phase Equilibria, 2008. **264**(1–2): p. 184-200.
171. Barreau, A.B., I ; de Hemptinne, JC; Coupard, V ; Canet, X ; Rivollet, F, *Measurements of Liquid-Liquid Equilibria for a Methanol plus Glycerol plus Methyl Oleate System and Prediction Using Group Contribution Statistical Associating Fluid Theory*. Industrial & Engineering Chemistry Research, 2010. **49**(12): p. 5800-5807.
172. Llovell, F., et al., *Water+1-alkanol systems: Modeling the phase, interface and viscosity properties*. Fluid Phase Equilibria, 2013. **360**(0): p. 367-378.
173. Gross, J. and G. Sadowski, *Application of perturbation theory to a hard-chain reference fluid: an equation of state for square-well chains*. Fluid Phase Equilibria, 2000. **168**(2): p. 183-199.
174. Jessica D. Haley, G.D., and Clare McCabe. *Developing a Model for Carbon Dioxide using the modified Group Contribution-SAFT-VR with Dipole Theory*. in *American Institute of Chemical Engineers*. 2014. Atlanta, GA.
175. Konynenburg, P.H.v. and R.L. Scott, Phil. Trans., 1980. **A298**: p. 495-540.
176. Scott, R.L. and P.H.v. Konynenburg, Discussion Faraday Society, 1970. **49**: p. 87-97.
177. Sivagurunathan, P., K. Dharmalingam, and K. Ramachandran, *FTIR Study of Hydrogen Bonding Between Acrylic Esters and Alcohols*. Journal of Solution Chemistry, 2006. **35**(11): p. 1467-1475.
178. Dharmalingam, K., et al., *Molecular interactions in alcohol–ethyl methacrylate mixtures*. Spectrochimica Acta Part A: Molecular and Biomolecular Spectroscopy, 2008. **69**(2): p. 467-470.
179. Dharmalingam, K., K. Ramachandran, and P. Sivagurunathan, *Hydrogen bonding interaction between acrylic esters and monohydric alcohols in non-polar solvents: An*

- FTIR study*. Spectrochimica Acta Part A: Molecular and Biomolecular Spectroscopy, 2007. **66**(1): p. 48-51.
180. Sivagurunathan, P., K. Dharmalingam, and K. Ramachandran, *Molecular interaction studies of acrylic esters with 1-alcohols*. Spectrochimica Acta Part A: Molecular and Biomolecular Spectroscopy, 2006. **64**(1): p. 127-129.
181. Shimoyama, Y., et al., *Measurement and correlation of vapor-liquid equilibria for ethanol+ethyl laurate and ethanol+ethyl myristate systems near critical temperature of ethanol*. Fluid Phase Equilibria, 2008. **264**(1-2): p. 228-234.
182. Carvalho, P.J. and J.A.P. Coutinho, *On the Nonideality of CO<sub>2</sub> Solutions in Ionic Liquids and Other Low Volatile Solvents*. The Journal of Physical Chemistry Letters, 2010. **1**(4): p. 774-780.
183. Roebuck, K., *CCS - Carbon Capture and Storage: High-impact Strategies - What You Need to Know: Definitions, Adoptions, Impact, Benefits, Maturity, Vendors*. 2012: Emereo Publishing. 212.
184. Li, H., *Thermodynamic Properties of CO<sub>2</sub> Mixtures and Their Applications in Advanced Power Cycles with CO<sub>2</sub> Capture Processes [Elektronisk resurs]*. 2008, Stockholm: KTH.
185. Li, H., et al., *PVTxy properties of CO<sub>2</sub> mixtures relevant for CO<sub>2</sub> capture, transport and storage: Review of available experimental data and theoretical models*. Applied Energy, 2011. **88**(11): p. 3567-3579.
186. Kraska, T. and K.E. Gubbins, *Phase Equilibria Calculations with a Modified SAFT Equation of State. 1. Pure Alkanes, Alkanols, and Water*. Industrial & Engineering Chemistry Research, 1996. **35**(12): p. 4727-4737.
187. Kraska, T. and K.E. Gubbins, *Phase Equilibria Calculations with a Modified SAFT Equation of State. 2. Binary Mixtures of n-Alkanes, 1-Alkanols, and Water*. Industrial & Engineering Chemistry Research, 1996. **35**(12): p. 4738-4746.
188. Huang, S.H. and M. Radosz, *Equation of state for small, large, polydisperse, and associating molecules: extension to fluid mixtures*. Industrial & Engineering Chemistry Research, 1991. **30**(8): p. 1994-2005.
189. Passarello, J.P., S. Benzaghrou, and P. Tobaly, *Modeling Mutual Solubility of n-alkanes and CO<sub>2</sub> Using SAFT Equation of State*. Industrial & Engineering Chemistry Research, 2000. **39**(7): p. 2578-2585.
190. Zhao, H. and C. McCabe, *Phase behavior of dipolar fluids from a modified statistical associating fluid theory for potentials of variable range*. The Journal of Chemical Physics, 2006. **125**(10): p. 104504.
191. Zhao, H., et al., *Predicting the Phase Behavior of Nitrogen + n-Alkanes for Enhanced Oil Recovery from the SAFT-VR Approach: Examining the Effect of the Quadrupole Moment*. The Journal of Physical Chemistry B, 2006. **110**(47): p. 24083-24092.
192. Gray, C.G. and K.E. Gubbins, *Theory of Molecular Fluids: I: Fundamentals*. International Series of Monographs on Chemistry. 1984: OUP Oxford.
193. Gray, C.G. and K.E. Gubbins, *Theory of Molecular Fluids: Fundamentals Volume I*. 1985: Oxford University Press, USA.
194. Barker, J.A. and D. Henderson, *Perturbation Theory and Equation of State for Fluids - Square-Well Potential*. Journal of Chemical Physics, 1967. **47**(8): p. 2856-2861.
195. Barker, J.A. and D. Henderson, *Perturbation Theory and Equation of State for Fluids .2. a Successful Theory of Liquids*. Journal of Chemical Physics, 1967. **47**(11): p. 4714-4721.
196. Barker, J.A. and D. Henderson, *What Is Liquid - Understanding States of Matter*. Reviews of Modern Physics, 1976. **48**(4): p. 587-671.
197. Boublik, T., *Hard-Sphere Equation of State*. Journal of Chemical Physics, 1970. **53**(1): p. 471-472.
198. Mansoori, G.A., et al., *Equilibrium Thermodynamic Properties of Mixture of Hard Spheres*. Journal of Chemical Physics, 1971. **54**(4): p. 1523-1525.



199. Galindo, A., et al., *The thermodynamics of mixtures and the corresponding mixing rules in the SAFT-VR approach for potentials of variable range*. *Molecular Physics*, 1998. **93**(2): p. 241-252.
200. Wertheim, M.S., *Exact Solution of Mean Spherical Model for Fluids of Hard Spheres with Permanent Electric Dipole Moments*. *Journal of Chemical Physics*, 1971. **55**(9): p. 4291-&.
201. Hore, M.J. and R. Composto, *Strategies for dispersing, assembling, and orienting nanorods in polymers*. *Current Opinion in Chemical Engineering*, 2013. **2**(1): p. 95-102.
202. Whitesides, G.M. and B. Grzybowski, *Self-Assembly at All Scales*. *Science*, 2002. **295**(5564): p. 2418-2421.
203. Boal, A.K., et al., *Self-assembly of nanoparticles into structured spherical and network aggregates*. *Nature*, 2000. **404**(6779): p. 746-748.
204. Knischka, R., et al., *Silsesquioxane-Based Amphiphiles*. *Langmuir*, 1999. **15**(14): p. 4752-4756.
205. Song, T., et al., *Aggregation behavior of two-arm fullerene-containing poly(ethylene oxide)*. *Polymer*, 2003. **44**(8): p. 2529-2536.
206. Song, T., et al., *Aggregation Behavior of C60-End-Capped Poly(ethylene oxide)s*. *Langmuir*, 2003. **19**(11): p. 4798-4803.
207. Storhoff, J., et al., *Sequence-Dependent Stability of DNA-Modified Gold Nanoparticles*. *Langmuir*, 2002. **18**(17): p. 6666-6670.
208. Waddon, A.J., et al., *Nanostructured Polyethylene-POSS Copolymers: Control of Crystallization and Aggregation*. *Nano Letters*, 2002. **2**(10): p. 1149-1155.
209. Westenhoff, S. and N.A. Kotov, *Quantum Dot on a Rope*. *Journal of the American Chemical Society*, 2002. **124**(11): p. 2448-2449.
210. Hill, H.D., et al., *Controlling the Lattice Parameters of Gold Nanoparticle FCC Crystals with Duplex DNA Linkers*. *Nano Letters*, 2008. **8**(8): p. 2341-2344.
211. Park, S.-J., et al., *The Structural Characterization of Oligonucleotide-Modified Gold Nanoparticle Networks Formed by DNA Hybridization*. *The Journal of Physical Chemistry B*, 2004. **108**(33): p. 12375-12380.
212. Sung, K.-M., et al., *Synthesis of Monofunctionalized Gold Nanoparticles by Fmoc Solid-Phase Reactions*. *Journal of the American Chemical Society*, 2004. **126**(16): p. 5064-5065.
213. Tokareva, I. and E. Hutter, *Hybridization of Oligonucleotide-Modified Silver and Gold Nanoparticles in Aqueous Dispersions and on Gold Films*. *Journal of the American Chemical Society*, 2004. **126**(48): p. 15784-15789.
214. Nie, Z., et al., *Self-assembly of metal-polymer analogues of amphiphilic triblock copolymers*. *Nature Materials*, 2007. **6**(8): p. 609 - 614.
215. Akcora, P., et al., *Anisotropic self-assembly of spherical polymer-grafted nanoparticles*. *Nature Materials*, 2009. **8**(4): p. 354 - 359.
216. Glotzer, S.C., et al., *Self-assembly of anisotropic tethered nanoparticle shape amphiphiles*. *Current Opinion in Colloid & Interface Science*, 2005. **10**(5-6): p. 287-295.
217. Kumar, S.K. and R. Krishnamoorti, *Nanocomposites: Structure, Phase Behavior, and Properties*. *Annual Review of Chemical and Biomolecular Engineering*, 2010. **1**(1): p. 37-58.
218. Zhang, Z., et al., *Tethered Nano Building Blocks: Toward a Conceptual Framework for Nanoparticle Self-Assembly*. *Nano Letters*, 2003. **3**(10): p. 1341-1346.
219. Song, T., S.H. Goh, and S.Y. Lee, *Mechanical behavior of double-C60-end-capped poly(ethylene oxide)*. *Polymer*, 2003. **44**(8): p. 2563-2567.
220. Moganty, S.S., et al., *Ionic-Liquid-Tethered Nanoparticles: Hybrid Electrolytes*. *Angewandte Chemie-International Edition*, 2010. **49**(48): p. 9158-9161.

221. Park, Y., et al., *CO<sub>2</sub> Capture Capacity and Swelling Measurements of Liquid-like Nanoparticle Organic Hybrid Materials via Attenuated Total Reflectance Fourier Transform Infrared Spectroscopy*. Journal of Chemical & Engineering Data, 2011. **57**(1): p. 40-45.
222. Goren, B.K., *Nanoparticle dispersion and foam morphology control of polymer nanocomposites via interface engineering and supercritical CO<sub>2</sub> assisted processing*, in *Polymer chemistry*. 2011, Rensselaer Polytechnic Institute.
223. Dutta, N., S. Egorov, and D. Green, *Quantification of Nanoparticle Interactions in Pure Solvents and a Concentrated PDMS Solution as a Function of Solvent Quality*. Langmuir, 2013. **29**(32): p. 9991-10000.
224. Dutta, N. and D. Green, *Nanoparticle Stability in Semidilute and Concentrated Polymer Solutions*. Langmuir, 2008. **24**(10): p. 5260-5269.
225. Lin, B., T.B. Martin, and A. Jayaraman, *Decreasing Polymer Flexibility Improves Wetting and Dispersion of Polymer-Grafted Particles in a Chemically Identical Polymer Matrix*. ACS Macro Letters, 2014. **3**(7): p. 628-632.
226. Yu, X., et al., *Giant surfactants provide a versatile platform for sub-10-nm nanostructure engineering*. Proceedings of the National Academy of Sciences, 2013. **110**(25): p. 10078-10083.
227. Chan, E.R., L.C. Ho, and S.C. Glotzer, *Computer simulations of block copolymer tethered nanoparticle self-assembly*. The Journal of Chemical Physics, 2006. **125**: p. 064905.
228. Chremos, A. and A.Z. Panagiotopoulos, *Structural Transitions of Solvent-Free Oligomer-Grafted Nanoparticles*. Physical Review Letters, 2011. **107**(10): p. 105503.
229. Horsch, M.A., Z. Zhang, and S.C. Glotzer, *Self-Assembly of Polymer-Tethered Nanorods*. Physical Review Letters, 2005. **95**(5): p. 056105.
230. Iacovella, C.R., et al., *A model-integrated computing approach to nanomaterials simulation*. Theoretical Chemistry Accounts, 2012. **132**(1): p. 1-9.
231. Iacovella, C.R. and S.C. Glotzer, *Phase behavior of ditethered nanospheres*. Soft Matter, 2009. **5**(22): p. 4492-4498.
232. Iacovella, C.R. and S.C. Glotzer, *Complex Crystal Structures Formed by the Self-Assembly of Ditethered Nanospheres*. Nano Letters, 2009. **9**(3): p. 1206-1211.
233. Iacovella, C.R., et al., *Phase Diagrams of Self-Assembled Mono-Tethered Nanospheres from Molecular Simulation and Comparison to Surfactants*. Langmuir, 2005. **21**(21): p. 9488-9494.
234. Iacovella, C.R., M.A. Horsch, and S.C. Glotzer, *Local ordering of polymer-tethered nanospheres and nanorods and the stabilization of the double gyroid phase*. The Journal of Chemical Physics, 2008. **129**.
235. Keys, A.S., C.R. Iacovella, and S.C. Glotzer, *Characterizing Structure Through Shape Matching and Applications to Self-Assembly*. Annual Review of Condensed Matter Physics, 2011. **2**(1): p. 263-285.
236. Nguyen, T.D. and S.C. Glotzer, *Switchable Helical Structures Formed by the Hierarchical Self-Assembly of Laterally Tethered Nanorods*. Small, 2009. **5**(18): p. 2092-2098.
237. Martin, T.B., A. Seifpour, and A. Jayaraman, *Assembly of copolymer functionalized nanoparticles: a Monte Carlo simulation study*. Soft Matter, 2011. **7**(13): p. 5952-5964.
238. Jayaraman, A. and K.S. Schweizer, *Structure and assembly of dense solutions and melts of single tethered nanoparticles*. The Journal of Chemical Physics, 2008. **128**: p. 164904.
239. Martin, T.B. and A. Jayaraman, *Effect of matrix bidispersity on the morphology of polymer-grafted nanoparticle-filled polymer nanocomposites*. Journal of Polymer Science Part B: Polymer Physics, 2014. **52**(24): p. 1661-1668.

240. Martin, T.B. and A. Jayaraman, *Identifying the Ideal Characteristics of the Grafted Polymer Chain Length Distribution for Maximizing Dispersion of Polymer Grafted Nanoparticles in a Polymer Matrix*. *Macromolecules*, 2013. **46**(22): p. 9144-9150.
241. McCabe, C. and A. Galindo, *SAFT associating fluids and fluid mixtures*. *Applied Thermodynamics of Fluids*, 2010: p. 215-279.
242. McCabe, C., et al., *Predicting the high-pressure phase equilibria of binary mixtures of n-alkanes using the SAFT-VR approach*. *International Journal of Thermophysics*, 1998. **19**(6): p. 1511-1522.
243. McCabe, C., et al., *Predicting the high-pressure phase equilibria of binary mixtures of perfluoro-n-alkanes plus n-alkanes using the SAFT-VR approach*. *Journal of Physical Chemistry B*, 1998. **102**(41): p. 8060-8069.
244. McCabe, C., et al., *Examining the Adsorption (Vapor–Liquid Equilibria) of Short-Chain Hydrocarbons in Low-Density Polyethylene with the SAFT-VR Approach*. *Industrial & Engineering Chemistry Research*, 2001. **40**(17): p. 3835-3842.
245. Zhao, H., M.C. dos Ramos, and C. McCabe, *Development of an equation of state for electrolyte solutions by combining the statistical associating fluid theory and the mean spherical approximation for the nonprimitive model*. *The Journal of Chemical Physics*, 2007. **126**(24): p. 244503.
246. Gil-Villegas, A., A. Galindo, and G. Jackson, *A statistical associating fluid theory for electrolyte solutions (SAFT-VRE)*. *Molecular Physics*, 2001. **99**(6): p. 531-546.
247. Anderson, J.A., Chris D. Lorenz, and A. Travesset, *General purpose molecular dynamics simulations fully implemented on graphics processing units*. *Journal of Computer Physics*, 2008. **227**(10): p. 5342-5359.
248. Lee, C.K. and C.C. Hua, *Nanoparticle interaction potentials constructed by multiscale computation*. *The Journal of Chemical Physics*, 2010. **132**(22): p. 224904.
249. Chan, E.R., et al., *Simulations of Tetra-Tethered Organic/Inorganic Nanocube–Polymer Assemblies*. *Macromolecules*, 2005. **38**(14): p. 6168-6180.
250. Martin, M.G. and J.I. Siepmann, *Transferable potentials for phase equilibria. 1. United-atom description of n-alkanes*. *Journal of Physical Chemistry B*, 1998. **102**(14): p. 2569-2577.
251. Jorgensen, W., D. Maxwell, and J. Tirado-Rives, *Development and Testing of the OPLS All-Atom Force Field on Conformational Energetics and Properties of Organic Liquids*. *Journal of American Chemical Society*, 1996. **118**: p. 11225-11236.
252. Shen, V.K., D.W. Siderius, and W.P. Krekelberg. *NIST Standard Reference Simulation Website, NIST Standard Reference Database Number 173*. 2013 8/27/2013; Available from: [http://www.cstl.nist.gov/srs/LJ\\_PURE/sattmmc.htm](http://www.cstl.nist.gov/srs/LJ_PURE/sattmmc.htm).
253. Pan, S., et al., *Particle Formation by Supercritical Fluid Extraction and Expansion Process*. *The Scientific World Journal*, 2013. **2013**: p. 1-6.
254. Sun, Y.-P. and H.W. Rollins, *Preparation of polymer-protected semiconductor nanoparticles through the rapid expansion of supercritical fluid solution*. *Chemical Physics Letters*, 1998. **288**(2–4): p. 585-588.
255. Thakur, R. and R.B. Gupta, *Formation of phenytoin nanoparticles using rapid expansion of supercritical solution with solid cosolvent (RESS-SC) process*. *International Journal of Pharmaceutics*, 2006. **308**(1–2): p. 190-199.